SCUOLA DI DOTTORATO
UNIVERSITÀ DEGLI STUDI DI MILANO-BICOCCA

Dipartimento di / Department of

Scienze dell'Ambiente e della Terra

Dottorato di Ricerca in/PhD program Scienze Chimiche, Geologiche e Ambientali Ciclo/Cycle XXXVI

Curriculum in (se presente / if it is) Scienze dell'Ambiente Terrestre e Marino

TITOLO TESI / THESIS TITLE

"Three-dimensional study of the atmospheric heating rate from Equator to the Arctic"

Cognome / Surname Losi Nome / Name Niccolò

Matricola / Registration number 748322

Tutore / Tutor: Citterio Sandra

Cotutore / Co-tutor:
(se presente / if there is one)

Supervisor: Ferrero Luca
(se presente / if there is one)

Coordinatore / Coordinator: Marco Giovanni Malusà

ANNO ACCADEMICO / ACADEMIC YEAR 2022/2023

INDEX

1. Introduction

From a general perspective, this work focuses on the link between short-lived climate forcers (SLCFs) and climate change. In the last decades rapid and intense changes occurred in the ocean, atmosphere, biosphere and cryosphere, and it is now established that human activity has played a major role in driving these changes [1]. Currently, there is very high confidence that atmospheric CH_4 concentration is higher than at any time in at least 800,000 years, while CO_2 concentrations is higher than it has been for the past 2 million years [1]. In addition to long-lived greenhouse gases (GHGs), increasing attention has been paid to SLCFs. They are substances, chemically and physically reactive, with a relative short atmospheric lifetime compared to CO_2 [2] (less than two decades). They include anthropogenic and natural aerosols (and their precursors), such as nitrate, sulfate and black carbon [3]. Aerosols have a lifetime in atmosphere from minutes to weeks and thus mitigation policies can provide near-term benefits for health and climate [4]. They can have either a cooling or warming effect on climate, altering the Earth's radiation budget in several ways: by interacting directly (absorption and scattering) with solar radiation (direct effect) and by affecting cloud formation, life-time and properties through indirect effects (they can act as cloud condensation nuclei and ice nuclei) [5] and semi-direct effects (they can alter the lightness of clouds and warm the surrounding atmosphere, causing evaporation of water droplets). CCN availability not only influence cloud formation, but also cloud properties: clouds formed in a particle-rich atmosphere have a greater number of drops but smaller in size, thus increasing the reflection of solar radiation. Moreover, smaller cloud particles decrease the precipitation efficiency, prolonging cloud lifetime. Therefore, indirect and semi-direct aerosol effects (related to clouds) affect climate, altering not only the radiation budget, but also the precipitation pattern. Among the different aerosol species, we focused on those ones capable of absorbing solar radiation, named light absorption aerosols (LAA); therefore we focused on their direct effect. LAA are explored in section 1.1.

Climate change is a global phenomenon, but it is not homogeneous across the globe. Indeed, the surface atmospheric temperature increase was faster in the Arctic region, due to some specific characteristics (such as the presence of sea-ice) that amplify warming through positive feedback. This phenomenon is known as Arctic Amplification (AA) and its causes (including the role of aerosols) will be discussed in section 1.2.

The purpose of this thesis is precisely to study the influence of LAA direct forcing on AA. As we will see in more detail in the following sections, the impact of LAA on Arctic climate is due to an interplay of local and remote effects: they can be emitted or transported in the Arctic and exert their forcing here, just as they can alter the atmospheric energy transport from tropics and mid-latitudes to the North Pole because of their forcing at lower latitudes. This topic is

particularly relevant in the Anthropocene, which is characterized by major changes in the Arctic region due to human impact. Most of the inherent studies are modelling [6–10] and there is a lack of experimental data concerning the LAA direct forcing from lower latitudes to the Arctic. Therefore, in order to investigate these mechanisms from an experimental perspective and better understand which of the two aerosol effects (local and remote) is prevalent, we took part in 5 measurement campaigns onboard two different research vessels. These expeditions made it possible to collect particulate matter on filters (so as to determine its chemical composition and hygroscopic properties) and measure solar radiation (and its components), LAA concentrations and absorption coefficients. From these data we computed the LAA direct forcing, using a completely experimental method developed by Ferrero et al. [11] and obtained by cumulatively taking into account LAA absorption coefficients and incident radiation (direct, diffuse and reflected) across the entire solar spectrum. The direct forcing is expressed in terms of K/day, through a parameter known as Heating Rate (HR) and described in the next chapter. Three of the five campaigns were carried out in summer between mid-latitudes (Gdansk, Poland) and Arctic (North of Svalbard) and lasted about three months. They represent the core of this research, having covered a wide area (in the latitudinal direction) and having been repeated over time. The other two campaigns, instead, were carried out in winter in different regions. The first one took place in the tropical North Atlantic (near Barbados) and lasted one month. It allowed us to collect data in the tropical area of the Northern Hemisphere as well, including these lower latitudes in the study. The second one took place in the Baltic Sea between Gdansk and the Gulf of Bothnia and lasted about two weeks. It allowed to collect data also in the winter season from mid to higher latitudes and make the first comparisons between different seasons in an area comparable, at least in part, to that of the summer campaigns.

All measurement campaigns, research vessels, specific routes, period and duration, instruments used and their installation are described in detail in the second chapter, devoted to methodology. Next chapter also contains all the information regarding the general methodology, common to all the following chapters. Indeed, most of the instruments used, computations and data processing, as well as analyses performed are the same. However, it is possible that some additional and specific methods may have been used to obtain the results of the individual chapters. Therefore, each chapter contains its own specific methodology section, also useful to clarify what data were used (from what campaigns or sections of campaigns and from what instruments/analysis). Besides the second one, all others are devoted to a specific topic. Chapter 3 describes the context and results from the campaign in the Tropics. Chapter 4 introduces the context of the Arctic campaigns, addressing the first macroscopic latitudinal differences (be-

tween mid-latitude and Svalbard Islands) from the perspective of particulate matter (PM) chemical composition. Chapter 5 focuses on high-resolution measurements only in the Arctic region, examining the local impact (direct forcing) of LAA and the differences between the pristine background of the Arctic Ocean and the local emission hotspots (such as the human settlements). Chapter 6 addresses the main focus of the research, describing high-resolution data and results from mid-latitudes to the Arctic. In this chapter the latitudinal HR gradient and energy gradient are shown, allowing to answer the key question of this research. There is obviously a further need to proceed with research on this topic, as several questions remain open. Therefore, the last short chapter (seven) focuses on the future perspectives.

Therefore, despite an underlying coherence and a common thread, each chapter was structured to stand on its own. Indeed, except for references to the common methodology, each topic contains its own introduction, specific methodology, results and conclusions (as a kind of stand-alone paper). Beyond this general introduction (useful for presenting the work), the specific introductions provide the theoretical framework and expand on the concepts of each specific topic. Finally, we draw the conclusions common to all the work.

1.1. Light Absorbing Aerosols

As previous mentioned, LAA are the aerosol species capable of absorbing solar radiation and heat the surrounding air, exerting a positive forcing. They are Black Carbon (BC), Brown Carbon (BrC) and mineral dust. Light absorption in the atmosphere is generally dominated by BC, with additional significant contributions by BrC and dust [12]. Their light absorption can contribute not only to the direct radiative forcing (which is the focus of this work), but also to the semi-direct radiative forcing, altering the atmospheric stability and cloud properties.

Mineral dust refers to particles in the form of aggregates containing a wide variety of minerals and more than half of its atmospheric burden originates from the Saharan region [12]. Except for mineral dust (whose source is crustal), other LAA are carbonaceous materials that result from incomplete combustion of fossil fuels, biofuels and biomass (or photochemistry in the atmosphere for BrC formation). These process produces a mixture mainly composed of BC and Organic Carbon (OC), but it can also include other materials, as metals or sulfates. The carbonaceous fraction made almost purely of carbon and black-colored is named BC. This material has a unique combination of physical properties [13] (e.g. is highly refractory and insoluble in water and common organic solvents) and the term BC refers to its optical properties (indeed is used when it is measured by optical instruments). When measured with instruments that rely on other methodologies and its other physical properties, it is called in different ways (e.g. elemental carbon if it has been determined thermally) [14]. BC is thus primarily formed in

flames (i.e. it is a primary particulate pollutant species) and exists as an aggregate of small spheres. In particular it is made of nanometric spherules (1 – 5 nm), with wrinkled graphite layers forming a shell around a hollow or disordered interior [15], which aggregate in particles (0.1 – 1 μm). Indeed, the graphitic spherules coagulate to form aggregates or fractal chain-like structures (composed of hundreds or thousands of spherules), on which water vapor and other gas-phase species can then condense (collapsing the aggregates into more densely packed clusters) [13]. BC particles are thus largely found in the Aitken mode (less than 100 nm diameter, i.e. nanoparticles) due to the formation mechanism (although a difference in size may exist based on the source [16]). Because of its size BC absorbs all wavelengths of solar radiation (from ultraviolet to infrared), especially visible light and the absorption is proportional to its mass and volume [12].

As mentioned above, the carbonaceous aerosol also consists of OC, which also contain hydrogen and oxygen and other heteroatoms [1]. Composition and ratio between OC and BC depend on the fuel burned and the source [17]. BrC is part of OC, with a brownish or yellowish visual appearance [12], that absorb solar radiation. BrC absorption has a greater spectral dependence (decreases more with λ) than BC, increasing sharply from the vis to the UV. Therefore, it absorbs less effectively than BC in the visible spectrum, while it absorbs mainly in the UV range. The complexity of light-absorbing organic compounds and variations in their relative concentrations make it difficult to characterize the molecular composition and determine which types of molecules or molecular aggregates dictate the optical properties of BrC [18]. While BC is only a primary aerosol, OC instead can be of both primary or secondary origin [1], as a result of chemical processes in the atmosphere [18].

Atmospheric removal occours whithin a few days to weeks via wet and dry deposition. As a result, BC is found in remote regions at concentrations much lower than in source regions. Gliß et al. [19] estimated a BC and BrC lifetime of 5.5 days ± 35% and 6.0 days ± 29% (median ± 1 standard deviation), respectively.

In general, multi-year decline in BC burdens over several Northern Hemisphere areas has been reported [1], but there is a large spread among models [19] in characterizing the global trends of carbonaceous aerosols, also because of the lack of global observations.

BC is one of the largest individual warming agents in the atmosphere and its contribution to global warming in mainly due to the light absorption (direct radiative forcing). Wang et al. [20] determined a BC radiative forcing (RF) of 0.61 W m^{-2}. More recently, the 2021 IPCC report estimated a BC effective RF (including all the direct and cloud effects) of 0.11 W m^{-2} ranging from -0.20 to 0.42 W m^{-2}, with a portion of the BC positive direct RF masked by BC effetcs on cloud changes and lapse rate and atmospheric water vapour changes [1]. However, a large

uncertainty (large range) about the BC total and direct RF was reported, due to uncertainties in BC emissions, lifetime, ageing and mixing process, as well as to neglect in composition and morphology variations. Indeed, Kelesidis et al. [21] have shown that models (also used in the AR6 IPCC report) could underpredict significantly the BC direct RF, mostly due to the assumed spherical BC morphology. They simulated BC direct RF accounting for the realistic BC morphology and coating, and found higher values (+22% on average), between 3 and 5 W m^{-2}, in East, South Asia, sub-Sahara, western Africa, and the Arabian peninsula (in agreement with RF satellite and AERONET observations). Therefore, simplifications and errors in BC morphology and coating, as well as its refractive index (which is often underestimated [21,22]) in models can still lead to biases in the estimation of regional and global BC effects on climate.

Direct effect of BC aerosol is the main focus of this research, but in addition it may exert indirect and semi-sirect effects. BC is co-emitted with a variety of other aerosols and aerosols precursor (i.e. gases) and, moreover, it mixes with other aerosol components in the atmosphere after its emission. These mechanisms increases its hydrophilicity and ability to act as CCN, influencing its atmospheric removal rate and its indirect and semi-direct forcings. Indeed, the incorporation of BC into cloud droplets can affect the cloud's albedo, water content and rainfall potential. Moreover its light absorption alters the atmospheric temperature structure within, below or above clouds, affecting the cloud distribution [13].

Finally, BC and other LAA can also deposit on snow and ice, reducing surface albedo and causing a positive climate forcing.

1.2. Arctic Amplification

As early as 1896, Arrhenius sensed that changes in the concentration of CO_2 in the atmosphere could alter the atmospheric surface temperature and that this warming would be especially high at the Poles. This behavior was then identified through modeling studies of Manabe and Wetherald [23] in 1975. To the present day, recent studies found that surface temperature increase in the Arctic is 3 [24] to 4 times faster than the rest of the globe [25], with significant consequences for the ecosystems [7]. This phenomenon is called Arctic Amplification (AA) and varies according to season and location (Figure 1). Indeed, it is maximum in the European sector of the Arctic region, near Svalbard archiplegao, and in fall and winter. As a result of the rapid warming, between 2011 and 2020 the annual average Arctic area covered by sea ice reached its lowest level since at least 1850 [1]; sea-ice cover in September 2019 was only about 28% of the March 2019 extension [26].

The AA concept will be addressed, deepened and specifically centered on our research in the introductions of chapter 5 and, especially, chapter 6. This is meant to be a general overview to introduce the topic.

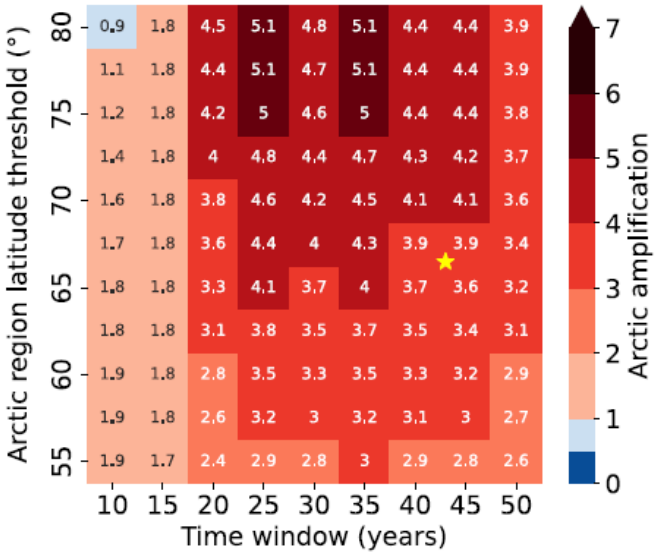

Figure 1. *The sensitivity of AA to the time window used in calculating the linear trends (x-axis) and the southern boundary of the Arctic (y-axis). The end year of all linear trends is fixed to 2021. The star marks the baseline value used in the study, corresponding to the 43-year linear trend and the southern boundary of 66.5°N. The observed AA is derived from the average of the four observational datasets. (Rantanen et ., 2022)*

The main mechanism beyond AA is related to the sea ice reduction, but the causes of AA are several and their relative role is still not entirely clear. They act at different spatial and temporal scales, and are related to both internal feedbacks and external factors. Here, we provide a quick overview of the different mechanisms and feedbacks that contribute to AA (Figure 2).

The temperature feedback is the modification in longwave radiative fluxes because of changes in surface and tropospheric temperaures [27,28] and it composed of the Planck feedback and the lapse rate feedback. The first one is not induced by an inhomogeneous vertical warming, but is the basic response of the Earth system in order to stabilize the climate, whereby higher temperatures lead to an increase in outgoing longwave radiation. This response is lower over the Arctic cold region than the global mean, thus the outgoing longwave radiation per unit of local warming is less then at lower latitudes [29]. The lapse rate feedback is due to vertical differences in warming; it is generally negative at lower latitudes, but it is positive at the Poles because there is a strong stratification, especially in winter, that greatly limits the vertical mixing [27] (confining the additional heat in the lower troposphere, resulting in a positive lapse rate feedback).

Along with temperature feedbacks, surface albedo feedback is considered to have the main role in AA. Higher temperatures cause snow and ice melt, exposing surfaces which have much

lower albedo (such as ocean water when sea-ice melts) and thus increasing the absorption of shortwave radiation. Obviously, in the Arctic this process is present only during summer (when sunlight is present). Its contribution is crucial, despite the fact that AA is higher in winter, because summer is a key season in triggering the processes that then lead to AA in subsequent months. Indeed, in a warmer climate, less sea ice is present in summer, the surface albedo is reduced and the Arctic Ocean absorbs more solar radiation. Moreover, if less sea ice is available, a larger fraction of this energy goes into increasing sea temperatures rather than into melting ice [28,30]. Following the seasonal cycle of the heat uptake/loss by the ocean, the additional energy stored in summer (in the ocean mixing layer) is then released back to the atmosphere in fall and winter, as latent and sensible heat and longwave radiation. Indeed there is a spatial correspondence between the sea ice-loss and the surface atmospheric warming [31]. Moreover, the moistening and warming of the lower troposphere enhances the surface downwelling longwave radiation, which in turn inhibits the growth of sea ice thus helping to maintain the increased energy flux between ocean and atmosphere [28].

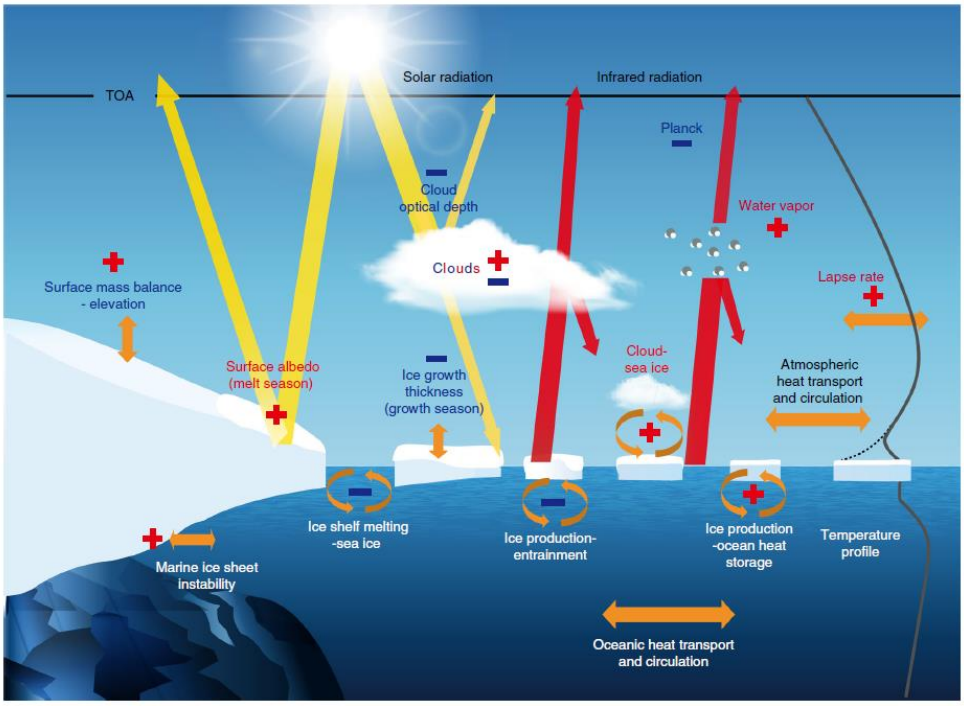

Figure 2. *Some important radiative and non-radiative feedbacks in polar regions involving the atmosphere, the ocean, sea ice and ice sheets. TOA refers to the top of the atmosphere. Shortwave (solar) radiation is in yellow and the longwave (infrared) radiation is in red. They represent the radiation exchanges. A red plus sign means that the feedback is positive, a negative blue sign corresponds to a negative feedback. The gray line on the right represents a simplified temperature profile in polar regions for the atmosphere and the ocean, the dashed line corresponding to a strong surface inversion. (Goosse et al., 2018)*

In addition, also water vapor and cloud feedbacks are present. In a warmer world, the water vapor content increases, enhancing the greenhouse effect (increase In surface downwelling

longwave radiation). It has a significant role, contributing to the atmospheric heating, however it is weaker at Poles and maximum at the tropics, thus contrasting the AA. Cloud feedbacks are very complex and subject to uncertainty, depending on several factors. In general an increase in low clouds is expected and was observed in last years [32]. This happens preferentially in fall and winter due to the heat and moisture fluxes from the ocean to the atmosphere. During the polar night the presence of low clouds increases the downwelling longwave radiation [27] and enhances the surface heating. Other processes not entirely clear may also take place, as the increase of water in mixed phase clouds. These cloud phase changes can led to addition downwelling longwave radiation, but at the same time increase the amount of reflected incoming radiation.

Over the land, in particular Greenland, the ice melting can lower the altitude of the ice sheet, exposing it to warmer atmosphere (surface mass balance elevation feedback) [33]. Moreover, also biological feedbacks exist. For example, a general greening of the Arctic region and a shift northward of the boreal forest are expected, leading to a surface albedo reduction and changing the interaction between vegetation, water vapor, clouds and sea ice [28,34]. An enhanced presence of phytoplankton in the Arctic Ocean can also led to an increase in solar radiation absorption (positive feedback) [35].

Another important contribution to AA is driven by the poleward heat transport from the ocean and the atmosphere. Oceanic transport into the Arctic is supposed to increase [36], as a result of a winter increase, but the causes are not completely clear. In addition, sea ice melting increases the vertical mixing and the entrance of warmer water from the lower levels into the mixing layer and most of this energy goes into warming the surface atmosphere and melting other sea ice [28]. Atmospheric transport can be divided in moisture transport and dry static energy (DSE). As mentioned above, the specific humidity increase is greater at the tropics than at higher latitudes, therefore the water vapor contributes to Arctic warming but counteracts AA (larger effect at lower latitudes). However, it can contribute indirectly to AA because this difference increases the poleward specific humidity gradient, enhancing the moisture transport [37]. Moreover, it has an additional positive contribution compared to DSE transport, because it increases the greenhouse effect (due to the water vapor itself and due to the enhanced cloudiness) [28]. DSE transport is influenced by mechanisms that increase or decrease the meridional temperature gradient. The magnitude of a reduction in DSE transport is the discriminant for the net sign of the total atmospheric transport northward. The interconnection between DSE transport and AA is strong and complex: DSE transport can be an important cause of AA, at the same time AA weakens the temperature gradient and thus the transport. The role of LAA in the DSE transport is the main topic of this research and it will be discussed

in particular in Chapter 6. Indeed aerosols can preferentially heat lower latitudes and thus increase the energy transport (remote effect), but they can also heat directly the Arctic atmosphere, inducing a local positive forcing and concurrently reducing the energy transport. The magnitude of the aforementioned heating rates is detailed and compared in chapter 6. This interplay determines the net effect ot the LAA on the Arctic climate. Finally, moisture and heating anomalies at midlatitudes and tropics can influence the large-scale circulation and can be propagated to the Arctic through synoptic eddies and Rossby waves [38,39]. Different sectors of the Arctic may be affected more by tropical anomalies or midlatitudes anomalies, because they act along different teleconnection pathways [40,41].

Obvioulsy, the mechanisms that act on AA are strongly linked. For example, energy transport influences the local feedbacks (e.g. surface albedo feedback), which in turn affect (decreasing) the energy transport (as seen for the aerosols). But they can worh also in the opposite direction: e.g., less sea ice enhances the atmospheric heat and moisture, which in turn affect (increasing) the loss of sea ice.

The causes of AA depends on the current climate state [28]. Indeed, AA is induced by the sea-ice cover, the latitudinal temperature gradient and the strong local atmospheric thermal inversion. However, these mechanisms will weaken as the Arctic warms and thus also AA will change.

1.2.1. Aerosol effects on the Arctic climate

BC and BrC (as well as dust) in the Arctic can exert a positive forcing. Their main sources at high latitudes, beyond local emissions by some hotspots, are the long-range transport from midlatitudes and summertime boreal fires [18]. In addition to the direct forcing in the atmosphere (which can influence the Arctic locally and remotely, as we discussed), aerosols can affect the AA also depositing on snow and ice (LAA decrease the surface albedo and thus accelerate the melting in spring and summer [42,43]) and through aerosol-cloud interactions. The role of aerosols in altering cloud formation and properites is particularly relevant in Arctic, mainly because they influence the low-level clouds, which are critical for the surface energy budget. Indeed, we have already discussed the fact that this kind of clouds contributes to the surface warming by re-emitting longwave radiation during the polar night (contrary to lower latitudes, where they have a cooling effect due to a predominant impact on short-wave radiation). Uncertainties in models about the aerosol species, concentration and processes (that are key controlling factors in cloud formation) are among the reasons for the difficulty in properly simulating low-level Arctic mixed-phase clouds [26]. The aerosol concentration is a limiting factor in this region, because it is sometimes too low to lead to low-cloud formation.

Therefore, perturbations (even minor) in the number and size of CCNs can strongly influence low-level clouds and the consequent surface warming (due to the lower solar radiation, especially in winter) [44]. An increase in aerosol concentration (and thus CCN) is expected due to both local human and natural activities. In particular, recent studies highlighted the importance of natural aerosol sources within the Arctic. These include mineral dust, which can increase due to the ice retreat and can exert an atmospheric direct radiative forcing, deposit on snow and ice (decreasing the surface albedo) and act as ice nucleating particle [26,45]. Also particles from forest fires are increasing due to increasingly frequent fires in high latitudes [46]. In particular, among the natural sources, is emerging the importance of the role of marine biogenic emissions during summer, which increase the number of CCN through secondary aerosol formation [47–49]. These emissions are increasing and are induced by the Arctic warming: sea ice loss exposes a larger ocean surface; as a result the ocean absorbs more sunlight, enhancing productivity (even an additional phytoplankton bloom in autumn was obeserved [50]), and emissions from the ocean to the atmosphere are facilitated. Moreover, the Arctic freshwater cycle (river outflow) is changing rapidly [51], modifying the microbial activity. Other secondary aerosol can result from iodic acid during autumnal freeze-up over the pack-ice and affect cloud formation [52]. Wrong natural aerosol concentrations and consequent feedbacks, as well as incorrect CCN number can be a source of error in models. Natural secondary aerosol is thus recognized to be increasingly important, especially given the change of the climate. However, biogenic sources dominate in summer, but are nearly absent in winter [28]. A foundamental role is played by the Arctic Haze in winter.

Arctic haze is a mixture of sulfate and organic aerosol and, in a lesser part, nitrate, ammonium, BC and BrC. It also includes relatively high levels of ozone precursors (e.g. NOx) and volatile organic compounds (VOCs) [53]. Aerosol haze particles are usually well aged. This phenomenon presents a clear seasonal cycle: it is maximum in late winter and early spring. Indeed, in this period, the Arctic atmosphere is stable and dry and thus the removal (deposition) processes are very slow; moreover, the polar dome extends southward (over enough cold lands), in particular over Nothern Eurasia, which becomes the major source of aerosols for the Arctic region via atmospheric transport. In the next months the polar dome retreats to the north and transportation is inhibited (also because of an increased wet deposition efficiency [54]). Therefore in winter and early spring higher concentrations of anthropic aerosols are present in Arctic. As a result, a seasonal cycle is observed in the Svalbard Islands: there is a maximum in particles mass in the arctic haze season, and a maximum in particle number concentration in summer due to the Aitken particles (that can be very important for low-level cloud formation) derived from secondary formation [28,54,55]. LAA concentrations are thus higher in the Arctic

haze season. Summer lower LAA concentrations exert a positive forcing. In winter there is no sunlight and LAA cannot exert their direct forcing in the atmosphere. However they can act as CCN, influencing the climate indirectly, and can deposit on snow and ice, altering the surface albedo in the following season. In early spring incoming shortwave radiation is present and can interact with LAA. However there is evidence that in spring long-range aerosol transport occurs at higher altitudes (above the inversion) in the Eurasian and Pacific sectors (in winter there is transport at lower levels, within the inversion, in much of the Arctic) [56]. LAA in the Arctic free troposphere could cool the surface, instead of heating it. In future, anthropic aerosols may increase in summer due to enhanced local human activities, while the transport from mid-latitudes may further decrease (Arctic aerosol burden already decreased over the past decades) due to mitigation policies at these latitudes.

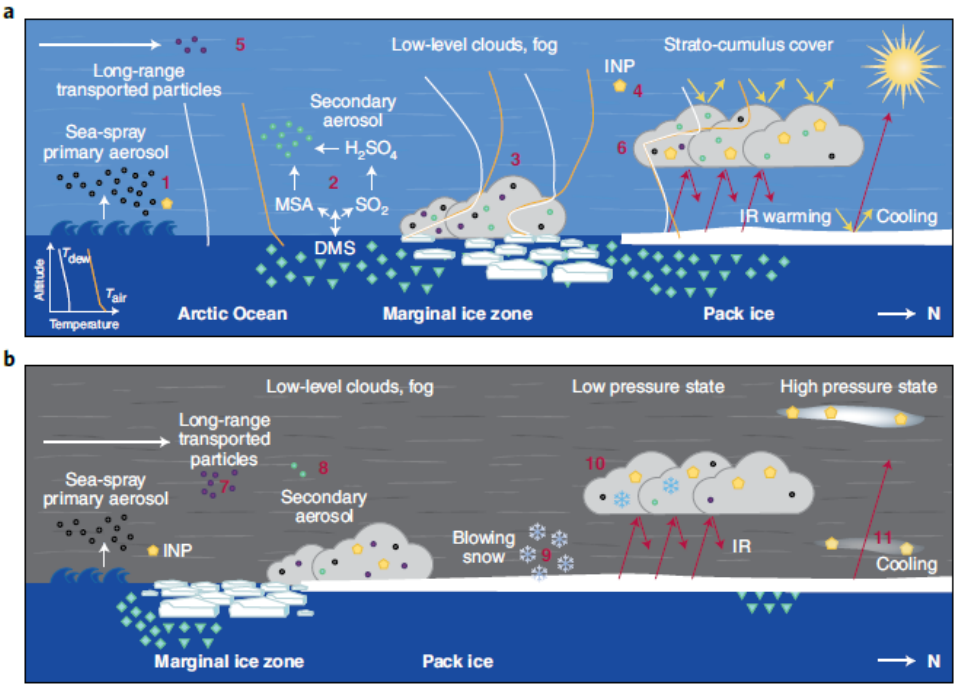

Figure 3. *Aerosol processes of climate relevance in the Arctic for polar day (**a**) and night (**b**). Process are explained in the main text. Illustrative temperature profiles are shown as white (dewpoint temperature) and orange (air temperature) curves, representing different atmospheric states during polar day in **a**. Yellow arrows indicate short-wave radiation, and red arrows indicate long-wave radiation. Light-blue shapes in the ocean represent various species of marine microorganisms. Circles in atmosphere and clouds represent secondary aerosols formed from marine microorganisms via process 2 (light blue), primary aerosols from sea spray (grey) and particles that arrive by long-range transport via processes 5 and 7 (purple). Yellow pentagons in atmosphere and clouds represent INPs (processes 4 and 9). (Schmale et al. 2021)*

Figure 3 shows the aerosol processes in Arctic during polar day and night, from Schmale et al. [26]: sea-spray primary emissions (in both seasons; **1**); long range transported particles (much higher in winter and early spring, **5**, and at lower altitudes in winter, **7**); marine and non-marine secondary aerosol formation (**2** and **8**; in winter, the biogenic marine emissions are

sharply reduced); particle processing in fog and low-clouds (**3**); Arctic INP concentrations (**4**); high Arctic cloud formation (**6**; downwelling longwave radiation but also shortwave radiation reflection when sunlight is present); wintertime cloud formation (**10**; not shortwave reflection and thus net surface warming, contribution of natural sources but also arctic haze anthropic particles); aerosol-sensitive clouds (winter; **11**); winter blowing snow (can contribute to CCN and INP; **9**).

Changes in the aerosol burden within the Arctic (both anthropic and natural) are already underway (e.g. more particles from Boreal forest fires, more sea-spray emissions and more marine primary organic aerosol, DMS and volatile organic carbon emissions). They will continue, modifying the aerosol–climate interactions [26].

2. Materials and Methods

This section aims to introduce the methodology common to all the measurement campaigns carried out to achieve the main purpose of this work: to experimentally determine the direct forcing (HR) of light absorbing aerosols from the tropics/mid-latitudes to the Arctic. Firstly, the campaigns in which we took part will then be presented (three AREX campaigns from mid-latitudes to Svalbard Islands, one EURC^{4}A campaign in the tropics and one winter campaign in the Baltic sea), describing the instrumentation used, the moving platform (research vessel) on which it was installed, the measurement period, and the route taken by the ship. Analytical techniques employed for offline analysis (aimed at defining the chemical composition of particulate matter) and instrumentation used for real-time (high resolution) measurements (aimed at determining LAA concentrations and HR) will then be described in detail. In particular, the methods common to all campaigns and, therefore, to all chapters that follow will be discussed here. Additional and topic-specific materials and methods will instead be described in the appropriate chapter (e.g elemental analysis in the third chapter, which deals in more detail with the chemical composition). Moreover, not all of the data obtained will be used in the various chapters. Thus, for each topic it will be specified which data (both off-line, i.e. analysed particulate matter filters, and on-line) were used and from which campaign, or campaign section. In fact, AREX campaigns are divided into sections by time and route (outward, central, and return) and by area (whole cruise or Arctic only).

2.1. Measurement campaigns

Five measurement campaigns were carried out for this work, which are presented here according to the area and with the same order in which they will appear in the following chapters: EURC^{4}A, AREX and BALTIC.

2.1.1. EUREC⁴A

EUREC^{4}A (ElUcidating the RolE of Cloud-Circulation Coupling in ClimAte) field campaign took place in the downstream winter trades of the North Atlantic, eastward and south-eastward of Barbados (tropical North Atlantic, Figure 4), and lasted more than four weeks, during which atmospheric, surface and oceanic processes operating across a very wide range of scales were investigated [57]. Several research vessels from different countries (France, Germany, U.S.) took part in this project, whose main purpose is to improve our understanding of the factors that influence clouds in the trades at different scales, how they will respond to warming, and their link to other components of the earth system, such as the mesoscale and sub-mesoscale dynamics of the upper ocean, the life-cycle of particulate matter, or air-sea gas

exchange [57]. Therefore, it was a wide campaign , with a broad and ambitious purpose. We focused on the particle scale, contributing to the ultimate goal through measurements of particulate chemical composition and concentration, LAAs and their direct forcing in terms of HR associated to different aerosol types. We also used LAA HR data to make a comparison between Tropics, mid-latitudes and North Pole in the framework of the present PhD program.

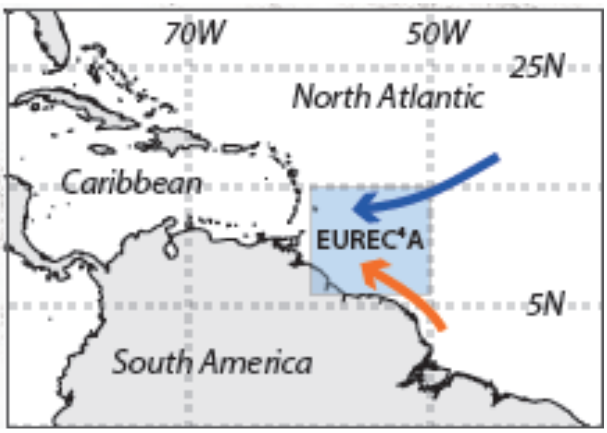

***Figure 4**. The EUREC4A study area in the lower trades of the North Atlantic. (Stevens et al., 2021)*

Intrumentation was installed on board the R/V L'Atalante (Figure 5). It belongs to the French oceanographic research fleet and is operated by IFREMER. . The ship performed a cruise from 20 January to 23 February 2020, sailing from Pointe-Pitre, Guadaloupe, and starting operations in Barbados water the following day. It collected ocean and atmosphere data from 6°N to 15°N and from 60°W to 52°W surveying the Tradewind Alley and the North Brazil Current eddy corridor (Boulevard des Tourbillons) in international waters and in the ZEEs of Barbados, Trinidad and Tobago, Guyana, Suriname, and French Guyana [57].

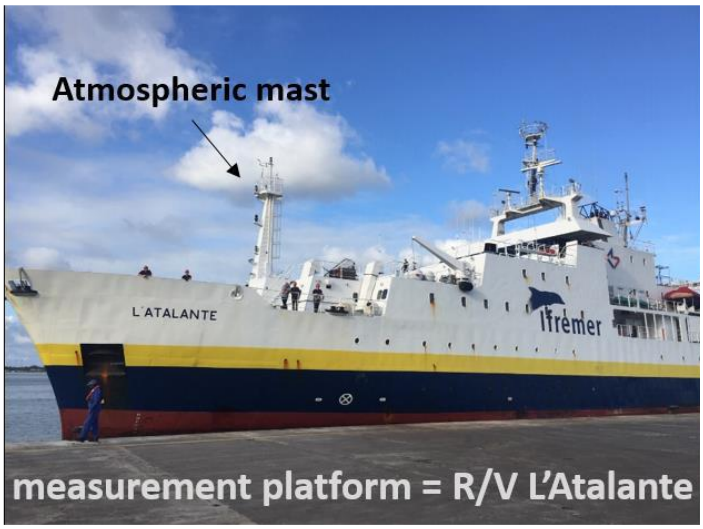

***Figure 5**. L'Atalante research vessel by IFREMER*

It was equipped with the following instrumentation: a NanoSCAN particle sizer (TSI inc., Shoreview, MN, U.S.) and an OPC (GRIMM Aerosol Technik, Ainring, Germany) to measure

particle number concentrations from 10 nm up to 32 μm; an Aethalometer (AE-33, Aerosol Magee Scientific, Slovenia) to infer LAA concentrations and absorption coefficients; a Hyperspectral radiometer ROX (JB Hyperspectral Devices, Düsseldorf, Germany) to measure direct, diffuse and reflected solar radiation divided into wavelengths and a SPN1 Pyranometer (Delta-T Devices, UK) for global and diffuse radiation; a high volume sampler ECHO-PUF (Tecora, Italy) to collect particulate matter on filters and infer the aerosol chemical composition. This is the same instrumentation that was also used for the other campaigns and will be illustrated below, with the exception of the particle counters, which in fact will be discussed in the specific methodology in the chapter on EUREC^{4}A.

Figure 6. *Instruments (AE33, OPC and NanoScan) installed inside the dedicated room*

The Aethalometer, as well as the particle counters were installed in a dedicated room inside the ship (Figure 6) in the bow area, in order to protect them. The sampling lines had an external outlet in the so-called atmospheric mast (Figure 5), ending in a small balcony (Figure 7a), where the high volume sampler (Figure 7b) and the radiometers (Figure 8) were also installed.

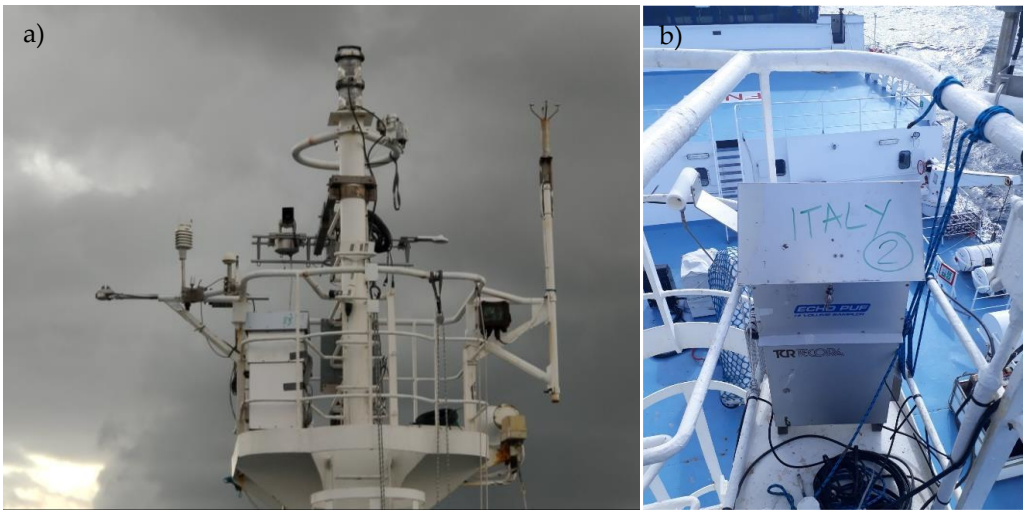

Figure 7*. Small balcony at the end of the atmospheric mast (**a**). High volume sampler (**b**).*

So as to to obtain accurate data and protect the Aethalometer from water condensation, a Sample Stream Dryer (Aerosol Magee Scientific) was used. It operates using a Nafion membrane to remove water vapor from the sample stream by permeation to an outer space maintained at a low absolute pressure by means of an external vacuum pump. A $PM_{2.5}$ cyclone at the end of the sampling line allowed to cut aerosol greater than 2.5 µm, while an insect and water trap allowed to further prevent the entry of rain or condensed water. Also the inlet of the particle counters was equipped with a dryer (based on silica gel) and the common stream was then directed to the individual instruments by means of an isokinetic split.

Figure 8. *Radiometers (SPN1 and RoX system) installed on the balcony*

2.1.2. AREX

AREX (ARctic EXpedition) campaigns were performed every summer since 1987 by the IOPAN (Institute of Oceanology Polish Academy of Sciences). We took part in 3 AREX cruises, in 2018, 2019 and 2021 on board the s/y Oceania, owned by the IOPAN (Figure 9).

Figure 9. *s/y Oceania*

The same instrumentation described for the EUREC^{4}A campaign was installed aboard the Oceania in 2018 and 2019, with the exception of the NanoSCAN and the OPC: AE-33 model Aethalometer, RoX spectroradiometer, SPN1 pyranometer and ECHO-PUF high volume sampler. As we will see in chapter five, particle number size concentration measurements were only available in 2019 through additional instruments installed by the Air-Sea Interaction Laboratory of IOPAN. During AREX 2021 an automatic equipment (AE-33 and SPN1) was only installed (to continue the BC and radiation measurements anyway), due to the SARS-CoV-2 pandemic. All campaigns left from the port of Gdansk in June and returned to the same place at the end of August or early September. Specifically, AREX 2018 began on June 11 and ended on August 30; AREX 2019 began on June 8 and ended on August 31; AREX 2021 began on June 14 and ended on September 8.

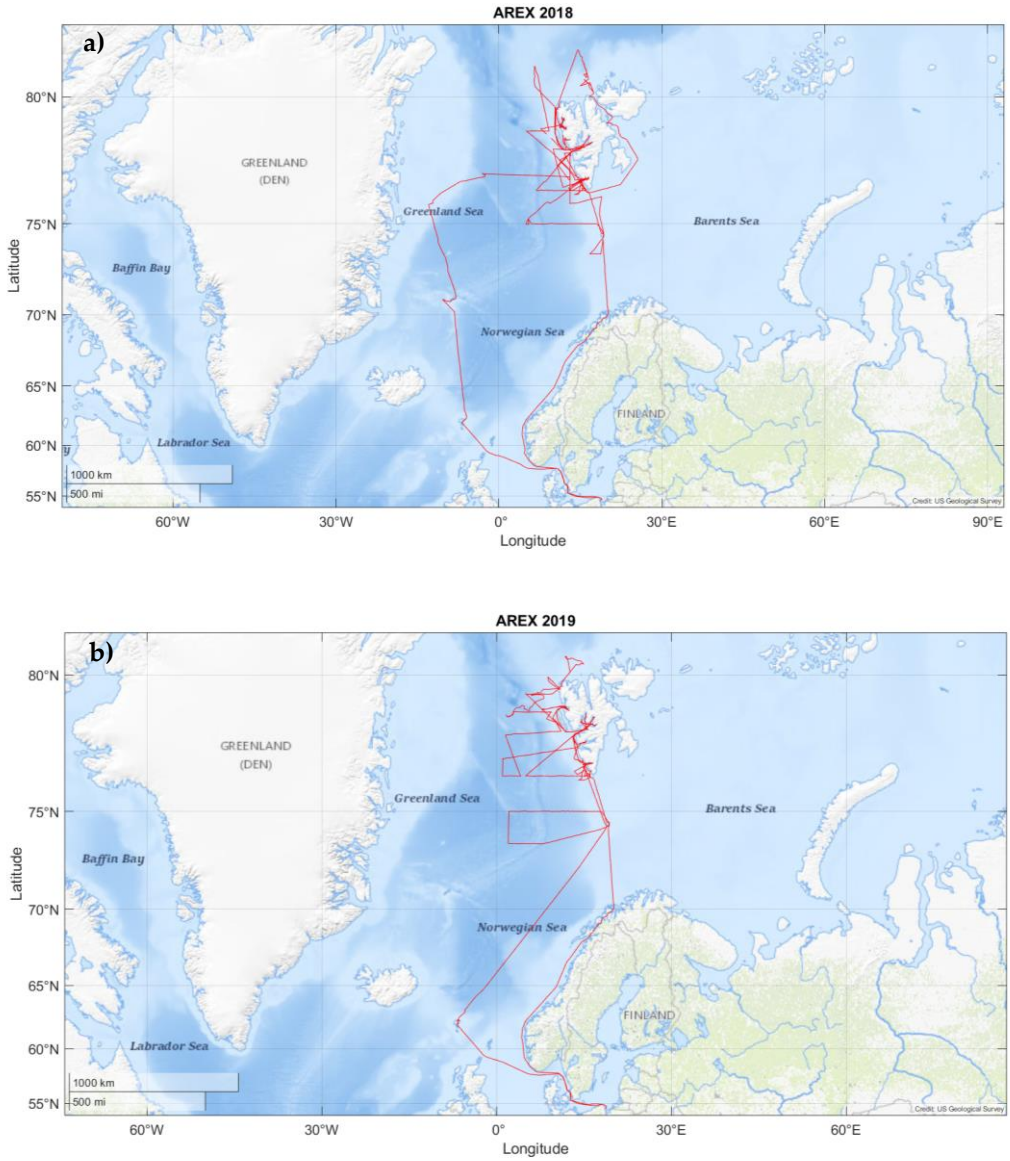

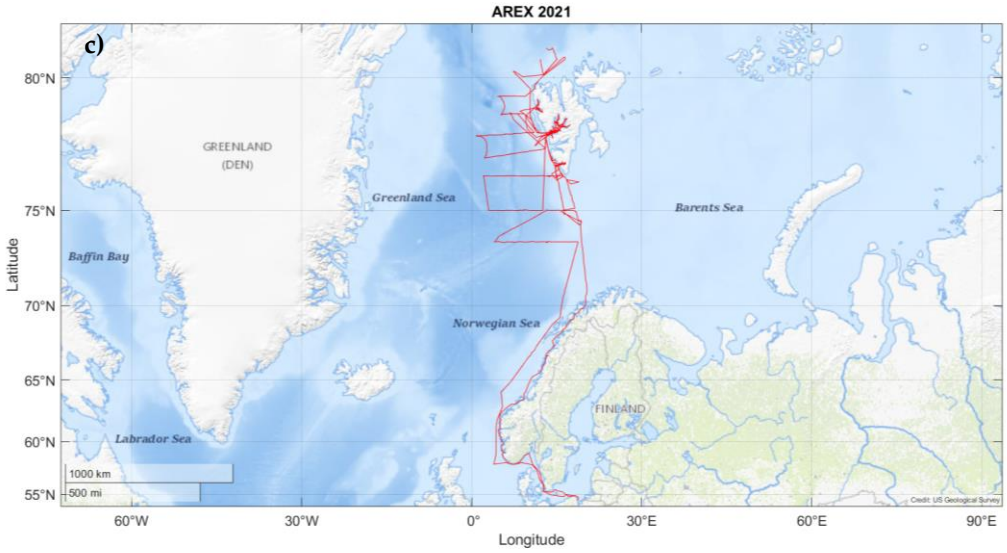

Figure 10. *Oceania's routes during AREX cruises in 2018 (**a**), 2019 (**b**) and 2021 (**c**).*

AREX cruises (Figure 10a-c) can be considered divided into 3 sections: outward, central and return sections. The outward section takes place between Gdansk (54 °N) and the North of Svalbard; it is the longest part of AREX and the part where the northernmost point is reached (over 80 °N). This section was very similar for all years: Oceania departed from Gdansk Bay, exited the Baltic Sea through the Skagerrak channel, skirted Norway, and reached Tromsø; then it spent most of the time in the sea south of Svalbard Islands, before reaching them; finally it sailed into the sea around Svalbard, reaching the northernmost point and occasionally entering Isfjorden to stop at Longyearbyen. The only clear exception in the outward section was in 2018, when the ship also sailed the east coast of Svalbard (in addition to the west coast) to escape bad weather, thus performing a kind of circumnavigation of the archipelago (Figure 10a). Central section was also similar for the three years. It is also named the fjord part, because it lasts about three weeks during which the ship sails exclusively within the Svalbard fjords (except when moving from one fjord to another). Fjords where the Oceania usually spends most of its time during this section are Isfjorden, Kongsfjorden and Hornsund fjord. Return section is the one with the largest differences between the three years. It is typically a fairly linear north-south route between Longyearbyen and Gdansk. In 2018 the ship sailed further west, approaching Greenland and stopping at Jan Mayen Island; then it reached the Faroe Islands, stopping at the harbor of Tórshavn and departing again for Gdansk via northern England. In 2019 it reached the Faroe by sailing further east and without passing through Jan Mayen: it sailed to Bear Island (south of Svalbard) and from there pulled straight for Faroe Islands. Then it returned to Gdansk tracing a very similar path to 2018. In 2021, on the other hand, Oceania followed a rather different return path than in previous years, very similar to the outward section (Figure 10c).

Indeed, it sailed back along the west coast of Norway, without stopping in Tromsø and staying a little further from the coast, and then re-entered the Baltic Sea and headed for Gdansk. In general, during the outward and return sections, Oceania stopped occasionally at Hornsund.

As we will see, the various chapters regarding AREX cruises are focused on different years and sections/areas based on the topic and measures covered: the fourth chapter, on aerosol chemical composition, discusses the outward sections of AREX 2018 and 2019 (those during which particulate filters were sampled); the fifth chapter focuses solely on the Arctic area, including the parts of the 2018/2019 outward and return sections beyond Tromsø and, most importantly, the entire central/fjords sections; the sixth chapter, which is instead centered on latitudinal differences, involves outward and return sections from all three years.

The shape of the Oceania forces it to sail mainly with the wind from the bow, and the presence of three sailing masts (that allow to reduce the engine use) decrease the ship's impact on aerosol sampling. Moreover, during AREX 2018 many measurement transects have been made on board from stern to bow with a miniDisc (Miniature Diffusion Size Classifier [58]), confirming the general absence of ship's influence, except on some the rare occasions when the wind comes from the stern.

Except for the Aethalometer, all the instruments (radiometers, Figure 12a, and high volume sampler, Figure 12b) were installed on the measurement platform (balcony) on the main (forward) mast (Figure 11a,b). The balcony is far about 20 meters from the chimney (placed aft) and further down, and it is high enough to avoid the waves (10 m above the sea level and 6 m above the deck of the vessel).

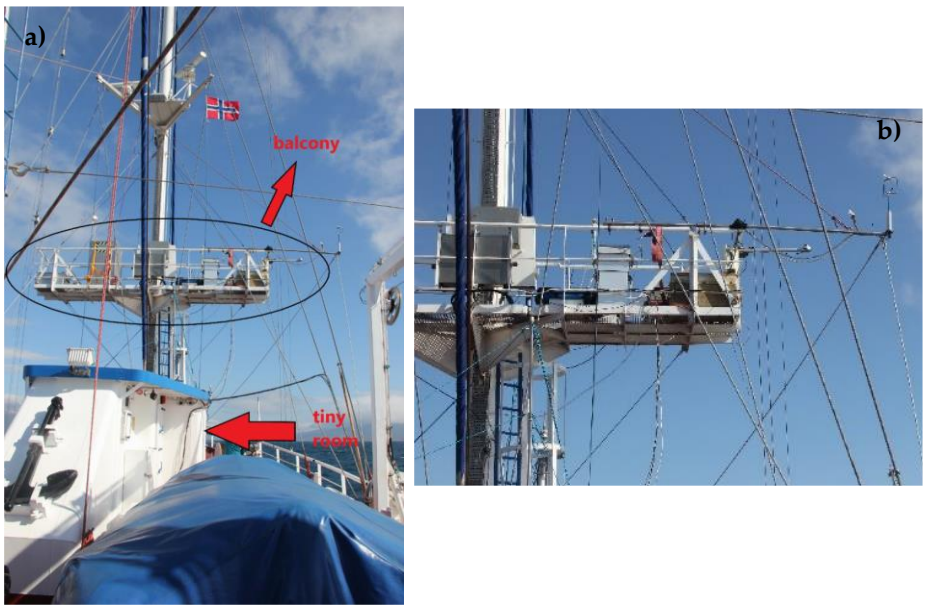

***Figure 11**. Tiny sealed room and main mast (with the balcony) at the bow (**a**). Balcony (**b**)*

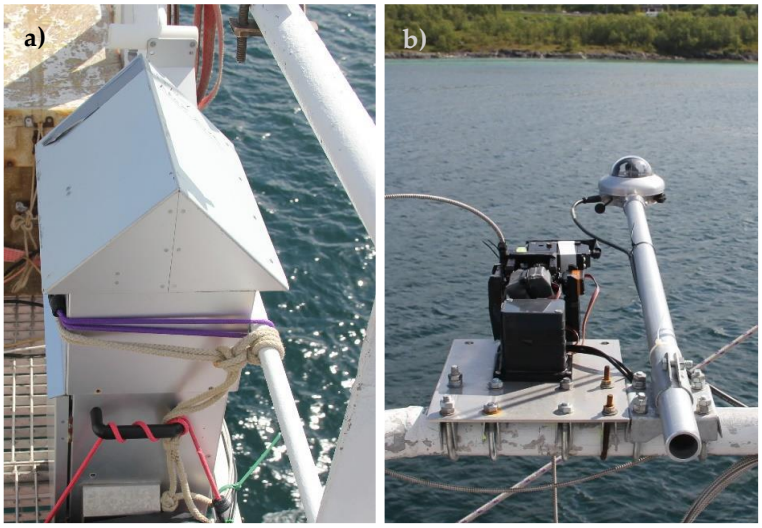

Figure 12. *High volume sampler* ***(a)*** *and radiometers (SPN1 and RoX system,* ***b****) on the balcony*

The AE-33 was installed, along with its Sample Stream Dryer and the external pump, in a sealed and tiny room in the bow (behind the main mast, Figure 11a) inside a special built protection box (Figure 13a), in order to preserve it from difficult environmental conditions (sea-spray, high humidity, ship movement). Aerosol sampling at 5 l min^{-1} was ensured trough a sampling line extended 2 meters from the roof of the room via a metal hollow pole and equipped with a $PM_{2.5}$ cyclone (Figure 13b). The cyclone was thus positioned 6 meters above the sea surface, avoiding most of sea waves, and it allowed to cut out aerosol greater than 2.5 µm (e.g. sea-spray), while an insect and water trap (before the dryer) prevented the entry of rain or condensed water, which can damage the Aethalometer.

Due to the duration of the campaign and the severe weather conditions, the instruments were subjected to constant maintenance and few times had to be also turned off.

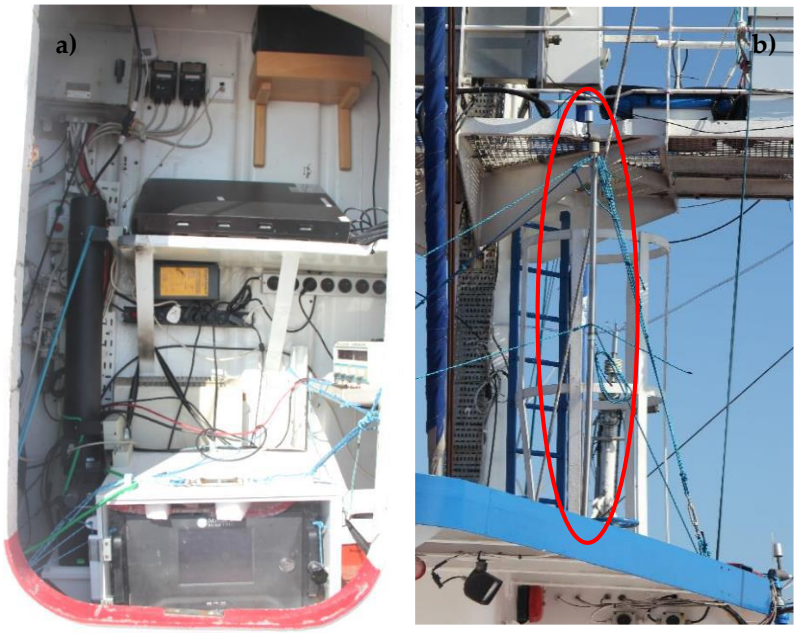

Figure 13. *Aethalometer inside a special built recovery box in the sealed room (****a****). metal hollow containing the sampling line and ending with a* $PM_{2.5}$ *cyclone (****b****).*

2.1.3. BALTIC

The BALTIC 2022 measurement campaign took place from 5th to 17th February 2022 in the Baltic Sea. The same instrumentation used for AREX expeditions was installed on board the s/y Oceania, in order to perform the same measurements and determine the LAA HR also in the winter season always along a south-north transect, although shorter. Indeed, the goal was to collect data at different latitudes only between Gdansk and the polar circle: beyond it the LAA HR is nearly 0 in winter because of lack of solar short-wave radiation (polar night); so it is not strictly necessary to reach particularly high latitudes, even given the difficulty of taking measurements in that season. However, we were unable to get as far as the polar circle due to extremely bad weather (Figure 14c) and the presence of ice in the northernmost area of the Baltic Sea. As a result, the ship traveled an approximately vertical transect (Figure 14b) from the harbor of Gdansk to about halfway up the Gulf of Bothnia (63°28'43.3"N - 20°21'16.6"E). Nevertheless, the days are already very short (the sun is above the horizon less than 8 hours) even at the maximum latitude reached anyway. On the way, the ship approached the island of Gotland both on the outward and return journeys, which were very similar (Figure 14a).

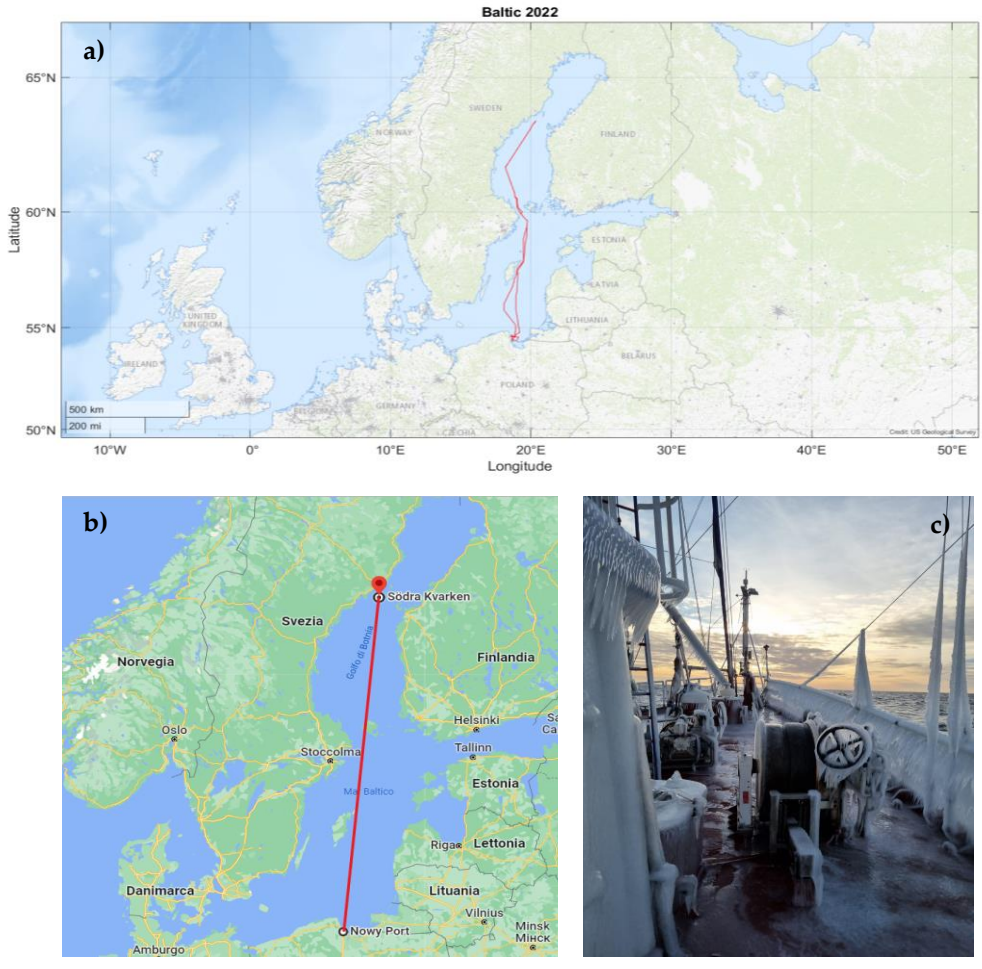

***Figure 14**. Route of the cruise (**a**); south-north transect in the Baltic Sea (**b**); Oceania during bad weather (**c**).*

The weather conditions were very turbulent for most of the expedition and the sea was very rough, making sampling and measurements sometimes quite difficult. Installation was almost identical to that of AREX campaigns: the Aethalometer was placed with its dryer in the sealed tiny room, while the other instruments were placed on the balcony.

2.2. Sample Collection, Extraction and Analysis

TSP samples were collected on quartz fiber filters (QFFs, 105 mm diameter, Whatman, Springfield Mill, UK; Figure 15a) using a ECHO HiVol sampler (TCR Tecora, Cogliate, Italy) during two of the three AREX campaigns (2018 and 2019) and the EUREC^{4}A campaign. Teflon (PTFE) filters were also used during the cruise in the tropics; they were devoted to a specific analysis (hygroscopic growth) that will be described in the methodology in the next chapter. The high volume sampler is a "stand alone" instrument designed to be used outdoor even in severe weather conditions (as in the case of our research).

QFFs were baked at 550 °C for 5 h before sampling (Figure 15b) to reduce impurities and stored in pre-cleaned (with Milli-Q water and acetone) aluminum foils at room temperature. After sampling they were stored in the same aluminum foils in a refrigerated (-20 °C) and dark environment. Before each analysis the filters were equilibrated for 48 h at less than 10% RH and room temperature (Figure 15c). Blank field filters were also collected to determine the detection limit (DL) of the different analytes. DL was calculated as the average value of all blank field filters plus three times the standard deviation [59].

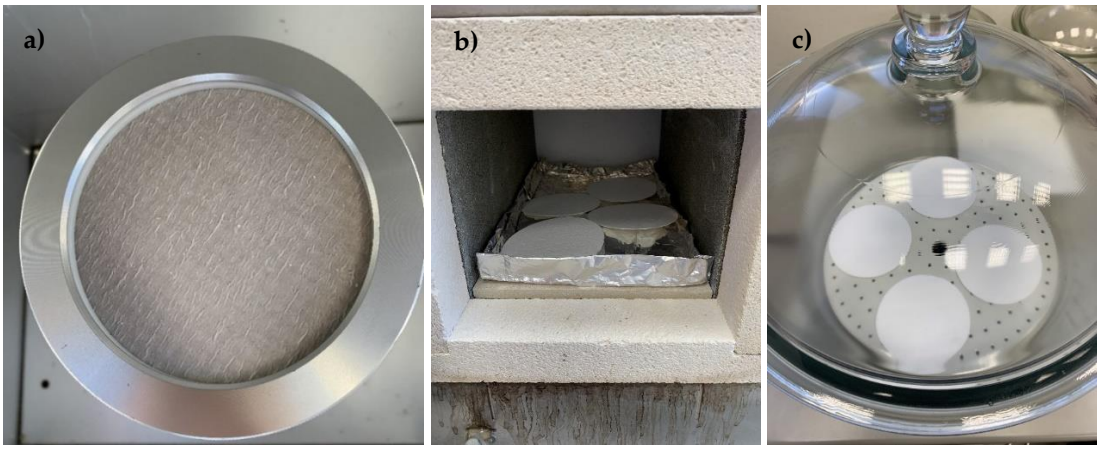

Figure 15. *sampled quartz filter (105 mm diameter, **a**); muffle oven (**b**); dryer where filters were equilibrated (**c**).*

Quartz filters were divided into two different punches (Figure 16a,b), devoted to the following analyses: ion chromatography (IC, ∅ 25 mm punch) in order to infer water-soluble inorganic ions and total carbon analyzer (TCA, ∅ 14 mm punch) in order to infer total carbon (TC) as well as organic carbon (OC). Uniformity of sampled aerosol on filters was demonstrated in a previous work [60].

***Figure 16**. die cutter (**a**) and punched filter (**b**).*

2.2.1. Water-soluble inorganic ions

Sampled filters were extracted one time in 3.0 mL of ultra pure water (18.2 MΩ cm resistivity, Milli-Q system; Millipore, Billerica, MA, USA) for 15 min in an ultrasonic bath (SONICA®; Soltec, Milan, Italy) to determine water-soluble inorganic ions content. The extract was filtered (0.45 µm PTFE filters; Alltech, Nicholasville, KY, USA) in order to remove the insoluble fraction [61]. Five main cations (Na^+, NH_4^+, K^+, Mg^{2+}, Ca^{2+}) and anions (F^-, Cl^-, NO_3^-, SO_4^{2-}, PO_4^{3-}) were analyzed using an ICS-90 and ICS-2000 coupled ion chromatography system (Dionex, Sunnyvale, CA, USA; Figure 17) respectively (both fitted out with a conductivity detector), equipped with an AS 3000 Autosampler (Dionex). The analytical principle of this technique is based on ion exchange between a mobile phase consisting of the eluent (which carries the sample) and a solid stationary phase (ion exchange resins). Charge of the ions in the mobile phase is opposite to that of the resin functional groups. The eluent is continuously eluted along the column (stationary phase), which retains the ions present in the sample. These ions are then replaced by the ions present in the eluent and are thus released from the exchange site of the column. In this way, sample ions migrate from one site to another, being progressively substituted and transported along the column by the mobile phase. The migration speed of the different ions depends on their different affinity with the ion exchange sites, allowing the physical separation of the ionic compounds present in the analyzed sample. Cation determination was accomplished through an Ion Pac CS12A-5µm analytical column (3 x 150 mm, Dionex) and an Ion Pac CG12A-5µm (3 x 30 mm, Dionex) guard column, together with a CMMS III (4 mm, Dionex) electrolytic suppressor, using 0.4 M methansulfonic acid (MSA) as eluent at 0.5 ml min^{-1}. Anion determination was accomplished through an Ion Pac AS11 analytical column (4 x 250 mm, Dionex) and an Ion Pac AG11 guard column (4 x 50 mm, Dionex), together with a ASRS-300 (4 mm, Dionex) electrolytic suppressor [62], using 50 mM KOH as eluent at 0.8 ml min^{-1}. Quantification was made by using the external standard method. Cations and anions standard

mixtures were prepared from mixing single liquid standards (1g L^{-1}; Fluka, Sigma-Aldrich, St. Louis, MO, USA) and then progressively diluting in Milli-Q ultra pure water to obtain the calibration curves. The areas obtained from the average of the blanks were subtracted from the results of the different ions (above the DL), before converting them into concentration values.

***Figure 17**. ICS-90 and ICS-2000 coupled ion chromatography system*

2.2.2. TC and OC

Total carbon content on TSP sampled filters was obtained by a thermal method, using a TCA-08 Total Carbon Analyzer (Aerosol Magee Scientific, Slovenia) in offline mode (Figure 18a): a filter punch (14 mm diameter) was placed over the installed cleaned 47-mm filter (Figure 18b) and heated almost instantaneously in a small flow of 'analytical carrier gas' (ambient air). Thus, by means of complete combustion, all carbonaceous compounds are converted to CO_2, which is detected by a nondispersive infrared Licor CO_2 sensor. In this way, the CO_2 concentration over carrier-gas baseline (the transient concentration of CO_2 exceeds the carrier-gas by far, due to the small internal volume of the system) is accurately measured and integrated to give the Total Carbon content of the sample. "Clean chamber test" and "Zero verification test" (to correctly determine the ambient-air baseline) were performed before each cycle of offline analysis. Then, Organic Carbon (OC) was obtained by combining the thermal method for TC determination with the optical method for eBC determination (TC-BC method [63]). Indeed, the eBC provided by the Aethalometer was averaged over the time periods of each TSP filter. These mean eBC values were subtracted from the total carbon ones, achieving the organic carbon

content. Finally, OC was converted to Organic Matter (OM) using a factor 2.1 for remote Arctic regions [64,65].

*Figure 18. TCA08 analyzer used for TSP samples (**a**); punchesd filter over the installed 47mm filter (**b**).*

2.3. Black carbon and related absorption coefficient data

eBC concentrations and LAA absorption coefficients (at 7 wavelengths) were determined using a dual-spot Aethalometer model AE33 (Aerosol Magee Scientific, Slovenia) with real-time loading compensation [66,67]. As mentioned in the previous sections, the AE33 was always coupled with a Sample Stream (nafion) Dryer and an external pump to ensure accurate data and protect the instrument from water condensation. Moreover, all the used sampling lines consisted of a tube made of static-dissipative polymers to minimize particle loss.

The Aethalometer collects the sample on a fiber filter tape and is based on an optical method using the estimations of attenuation (ATN) of transmitted light:

$$ATN = \quad -100 * \ln(I/I_0) \tag{1}$$

The factor 100 is only for numerical convenience; without this factor, the definition is simply that of absorbance. I represents the light passing through the aerosol-loaded filter spot, while I_0 is the light passing through an unloaded part of the filter (Figure 19). Therefore, the intensity of transmitted light is measured through both the 'sensing' portion of the filter (i.e. the filter spot on which aerosol is being collected) and a 'reference' (blank) portion of the filter, in order to check the stability of the optical source and correct any variations in incident light intensity and drift in electronics [68]. The AE33 performs a continuous optical analysis (while sampling is in progress) to give a continuous readout of real-time data. The time-base period was set with a 1 minute resolution for all campaigns. The filter tape only moves forward (to the

next spot) when the spot has reached a certain load. Usually, in a city the tape may advance 3-4 times per day, but over the Arctic sea each spot lasted several days.

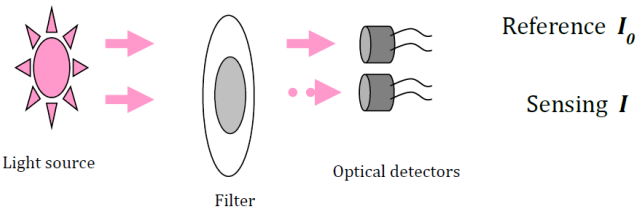

Figure 19. *Scheme of the light on AE33 filter. I represents the light passing through the aerosol-loaded filter spot, while I_0 is the light passing through an unloaded part of the filter.*

Since the AE33 is based on an optical method, we define what it measures as black carbon (rather than elemental carbon, whose definition is instead based on thermal methods). Several published works show that the Aethalometer BC measurement is closely proportional to filter-based EC measurements [69–72].

The attenuation coefficient (b_{ATN}) of the sampled aerosol particles can be calculated from the change in light attenuation as a function of time, the volumetric flow rate (F_{in}) and the filter spot area (S):

$$b_{ATN} = \frac{S * (\Delta ATN/100)}{F_{in} * \Delta t} \quad (2)$$

Since we are measuring the attenuation of particles deposited on filter, some inherent artifacts in the filter-based optical method must be corrected in order to convert the attenuation coefficient to the 'real' absorption coefficient (b_{abs}), which refers to aerosol particles suspended in air. Therefore, the absorption coefficient is calculated from the attenuation coefficient as follows:

$$b_{abs} = \frac{b_{ATN}}{C * (1 - k * ATN)} \quad (3)$$

where k and C are the loading effect parameter and the multiple scattering parameter, respectively. C describes the enhancement of optical path (and consequently of the absorption) of aerosol on filter due to the multiple scattering of light within the filter fibers when the filter is relatively unloaded (i.e. incident light can scatter from the unloaded filter matrix) [73,74]. This parameter is thus needed for multiple scattering correction, otherwise the BC concentration is overestimated because of the increase in the sample path [75] and attenuation. The value of C may depend on the particle properties, but mainly it depends on the apparatus and filter type [12,76]. The multiple scattering parameter used by default for T60 tape (TFE-coated glass filter, Pallflex "Fiberfilm" T60A20) in the AE33 is 1.57. At low aerosol loadings the attenuation is

linearly proportional to the amount of LAA deposited on the filter; however, this relationship becomes non-linear when the attenuation values are high due to a filter saturation effect [77]. The loading effect parameter compensates for the non-linear loss of the measurement sensitivity as the load on the filter spot increases: as the loading builds, the optical path decreases leading to an underestimation of the BC concentration [78]. This phenomenon is also named shadowing effect [74]. Obviously k depends on the amount of absorbing material loaded onto the filter, but it also depends on the optical properties of the collected aerosol (such as the single scattering albedo), changing with time of the year and location [79,80]. For example, the shadowing effect is drastically reduced for aged aerosol because it is partially compensated by the embedding of scattering particles in the fiber matrix. However, in the dual spot Aethalometer k is inferred at the same time resolution as the measurement itself by means of a real-time compensation algorithm [66]. For this reason, the input air stream of 5 l/m is splitted through two different spots, obtaining two simultaneous measurements at different rates of accumulation: the flow rate is 3.8 l/m for the first spot and 1.2 l/m for the second one. Any nonlinearity (that arises as the load increases) will have the same fundamental characteristics (the same aerosol is sampled on the spots), but the magnitude of saturation will be different [66]. The two results can be combined to eliminate nonlinearities and provide the compensated absorption coefficient.

BC atmospheric concentration can be finally obtained using the apparent mass attenuation cross-section (MAC) value at the same wavelength:

$$BC = \frac{b_{abs}}{MAC} \quad (4)$$

As mentioned at the beginning of this section, the light attenuation is measured at 7 wavelengths, ranging from the near-ultraviolet (370 nm) to the near-infrared (950 nm), and data obtained from the sixth channel (880 nm) is the reference standard for eBC concentration. Indeed, at this wavelength other LAA particles absorb significantly less and absorption can be largely attributed to BC (this assumption is no longer valid for samples containing a very high amount of mineral dust, which exceeds the BC content by more than 100 times). Data from other channels are useful for source (biomass burning and fossil fuel) and species (brown and black carbon) apportionment. MAC is wavelength dependent; at 880 nm it is equal to 7.77 $m^2 g^{-1}$ [66,77] and is provided by the manufacturer.

eBC concentrations calculated with equation 4 still depend on the whole amount of LAA in the atmosphere (BC absorption at that wavelength is predominant but not exclusive) and above all depend on MAC, which is not constant. Indeed, MAC depends on the dimension,

morphology, composition and mixing of aerosol particles, as well as on the filter material, relative humidity and airflow [81–83]. Predetermined MAC values are averages that take into account different world experiment and experiences. For these reasons we refer to the BC determined by this methodology as "mass-equivalent-BC" (eBC) [64,84,85].

eBC data are computed by the Aethalometer with standard pressure and temperature values of the instrument. Therefore, they must be corrected in post processing with real meteorological data to report eBC concentration to the real ambient volume of air measured at the thermodynamic conditions of the atmosphere really present during each measurement.

Below we briefly illustrate the algorithm **(**dual-spot loading compensation algorithm) included in AE33 needed to compute the *k* paramter at high time resolution. As stated above, the light attenuation is measured on two samples spots with different loading (different flow rate); this information is used to extrapolate the measurements to zero loading and eliminate the non-linearity [66]. The relationship between ATN and filter surface loading (B) can be parametrized the following empirical equation:

$$ATN = \frac{1}{k} (1 - e^{-kB\sigma}) \quad (5)$$

Because the same aerosol is collected on the two spots, even if at a different flow rate, the loadings are different but the value of *k* is the same:

$$e^{-\sigma k B_1} = (1 - k * ATN_1) \quad (6)$$

$$e^{-\sigma k B_2} = (1 - k * ATN_2) \quad (7)$$

ATN_1 and ATN_2 are measured, while B_1 and B_2 are proportional to the airflows of the respective spots. Therefore, loading effect parameter is computed by solving the following equation:

$$y = \frac{F_2}{F_1} = \frac{\ln(1 - k * ATN_2)}{\ln(1 - k * ATN_1)} \quad (8)$$

Finally, because *k* value depends on the particle optical properties, additional informations on LAA physical properties are provided by its real-time calculation, such as aerosol is freshly emitted or aged.

2.4. Solar radiation measurements

Solar radiation measurements are necessary to experimentally determine the LAA Heating Rate as shown in section 5.5. Therefore, one pyranometer (SPN1) and one spectroradiometer (RoX system) were installed on board the research vessels during the campaigns. The

pyranometer provided the absolute values of solar total and diffuse radiation radiation (consequently also of direct radiation), while the spectroradiometer provided radiation values divided into wavelengths and the reflected component. SPN1 has been employed in all measurements campaigns, while the RoX was not employed only during AREX 2021, when no one from the research team was allowed to be on board due to the SARS-CoV-2 pandemic. Indeed, the RoX is more delicate than the SPN1 and requires more maintenance, especially in severe weather conditions. Moreover (as we will see more clearly below), it was equipped also with a shadow band and a gimble, which have been fundamental to our purposes, but which require a continuos control and maintenance during long-term field campaigns. Both SPN1 and RoX acquired absolute and spectral data each minute, the same time resolution of the Aethalometer.

2.4.1. SPN1 Radiometer

SPN1 pyranometer (Delta-T Devices, UK) measures short wave radiation (W m^{-2}) between 400 and 2700nm and returns 3 outputs: global or total solar radiation, diffuse radiation and sunshine status (which indicates if the energy in the direct beam exceeds the WMO standard threshold value of 120 W m^{-2}). It is fitted with a ground glass dome and it is designed for long-term outdoor exposure. An internal heater keeps the dome clear of snow and ice, making it suitable for campaigns in difficult weather conditions, such as AREX and BALTIC campaigns. Moreover, it needs no polar alignment and works at any latitude. For these reasons, it has already been used in other Arctic campaigns, such as MOSAiC expedition [86]. It has no moving parts, such as motorised solar trackers, and measures the radiation regardless of azimuthal orientation. These characteristics make its use suitable for mobile platforms (e.g. aircrafts and ships). However, its immobility on the horizontal and vertical axes requires post-processing to correct the error induced by the rolling and pitching of the ship.

SPN1 was coupled with a GP1 Data Logger (Delta-T Devices). The sensors of the pyranmeter generate a voltage, due to the temperature difference between two metals (one exposed to the sun and one shaded). This voltage is read from the data logger and converted in W m^{-2}.

The hexagonal arrangement of the 7 radiation sensors and the hemispherical shadowmask (Figure 20), with specific areas cut away, allow to always have at least one sensor exposed to direct solar radiation and at least one sensor completely shaded, while all sensors receive about half of the diffuse radiation equally (assuming that the diffuse sky radiance is isotropic) [87–89]. Therefore, the fully exposed sensor always receives the maximum (MAX) radiation, which is equal to the direct radiation plus half of the diffuse; the sensor completely shaded, instead,

always receives the minimum (MIN) radiation, which is equal to half of the diffuse. Consequently, adding MIN to MAX gives the global radiation, while multiplying MIN by two gives the diffuse radiation. This is the reason why the SPN1 can measure the diffuse radiation without moving parts (e.g. shadow bands or solar trackers). The direct radiation can also be easily obtained by subtracting the diffuse component from the total one.

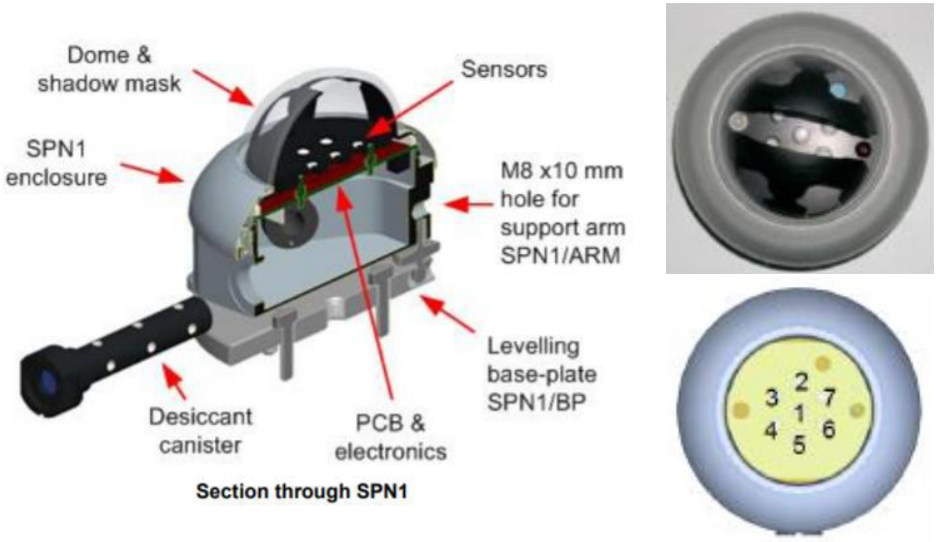

Figure 20. *SPN1 scheme and view above the instrument where it is visible the typical shadowmask; scheme of the seven sensors. (Badosa et al. 2014).*

In addition to the common errors in radiometers, there is a specific one indiced by the SPN1 design: since the sensor sees only a 50% of the diffuse sky, variations in diffuse intensity on a scale similar to that of the shading pattern will also show up as variation in the instrument output [87].

The main problem on moving platforms, such as aircrafts and ships is the tilt of the instrument and the consequent error induced in the measurement of the direct component. The diffuse component, which is considered isotropic, is not affected by this problem. Therefore, the direct component must be corrected in order to obtain a correct global radiation, given by the sum of the new direct radiation and the diffuse one (unvaried).

To correct the SPN1 direct radiation, the method shown by Wood et al. [88] and derived from Long et al. [87] was used. To apply this method, it is necessary to know the position of the sun (solar zenith and azimuth angles) and the angle of incidence on the tilted instrument plane, which is calculated from the ship's orientation values (pitch, roll and yaw from an Ellipse-E Inertial Navigation Sensor, by SBG systems):

$$I_{Hcorr} = \frac{I_{Hmeas}}{cos\theta_{rs}} \; cos\theta_s \tag{9}$$

Where I_{Hcorr} is the direct component of solar radiation corrected for the tilt of the instrument, I_{Hmeas} is the direct radiation measured, Θ_s is the solar zenith angle and Θ_{rs} is the angle of incidence to plane of detector, which is calculated as follows:

$$cos\theta_{rs} = cos\theta_s \ cos\alpha_{sf} + sin\theta_s \ sin\alpha_{sf} \ cos(\varphi_s - \beta_{sf}) \quad (10)$$

Φ_s is the solar azimuth angle, while α_{sf} and β_{sf} are the surface zenith and azimuth angles respectively, which are calculated using pitch, roll and yaw data.

2.4.2. RoX System

The RoX (reflectance box) spectroradiometer (JB Hyperspectral Devices, Düsseldorf, Germany) is based on the Multiplexer Radiometer Irradiometer (MRI) described in the work of Cogliati et al. [90], and it collects incident and reflected radiation in the Visibile/Near Infrared region (350-950nm), by exploiting the Flame spectrometer from Ocean Optics (USA). It applies an automatic signal optimization according to different light conditions and performs an accurate dark current determination at each measurement cycle. The raw data of the RoX was processed using the open source R-package provided by JB company. Moreover, the RoX used during the campaigns was customized by the manufacturer according to specific requirements: a gimbal and a rotating shadowband had been added (Figure 21). The gimbal was used to compensate for ship motion (by means of two servomotors and an accelerometer), keeping the sensors perfectly horizontal. Therefore, it was not necessary to correct data afterwards, as was done for SPN1. The shadowband rotates 5 degrees per minute to cover step by step all the 180 degrees of the upwelling sensor's field of view. So, the upwelling sensor is obscured at regular time intervals. When the sensor is uncovered global radiance is measured, instead diffuse radiance is measured when the band shades it. This improvement allows to separate the diffuse radiation from the global one and obtain also the direct radiation by subtracting the direct component from the total (as previously done in Ferrero et al. [11]).

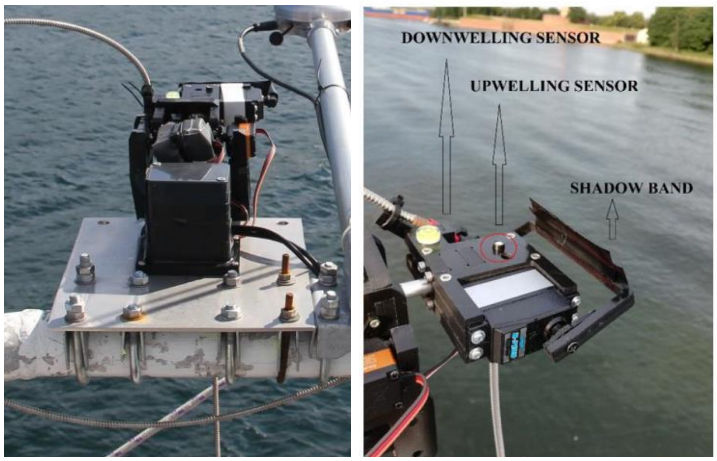

Figure 21. *Gimble system for the optical fibers of the RoX (left) and shadowband (right).*

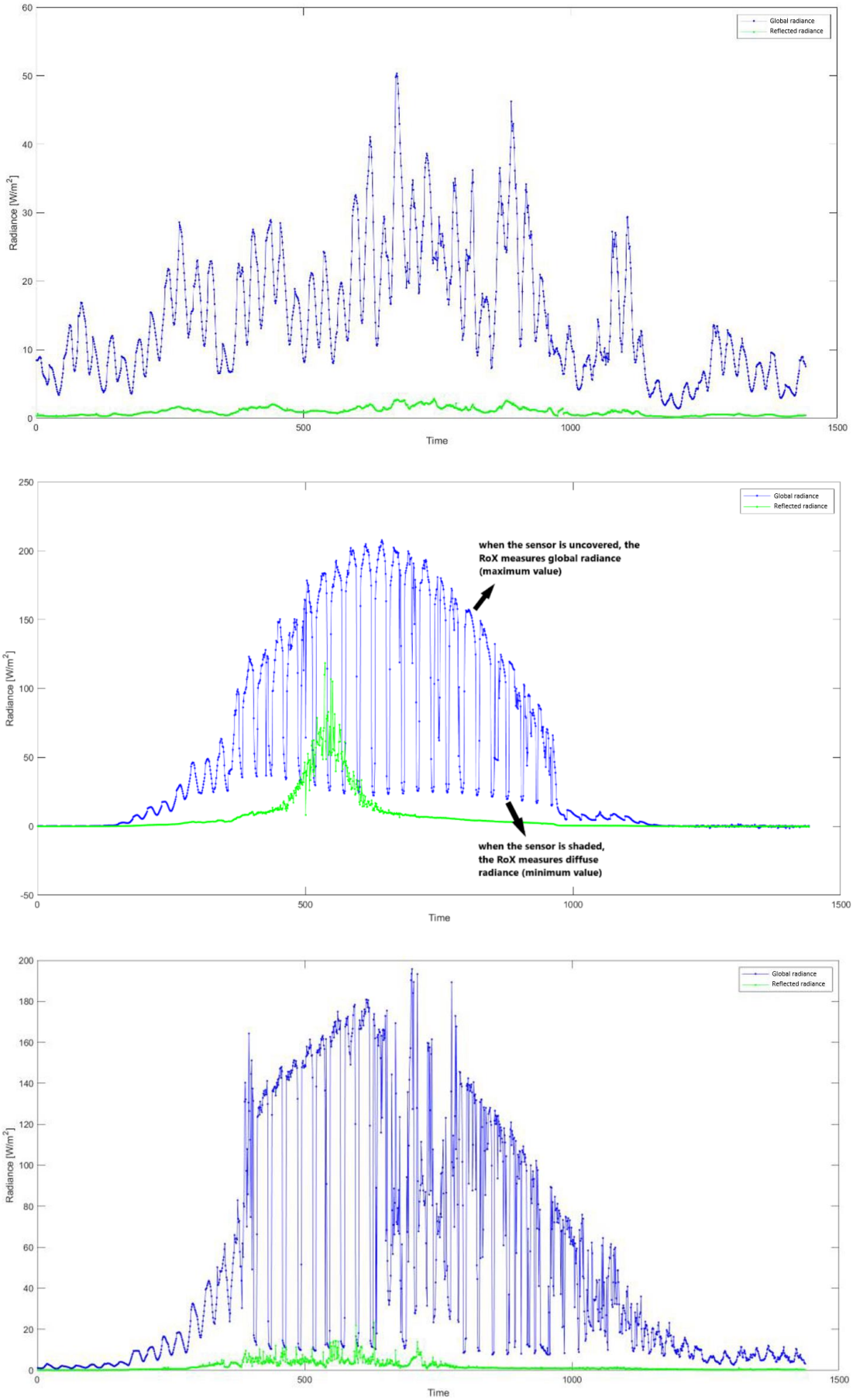

Figure 22. *Trend of global (blue line) and reflected (green line) radiation during cloudy day (**a**), clear sky day (**b**) and partial day (**c**). Lower values indicate the passage of the shadowband.*

During cloudy days the role of the shadowband is obviously much less relevant (because global and diffuse radiation almost coincide) and the passage of band on the sensor is not evident (Figure 22a). During sunny (clear sky) days the passage of the shadowband is clearly evident and makes it possible to separate the diffuse radiation from the global one (Figure 22b): maximum grouped values are ascribed to the global radiation, while groups of minimum values ascribed to the diffuse radiation; single values present in the falls and rises between the two groups are instead eliminated, because they are the result of partial sensor darkening during shadow band passes. The direct radiance is then obtained by subtracting the diffuse radiance from the global one. Figure 22c shows a partial day, characterized by alternating sunny and cloudy periods. Average spectra (global, diffuse and direct) of the campaign were used when RoX data for a specific day was missing.

2.5. Heating Rate determination

Once suspended in the atmosphere, the LAA absorb the solar radiation (direct effect) and instantly release energy in the form of heat to the surrounding atmosphere (Figure 23) with a specific heating rate [13,85,91–97], exerting a positive forcing. HR is usually expressed in units of K/day [97,98]. By means of LAA absorption coefficients and radiation measurements described above, it was possible to determine the surface atmospheric Heating Rate related to LAA, using the methodology developed by Ferrero et al. [11].

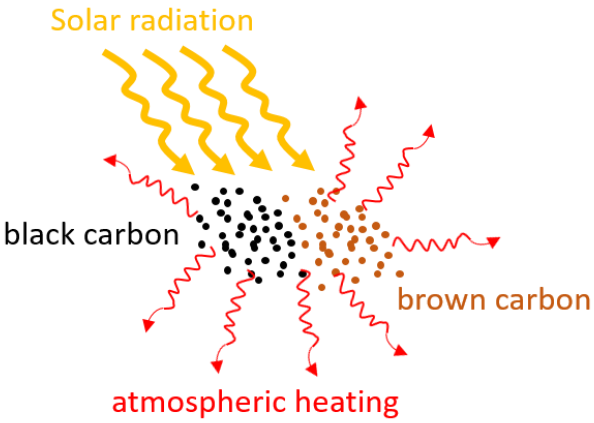

Figure 23. *Scheme of absorption of solar radiation by BC and BrC*

The novelty of this method is that it allows to assess in a completely experimental way both the radiative power density absorbed into a near-surface atmospheric layer and the consequent HR. Instead, most of the studies concerning radiative forcing are conducted through a hybrid [94,99–102] (experimental measurements of LAA properties coupled with radiative transfer calculations) or purely modeling [6,9,103,104] approach, affected by uncertainties related to input parameters [105] , such as modelled aerosol concentrations and optical properties, and to the

frequent assumption of clear-sky conditions. Thus, this experimental method enables to determine the HR in any sky condition. Another advantage is the opportunity to apportion the HR in function of LAA species (BC and BrC), sources (fossil fuel and biomass burning) and different radiation components (direct, diffuse and reflected).

This HR computation methodology starts from the consideration that aerosol measurements are usually expressed as mass (or number of particles) per unit volume of air (cubic meters in the denominator). Therefore, it is more useful to define the HR, generally expressed as:

$$HR = \frac{\partial T}{\partial t} = -\frac{g}{C_p}\frac{\Delta DRE}{\Delta P} \tag{11}$$

in terms of thickness of the atmospheric layer (Δz) rather than pressure variation (ΔP), as follows:

$$HR = \frac{\partial T}{\partial t} = \frac{1}{\rho C_p}\frac{\Delta DRE}{\Delta z} \tag{12}$$

Equation 12 can be obtained by exploiting the hydrostatic equation:

$$dp = -\rho g \ \ dz \tag{13}$$

In equation 12 ρ is the air density (kg m^{-3}), while Cp (1005 J kg^{-1} K^{-1}) is the isobaric specific heat of dry air. The benefit of this HR definition is due to the fact that the last term ($\Delta DRE/\Delta z$), the so-called *ADRE* (absorptive direct radiative effect) [94], is the radiative power absorbed by the aerosol for unit volume of the atmosphere: its unit of measure (W m^{-3}) is thus consistent with aerosol volume concentrations in the air. Indeed, ΔDRE is the instantaneous radiative power density absorbed by the aerosol (W m^{-2}) [97] and is given by the difference between the instantaneous aerosol direct radiative effect (*DRE*; W m^{-2}) at the top and the bottom of an atmospheric layer of thickness Δz:

$$\Delta DRE = DRE_{z+\Delta z} - DRE_z \tag{14}$$

The quantity of radiation absorbed by LAA (ΔDRE) within an atmospheric layer (near surface layer for our study, but can be applied to any atmospheric layer) of thickness Δz on which an nth kind (direct, diffuse, or reflected) of monochromatic radiation ray $F_{n(\lambda,\theta)}$ of wavelength λ arrives with a zenith angle θ can be expressed as [11,97]:

$$\Delta DRE_{n(\lambda,\theta)} = F_{n(\lambda,\theta)} \ \ (1-\omega_\lambda) \ \ (1-e^{-\tau_\lambda/\mu}) \tag{15}$$

where ω_λ is the single scattering albedo of the aerosol present in the atmospheric layer, τ_λ is the aerosol optical depth and μ is the cosine of θ. Considering an atmospheric layer thin enough, then $\tau_\lambda << 1$ and the last term of equation 15 ($1 - e^{-\tau\lambda/\mu}$) can be simplified using the Taylor series:

$$\Delta DRE_{n(\lambda,\theta)} = F_{n(\lambda,\theta)} \ (1-\omega_\lambda)^{\tau_\lambda}/\mu \tag{16}$$

Aerosol optical depth is usually inferred from the extinction coefficient ($b_{ext(\lambda)}$):

$$\tau_\lambda = \int_0^{\Delta z} b_{ext(\lambda)} \ dz \tag{17}$$

Since τ_λ is integrated along the vertical direction, ΔDRE in equation 16 still is a columnar quantity. Indeed, aerosol absorption is typically reported in W m^{-2} over the whole column of atmosphere or over an altitude thick layer [1,96,106,107]. The single scattering albedo, instead, is determined by the scattering and absorption coefficients:

$$\omega_\lambda = \frac{b_{sca(\lambda)}}{b_{sca(\lambda)} + b_{abs(\lambda)}} \tag{18}$$

Considering a thin enough layer so that $\tau_\lambda << 1$, it also means that $F_{n(\lambda,\theta)}$ and ω_λ are roughly constant within the whole Δz layer . Therefore, combining equation 16 with equations 17 and 18, the *ADRE* for this specific atmospheric layer can be rewritten as:

$$ADRE_{n(\lambda,\theta)} = \frac{dDRE_{n(\lambda,\theta)}}{dz} = F_{n(\lambda,\theta)} \frac{(1-\omega_\lambda)}{\mu} \ \frac{d\tau_\lambda}{dz} = \frac{F_{n(\lambda,\theta)}}{\mu} \ b_{abs(\lambda)} \tag{19}$$

Therefore, looking at equation 19, it is clear that the *ADRE* and the consequent HR can be calculated using the LAA absorption coefficients (given by the Aethalometer) and radiation measurements. *ADRE* can be then integrated for all shortwave wavelengths and incident angles

$$ADRE_n = \int_\theta \int_\lambda \frac{F_{n(\lambda,\theta)}}{\mu} \ b_{abs(\lambda)} \ d\lambda \ d\theta \tag{20}$$

Taking into account all the three components of shortwave radiation (direct, diffuse and reflected) and recalling the heating rate definition in equation 12, total LAA HR can be calculated:

$$HR = \frac{1}{\rho C_p} \sum_{n=1}^{3} \int_\theta \int_\lambda \frac{F_{n(\lambda,\theta)}}{\mu} \ b_{abs(\lambda)} \ d\lambda \ d\theta \tag{21}$$

where *n* is the *n*th kind of radiation ($F_{dir(\lambda,\theta)}$, $F_{dif(\lambda,\theta)}$, $F_{ref(\lambda,\theta)}$). As already assumed in relation to the radiation measurements (SPN1 and RoX), ADRE and consequent HR are calculated with equations 20 and 21 treating the measured diffuse radiation under the isotropic assumption [108].

This method thus allows to consider the components of radiation separately, investigating the interaction of each of them with the LAA. Furthermore, whether a LAA source and species

apportionment is performed obtaining the individual absorption coefficients for each species/source, the HR can then also be apportioned accordingly. Therefore, all combinations of LAA sources/species and type of radiation can be studied independently.

HR was computed also over the broadband range of SPN1 (using the Angstrom exponent of $b_{abs(\lambda)}$), but the HR reported in this work is the one obtained only in the range covered by the wavelengths of the Aethalometer (370-950 nm).

This recent experimental HR method, which is independent of the thickness of the atmospheric layer considered (because ADRE, i.e. the vertical derivative of DRE, is directly used in the computation of HR instead DRE), was applied to the atmospheric surface layer. The use of ADRE thus allowed for temporal continuity in the calculation of HR, but at the expense of vertical information (there is a loss of vertical information). However, the surface results obtained can be representative of the mixing layer height when there are no specific gradients of LAA concentrations in the lower atmosphere [11,94,100]. Moreover, the methodology can ideally be applied to an atmospheric layer at any altitude (e.g. using a UAV system), transcending the vertical limit.

3. Aerosol chemistry and Heating Rate in the Tropics

3.1. Introduction

The results presented in this chapter are based on measurements performed in the framework of the EUREC^{4}A (see section X.X) field campaign [109], which took place in January–February 2020 over the tropical North Atlantic, near Barbados [57]. It was an international initiative in support of the World Climate Research Programme's Grand Science Challenge on Clouds, Circulation and Climate Sensitivity. A massive set of measurements was carried out by exploiting research ships and aircraft from different nations (e.g. Germany, French, U.S.) as mobile platforms, in order to study clouds and their link to equatorial and subequatorial dynamics [110]. The main objective of EUREC^{4}A is to improve our comprehension of the factors that influence clouds across a wide range (from mm to Mm) of relevant scales, how they will respond to global warming and their connection with other component of the Earth system, such as the mesoscale and sub-mesoscale dynamics of upper ocean, ais-sea interactions and the life-cycle of particulate matter [57].

For our purpose we focused on the particle scale, where the role of aerosols is critical. Indeed, aerosol properties (i.e. chemistry) and turbulence both imprint themselves on the cloud microstructure, and therefore affect the formation of precipitation [111–114]. In particular particles can serv as seeds from which liquid water droplets initiate and grow and these particles are called cloud condensation nuclei (the potential for an atmospheric particle to act as CCN, named CCN activity, is ranked by the atmospheric water vapor pressure required for it to nucleate into a droplet and depend on both its size and chemical composition [115]). Moreover, LAA species (BC, BrC, dust) can absorb sunlight and heat the atmosphere, thus altering the final radiative budget at the surface and acting on the available energy for cloud formation and dynamics. Therefore, the LAA HR is one of the factors influencing the energy balance in the sub-cloud layer.

A wide variety of different aerosol species is present in the study area, such as sea-spray, biomass burning (BB) and dust aerosol [116]. In particular dust is a major contributor to the atmospheric aerosol mass burden [117] and it play a main role on the radiative balance over the tropical Atlantic and Carribean [118]. BB and mineral dust have a non-local origin; they can be transported and mixed with local sea-salt and sulfate aerosols [110]. The dominant source of mineral dust is the Sahara region, especially West Africa [119,120]. Long-range transport of Saharan dust (and to a lesser extent also BB aerosol) from West Africa to Barbados across the tropical North Atlantic Ocean is favored by trade winds [121] and is characterized by strong seasonality [110,122] with a summer maximum. It depends on the large-scale synoptic situation

and the meteorological conditions over both Africa and the tropical North Atlantic [116,119,123,124]. During summer dust particles are advected westwards at higher latitudes due to the northernmost position of the Intertropical Convergence Zone (ITCZ) [125,126] and higher altitudes due to the deeper boundary layer over Sahara region [127], frequently reaching the Caribbean. During winter, instead, the ITCZ is shifted southward and dust plumes reach the Caribbean more rarely (following a transportation route further south) and at lower altitudes (< 3 km). Moreover, due to the low level transport, mixing of mineral dust with BB aerosols from West Africa and South America and/or marine aerosols above and inside the marine boundary layer [128,129] is favored. This mixture can exert direct forcing, affecting the evolution of shallow marine clouds [119], and behave as cloud condensation and ice nuclei [130,131]. Winter transport events to Barbados area are thus less frequent but still possible. During EUREC^{4}A campaign several dust plumes were observed, always mixed with marine and BB aerosols (no pure dust regimes were present) [110,116,119]. In particular, mineral dust were mixed mainly (but not exclusively) with BB aerosol from forest fires in West Africa atop the marine boundary layer and marine aerosol within it [119]. An increased atmospheric load of sea-spray (because of greater surface wind speed) and a more direct transport of aerosols from West Africa in shallower layers were related to weather tropical regime, rather than the more complex trade wind regime.

In this context, our measures can help to better understand the link between aerosol and clouds in this region, through its chemical composition, hygroscopic properties and HR. However, the campaign also represented a more general opportunity to characterize the chemistry and the optical properties of particulate and their transport across the tropical Atlantic [110]. Specifically, it allowed us to expand the study area of this project, whose main focus is both local and remote effects of LAAs on Arctic climate. Therefore, we have been able to include also the tropical latitudes (although a specific area) in the research, making a comparison between the chemical composition, concentration and properties of the aerosol in this region and the higher latitudes (mid-latitudes and North Pole). The Arctic warming, indeed, is also influenced by the forcing of LAA at lower latitudes, which alters the poleward heat transport [7,9]. Shindell et al. [6] demonstrated that in the tropical latitudinal band the SAT (superficial atmospheric temperature) response is slightly higher for local forcings, but generally is quite independent of the forcing location. The extratropic areas, instead, are more sensitive to local forcings, with reduced response to forcing in the tropics and, above all, the other hemisphere. However, in the polar latitudinal band the SAT response is positive for aerosol forcings applied to mid-latitudes. The Arctic response to the aerosol forcing is thus due to an interplay of local and remote effects and it is difficult to establish which of the two effects plays a greater role (our

work wants precisely to investigate this aspect). Moreover, while the influence of mid-latitudes on Arctic climate is more fully investigated, the role of the tropics remains less clear, although it is possible that it is minor. This research is also more focused on the midlatitudes – Arctic range, but still try to take a first step in including even the tropical latitudes of the Northern hemisphere in the discussion. Indeed, Arctic campaigns were repeated over time and carried out along a specific route between Europe and northern Svalbard. EUREC^{4}A measurements were more localized and performed only once and in a different season (i.e. winter). Hence, it was not possible to include this band in the final calculation of the LAA induced energy gradient between lower latitudes and the North Pole (chapter 6), but it was still possible to compare LAA concentrations and the resulting HR in this region with the other areas investigated.

3.2. Specific methodology

TSP samples were collected and high temporal aerosol and radiation measurements were performed on board the R/V L'Atalante from 20 January to 23 February 2020 during the EUREC^{4}A campaign in the sea area near Barbados, Trinidad and Tobago, Guyana and Suriname, as explained in section 2.1.1. Instruments used, installation criteria and chemical analysis (ion chromatography and total carbon) are outlined in the materials and methods chapter, with the exception of the particle concentration measurements and hygroscopicity analysis. This information is provided below along with specific information regarding sampled filters.

TSP were collected on both quartz (12) and teflon (11) filters alternately for a total of 23 samples. Figure 24a,b shows ship's path for each filter for quartz and teflon respectively. The sampling flow was set at 200 L/minute, while the average sampling time was 24 h. Quartz filters were dedicated to ion chromatography and TC analysis to infer the chemical composition, while teflon filters were dedicated to hygroscopic analysis and ion chromatography to infer deliquescence and crystallization relative humidity (DRH and CRH) and related phase transition regions.

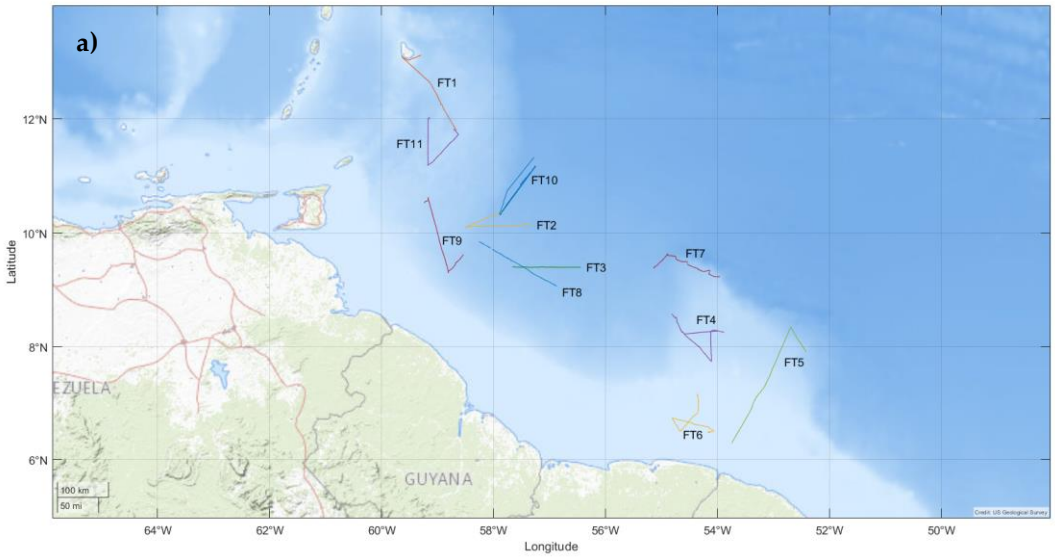

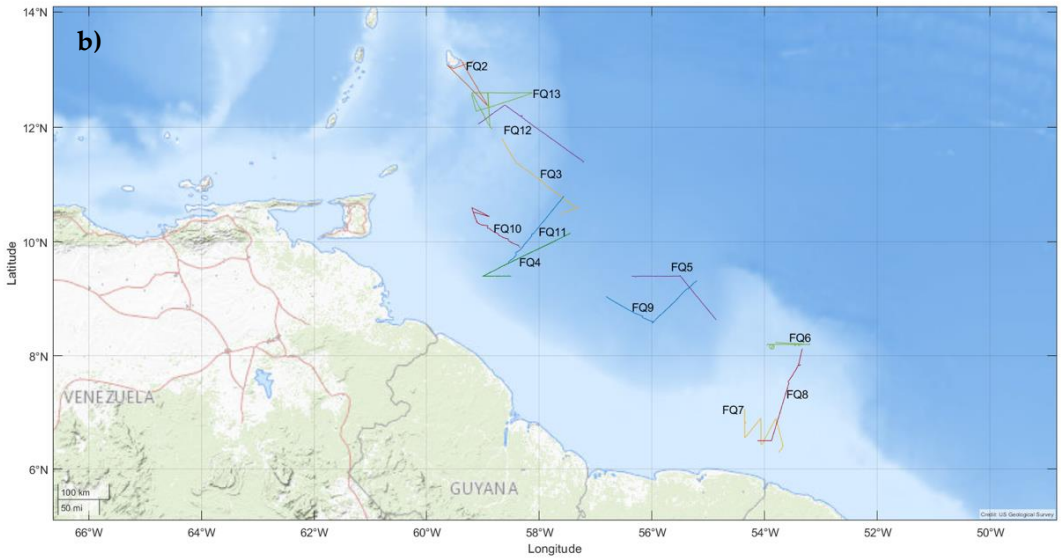

Figure 24. *Ship's path for each filter for quartz* ***(a)*** *and teflon* ***(b)*** *filters.*

Regarding ion chromatography, all ions calibration curves had a regression coefficients (R^2) > 0.996. Collected blank filters allowed to determine the DL of the different analytes and the studied filters were all above the DL. Figure 25 shows a very good balance between positive and negative ion charges of quartz filters (slope≈1), confirming the reliability of the analyses performed.

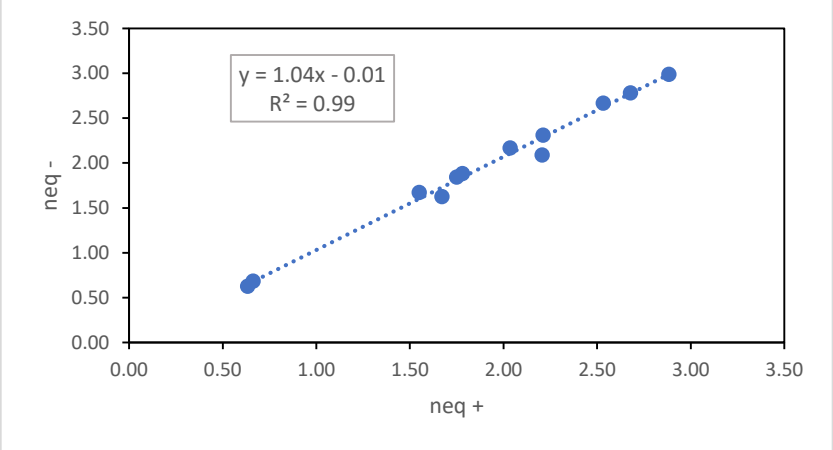

Figure 25. *Regression line between positive and negative charges show a very good balance. Slope is around 1 while the* R^2 *is 0.99.*

Real-time measurements of eBC concentration, LAA absorption coefficients and solar radiation were performed at 1 minute time resolution. GPS and accelerometric data, provided by IFREMER, were used to correct the SPN1 direct radiation measurements, while weather data were used to correct eBC data from the AE33. Vessel speed and apparent wind data allowed to apply a filter (180° ± 40°) in order to remove the interference of the vessel exhaust. Surface LAA HR was computed entirely experimentally [11] (see section 2.5) from LAA absorption coefficients and radiation data in the range between 370 and 950 nanometers.

In addition to LAA and radiation measurements, particle number concentrations from 10 nm up to 32 μm were also considered in order to investigate more deeply the differences between transport events and the formation of secondary aerosol.

3.2.1 Particle measurements

Nanoparticles were inferred by means of a NanoScan 3910 particle sizer (TSI inc., Shoreview, MN, U.S.), which measures the aerosol number size distribution from 10 nm to 400 nm in 13 size classes. The NanoScan is an intrument based on a radial diffusion mobility analyser coupled with a condensation particle counter in which aerosol size is magnified (after size selection) via isopropyl alcohol (>99%) for its quantification inside a laser optical chamber. NanoScan data allowed the determination of the Count Mean Diameter (CMD) and Geometric Standard Deviation (GSD) of the aerosol lognormal number size distribution [132]. Nanoparticles data were collected at 1 min time resolution and treated with the same apparent wind filter as the eBC data.

The OPC 1.107 (GRIMM Aerosol Technik, Ainring, Germany) measures the aerosol number size distribution from 250 nm to 32 μm in 31 size classes. It is based on the laser scattering at 655 nm for particles number quantification and sizing into a laser optical chamber. It allowed the estimation of PM_1, $PM_{2.5}$ and PM_{10} concentrations at 5 min time resolution [133].

3.2.2 Hygroscopicity measurements

DRH, CRH and related phase transition regions were identified with the method described in Ferrero et al. [62] and D'angelo et al. [134], coupling the gravimetric sampling method for TSP with a gravimetric hygroscopic determination. Therefore, an Aerosol Exposure Chamber (AEC, Figure 26) of 1 m^3 volume located in the atmosphere chemistry laboratory (Bicocca University, Milan) was improved to achieve a better insulation from the external environment and a greater control of temperature and humidity and then used.

Within the AEC, the RH was varied by 2% at a time, from 20% up to 90% (phasing ultrapure water vapours into the AEC) during humidification (i.e. deliquescence cycle) and vice versa (phasing into the AEC pre-filtered pure air; Aria Zero by Sapio) during dehumidification (i.e. crystallization cycle). Experiments were carried out at mean sampling temperature (300 ± 1 K) for the entire duration of the cycle. Thermodynamic conditions within the AEC were monitored by means of two thermo-hygrometric sensors (DMA572 and DMA672, LSI-LASTEM, with a resolution of 0.25% for RH and of 0.035 °C for temperature) with 1s time resolution. The hygroscopic growth, the DRH and CRH were identified by means of a gravimetric method: a precision weighting analytical balance (Sartorius SE-2F; precision ±0.1 μg) was placed in the AEC and the increasing (decreasing) mass measures were recorded for each RH step. By the

knowledge of the aerosol mass deposited on teflon filters and the mass of the water absorbed by the aerosol, the mass Hygroscopic Growth Factor was computed as follows:

$$HGF_{mass} = (N_{mass} + D_{mass})/D_{mass} \quad (22)$$

Where HGF_{mass} is the mass Hygroscopicity Growth Factor, N_{mass} is the Net mass (water mass over filter) and D_{mass} is the Dry mass (sample over filter; 20% RH).

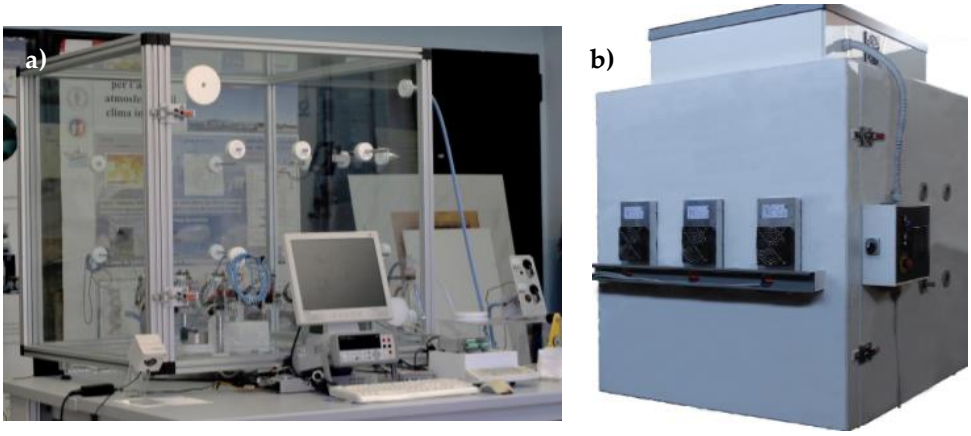

Figure 26. *Aerosol Exposure Chamber, used for aerosol hygroscopicity measurements, before (**a**) and after (**b**) the improvements.*

3.3. Results and discussion

3.3.1. High time resolution aerosol measurements

Average total aerosol concentration for the whole campaign was 5.229 ± 0.248 *10^3 cm^{-3}, ranging from 203 cm^{-3} to 3.147 *10^5 cm^{-3}. eBC concentration was on average 553 ± 10 ng/m^3, ranging from 7 ng/m^3 till 2168 ng/m^3. Figure 27 shows the temporal series of eBC and total aerosol concentration along the whole EUREC^{4}A cruise (from Pointe-à-Pitre to the French Guyana Atlantic waters and the way back). During this time two distinct events of increasing eBC concentration were observed: the first one from 29/01/2020 to 05/02/2020 and the second one between 09/02/2020 and 11/02/2020. These two events were related to transport from North-West Africa by means of backtrajectories computed 240 hours back in time for January 31 and February 10, i.e. two days in the midst of the two events (Figure 28). They were calculated using the on-line version of the hybrid single particle Lagrangian integrated trajectory model (HYSPLIT) developed by the National Oceanic and Atmospheric Administration Air Resource Laboratory (NOAA, http://ready.arl.noaa.gov/HYSPLIT.php). During the first transport, air masses passed at low altitude close to the western coast of Africa, while travelled at low altitude over the inland of West Africa in the second case.

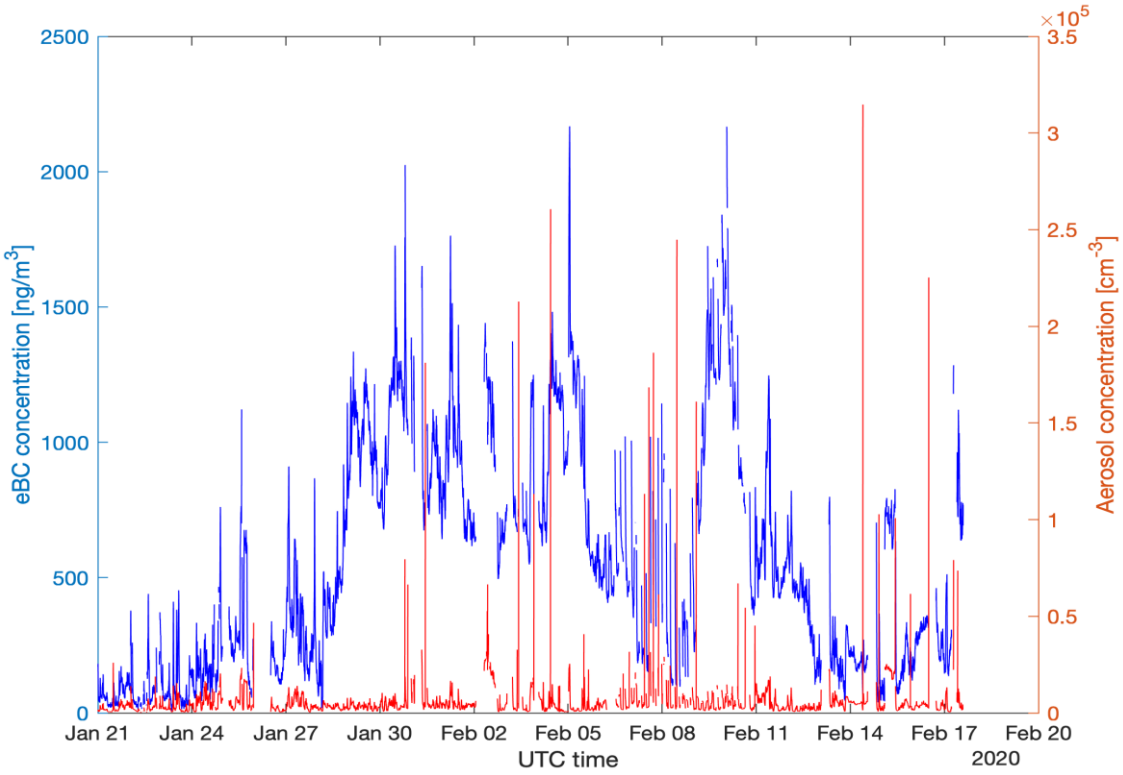

Figure 27. *eBC and total aerosol concentration (5 min time resolution) along the whole EUREC⁴A campaign.*

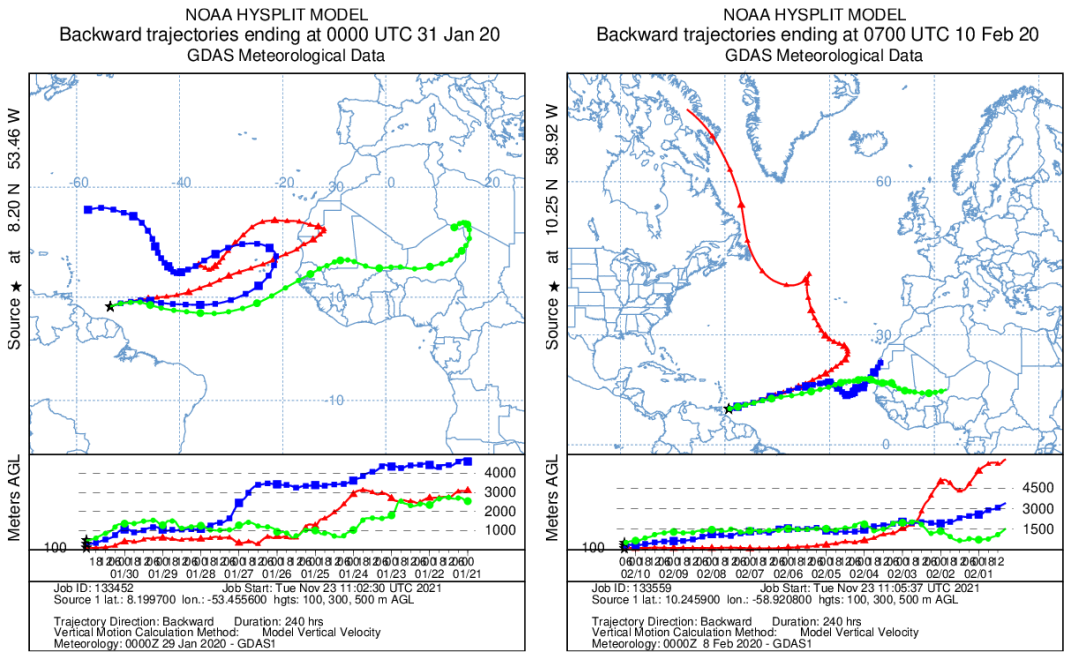

Figure 28. 240 hours run time back-trajectories obtained using Hysplit for January 31 (left) and February 10 (right).

The eBC was inferred based on the absorption coefficient measurements (optical method). Therefore, as explained in section 2.3, it is sensible to any aerosol absorbing species present in the atmosphere, especially when dealing with high concentrations of mineral dust. Accordingly, considering also the origin of the air masses, PM data, the weather regime of the region and other aerosol studies concerning EUREC⁴A, the two events were linked to dust transport with

a non-negligible biomass burning contribution in the second case as demonstrated by the chemical fingerprints discussed in section 3.3.2. The two periods of higher LAA concentrations corresponded to days associated with non-pure dust transport events (from West Africa) in other literature works [110,119] via airborne lidar measurements. The periods outside the days of particle transport, especially the period before the first event, can be considered as aerosol background conditions, characterized by an atmospheric composition dominated by local sources (such as sea-spray). The eBC average concentration during the background period was 177.20 ± 3.10 ng/m^3, while eBC average values during the two transport events were 965.18 ± 5.43 ng/m^3 and 770.21 ± 11.17 ng/m^3 respectively. OPC mass concentration data enabled to identify the fine (PM_1) and coarse (PM_{1-10}) mass concentration, and the fine PM_1 fraction (PM_1/PM_{10}). As shown in Figure 29, the PM_{1-10} mass concentration reached maximum values during transport events, being 4.2 ± 0.4 µg/m^3 and 2.6 ± 0.3 µg m^3 respectively. These values were significantly higher than the average background coarse aerosol mass concentration (1.0 ± 0.1 µg/m^3), measured during L'Atalante cruise outside of the two transport events. Moreover, the PM_1/PM_{10} ratio was 0.48 ± 0.03 and 0.59 ± 0.03 during the two events. Only the first one was statistically different from the background value of 0.57 ± 0.02, suggesting the presence of a finer aerosol source during the second event, which acted along with the dust source. Biomass burning events in sub-equatorial North Africa were documented by satellite images during the previous days (Figure 30).

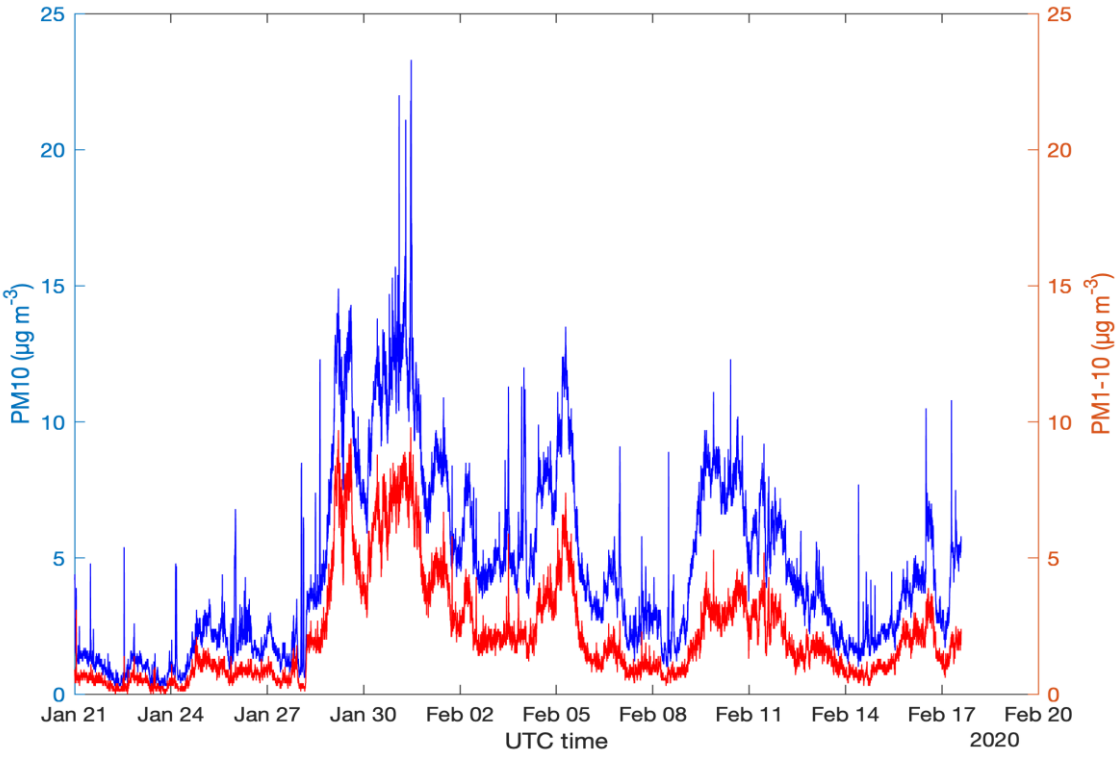

Figure 29. *PM_{10} and PM_{1-10} mass concentration time series along the EUREC4A campaign*

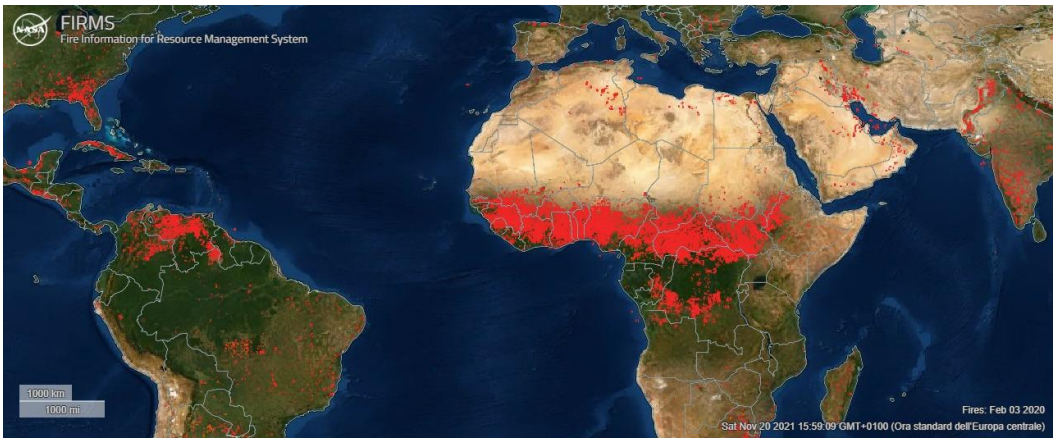

Figure 30. *Satellite active fire map.*

The aforementioned transport events affected the eBC concentration spatial distribution along the cruise. Indeed, from Figure 31a it is evident the increase of concentration close to the French Guyana and around 10°N in keeping with the arrival of long-range transported air masses. The two cases were thus intersected in the southernmost area of the campaign (causing a rise in eBC concentrations). This is in agreement with the seasonality: during winter the transport route is further south, due to the southernmost position of the ITCZ [110,119]; therefore, particles (primarily Saharan dust) are transported from West Africa towards the South America and the Amazon region [135], reaching more rarely the northern Caribbean.

Interestingly, the total aerosol number concentration did not show exactly the same spatial and temporal pattern (Figure 31b) of eBC concentrations. This may be due to the fact that eBC is a marker of primary origin of aerosol (either anthropogenic or natural one), while the aerosol number concentration (N) includes particles of both primary and secondary (e.g. from biological precursors emission) origin. Therefore, the N/eBC ratio can be considered a marker of aerosol secondary origin [136] and was used in order to estimate the contribution of locally formed aerosol along the route of L'Atalante.

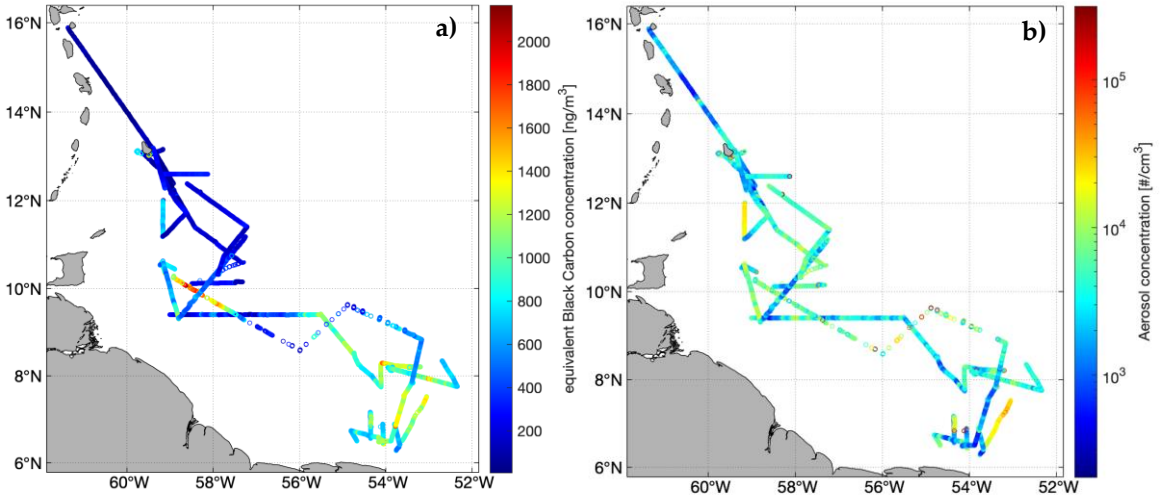

Figure 31. *Spatial distribution of eBC concentrations (**a**) and aerosol number concentrations (**b**) obtained during the EUREC⁴A campaign.*

N_p primary (primary number concentration) and N_s secondary (locally formed secondary aerosol) were computed following the work of Ferrero et al. [64]: N_p was thus obtained by multiplying eBC by 2.5. This value may be subject to variability; however, regardless of the multiplication coefficient, what we are most interested in is the relative trend, i.e. how the signals (primary and secondary) decouple during the two transport events with respect to the background period. Indeed, there was a growth in the N_p value during the transport phenomena, as visible from Figure 32 (showing the temporal series of N_p and N_s).

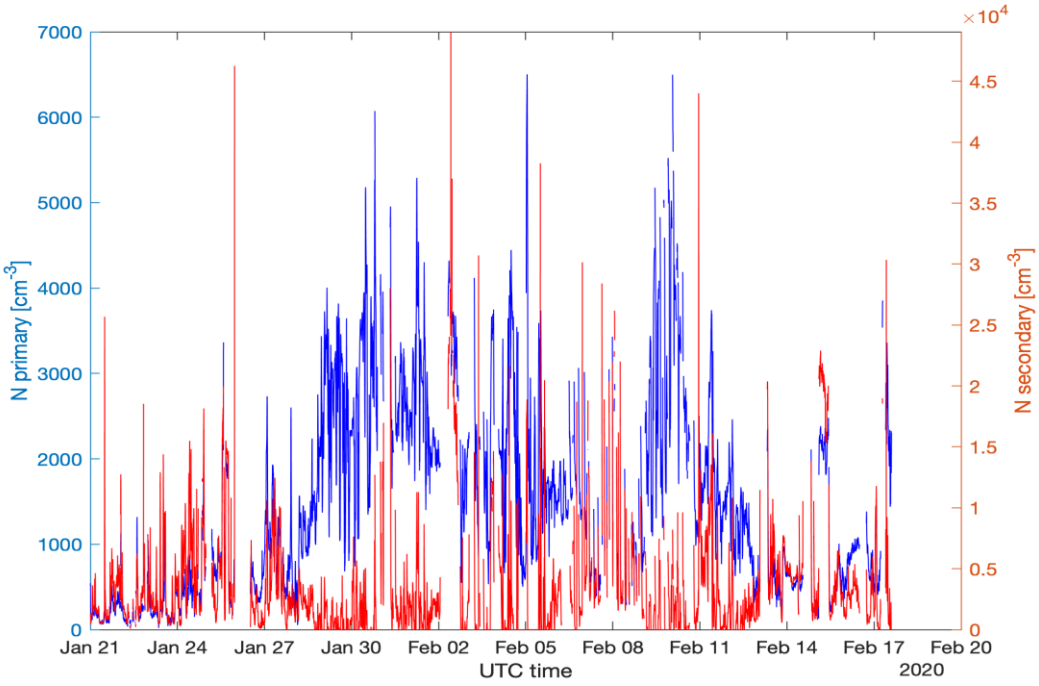

Figure 32. *Primary and secondary aerosol concentration time series (5 min time resolution).*

The general importance of secondary aerosol concentrations along the cruise is clearly visible. They accounted on average for 87 ± 9% in background conditions (4.234 ± 0.323*10^3 cm^{-3} of secondary aerosol and 643 ± 36 cm^{-3} of primary aerosol). During the two transport events they dropped down to 56 ± 13% (2.691 ± 0.521*10^3 cm^{-3} of secondary aerosol and 2.078 ± 0.121*10^3 cm^{-3} of primary aerosol) for the first case and to 59 ± 14% (2.618 ± 0.512*10^3 cm^{-3} of secondary aerosol and 1.813±0.127*10^3 cm^{-3} of primary aerosol) for the second case, respectively.

During background conditions the N/eBC ratio reached an average value of 26.5 ± 3.5 m^3 ng^{-1} cm^{-3} clearly indicating the presence of secondary formed aerosol [64,137,138]. This is evident from Figure 33, where the spatial distribution of N/eBC is inversely correlated with the CMD of aerosol, highlighting the contribution of finest particles to secondary formed aerosol.

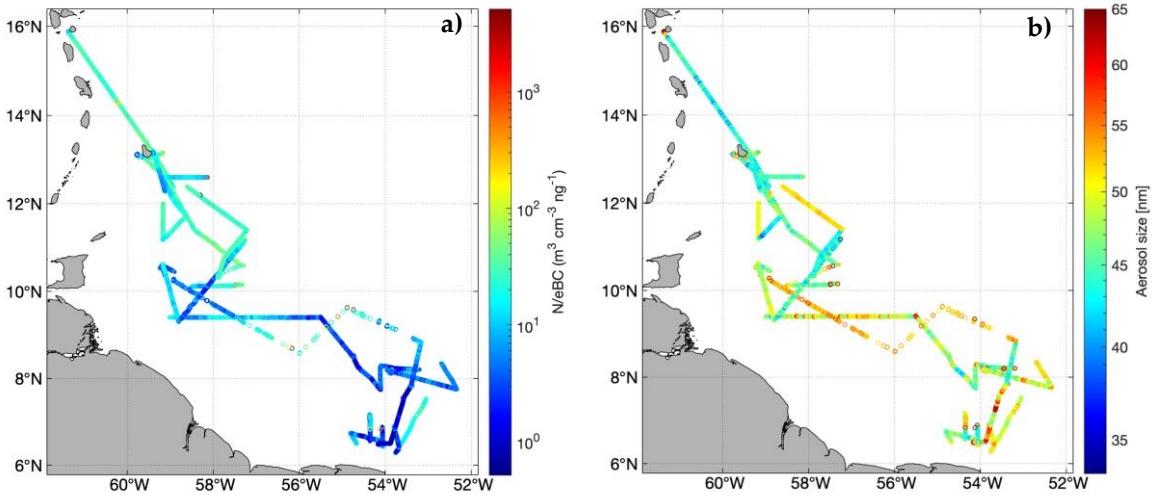

Figure 33. *Spatial distribution of N/eBC ratios (**a**) and count mean diameter (**b**) obtained during the EUREC⁴A campaign.*

Figure 34 shows an example of the diurnal cycle of marine aerosol number concentration and size distribution. It represents the diurnal cycle during the first transport event, but in general for all cases (background and transport events) the lowest diameters were registered after 10 UTC, during sunlight conditions in agreement with atmospheric photochemical processes responsible for secondary aerosol formation**.** It noteworthy that the interpretation of the diurnal behavior of secondary formed aerosol concentration is more complex, being affected not only from its formation but also from dilution and dispersion phenomena within the marine boundary layer.

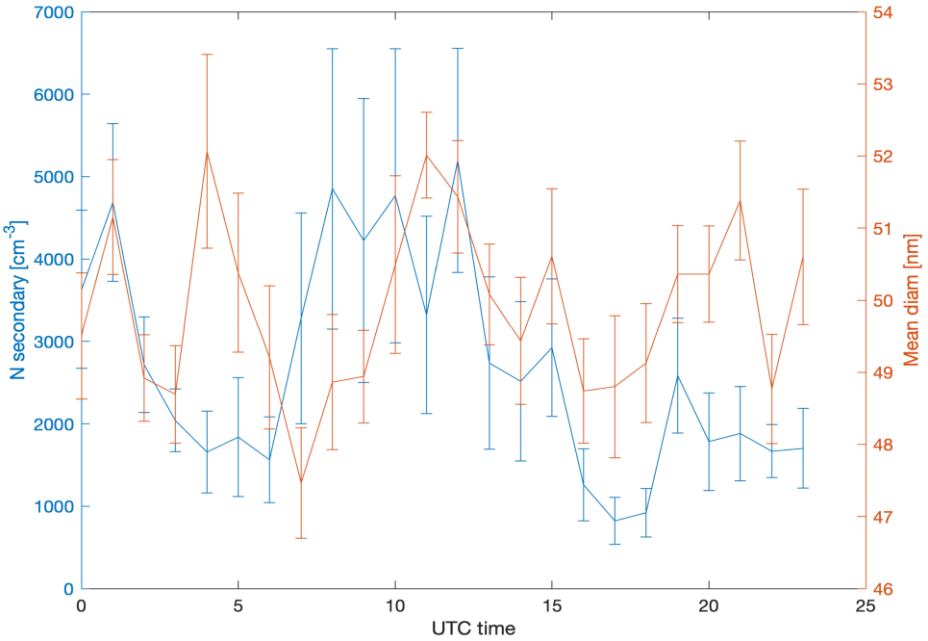

Figure 34. *Diurnal pattern of secondary aerosol and related count mean diameter obtained during the first transport event (29/01/2020 - 05/02/2020) .*

3.3.2. Aerosol chemical composition

TSP chemical composition was inferred by analyzing quartz fiber filters in order to know the amount of water-soluble inorganic ions and OM (obtained by subtracting the eBC from the TC data). Average atmospheric concentrations of the detected species are reported in Table 1. Since it is a typical marine aerosol, the most abundant ions were Cl^- and Na^+ with concentrations of 7611 ± 1643 ng/m^3 and 4320 ± 896 ng/m^3, respectively. The sea salt aerosol concentration was calculated referring to Bates et al. [139]:

$$sea\ \ salt\ \ [\mu g/m^3] = \ \ Cl^-[\mu g/m^3] + 1.47 * Na^+[\mu g/m^3] \quad (23)$$

where 1.47 is the mass ratio of the sum of Na^+, Ca^{2+}, Mg^{2+}, K^+, SO_4^{2-} and HCO_3^- to Na^+ in sea water. This method allows to avoid the inclusion of non-sea-salt (nss) Ca^{2+}, Mg^{2+}, K^+ and SO_4^{2-} and permits also to consider the loss of Cl^- due to the Cl^- depletion processes. Moreover, the sea salt contribution to the observed concentrations of Ca^{2+}, Mg^{2+}, K^+, Cl^- and SO_4^{2-} were determined according to Mihalopoulos et al. [140]:

$$ss_x\ \ [\mu g/m^3] = \frac{X}{Na^+} * Na^+{}_{measured}\ \ [\mu g/m^3] \quad (24)$$

where X is the selected species and X/Na^+ is the mass ratio of its concentration to that of Na^+ in the sea water. The average concentration of sea salt aerosol was 14 ± 3 μg/m^3. This value is quite high and could be related to a relatively high average wind speed close to the sea surface (8.92 ± 0.03 m/s), which is consistent with the weather regime of the study area (characterized by trade winds). Indeed, the ocean can act as a primary direct source of aerosol due to the turbulence at the surface, through the process of bubble-bursting emissions [139] (Bates et al., 2001).

Compound	Mean (ng/m^3)	σ_m
Cl^-	7611	2940
Na^+	4320	1583
SO_4^{2-}	1899	772
NO_3^-	803	649
Ca^{2+}	467	323
Mg^{2+}	461	178
K^+	275	141
NH_4^+	51	97
PO_4^{3-}	10	12
F^-	6	2
OM	2369	2307
eBC	683	475

Table 1. Average chemical composition.

Figure 35 shows the sea salt percentage of the major inorganic ions. All the $Mg^{2+}$and Cl^- derived from sea salt aerosol. More than half of the K^+ and SO_4^{2-} derived from sea salt with average values of 66.43 ± 11.45 % and 58.98 ± 6.53 % respectively. Instead, Ca^{2+} was mostly associated with a nss-origin (ss-Ca^{2+} = 44.86 ± 10.39 %). The sea salt origin of the ions is due to the primary emissions from the sea (i.e. sea-spray). However, the sea can also be a source of aerosols through secondary emissions. Indeed, part of the nss-SO_4^{2-} can derived from secondary formation, as a consequence of the reactions from precursors emitted by the sea into the atmosphere: the enzymatic cleavage of dimethylsulfonium propionate in surface seawater produces the dimethylsulfide (DMS), which is converted to SO_4^{2-} in the atmosphere. Sulfate was the most plentiful ion after Cl^- and Na^+ and the average concentration of nss-SO_4^{2-} was 813 ± 267 ng/m^3; this value can indicate high marine biogenic emissions. However, nss-SO_4^{2-} is also related to a secondary origin from anthropogenic precursors, emitted by combustion of fossil fuels (coal and petroleum derivatives). Part of the sulfates can thus derive from ship emissions and also other continental anthropogenic sources, being rather stable in the atmosphere and subjected to transport processes.

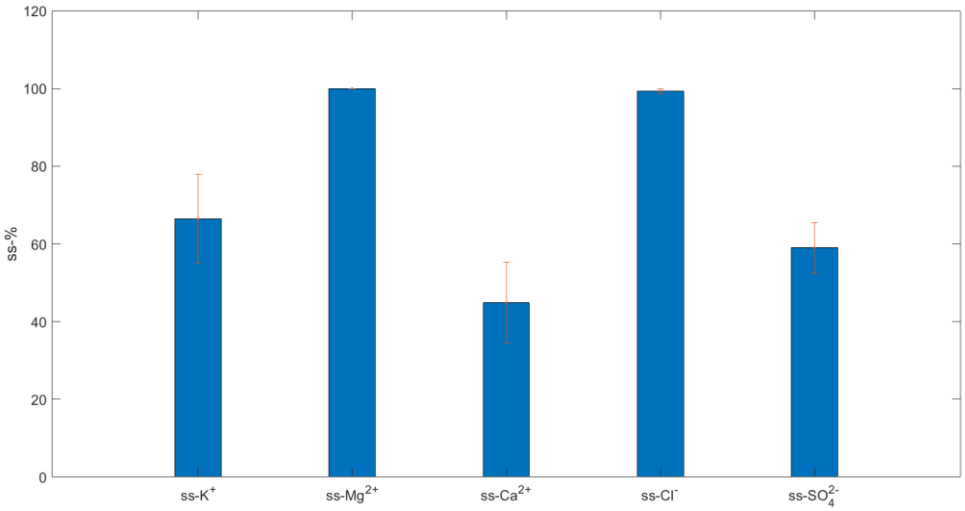

Figure 35. *Average sea salt percentage of the major inorganic ions.*

While all the magnesium ion originated from sea-spray emissions, Ca^{2+} was the ion with the lowest marine origin due to the predominantly crustal sources (such as mineral dust transport). nss-K^+ can have instead both terrigenous and forest fires origin and (over the ocean) can be used as a proxy of fire particles. Therefore, as better explained below, we used nss-K^+ and nss-Ca^{2+} as markers for long-range transport and continental origin of air masses, more specifically for biomass burning and dust transport respectively.

NO_3^- was the fourth most abundant water-soluble inorganic ion in the samples. It was less abundant than sulfate because it only has a secondary origin from anthropogenic precursors (i.e. continental sources, except for ship emissions).

NH_4^+ was detected only in 3 of the 12 quartz fiber samples analyzed. Considering only the 3 samples in which it was present, the average NH_4^+ concentration was 206 ± 75 ng/m^3; this value is obviously higher than the average of the entire campaign (51 ± 55 ng/m^3), obtained by considering that the concentrations of the other samples were below the detection limit (for this reason the confidence interval is so high). The average concentration of the whole campaign is similar to those of the Arctic Ocean (47 ± 33 ng/m^3) [61] and the Southern Ocean (42 ± 31 ng/m^3) [141]. The primary source of ammonium may be the long-range transport of substances from the continents. Moreover, some NH_3 could be also emitted from seabirds (this kind of origin can explain 1.8 – 2.7 % of oceanic emissions converted into ammonium) [142–144].

Finally, PO_4^{3-} and F^- had negligible concentrations (10.09 ± 7.09 ng/m^3 and 6.03 ± 1.3 ng/m^3 respectively) and PO_4^{3-} was detected only in 5 of the 12 samples.

Average concentration of total carbon in the collected samples was 1811 ± 849 ng/m^3. The organic fraction (OC), obtained by subtracting the eBC given by the Aethalometer (at the quartz filter sampling periods) from the TC, accounted on average alone for 62% of the total carbon (OC average value = 1128 ± 622 ng/m^3). The remaining TC is due to eBC, whose average value was 683 ± 269 ng/m^3 (considering only the eBC values corresponding to the sampling period of the quartz filters). When the OC was converted to OM (using a factor of 2.1 [65]) the average value of the campaign increased up to 2369 ± 1305 ng/m^3. The high concentration of OM (the highest value after Na^+ and Cl^-) can be attributable to both combustion (e.g. biomass burning) and biogenic activities from the sea. While in the Arctic remote areas, where sulfates and OM values were relatively high despite very low eBC concentrations (as shown in the next chapter), it is highly likely that the role of biogenic activity was prevalent, this assumption cannot be made in this case because eBC concentrations are comparable to those found at mid-latitudes. Therefore, further studies are required to determine the biogenic fraction of nss-SO_4^{2-} and better understand the importance of biogenic activity (also in contributing to OM).

As discussed in previous section, two main aerosol transport events were identified along the campaign, which alter the background concentrations (significantly higher concentrations of PM during these two events). The aerosol chemical composition during the two events can be investigated: Figure 36 show the chemistry of quartz filters FQ6 and FQ10, which are representative of the first and second transport events respectively. They can be compared to the filters that represent background conditions (Figure 37).

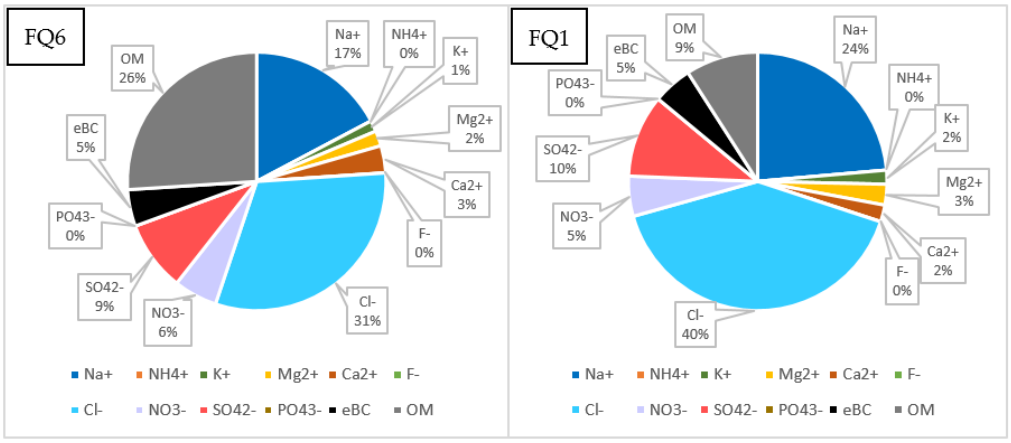

Figure 36. *Aerosol chemical composition (relative percentages) of quartz filters during the first (left) and second (right) transport events*

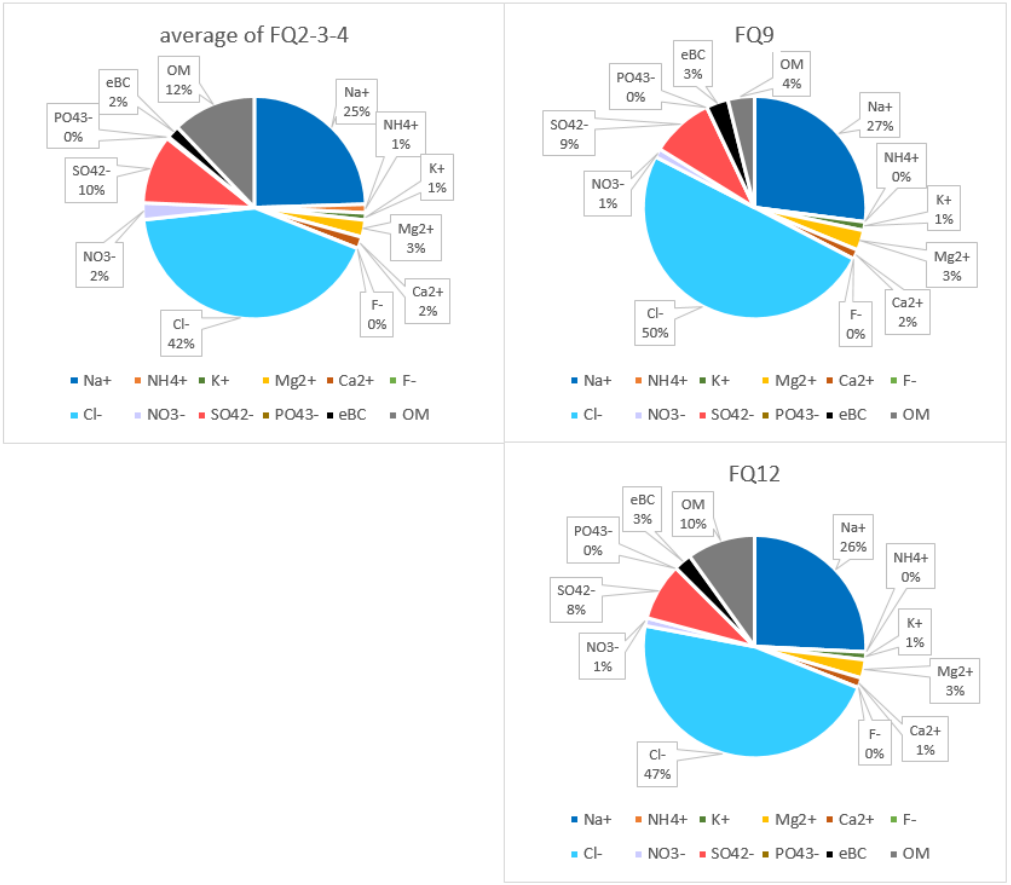

Figure 37. *Aerosol chemical composition (relative percentages) of quartz filters that represent background conditions*

The pie charts (Figures 36 and 37) represent the relative percentages, i.e. the relative contribution of the different chemical species with respect to their total sum. Generally, we can affirm that the background is not completely free from other natural sources (different from the sea, e.g. nss-Ca^{2+} and nss-K^{+}) anthropogenic influences (e.g. eBC and nitrates). However, comparing it with the transport cases, the sea influence is greater, as demonstrated by higher relative percentages of Cl^{-} and Na^{+} and by a much more prominent origin of the ions present also in sea water. Moreover, some ions can be used to better understand the nature of the two

transport events. As already mentioned and as show in Figure 38, a higher intensity and a greater difference between $PM_{2.5}$ and PM_1 in the first event seems to suggest an event linked to the coarser fraction of the aerosol, such as Saharan Dust. Instead, a greater proximity between the two curves and the presence of the highest spike in eBC concentrations of the entire cruise (despite the lower intensity of the event) could indicate a partially different origin for the second event (e.g. Biomass Burning). Moreover, during the two events the percentage contribution of sea-salt to the concentration of K^+ and Ca^{2+} remarkably decreases, confirming the presence of another kind of origin. Nss-Ca^{2+} can be considered a marker of Saharan dust, while K^+ can be considered a marker of fires (sampling over the sea, potassium is a better marker of fires than sampling on the continents). Although the non-marine source of both ions becomes more important during both events, it seems that the increase in nss-Ca^{2+} is greater in the first event, while the increase in nss-K^+ is greater during the second event. Therefore, looking at the nss-K^+/nss-Ca^{2+} ratio (Figure 39), it is evident how this ratio is higher in the second event (FQ10). This confirms that the first transport case is more characterized by Calcium, while the second one is more related to Potassium, allowing recognition of a greater presence of BB particles in the second aerosol plume.

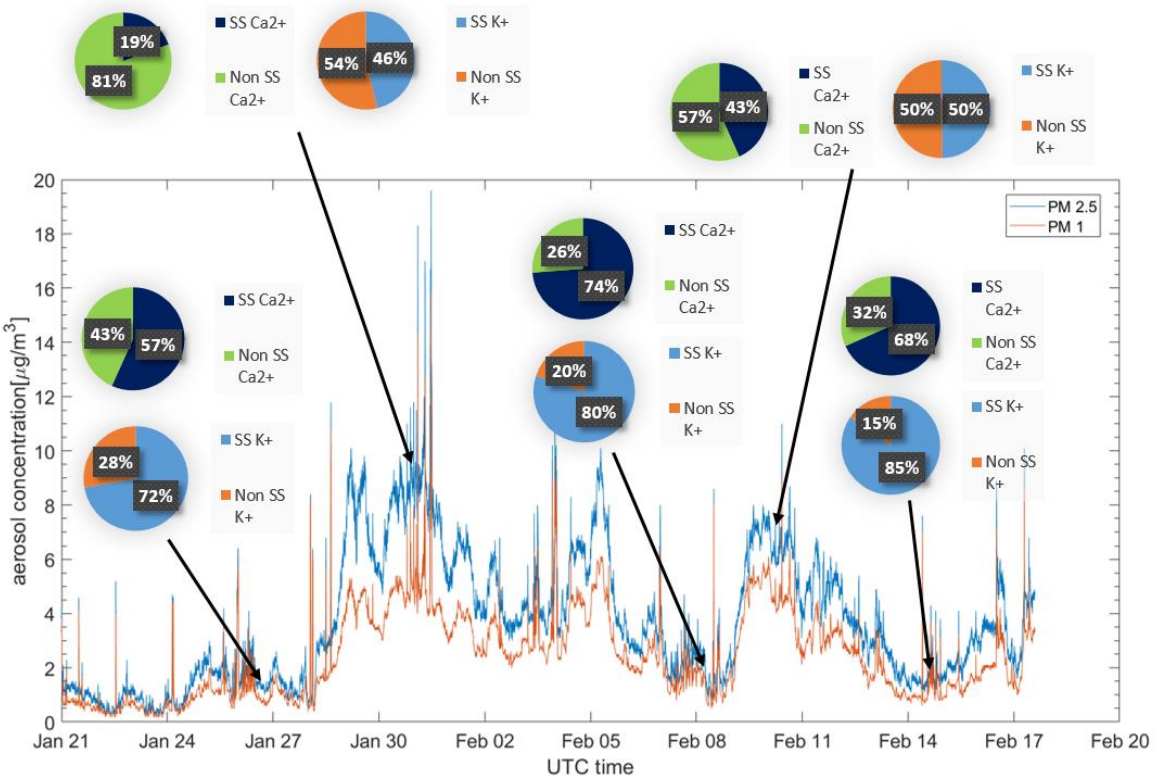

Figure 38. *Sea salt and non-sea salt origin of Ca^{2+} and K^+ cations during the two events compared to the background.*

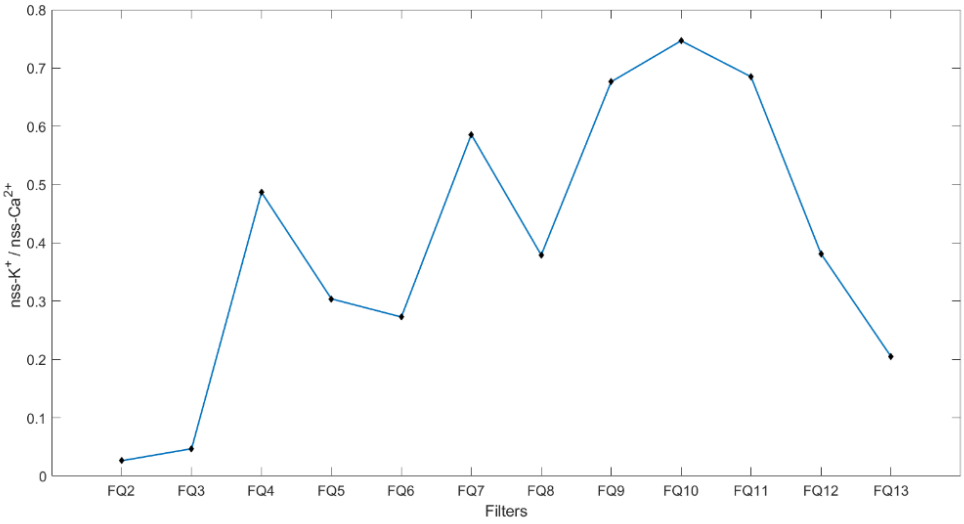

Figure 39. *nss-K^+/nss-Ca^{2+} ratio. It is higher in correspondence of FQ10, i.e. during the second event, that seems thus more contaminated by biomass burning than the first event.*

Finally, also sea-spray concentrations reached their maxima (≈20 μg/m^3) during the period of the two transport events, in accordance with greater ocean surface wind speeds [145].

Our evidence for an increased contribution of BB aerosols during the second event do not agree closely with the measurements of Chazette et al. [110], which hypothesize a dust plume less mixed with BB aerosols during the second event. Also Gutleben et al. [119] found an influence of BB in the first event (they focused only the days of the first transport). However, no pure dust plumes were identified during EUREC^{4}A, because it was always mixed with other species, in particular marine and BB aerosols (i.e. during both transport events). Moreover, there are two relevant differences with our measurements: chemical off-line data have a lower temporal resolution than lidar data, so information about mixing variations at short temporal scale (i.e. changes in the relevance of BB aerosol within the same transport event) is lost; second, our data come from surface measurements, while the literature data cited come from airborne measurements. Indeed, depolarization and lidar ratios related to the first transport event demonstrated that the contribution of BB aerosol to the aerosol mixture (dominated by dust) was higer at high altitude (i.e. above 2 km), while the lower levels (i.e. from the surface to 700 m) were characterized by a mixture dominated by marine aerosol and dust. Additionally, BB particles were not mixed to low atmospheric levels [119], being thus present at higher altitudes in these days. From these considerations, it is hence reasonable that we found no indication at the surface level of a prevalence of BB aerosol in the dust mixture during the first event. Further chemical investigations (e.g. elemental analysis) will help to better understand the nature of aerosol during transport events.

3.3.3. Direct climate forcing (HR) of LAAs

From the absorption coefficients and radiation measurements was possible to compute the LAA HR. The average HR value of the entire campaign was 0.175 ± $3*10^{-3}$ K/day. It is an order of magnitude lower than the values found by Tripathi et al. [99] in northern India (urban area of Kanpur) with a radiative transfer model and by Ferrero et al. [11] in the Po Valley in the same season (1.83 ± 0.02 K/day) and in similar sky conditions, i.e. clear sky (1.75 ± 0.03 K/day for clear sky conditions), with the same experimental methodology. Indeed, as shown in Figure 40, the average daily trend of solar radiation (for the whole campaign) exhibited a bell-shaped pattern, typical of days with very little cloud cover. The average HR daily trend follows that of radiation. As will be better seen in chapter six, average HR value is very similar to the average HR found in Gdansk area at 54 °N during the AREX campaigns and 2 orders of magnitude greater than HR measured by the same methodology in the Arctic ocean. Thus, if a HR gradient due to LAA is present in summer between the mid-latitudes and the Arctic, it appears that it may also exist in winter between the tropical North Atlantic and the pole (where HR tends to 0 in winter). However, it is likely that in the tropics the role of other absorptive species, particularly dust, is greater than in the mid-latitudes, where BC dominates. In order to better investigate the importance of dust, the source apportionment needs to be improved so that mineral dust can be separated from other sources/species.

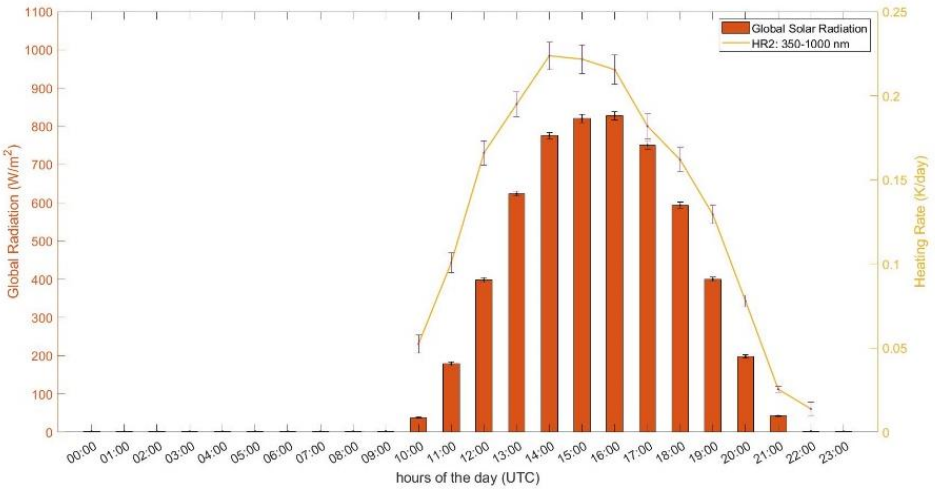

Figure 40. *Average daily trend of solar radiation and HR*

Maximum values of HR measured during EUREC^{4}A were just below 0.8 K/day. In accordance with the eBC trend, the lowest values were measured in the first part of the campaign, near Barbados, while the highest values were recorded in the southeastern area because of the two transport events from West Africa. Figure 41 shows the HR daily averages (and the relative 95% confidence intervals) for the whole cruise. The initial background period, characterized by lower daily averages, and the two subsequent transport events are clearly visible. Maximum daily average was in 9 February in the middle of the second event (0.372 ±

0.011 K/day). Long-range transport of dust and BB aerosol, which is frequent in this region, can therefore significantly alter the background HR induced by locally emitted LAA. Looking at Figure 42, which shows the global radiation and HR averages for background and tranport periods, it is evident that global radiation changed little between background and the other cases, while the HR varied widely: 0.047 ± $2*10^{-3}$ K/day, 0.279 ± $5*10^{-3}$ K/day and 0.186 ± $6*10^{-3}$ K/day for background, first and second transport events, respectively. The highest value was reached during the first dust transport, which was very intense and lasted for several days. The main driver of HR variation thus were the LAA absorption coefficients, which clearly increased during the transport events (Figure 43) both at 370 nm and 880 nm. 880 nm is the reference wavelength for black carbon in the Aethalometer, but also other LAA can influence the measurements especially when dust is present in large quantities. Moreover BB can produce also BC in addition to organic carbon, such as BrC. These may be the reasons why b_{abs} rose also in the infrared region and not only in the UV. Due to the non-negligible presence of mineral dust, the source/species apportionment between FF /BB and BC/BrC applied to AREX campaigns risks being untrue; so an apportionment that includes dust must be implemented if the role of BB and dust during transport events is to be investigated in depth from a spectral point of view.

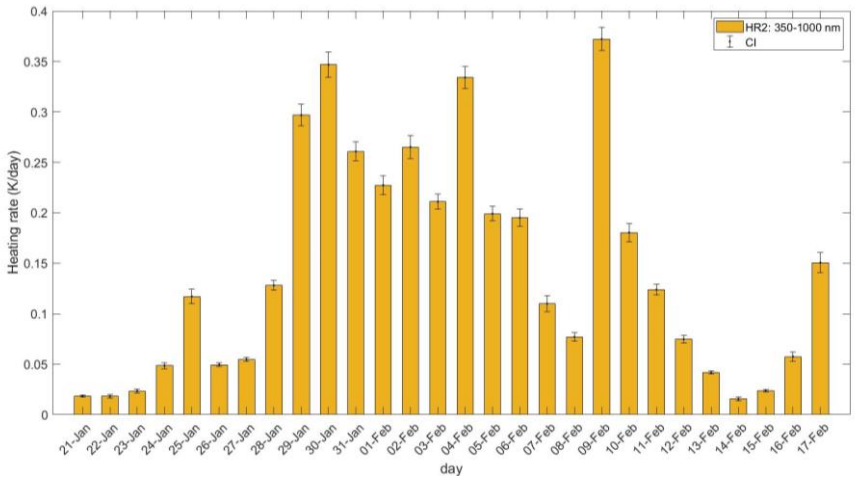

Figure 41. *HR daily averages (and the relative 95% confidence intervals) for the whole cruise.*

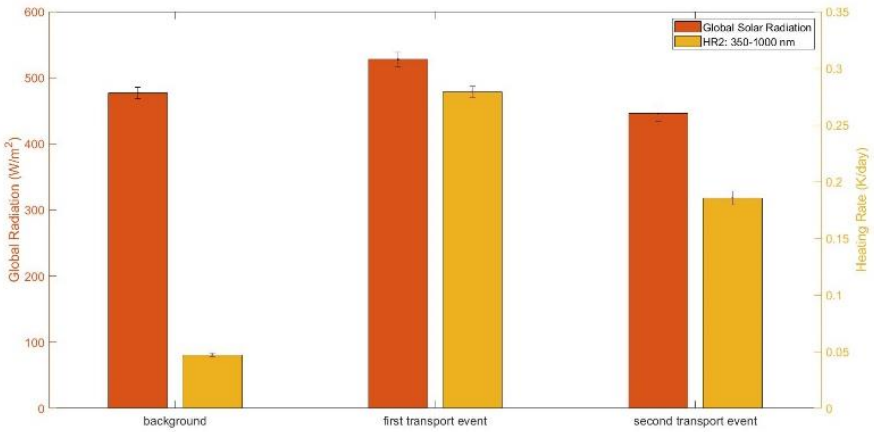

Figure 42. *Global radiation and HR averages for background and two tranport periods.*

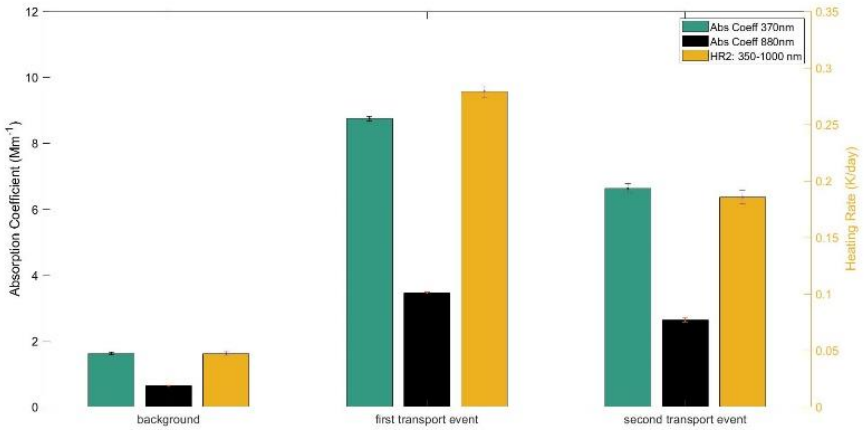

Figure 43. *Averages of HR and absorption coefficients (at 370 nm and 880 nm) for background and transport periods.*

3.3.4. Hygroscopic data

Hygroscopic data can be a starting point for correlating aerosol to clouds. Aerosol hygroscopicity measurements (humidification and crystallization cycles) carried out in the AEC are presented here averaged in Figure 44.

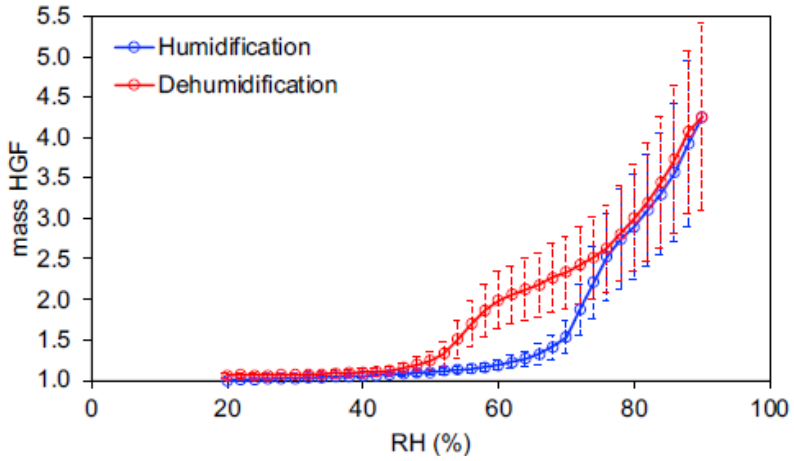

Figure 44. *Humidification and dehumidification average curves of mass HGF obtained on PTFE filters*

By the knowledge of the aerosol mass deposited on PTFE filters and the mass of the water absorbed by the aerosol the mass HGF was computed following equation 22. The humidification branch is reported in blue while the dehumidification in red. The average DRH is clearly visible between 70% (DRH_{start}) and 76% (DRH_{end}) with the highest gradient at 74% RH ($DRH_{gradient}$) in keeping with the aerosol chemical composition (section 3.3.2) dominated in mass by sea spray aerosol (ion chromatography on Teflon filters gave results completely in agreement with those on quartz filters). Similarly, the CRH started from 58% (CRH_{start}) ending at 44% (CRH_{end}) when the aerosol came back to a dry state; the highest gradient was at 48% RH ($CRH_{gradient}$) again in keeping with the aerosol chemical composition and with DRH, CRH values reported

by Martin [146]. A further increase in the RH above DRH_{end} leads to hygroscopic growth due to the continuous condensation of water.

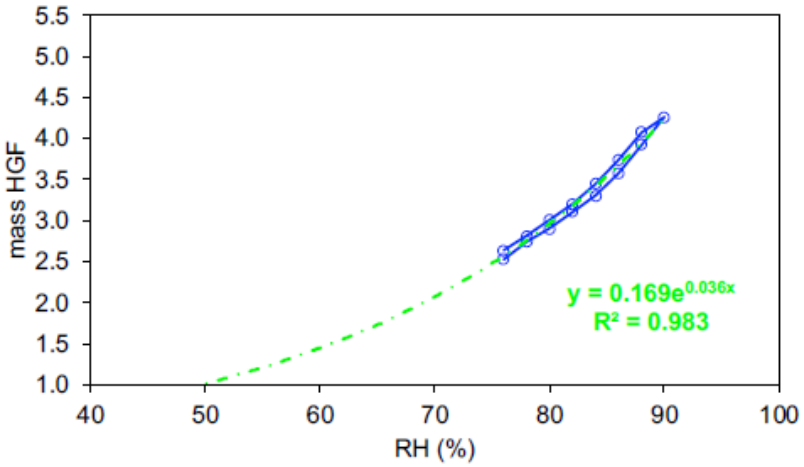

Figure 45. *Exponential fitting of the humidification and dehumidification curves of mass HGF above the* DRH_{end}.

The mass HGF at 90% RH was computed, being 4.3 ± 1.2, a value ~2 times higher than continental aerosol [134] due to the high hygroscopicity of sea emissions. The mass HGF in the condensation/evaporation region (RH>DRHend) can be fitted with an exponential line (y=0.169e0.036RH, R2=0.983; Figure 45), which will allow a comparison with model forecast for Cloud Condensation Nuclei (CCN) behaviour and their growth in the atmosphere for cloud formation.

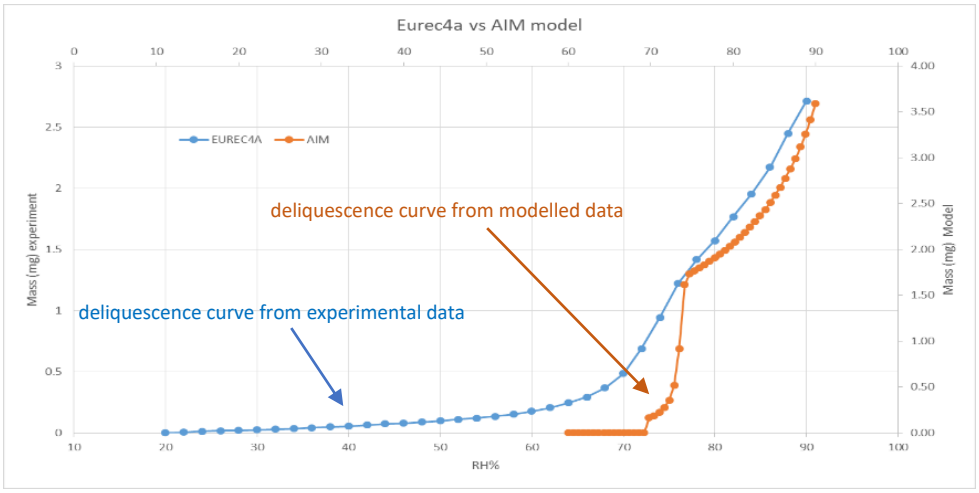

Figure 46. *Comparison between deliquescence curve from the experimental data and the modeled data (from the E-AIM model).*

Data from ion chromatography (water-soluble inorganic ions content on PTFE filters) was also used in the Extended AIM Aerosol Thermodynamics Model [147]. Comparing the deliquescence curve from experimental data with the modelled data, the humidographs closely resemble each other: DRH from the model is 73%. Shapes of the curves are similar, but there is a difference in scale: the modelled mass of water is about 28% more than the experimental one. The agreement between experimental and modelled curves suggests that data obtained from

future chemical analysis can be applied to the E-AIM model to interpret the deliquescence process occurring in other regions.

Finally, hygroscopic data, together with dimensional data of aerosol particles, will allow to calculate the k parameter [148], related to the activation of particles as Cloud Condensation Nuclei. This topic, however, is beyond the aim of the present work.

3.4. Conclusions

The study area, i.e. the tropical North Atlantic (in particular the sea near Barbados, Guyana and Suriname), is characterized by a wide variety of aerosol species. During winter, depending on the large-scale synoptic situation, Saharan dust particles can be transported from West Africa to this region. Aerosol transport occurs at lower latitudes and altitudes than in summer (due to the shifting southward of the ITCZ and the lower boundary layer over the Saharan region) and dust particles are often mixed with marine and BB aerosols within the marine boundary layer. Therefore, dust plumes reach the Caribbean more rarely in winter, but the arrival of particulate matter from the west over the Atlantic to Barbados is still possible and there are several evidences about that [110,116,119]. The mixture of mineral dust, sea spray and BB aerosol at lower levels can influence the energy balance in the sub-cloud layer through direct interaction with solar radiation and can alter the cloud formation and life acting as CCN.

Several studies [110,116,119] highlighted that no pure dust regimes were observed during EUREC^{4}A campaign, since they found depolarization ratios typical of aerosol regimes characterized by a mixture of dust particles and marine or BB aerosol [149,150]. By means of eBC and particles concentrations and aerosol chemical composition we found background conditions (especially during the first part of the cruise), with lower aerosol concentrations and chemistry most influenced by marine and/or local sources, and two transport events from West Africa (the first one from January 29 to February 5 and the second one between February 9 and February 11), characterized by significantly higher PM and eBC concentrations. The higher abundance of fine versus coarse particulate matter during the second transport case and the higher nss-K^+/nss-Ca^{2+} ratio (K^+ was considered as a marker of fires, while Ca^{2+} was used as a marker of Saharan dust) have suggested a greater influence of BB aerosol on the transported dust mixture in the second event. The presence of BB aerosol can be explained by the occurrence of several fires in subequatorial Africa during the measurement period and by the low latitudes together with low transportation altitudes [119]. The high concentration of marine aerosol, instead, can be explained by the high surface wind speed, in agreement with the region where the trade winds blow. Moreover, transported particles were detected at lower latitudes of the campaign, south of Barbados, in keeping with the weather regime of the season.

Generally, aerosol chemical composition for background conditions was not free of anthropogenic influences, unlike remote areas (e.g. over the Arctic Ocean, as we will see in the next chapter), but still mainly influenced by the local marine source. eBC background average concentrations was 177.20 ± 3.10 ng/m^3 (this value is comparable to the concentrations found in the Baltic and along the coast of Norway during the AREX campaigns). However, during the two transport events eBC concentrations increased significantly, reaching values comparable to those in mid-latitudes (965.18 ± 5.43 ng/m^3 and 770.21 ± 11.17 ng/m^3 for the first and the second case of transport respectively), and consequently their direct climate impact (HR). Indeed, the HR was 0.047 ± 2*10^{-3} K/day, 0.279 ± 5*10^{-3} K/day and 0.186 ± 6*10^{-3} K/day for background, first and second transport events. This values, particularly when transport is present, are not negligible and can affect the energy balance and consequently the cloud dynamics in the region. The variation in HR between background and transport were due almost exclusively to differences in LAA absorption coefficients, because solar radiation was quite constant. The average HR of the entire campaign was 0.175 ± 3*10^{-3} K/day. It is comparable to average HR found in Gdansk (Poland) and at 54 °N during AREX campaign and 2 order of magnitude higher than HR over the Arctic Ocean. Therefore, a notable difference in terms of HR induced by LAAs between the tropical North Atlantic Ocean and the Arctic is present in winter (when short-wave radiation is practically absent at higher latitudes, i.e. polar night). Obviously the average EUREC^{4}A HR value was influenced by the transport events. However, aerosol transport from West Africa is very frequent in that area, so these are not exceptions that rarely alter background conditions. Unlike eBC concentrations and HR measured in northern Europe, which are highly influenced by black carbon emissions, in the investigated tropical area the role of mineral dust in LAA concentrations and climatic impact is very important. A future goal is therefore to improve the apportionment of HR, so as to investigate the role of dust separately and compare it to other species and sources.

Lastly, hygroscopic data showed DRH and CHR values in keeping with the aerosol chemical composition, while the HGF at 90% RH (4.3 ± 1.2) was ~2 times higher than continental aerosol due to the high hygroscopicity of sea emissions. Moreover, HGF in the condensation/evaporation region was fitted with an exponential line, which will allow a comparison with model forecast for Cloud Condensation Nuclei (CCN) behavior and their growth in the atmosphere for cloud formation. Our hygroscopic measurements, together with dimensional data of aerosol particles will allow also to calculate the k parameter [148], related to the activation of particles as Cloud Condensation Nuclei. Therefore, the link between aerosol and clouds in this region will be further investigated, improving our comprehension of the factors that influence clouds at the particle scale.

4. Environmental context: macroscopic latitudinal differences

In this chapter we introduce the macroscopic differences between the aerosol chemical composition determined at different latitudes and specific areas during the AREX campaigns. Indeed, the chemical composition helped us to assess the first, rough geographical differences in terms of aerosols properties, according to latitude. These distinctions are explored in more detail in the next two chapters, thanks to the high temporal resolution measurements, which allowed us to determine the direct climatic impact of LAA.

The Arctic lower troposphere is influenced by pollution from lower latitudes (North Eurasia and North America) and local sources [151] (e.g. human settlements in the region, ship traffic, mining activities and gas flaring). During summer the arctic haze phenomenon [152] is absent and long-range transport towards the pole is greatly reduced. Therefore, emissions within the Arctic itself must thus be considered, especially in summer, to determine a comprehensive assessment of particle load in this area [151]. We therefore took into consideration the results from the chemical analysis of the quartz fiber filters, sampled during the outward sections of 2 of the 3 AREX campaigns (summer of 2018 and 2019; in 2021 only automatic high resolution measurements were collected due to the COVID pandemic), to better understand the extent of anthropogenic influence (even at the macroscopic, less resolute level) on the different areas considered in this work: both at the larger latitudinal scale (differences between areas at different latitudes, from mid-latitudes to Arctic) and at a more local scale (differences between macro-areas within the Arctic itself). Indeed, some aerosol components, such as black carbon, nitrates and, to some extent, sulfates, are indicative of an anthropogenic impact that may vary moving northwards and away from human settlements, as opposed to other purely natural components (marine origin) such as chlorine and sodium. Moreover, elements can help to understand the type of source (natural or anthropogenic) and the origin (transport from lower latitudes or more local origin) of the aerosol. The main chemical analyses involved have already been described in the methodology chapter: ion chromatography (Section 2.2.1) for water-soluble inorganic ions and TCA (Section 2.2.2) to infer the total carbon content. The specific methodology for this chapter, instead, is outlined in the following section (4.1) and describes: the general information concerning the sampling (areas considered, number of filters etc.), the intercomparison of total carbon content from different instruments and the elemental analyses. Results and discussion follow in section 4.2.

4.1. Specific methodology

AREX 2018 and 2019 outward sections lasted from 11 and 8 June to 24 and 21 July respectively. During the outward routes of these two campaigns 20 valid quartz filters were collected using a high volume sampler (see section 2.2) and 15 of them represent the TSP content of the following specific areas (Figure 47): Gdansk (1 filter); Baltic and south of Norway (2 filters); west coast of Norway (2 filters); Tromsø (1 filter); sea north of Tromsø (1 filter); Arctic Ocean south of Svalbard (2 filters); Arctic Ocean west of Svalbard (3 filters); Arctic Ocean east of Svalbard (1 filter); Arctic Ocean north of Svalbard (1 filter); Longyearbyen (1 filter). The remaining filters were sampled under hybrid conditions, i.e. both in one of these environments and in the anthropic fjords present on Svalbard. Therefore, they are not exclusively representative of the specific areas mentioned above. Gdansk included sampling at the dock of the harbor where the Oceania was located and in the bay in front of the city. The second area included the route from Gdansk bay to the Baltic Sea exit (Skagerrak strait) and the North Sea along the south-west coast of Norway up to 63 °N. The third area was the route along the west coast of Norway (North Sea) from 63 °N to Tromsø (69.649°N). Tromsø included sampling in the harbor and in the fjords at the entrance and exit of the city. The fifth area included an almost vertical transept in the sea north of Tromsø, from 70.7 °N to about 74 °N. The subsequent sampling area covered the sea area (called Arctic Ocean from this point) from about 73.5-74 °N, located south and south-west of Svalbard archipelago. The Arctic Ocean west of Svalbard included sampling from about 76.5 °N to about 79.5 °N, between 1 °E and 11.7 °E. Arctic Ocean east of Svalbard included instead the sampling along the entire east coast of Svalbard, from about 76.5 °N to 80.3 °N. The ninth site covered an area north and north-west of Svalbard from about 79.5 °N to about 80.5 °N and between about 7 °E and 14.8 °E. Finally, Longyearbyen (78.23 °N, 14.9 °E) included sampling in the harbor and in the fjord branch where the human settlement is located.

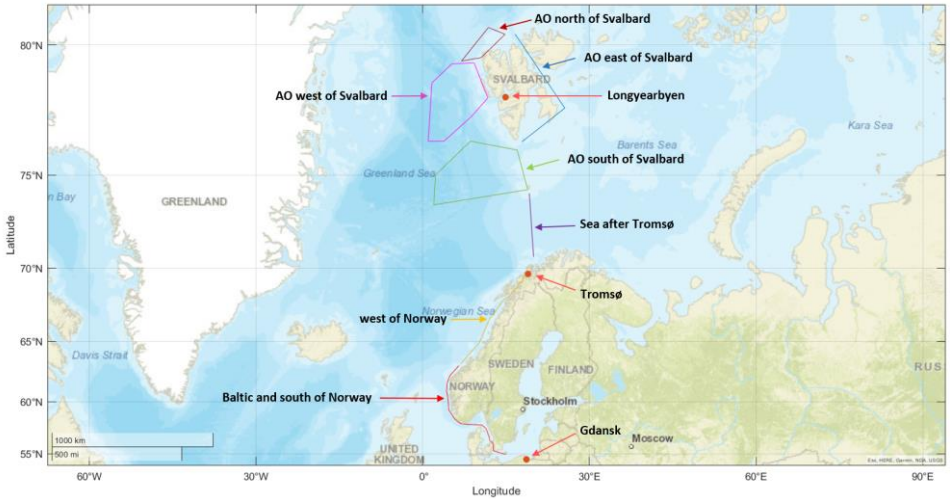

Figure 47. *TSP filters sampling areas during AREX 2018 and 2019 campaigns*

TSP samples were pre-treated, sampled and stored as described in section 2.2. The sampler was placed on the measurement platform (balcony, Figures 11 and 12) of the s/y Oceania and the sampling flow was set at 700 L/minute for 2018 and 180 L/minute for 2019. The lower flow during 2019 was due to a longer sampling time and the presence of a white filter underlying the sampled filter, in order to obtain a more homogeneous aerosol distribution on the filter surface for subsequent analysis. The average sampling time was 96 h over the Arctic ocean, 72 h in the Baltic Sea and along the coast of Norway, and 48 h in the harbous/emission hotspots (Gdansk, Tromsø and Longyearbyen).

The filters were analyzed by ion chromatography and TCA. Regarding ion chromatography, collected blank filters allowed to determine the DL of the different analytes and the studied filters were all above the DL. Moreover, all ions calibration curves had a regression coefficients (R^2) > 0.995. Positive and negative equivalents have been calculated, resulting in a very good balance of charges for both 2018 (R^2 = 0.996 and slope≈1, Figure 48a) and 2019 (R^2 = 0.996 and slope≈1, Figure 48b), confirming the reliability of the analyses performed.

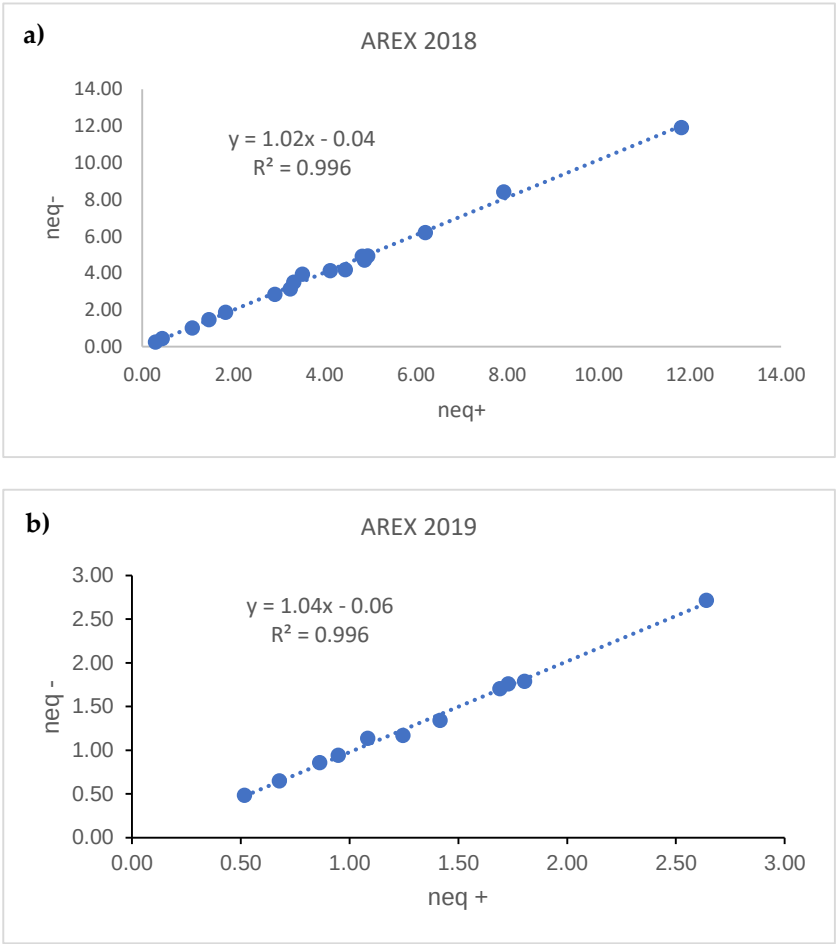

***Figure 48**. Regression lines between positive and negative charges (number of equivalents over volume, ml) for 2018 (**a**) and 2019 (**b**) samples. There was a very good balance (slope around 1 and R^2=0.99 for both years.*

4.1.1. Total Carbon intercomparison

The reliability of off-line TCA measurements was verified by analyzing the total carbon content on AREX 2019 filters also using the DRI (DRI 2015 Series 2, Aerosol Magee Scientific, Slovenia) and the offline laboratory version of the Sunset analyzer (Sunset Laboratory Inc., Tigard, OR, USA).

The Sunset performs thermo-optical-transmittance (TOT) measurements; samples are thermally desorbed from the filter medium under an inert helium atmosphere followed by an oxidizing atmosphere using carefully controlled heating ramps. A flame ionization detector is used to monitor the analysis. The analyses were carried out at the LABEC laboratory in Florence on a 1.5 cm^2 filter-spot, using the NIOSH870 protocol with temperature offset correction; as there are no major systematic differences between different protocols regarding TC measurements (the most relevant differences concern the split between EC and OC) the obtained data are suitable for TC intercomparison between different instruments). The detection limit is 0.2 $\mu g/cm^2$ for both fractions (EC and OC) and the data were validated through a standard at a known concentration.

The DRI Model 2015 [153] is a multi-wavelength thermal/optical carbon analyzer, which employs a 7-wavelength laser (from 405 to 980 nm) to measure the intensity of light both reflected from the sample and transmitted through the sample. The analysis is based on the progressive decomposition of OC and EC fractions at increasing temperatures (programmed temperature steps) and in inert or oxidizing atmospheres. First, organic compounds are released in an inert helium atmosphere at temperatures up to 580 °C; then, the 'elemental' carbon is combusted in an oxidizing atmosphere (helium plus oxygen) at temperatures up to 840 °C. Carbon released from the sample is converted to CO_2 by a heated manganese dioxide catalyst oven, and the carbon dioxide is quantified via an NDIR detector. The measurement range is 0.05 to 750 μg carbon/cm^2, while the TC minimum detection limit is 0.22 ± 0.06 μg carbon/cm^2. The analyses were carried out at the Aerosol d.o.o. headquarters in Ljubljana on a 1.54 cm^2 filter-spot, using the EUSAAR_2 thermal protocol [154].

Figure 49a,b shows the intercomparison between the TC atmospheric concentration obtained by TCA off-line and SUNSET (a) or by TCA off-line and DRI (b). We found a good correlation between the TCA and the DRI (R^2 = 0.94 and slope=1.17) and a very good correlation between the TCA and the SUNSET (R^2 = 0.98 and slope=1.08). Therefore, after demonstrating the reliability of the measurements, we used the TC results from the TCA. The OC was then obtained by subtracting the eBC (from the aethalometer, i.e. optical method) from the TC (from thermal method), referring to Ivancic et al. [155]. We are aware of the limitations of this

method, induced by the difference between eBC and EC due to the MAC and C (for the Aethalometer) values used, as recently pointed out by Savadkoohi et al. [156]. However, we chose to use this kind of OC, so as to describe the data from the different campaigns in a consistent way (SUNSET analyses were available only for AREX 2019 filters) and because the OC results from the SUNSET also presented some issues. In particular, for filters where the BC content was particularly low, the EC value from SUNSET was very close to 0 (thus overestimating the OC). Figure 49c shows how the OC from the SUNSET was generally greater than the OC from the TC – eBC method. DRI was not included in the comparison because of the uncertainty in determining the splitting point (between OC and EC) during analysis.

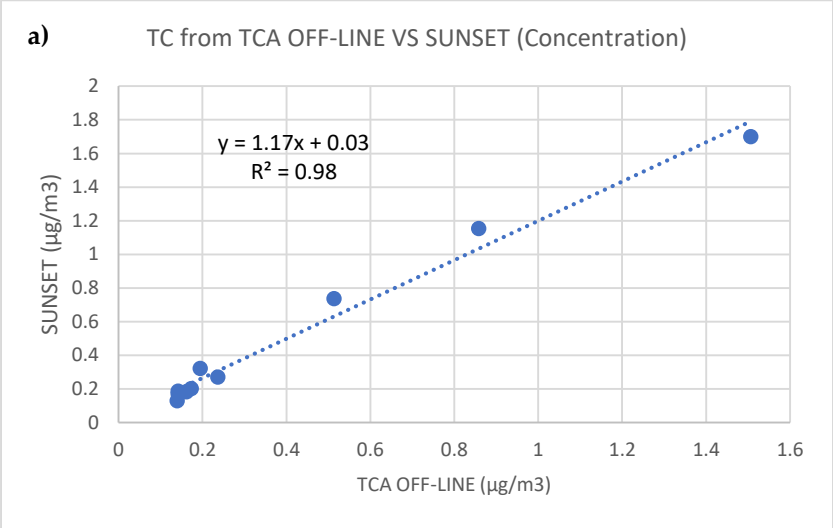

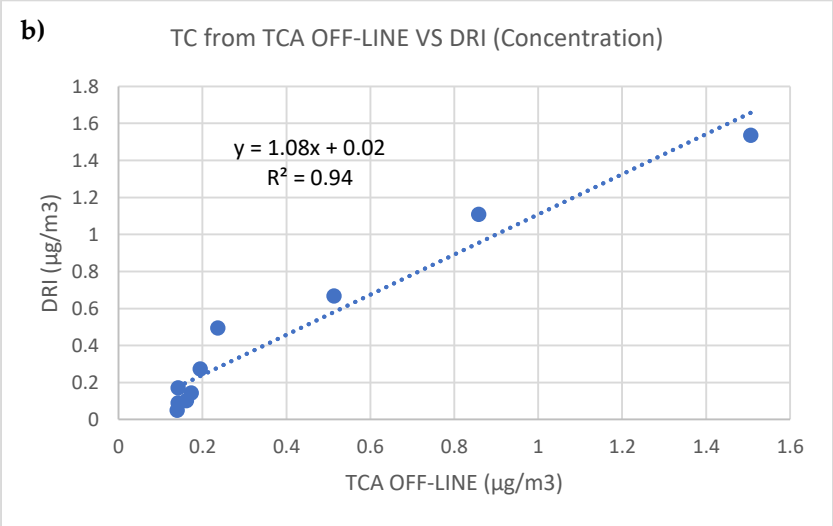

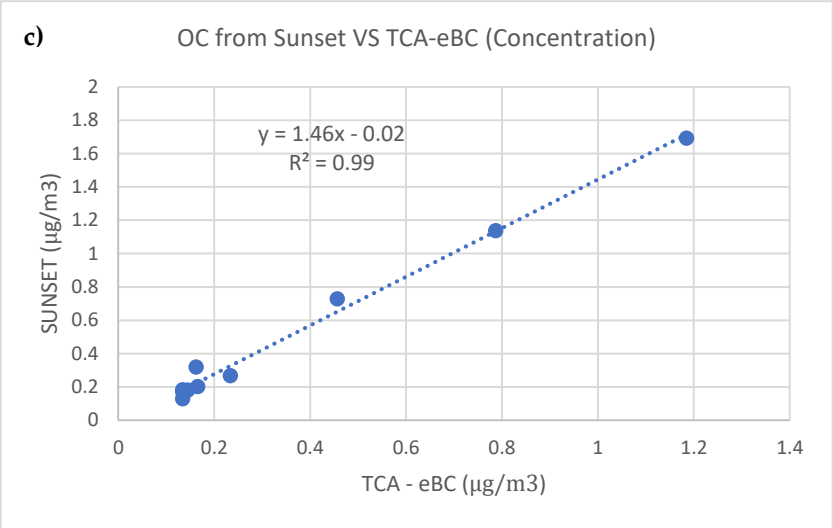

Figure 49. *Regression lines between total carbon results of TCA and SUNSET (a) and of TCA and DRI (b); regression line between organic carbon results from TC (obtained by TCA analysis) – eBC method and SUNSET (c).*

4.1.2. Elemental analyses

13 elements were determined on AREX samples by "Inductively Coupled Plasma – Optical Emission Spectroscopy" (ICP-OES; Cr, Fe, Mn, Ni, Ti, V, Zn, Cu, Ca, Se, Cd) and by "Graphite Furnace Atomic Absorption Spectrometry" (GFAAS; As and Pb). Before analysis, the samples were extracted via microwave acid digestion. The filter spots were placed in teflon reaction vessels and the following reagents were added: HNO_3 65% (4 mL), H_2O_2 30% (2 mL) and Milli-Q water (2 mL). A blank was done for each set of samples. The teflon vessels were then placed in the mineralizer, model Multiwave 5000 (Anton-Paar, Graz, Austria). The microwave programme included two steps: during the first step a temperature of 220°C is reached in 20 minutes; during the second step this temperature is maintained for a further 20 minutes, in order to complete the digestion. A cooling time is then foreseen. After the digestion each sample was transferred into a 50 mL vial and 12 mL of Milli-Q were added so as to have the HNO_3 concentration at 13% (in this way, instrumental reading is not compromised). Samples were then filtered with 0.45 mm syringe filters. Perkin Elmer standards for each analyte (concentration of 1000 mg/L) were used to calibrate the instruments and they were diluted with a 2% HNO_3 solution for ICP-OES and with a 0.2% HNO_3 solution for GFAAS.

For the ICP-OES analysis, an Optima 7000 DV model (PerkinElmer, Waltham, MA, USA) was used and a calibration line was built at 3 concentration levels for each standard. For the GFAAS analysis, instead, an Aanalyst 600 model (PerkinElmer, Waltham, MA, USA) was used and a calibration line was built at 4 concentration levels for each standard. Sample concentrations were retrieved by means of software processing (WinLab32) on the basis of the calibration line. The results were reprocessed taking into account the dilutions applied to the sample. Prior

to GFAAS analysis (because analysis is performed using a graphite furnace), a matrix modifier has been added to the sample to eliminate the chemical interference induced by the formation of compounds that are refractory to atomization. Matrix modifiers consist essentially of three reagents: $Pd(NO_3)_2$ - $Mg(NO_3)_2$ - $(NH_4)H_2PO_4$. They were used individually or mixed, depending on the element under investigation.

4.2. Results and discussion

4.2.1. Chemical composition in different areas

Water-soluble inorganic cations (Na^+, Ca^{2+}, Mg^{2+}, K^+ and NH_4^+) and anions (Cl^-, SO_4^{2-}, NO_3^-, PO_4^{3-} and F^-), and organic matter were detected on filter samples. First of all, a cluster analysis helped to classify and group filters collected during the two research campaigns on the basis of common characteristics. The input consisted of the chemical species examined and the PCA toolbox for MATLAB [157] was used to carry out the cluster analysis. It is a collection of MATLAB modules for calculating unsupervised multivariate models for data structure analysis (Principal Component Analysis, Multidimensional Scaling and Cluster Analysis). We used the euclidean distance, autoscaling for data scaling and the linkage was based on the average.

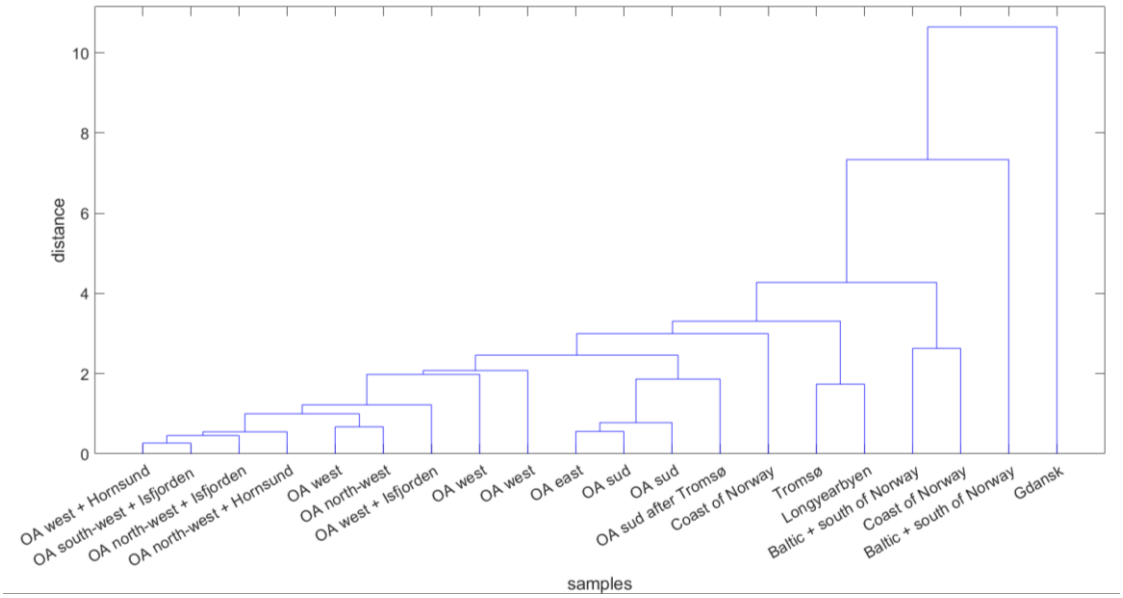

Figure 50. *Cluster analysis on the basis of the aerosol chemical composition of quartz filter collected during AREX 2018 and 2019 campaigns*

All 20 valid filters collected were included in the cluster analysis, both those representative of a specific area and those defined as hybrid filters. From Figure 50 it is evident how the filters were grouped on the basis of the sampling areas. The samples feature common characteristics according to the geographical site of origin. Therefore it was possible to average the filters coming from the same area (in case there were more than one) on the base of the cluster analysis.

TSP chemistry of these areas is shown in Figure 51 and the percentages are expressed in terms of relative mass. Baltic and southern Norway, coast of Norway, southern Arctic Ocean (AO) and western Arctic Ocean chemical composition were obtained by averaging several filters (so results are expressed in terms of mean ± confidence interval), while TSP chemical composition of other areas was obtained from a single filter. The sea area after Tromsø was not included in the south AO, due to the lower sampling latitude and the fact that it is still slightly affected by the anthropogenic influence from the north of Norway (as will be seen below from the chemical composition results). Clustering also confirmed the decision to exclude the hybrid filters from the analysis of the results. Indeed, they have all been grouped apart (left side of Figure 50), with the only exception of the filter named "OA west + Isfjorden" (however it was grouped with the western Arctic Ocean filters, with which it partly shares the area of origin). Hybrid filters are labelled 'AO + Hornsud' or 'AO +Isfjorden', because Hornsund and Isfjorden are some of the anthropic fjords in the Svalbard archipelago (which will be classified and examined in more detail in the next chapter).

Filters from the northern and western AO were grouped together, as were filters from the eastern and southern AO. One filter from the coast of Norway was placed between the sea after Tromsø and Tromsø itself. It is therefore not particularly close to the other filter from the same area, but it is nevertheless on the same (right) side of the dendrogram and is close to Tromsø, to which it is indeed close also in terms of geographical origin (coast of Norway represents the coastal area south of Tromsø). It is interesting that Tromsø and Longyearbyen have been grouped together. In fact, they are the two main emission hotspots in the Arctic area considered (Tromsø could also be considered a subarctic site, but it is still located beyond the polar circle). The two hotspots are followed by the filters from the Baltic and southern Norway and the other filter from the coast of Norway. Their positioning in the dendrogram agrees with the still important anthropogenic influence present in these areas. Finally, Gdansk, due to the significantly higher anthropogenic emissions, was grouped alone.

From the pie charts in Figure 51 it is evident that anthropic impact and consequently the chemical composition of aerosol changed moving northwards: the relative importance of BC, nitrates and sulfates decreased, while the natural marine components (Cl^- and Na^+) became more relevant. BC (which has only primary origin from incomplete combustion) counted for about 6% in Gdansk (1.387 ± 0.16 $\mu g/m^3$), 2% in the Baltic and southern Norway area (0.187 ± 0.004 $\mu g/m^3$), 1% (0.083 ± 0.001 $\mu g/m^3$) along the west coast of Norway and in the sea area after Tromsø (0.030 ± 0.001 $\mu g/m^3$), while over the Arctic Ocean counted always less than 1%, reaching the minimum (4.2 ± 0.5 ng/m^3) north of Svalbard. As stated in section 3.3.2, NO_3^- has only secondary (photochemical) origin from anthropogenic precursors (e.g., NOx) present

on land (except for ship emissions) and NH_4NO_3 is not very stable in the atmosphere, tending thus to volatilize during the long-range transport. Indeed, there is a clear latitudinal decrease, both in terms of relative contributions and absolute values. In Gdansk the percentage was relatively low (6%) because of the high total concentration of TSP, due in particular to organic carbon from combustion, but its absolute value was still high (1.520 µg/m^3). Highest NO_3^- relative percentage and absolute value were in the Baltic and southern Norway area (18 % and 1.870 ± 1.207 µg/m^3). These values then diminished progressively towards the north: 13% (0.701 ± 0.169 µg/m^3) in the Norwegian area, 3% (0.127 µg/m^3) after Tromsø and values always around 1% over the Arctic Ocean (from 0.017 to 0.029 µg/m^3).

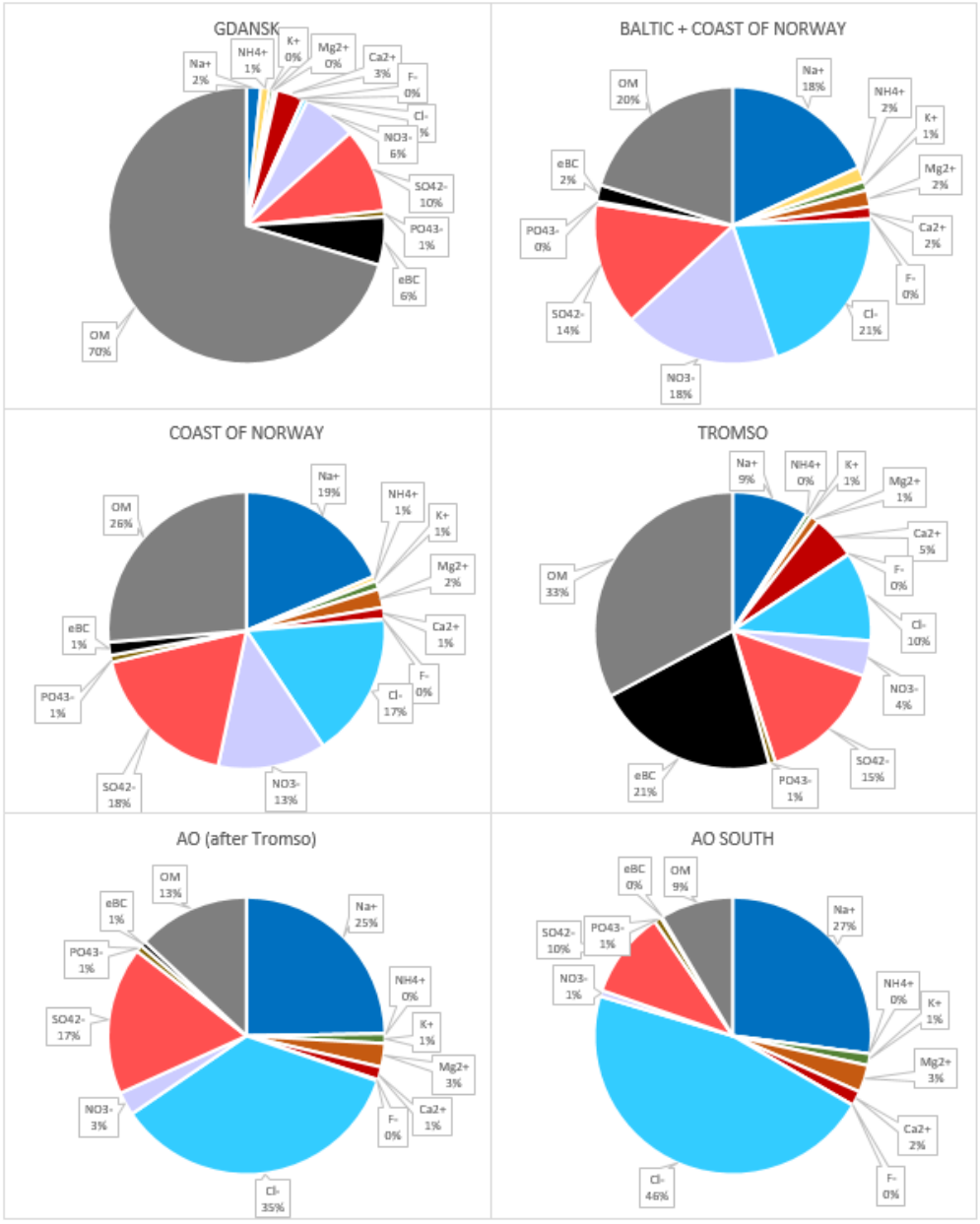

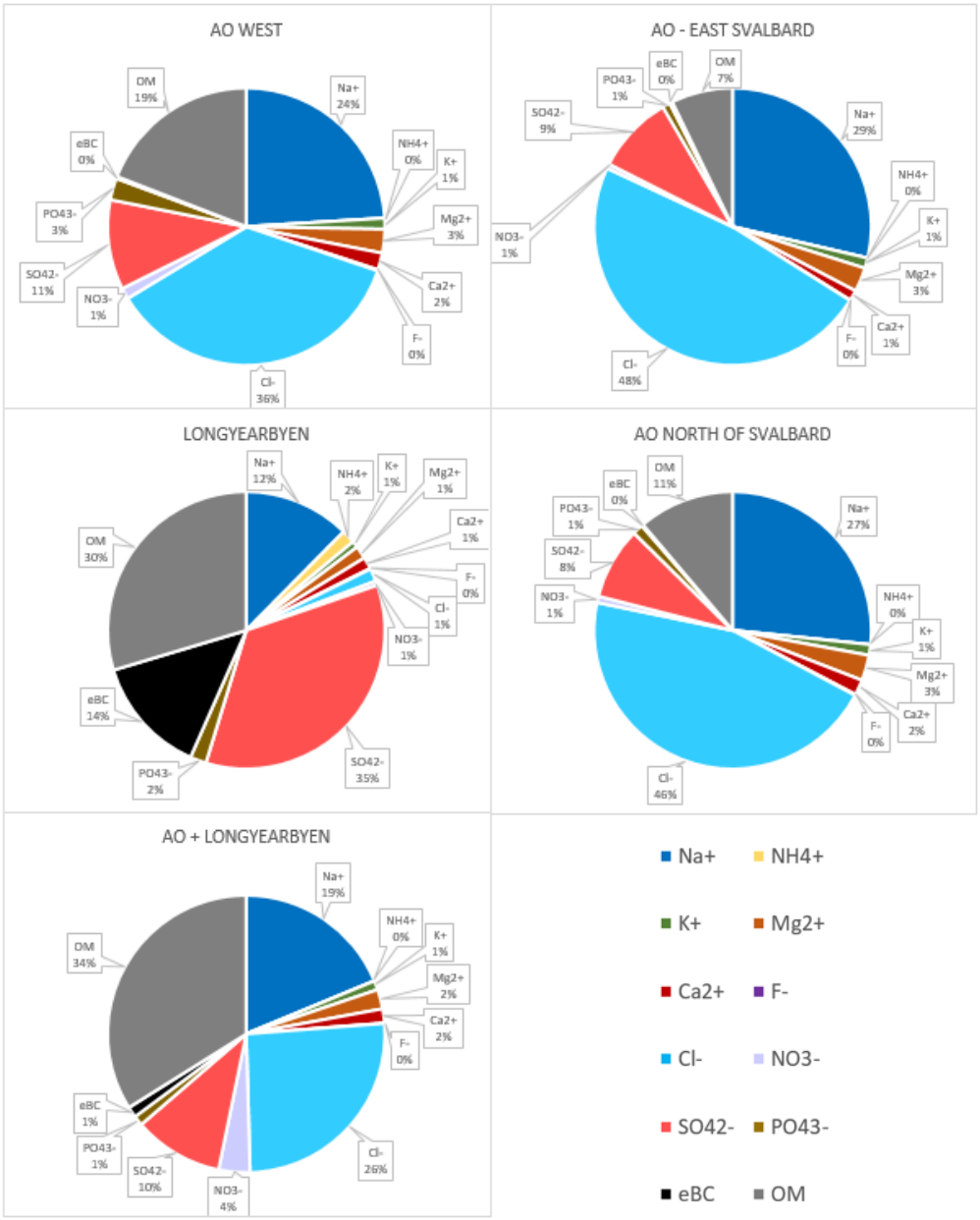

Figure 51. *TSP chemical composition in different areas of the campaigns. Percentages are expressed in terms of relative mass.*

Organic matter showed a similar behavior, decreasing northwards, but its relative importance was considerable even in the Arctic area. Indeed, OM is due to both anthropogenic emissions (combustion) and biological emissions from the sea: anthropogenic influence diminished with latitude, but natural influence remained (or increased) over the Arctic Ocean. Its absolute value was particularly high in Gdansk (17.426 $\mu g/m^3$) because of combustion processes. In the Baltic and southern Norway area it ranged between 1.317 and 2.896 $\mu g/m^3$, while along the west coast of Norway it ranged between 1.107 and 2.273 $\mu g/m^3$. Values on the Arctic

Ocean were quite similar, ranging from 0.262 μg/m^3 (North of Svalbard) to 0.438 ± 0.126 μg/m^3 (West of Svalbard) and 0.607 μg/m^3 (after Tromsø).

Sulfates are due to the contribution of several factors: primary emissions of sea spray, secondary formation from DMS precursor, emitted by phytoplankton activities, (both represent a natural marine origin) and secondary formation from precursors emitted by fossil fuel combustion (anthropogenic origin). Their stability in the atmosphere favors the long-range transport from continents; therefore, an anthropogenic contribution to their concentration can also be found in the northernmost marine areas. The highest concentration was in Gdansk (2.447 μg/m^3), followed by Baltic/southern Norway (1.409 ± 0.373 μg/m^3) and by the Norwegian area (1.086 ± 0.321 μg/m^3). SO_4^{2-}concentration became even lower after Tromsø (0.799 μg/m^3), but the relative percentage (17%) was similar to the previous areas, highlighting a minor decrease compared to nitrates because of the higher stability and the other natural origins. Indeed, also in the areas of the Arctic Ocean near the Svalbard archipelago, the relative percentage decreased, but still remained significant, varying from 10-11% (south and west of Svalbard respectively) to 8-9% (north and east of Svalbard respectively). Here SO_4^{2-} was the third most plentiful ion after Cl^- and Na^+, ranging between 0.197 and 0.429 μg/m^3. Figure 52 shows how the contribution from sea salt to the SO_4^{2-} concentrations increased northwards, with much higher percentages over the Arctic Ocean (where the relative percentages and the absolute values of total SO_4^{2-} are lower). Despite not striking differences between the sites on the Arctic Ocean, it is notable that the areas with the lowest relative percentages (east and north of Svalbard) coincided with the areas where the sea salt contribution was greater (79% and 80% respectively). This underlines how the further decrease in the relative percentage in the remotest areas may be due to a reduction in the anthropogenic contribution. Sea salt contribution to the ions, which are part of the major ions in seawater, was determined according to Mihalopoulos et al. [140], following equation 24 (see the previous chapter).

Except for harbors (i.e. Gdansk, Tromsø and Longyearbyen), Cl^- and Na^+ always had among the highest relative percentages (as expected since marine aerosol was sampled), with concentrations ranging from 0.837 to 2.254 μg/m^3 and from 0.624 to 1.780 μg/m^3, respectively. Moreover, they were the most abundant chemical components in all areas of the Arctic Ocean, reaching their maximum relative percentage values east of the Svalbard (48% and 29% respectively). The chlorine ion always had a purely sea-salt origin.

Regarding the other ions, the relative contribution of fluoride was negligible (always less than 1%); it reached the maximum concentration in Gdansk (0.015 μg/m^3), while in all other areas the value was less than 0.008 μg/m^3. NH_4^+ was below the detection limit in any of the samples from the Arctic Ocean. This is consistent with the fact that its main source in the Arctic

is related to long-range transport from continents, which is more relevant in the arctic haze season (we sampled during the summer season), and with the negligible concentrations also found by Ferrero et al. [64] during spring. Indeed, it was present only in Gdansk (1%; 0.252 $\mu g/m^3$), in Baltic and southern Norway area (2%; 0.188 ± 0.199 $\mu g/m^3$), along the west coast of Norway (1%; 0.026 ± 0.051 $\mu g/m^3$) and in Longyearbyen (2%; 0.013 $\mu g/m^3$), with a progressive decrease in concentrations towards the north. Except for Gdansk, where the concentration was higher (0.182 $\mu g/m^3$), but only contributed 1% in terms of relative mass, PO_4^{3-} showed quite similar concentrations in other areas, ranging from 0.029 $\mu g/m^3$ (north of Svalbard) to 0.060 $\mu g/m^3$ (west of Svalbard). Its relative contribution was never more than 1%, except in the west of Svalbard, where it reached 3%.

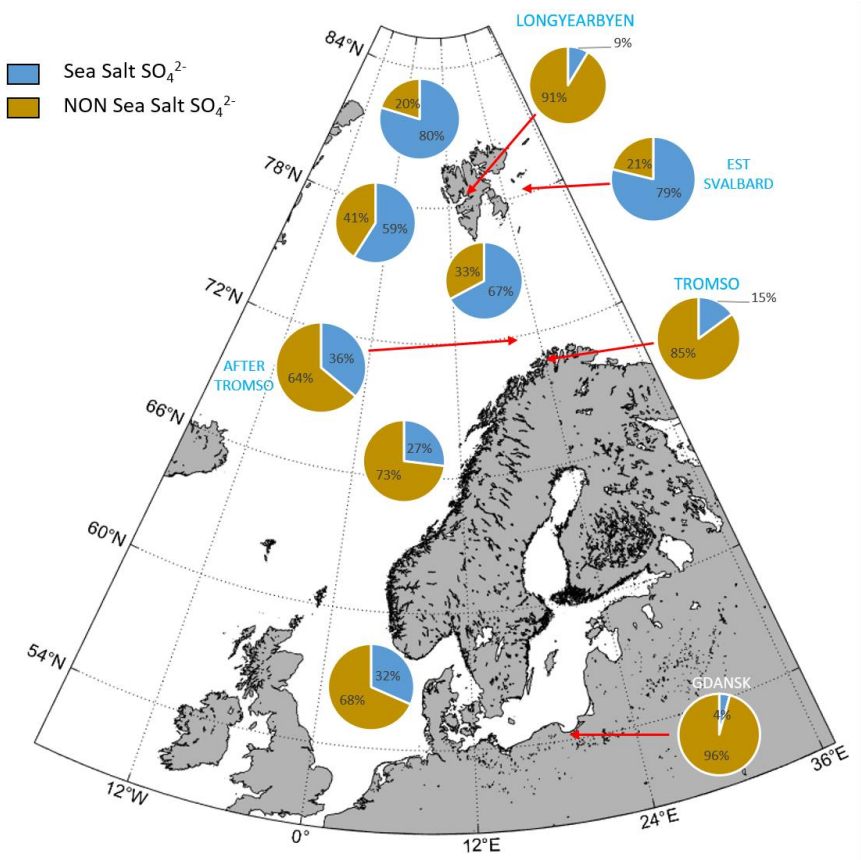

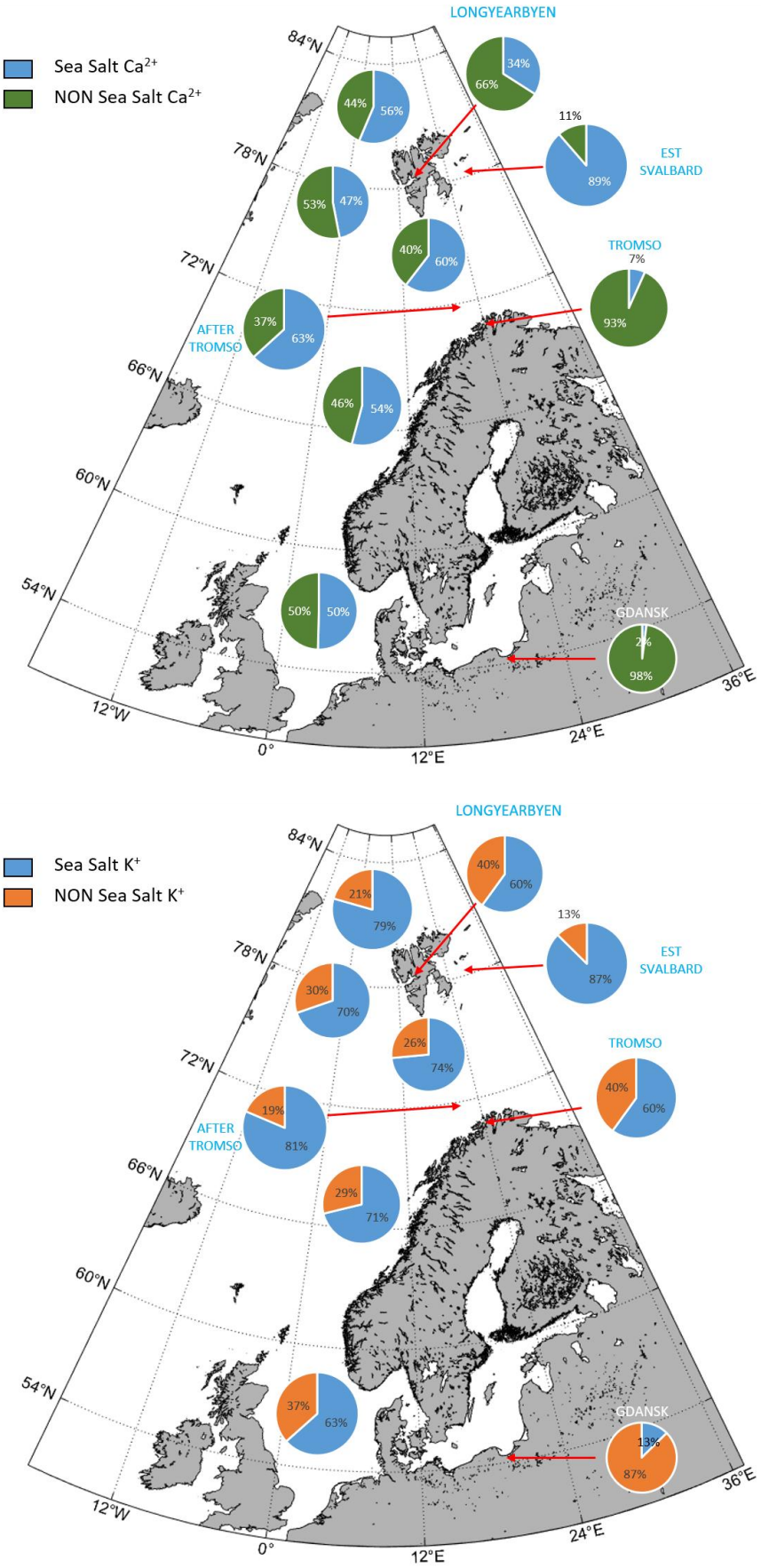

Figure 52. *Percentages of ss and nss origin for sulfates (top), calcium (middle) and potassium (bottom) in different latitudes and areas of the campaign*

The remaining ions (Mg^{2+}, Ca^{2+} and K^{+}) are part of the major ions in seawater, together with Cl^{-} and SO_4^{2-} [158]. Mg^{2+} contributed less than 1% to the relative mass in Gdansk (0.097 $\mu g/m^3$), while this percentage rose to 2% in the Baltic and Norwegian areas (where it ranged from 0.143 $\mu g/m^3$ west of Norway to 0.191 $\mu g/m^3$ south of Norway) and 3% (constant percentage value) in the Arctic Ocean areas (where it ranged from 0.064 $\mu g/m^3$ west of Svalbard to 0.134 $\mu g/m^3$ south of Svalbard). This agrees perfectly with the marine origin of Mg^{2+}: except for Gdansk, where about 50% of Mg^{2+} derived from sea-salt, in all other cases it had an exclusively sea-salt origin; therefore, its relative importance increased by moving towards the Arctic Ocean. Indeed, if we look at the values in the other harbors/emission hotspots (Tromsø and Longyearbyen, which will be examined in more detail below), the relative percentage dropped to 1%. Ca^{2+} presented the highest value in Gdansk (0.777 $\mu g/m^3$) and a progressive decrease from the Baltic to the Arctic Ocean. Indeed, concentration was 0.134 ± 0.004 $\mu g/m^3$ (relative contribution of 2%) in the Baltic and southern Norway, 0.089 ± 0.081 $\mu g/m^3$ along the west coast of Norway (relative contribution of 2%), and slightly lower in Arctic sea areas, ranging from 0.042 $\mu g/m^3$ to 0.072 $\mu g/m^3$ and contributing between 1% and 2% depending on the site. Figure 52 shows how the sea-salt origin of calcium increased northwards, reaching the highest sea-salt percentage east of Svalbard. However, compared to sulfates and potassium, the difference (in terms of marine) origin was not so marked with respect to lower latitudes and sea-salt percentages were not particularly high in the Arctic Ocean, especially if we consider the area north of Svalbard (56% of ss-Ca^{2+} versus 80% of ss-SO_4^{2-} and 79% of ss-K^{+}). This agrees with a possible relevant crustal origin of calcium, already reported in the literature [159,160]. K^{+} contributed 1% to the total relative mass in all areas (both before Tromsø and in the sea areas after Tromsø), except in Gdansk, where it contributed less than 1%. Absolute values were quite low everywhere and they gradually decreased from Gdansk (0.120 $\mu g/m^3$) to the Baltic and Norwegian areas (0.107 ± 0.051 $\mu g/m^3$ and 0.065 ± 0.055 $\mu g/m^3$) and to the Arctic Ocean areas (where K^{+} concentrations ranged between 0.029 $\mu g/m^3$ north of Svalbard and 0.058 ± 0.003 $\mu g/m^3$ south of Svalbard). Sea salt origin of K^{+} increased northwards, but it was quite high also at lower latitudes (excluding Gdansk). Indeed, among the three ions with both non sea-salt and sea-salt origin (SO_4^{2-}, K^{+} and Ca^{2+}), it was the one with the largest marine origin. The nss-K^{+} can have both crustal and forest fires origin.

The last pie chart (AO + Longyearbyen) in Figure 51 shows the chemical composition of one of the filters sampled under hybrid conditions, i.e. both in one (or more) of the Arctic Ocean areas (listed above) and in one of the anthropic fjords in Svalbard (fjords where there is at least one anthropic settlement, such as Longyearbyen; they will be discussed in detail in the next chapter). From this example, it is evident how the aerosol chemistry of a rather pristine

marine environment was influenced by anthropogenic emissions. eBC for this filter was 1%, while in Arctic sea areas it was less than 1%. Nitrates increased from 1% to 4% and, above all, OM rose significantly to 34%. OM concentration was 1.429 $\mu g/m^3$, while Cl^- and Na^+ concentrations were 1.087 $\mu g/m^3$ and 0.790 $\mu g/m^3$ respectively. Thus, Cl^- and Na^+ were no longer the most abundant ions, but have been overtaken by OM, because natural OM has been supplemented by the OM derived from anthropogenic OC (i.e. from combustion).

Therefore, beyond the latitudinal (i.e. moving northwards) decrease in anthropogenic impact, there is also a decrease away from the emission hotspots which are present in the sub-Arctic and Arctic areas. The clearest examples are Tromsø and Longyearbyen, whose aerosol chemical composition is shown in Figure 51. In fact, Tromsø is the main city in northern Norway, while Longyearbyen is the main human settlement in the Svalbard Islands. The analysis of hotspots in the Arctic region, the differences between them and with the Arctic ocean are presented in detail in the next chapter, which specifically examines only the Arctic region. In particular, it focuses on the impact of the anthropic settlements on the eBC concentrations and heating rate in the Arctic. Particle concentrations and the LAA direct forcing have been determined by means of high temporal resolution measurements. However, the chemical composition of Tromsø, Longyearbyen and the entire Arctic Ocean around Svalbard is also described here in order to introduce the first macroscopic differences between emission hotspots and the Arctic Ocean, which are then further explored through high temporal resolution measurements. The entire sampled Arctic Ocean area was thus averaged (without divisions between specific sites, e.g. south or west of Svalbard) and results are shown in Figure 53: only filters from the pristine Arctic Ocean were considered (not hybrid ones), excluding the filter sampled in the stretch of sea after Tromsø, because it is still partly influenced by emissions from northern Norway. This made it possible to compare Tromsø and Longyearbyen not only to all other individual areas considered from mid-latitudes to north of Svalbard, but also to the average pristine Arctic Ocean (i.e. Arctic Ocean background). The pie charts of the two human settlements in Figure 51 have also been included in Figure 53 to facilitate comparison between them and the Arctic Ocean background.

The difference in chemical composition between the Arctic Ocean background and the two emission hotspots is clearly evident. Obviously, averaging data from the sea, the most abundant ions were Cl^- and Na^+ (mean concentrations of 1.247 $\pm$ 0.456 $\mu g/m^3$ and 0.762 $\pm$ 0.245 $\mu g/m^3$ respectively), while the mean relative contribution of eBC was minimal (about 0.2%; mean concentration of 5.5 $\pm$ 0.2 $ng/m^3 \approx$ half of the value found by Massling et al. [161] at the Villum Research Station, North Greenland, but within the range of its confidence interval), indicating a pristine environment in the absence of evident transport phenomena, with a low

presence of anthropogenic or natural combustion products, especially fossil fuel. Organic matter was on average the third most abundant compound, suggesting the possible presence of important biological emissions from the sea. The organic fraction, indeed, accounted alone on average for 95.5% of the total carbon content. OM mean value was 383.3 ± 79.9 ng/m^3. As already mentioned for the different Ocean Arctic sites, sulfates concentrations were also important over the sea because of the natural contribution: they have a mean Arctic background concentration of 293.3 ± 84.4 ng/m^3 and 65.2 ± 2.3% was due to primary emissions from the sea. Nss-SO_4^{2-} mean value was 102.1 ± 29.4 ng/m^3, very similar to that reported at Villum Research Station (North Greenland) by Massling et al. [161]. Nss-SO_4^{2-} percentage was thus relatively high (on average) also over the Arctic Ocean area. Considering the sampling site (sea) and season (i.e. not during the arctic haze period, but during summer when the biogenic fraction is more relevant [162], especially taking into account the positive summer trend over the past decades due to temperature increase and the related loss of sea-ice [162,163]), it is possible that a significant part of the nss-sulfate comes from marine biogenic emissions, according to the high value of OM found and to Udisti et al. [164] too. The other chemical species analyzed were less significant in terms of concentration. NO_3^- was remarkably less abundant than SO_4^{2-} because of its secondary anthropogenic origin. The average value (26.9 ± 7.0 ng/m^3) is slightly lower (but in the same order of magnitude) than that reported by Xu et al. [141] for the Southern Ocean. The relative mean contribution of the fluoride ion was less than 0.1%, while NH_4^+, as already mentioned, was below the detection limit over the Arctic Ocean. The mean concentration of PO_4^{3-} was 46.7 ± 21.2 ng/m^3. Mg^{2+} (which derived completely from sea-salt aerosol) average concentration was 88.2 ± 29.5 ng/m^3. The mean Arctic Ocean concentration of Calcium was 53.9 ± 13 ng/m^3 and it was the ion with the lowest marine origin (53 ± 1.7%;) due to the fact that it is also influenced by a crustal origin (e.g. material transported from Greenland and Iceland can be enriched in gypsum [159,160]. Almost three quarters (72.6 ± 1.3%) of the K^+ concentration (38.8 ± 12.1 ng/m^3) derived from sea salt.

In Tromsø and Longyearbyen the relative percentages of Na^+ and Cl^- (typical ions of sea salt aerosols) decreased considerably, reaching the lowest concentrations together with Gdansk: 0.239 μg/m^3 of Na^+ and 0.276 μg/m^3 of Cl^- in Tromsø; 0.105 μg/m^3 of Na^+ and 0.013 μg/m^3 of Cl^- in Longyearbyen. Therefore, the natural component decreased, while the anthropogenic one increased. eBC in Tromsø achieved the highest concentration after Gdansk (0.568 ± 0.026 μg/m^3; 21% of the relative mass) and eBC in Longyearbyen (0.117 ± 0.016 μg/m^3; 14% of the relative mass) was comparable to values at much lower latitudes, such as the Baltic and the coast of Norway, and it was far greater than the mean value of the Arctic Ocean. OM in Tromsø was lower than in areas further south (0.869 μg/m^3), but accounted for 33% of the relative mass and

was higher than in Arctic areas. OM in Longyearbyen (0.251 μg/m^3), instead, was lower than the Arctic background and all other individual Arctic sites, probably due to a reduced natural component (not totally offset by the anthropogenic one), but accounted for 30% of the relative mass. Considering the high concentration of eBC and the very high percentage of nss-SO_4^{2-}, it is highly probable that the OM here was more linked to combustion. Sulfate concentrations in the two hotspots were comparable to those of the Arctic Ocean (0.390 μg/m^3 in Tromsø and 0.297 μg/m^3 in Longyearbyen), but in Longyearbyen they constituted the largest part of the relative mass (35%). Moreover, in these sites, most SO_4^{2-} was of non-marine origin (higher nss-SO_4^{2-} percentages after Gdansk), in particular in Longyearbyen where nss-SO_4^{2-} accounted for 91% of the total. Therefore, although the total-SO_4^{2-} was similar to that of the Arctic Ocean, the nss-SO_4^{2-} was far greater (329.7 ng/m^3 in Tromsø and 270.3 ng/m^3 in Longyearbyen). Consequently, while the sulfate concentration over the sea (in the Arctic region) was mainly due to sea-salt primary emission, in these sites it was almost entirely due to anthropogenic emissions. In fact, nss-SO_4^{2-} concentrations in the two hotspots were much more due to local anthropogenic emissions than to biogenic marine activity (in contrast to Arctic Ocean samples), also in Longyearbyen: it is not a remote station, but a hotspot located on land, where fuel (in particular coal and diesel) is burned for the production of energy and for heating. This agrees with the sharp rise in eBC concentrations and with literature too: measurements in Ny-Ålesund showed that anthro-SO_4^{2-} remains the principal component of nss-SO_4^{2-} also during summer, although it decreases compared to spring when the arctic haze phenomenon is present [162,164]. NO_3^- concentration in Tromsø (0.110 μg/m^3 contributing 4% to the total relative mass) was smaller than at lower latitudes, similar to the value found in the sea after Tromsø and higher than the concentrations in the Arctic Ocean areas. This is in agreement with the location and the dimension of the city, with the presence of anthropogenic sources and with the low atmospheric stability of nitrates. NO_3^- concentration in Longyearbyen were negligible, contributing only 1% to the relative mass. As for the other cases, F^- was negligible (less than 1%), while PO_4^{3-} concentrations were similar in both cases (18.9 ng/m^3 and 1% of the relative mass in Tromsø; 16 ng/m^3 and 2% of the relative mass in Longyearbyen) and were the lowest of the entire campaign. As already mentioned, at higher latitudes NH_4^+ was detected only in Longyearbyen (not in Tromsø) and accounted for 2% of the total relative mass. In accordance with its exclusively marine origin, concentrations of Mg^{2+} in Tromsø and Longyearbyen (0.027 μg/m^3 and 0.013 μg/m^3) were the lowest. ss-K^+ percentage decreased slightly (60% in both cases) reaching the lowest values after Gdansk (13%), but the marine origin remained predominant. Also for K^+, concentrations were the lowest of the entire campaign (0.015 μg/m^3 in Tromsø and 0.006 μg/m^3 in Longyearbyen) and contributed 1% to the relative mass, as well as in all

other cases except Gdansk. Ss-Ca^{2+} percentage decreased (34% in Longyearbyen, the lowest values after Tromsø and Gdansk), especially in Tromsø (7%, a value similar to the 2% found in Gdansk). Ca^{2+} concentration in Tromsø (0.136 μg/m^3) was very similar to that of the Baltic and southern Norway area and contributed 5% to the relative mass, the highest percentage of all sites surveyed. Concentration in Longyearbyen (0.012 μg/m^3), instead, was the lowest and contributed 1% to the relative mass.

The differences between the two hotspots are firstly due to their different size; one is the main city of the north of Norway, while the other is a smaller settlement although its emissions are important in the Arctic context. Therefore, absolute concentrations are generally higher in Tromsø. Looking at the relative percentages, differences in the anthropogenic derivatives (eBC and SO_4^{2-}) can be probably ascribed to the use of different fuels. Indeed coal is still a primary fuel for the local production of heat and electricity at Svalbard, where there are two coal fired power plants in Longyearbyen and Barentsburg [165–167]. This agrees with the fact that nss-SO_4^{2-} concentrations were similar in the two hotspots, although almost all the other investigated species were decidedly greater in Tromsø and although it was not the Arctic haze season (thus highlighting the importance of local sources).

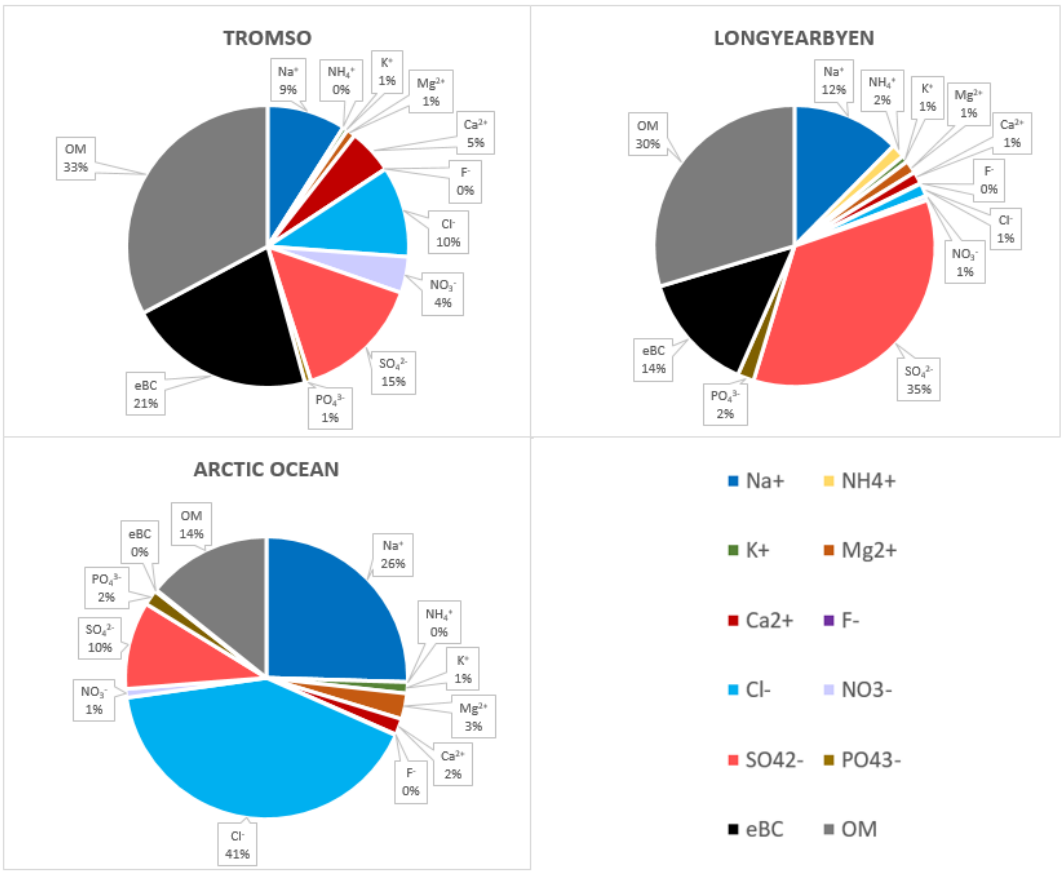

Figure 53. *Aerosol chemical composition (relative percentages) for two important emission hotspots in the Arctic area (Tromsø and Longyearbyen) and for the Arctic Ocean around Svalbard Islands.*

4.2.2. Elements in the Arctic

13 elements were also detected on quartz filter samples: Cr, Fe, Mn, Ni, Ti, V, Zn, Cu, Ca, Se, Cd, As and Pb. The results focus on the Arctic area after Tromsø and were divided according to the sampling area: pure Arctic Ocean and hybrid areas, i.e. involving sampling both on the open sea and within anthropic fjords.

Information about elements in the Arctic are rather scarce because their atmospheric concentration in this region is quite low, so low temporal resolutions [168] or high performance analytical techniques [151,169] are needed. However they can be used as markers for source identification. In this work chemical composition and in particular elements are not the main goal. Moreover, elements have generally lower concentrations than the other chemical compounds considered in this chapter (water-soluble ions and OM; eBC despite low concentrations in the Arctic was inferred by high temporal resolution measurement); therefore, more filters (corresponding to a longer time period) would be needed for a more detailed analysis. For this reason we considered here the Arctic Ocean area and the hybrid areas, for which the largest number of filters (to be averaged) was available. In addition, we included the elements only to add information regarding the chemical composition of the collected samples and to compare our results with literature data.

The main sources of heavy metals in the Arctic atmosphere are sea salt and resuspension of soil particles (natural sources), and long-range transport from Europe and Russia (anthropogenic sources) [170–172]. Measurement campaigns were carried out in summer, when the arctic haze phenomenon is not present. Indeed, we did not find typical elements of arctic haze aerosol, but a predominance of natural and anthropogenic elements that can be attributed to emissions within the arctic itself rather than to long-range transport from southern latitudes. In summer both a greater portion of the Arctic Ocean is free from sea ice and a smaller area of land is covered by snow. Therefore, concentration of elements with sea-salt and crustal origin is higher in this season. Anthropogenic elements emitted by local sources in the Arctic region, instead, may come from mining, heavy industry in northern Siberia (especially Norilsk) and Kola peninsula [173–175], exploitation of oil and gas [176], power generation in the human settlements os Svalbard [166] and ship emissions (tourist cruise, cargo transport and fishing vessels) [177].

Se, an element associated almost exclusively with an anthropogenic origin, was not detected in any of the Arctic filters, nor was Cd. The absence of Cd agrees with the fact that it is a characteristic element of arctic haze and with the very low concentrations found by Paatero et al. [170] during a summer expedition (ASCOS expedition) in the Arctic Ocean. As and Pb are also typical elements of arctic haze; indeed they have only been detected on one filter each (one

filter from the ocean and one hybrid filter respectively). As mean concentration on the sea (obtained by setting to 0 the concentration of the filters on which it was not detected) was 0.032 ng/m^3, an average value in the same order of magnitude of that found during the ASCOS expedition. Pb average concentration for hybrid conditions was 0.095 ng/m^3, while the only detected value was 0.48 ng/m^3 (about half of the average value found by Paatero et al. [170]). The low concentration and few detections of these elements confirm the lack of a general long-range transport (only a few isolated long-range transport events occur in summer, as also highlighted by the high-resolution data shown in the next chapter).

Cu, V, Ni, Cr and Zn are typically assumed to have an anthropogenic origin. In particular, Cu is usually associated with industry in the northern Siberia and Kola peninsula. Cu average concentration for the Arctic Ocean area was 0.80 ng/m^3 (0 – 5.11 ng/m^3), perfectly in keeping with that found during the ASCOS expedition (1 ng/m^3). Average concentration for hybrid conditions, instead, was higher (3.22 ng/m^3, range 0.23 – 5.23 ng/m^3), suggesting a greater anthropogenic influence in these areas. Indeed, looking at the filters sampled in the human settlements, i.e. Longyearbyen and Tromsø (although they are only one per site), Cu values are larger (9.18 and 7.74 ng/m^3 respectively). The high value measured at Longyearbyen suggests a possible local anthropogenic influence, which may be responsible for the concentration value of the hybrid conditions. Moreover, these values, although high, were still lower than the highest concentration observed during ASCOS. Cr average concentrations were 0.11 ng/m^3 (0 – 0.75 ng/m^3) and 0.81 ng/m^3 (0 – 2.86 ng/m^3) for Arctic Ocean and hybrid areas respectively. The first value is consistent with those found by Becagli et al. [151] at Thule (Greenland), by Nguyen et al. [175] at Station Nord (Greenland) and by Kyllonen et al. [174] at the subarctic site of Pallas (Finland), and with that reported by Sander and Bottenheim [178] for the Arctic. The second value, instead, is higher, again indicating the possible presence of a local anthropogenic source at the Svalbard. Ni exhibited similar behavior: the Arctic Ocean concentration (0.26 ng/m^3, range 0 – 0.52 ng/m^3) was close to those of the ASCOS campaign (slightly higher) and Pallas and slightly higher than that of Station Nord, while the hybrid average was is a bit greater (0.60 ng/m^3, range 0 – 1.96 ng/m^3). V concentrations were similar for both cases (0.13 ng/m^3, range 0 – 0.46 ng/m^3, over the ocean and 0.11 ng/m^3, range 0 – 0.31 ng/m^3, for hybrid areas) and close to the values found in Greenland (Thule and Station Nord) and reported by Sander and Bottenheim [178]; they were about half of the values at Pallas and during ASCOS. V tipically indicates fossil oil combustion [175]. Therefore, the presence of vanadium over the ocean (although not particularly high) could be attributed to ship emissions. Using COPREM and PMF analysis, Nguyen et al. [175] found an anthropogenic source with high NO_3^-, SO_x and BC and with low V, and they linked this source to combustion processes fuelled by coal. This is in

agreement with the fact that we found V in Tromsø (high value; 1.05 ng/m^3) where fossil fuel is used, as well as on the Arctic Ocean, but we did not find V in Longyearbyen (despite the high concentrations of eBC and sulfates) where coal is still used. Even if V, Ni and Cr are generally considered anthropogenic, Becagli et al. [151] reported an important natural crustal origin for these elements in Greenland. Also Heidam et al. [173] and Nguyen et al. [175] associated V with the crustal/soil source (in particular Nguyen et al. [175] attributed about one-third of total V to this source). Indeed V can be present in 65 distinct minerals [179]. Moreover, V may also be present in open ocean waters [179]. Therefore, also these surces in addition to the ship traffic could explain the presence of V over the ocean and in the fjords of Svalbard. Zn was the most abundant element along with Fe after calcium, despite its non-crustal origin (it is usually mostly attributed to the combustion source [175]): 8.95 ng/m^3 (7.10 – 12.43 ng/m^3) in the Arctic Ocean area and 2.12 ng/m^3 (0 – 10.57 ng/m^3) for hybrid conditions. The ocean average concentration is very high and is greater than the values found during ASCOS and at Pallas and Station Nord. However it is lower than the considerable concentration found at Thule (15.50 ng/m^3) by Becagli et al. [151]. Instead, the lowest value found in hybrid areas is quite similar to that reported by Sander and Bottenheim [178] and those found at Pallas and Station Nord. Nguyen et al. [175] found an anthropogenic source dominated by Zn with a different origin than Siberia and Eurasia. This Zn source has also been present in summer, when the arctic haze transport is absent, i.e. the same season of our measurement campaigns. They associated high Zn concentrations predominantly with westerly winds, pointing out the Canadian Arctic as the most probable origin, in particular Baffin where there is the major Zn mine closest to Station Nord. Therefore, it is interesting to note that we found the highest Zn concentrations over the ocean, which included sampling areas largely west of Svalbard. The highest Zn values thus corresponded with the areas furthest west. Lower Zn values, instead, were found in the hybrid areas, which include stretches of seas closer to Svalbard and fjords of Svalbard itself, i.e. areas further east. Moreover Zn was detected in all filters representative of the Arctic Ocean west of Svalbards, while it was not detected only in the filter representative of the Arctic Ocean east of Svalbard. The correspondence between the westernmost sites and the high Zn concentrations suggests that these may have been influenced by the source in the Canadian Arctic identified by Nguyen et al. [175]. Li and Cornett [180] found a long-term increase in Zn concentration in the Canadian Arctic from 1973 to 2000. Obviously the period considered in that study is much older and there are few recent data regarding Zn concentrations in the Arctic region, but data reported by Becagli et al. [151] and by our study seem to be in keeping with this trend.

Ti, Mn, Fe and Ca are elements with a natural, crustal origin. Mn and Ti had the lower concentrations among crustal elements, as reported also by Becagli et al. [151]. Mn

concentrations were 0.21 ng/m^3 (0 – 0.81 ng/m^3) over the Arctic Ocean and 0.34 ng/m^3 (0.03 – 0.93 ng/m^3) for hybrid conditions. These values are consistent with those found at Thule and Station Nord in Greenland and at the subarctic site of Pallas. They are a bit higher than that found durig ASCOS expedition (0.08 ng/m^3), as might be expected from the greater proximity to lands during our campaigns compared to the ASCOS. Ti concentrations were 0.90 ng/m^3 (0 – 4.53 ng/m^3) for oceanic areas and 1.08 ng/m^3 (0 – 2.90 ng/m^3) hybrid areas. These values are very similar to the Thule mean concentration. Fe concentrations were higher: 2.06 ng/m^3 over the Arctic Ocean (0 – 3.11 ng/m^3) and 7.92 ng/m^3 for hybrid conditions (0.57 – 16.87 ng/m^3). The first value is about half of that of ASCOS, while the second one is lower, but comparable, to those found in the Greenlandic sites and at Pallas (which are similar to each other). Ca concentrations were extremely high in both cases (192.61 ng/m^3, range 97.26 – 350.61 ng/m^3, and 121.36 ng/m^3, range 67.23 – 258.74 ng/m^3, respectively). Total calcium values in the Arctic area are less frequent than for other elements, particularly in the Arctic Ocean. However our values are significantly higher than that reported by by Sander and Bottenheim [178] (51.66 ng/m^3) and the highest concentration observed at Station Nord by Nguyen et al. [175] (85.50 ng/m^3).

4.3. Conclusions

We used the chemical composition to infer the macroscopic differences in terms of aerosol and anthropogenic impact between the areas sampled during the AREX 2018 and 2019 campaigns, both between areas at different latitudes and between areas within the Arctic region. TSP was collected on quartz fiber filters on board the research vessel Oceania and then analyzed by ion chromatography for water-soluble inorganic ions and by Total Carbon Analyzer for total carbon and organic matter content. 13 elements were also detected on Arctic filters by means of ICP-OES and GFAAS analysis.

We found that the anthropic impact decreased northward and away from human settlements, while the natural components increased: moving toward the pole (except for hotspots in the Arctic) the contribution of Cl^- and Na^+ to the relative mass rose, while the percentages of OM (due to the reduction of OC from combustion), NO_3^- and eBC decreased. Moreover, the sea-salt contribution to total concentrations of SO_4^{2-}, Ca^{2+} and K^+ grew from south to north too. In addition to clear latitudinal dissimilarities, there were also some differences within the Arctic itself. Indeed, marine areas around Svalbard Islands were all characterized by a more natural footprint (high concentrations of Cl^- and Na^+), but it was still greater in some areas than others. In particular, the stretch of sea after Tromsø was most affected by its proximity to

northern Europe, showing concentrations of NO_3^- and SO_4^{2-} higher than the Arctic Ocean further north. Nitrates were very low in the other Arctic sea areas, while sulfates, on the other hand, maintained higher concentrations, because they are more stable in the atmosphere and have also an important natural origin: in these areas they were mainly derived from marine emissions (especially primary, but also secondary). The lowest anthropogenic influence was found in east and north of Svalbard, which represented the most pristine sites among the different Arctic Ocean areas: here absolute SO_4^{2-} concentrations were even lower (because of the small anthropogenic contribution), while the sea-salt percentages of the ions also presents in sea water (SO_4^{2-}, Ca^{2+} and K^+) further increased. However, the biggest differences within the Arctic region were between the Arctic Ocean and the human settlements (Tromsø and Longyearbyen), which are important emission hotspots in the region. The average chemical composition of Arctic Ocean background was dominated by the sea source (with Cl^- and Na^+ explaining 41% and 26% of the mass, respectively), while the eBC contributed less than 1% and NO_3^- just over 1%. Sulfates and OM were relatively low and due more to marine (from both sea-salt and biological activities) emissions. In contrast, Tromsø presented very high concentrations of OM (related to combustion; 33% of the relative mass), nss-SO_4^{2-} and, above all eBC (highest values after Gdansk; 21% of the relative mass). Longyearbyen is much smaller than Tromsø and thus presented lower total aerosol concentrations. However, it is the main human settlement in Svalbard archipelago and, unlike Tromsø which is situated further south (although already well beyond the polar circle), it is located in the middle of the Arctic (78°N). Considering its very northern location, it can have a major impact on the rather pristine Arctic atmosphere. Indeed, it showed an aerosol chemical composition entirely different than the average of the Arctic Ocean, with much higher concentrations of anthropogenic compounds: Na^+ and Cl^- contribution to relative mass was small, while OM percentages rose from 14% to 30% due to the combustion products; eBC relative percentage was 14% and its concentration was comparable to the values at much lower latitudes (e.g. the Baltic and the coast of Norway areas); SO_4^{2-} contributed 35% to the relative mass (highest value of the entire campaign), exhibiting an almost exclusively anthropogenic origin. Indeed, nss-SO_4^{2-} value was similar to that found in Tromsø. Such high nss-SO_4^{2-} concentrations were probably due to the use of coal as fuel (as also indicated by the absence of vanadium).

Therefore, the impact of hotspots within the Arctic seems to be not negligible, above all during summer when the long-range transport is strongly inhibited, as demonstrated by the significant reduction of nss-SO_4^{2-} and especially NO_3^- northwards, and by the almost complete absence of elements related to the arctic haze (in particular Cd, As and Pb). The impact of local anthropic sources, already evident through the aerosol chemical composition (low-resolution

measurements), will be further explored in the next chapter through the high-resolution measurements. The magnitude of this local impact will then be compared to the remote impact due to the effect of aerosols present at mid-latitudes, whose concentration and chemical composition are different as highlighted by the progressive decline in anthropogenic footprint moving northward.

5. Anthropic settlements impact on the light absorbing aerosol concentrations and heating rate in the Arctic

5.1. Introduction

The Arctic region has been experiencing a greater warming process than the rest of the globe since the 1980s, a process known as Arctic Amplification (AA) [6–8,24,25,181]. It has been demonstrated that the AA grew up from ~1980 till present after a period of Arctic cooling [182]; from ~1980 the Arctic temperature increase was 2 to 4 time faster than the rest of the globe depending on the Arctic region [6,25] and season [183]. As a result, the AA leads to a rapid reduction in sea-ice extent, earlier spring melt and a lengthening of the melt season, and land-ice retreat [10,24]. These changes are strengthened by local feedbacks, which in turn contribute to the AA, such as snow/ice albedo feedback and other feedbacks related to changes in heat fluxes between the ocean and the atmosphere and changes in cloud cover, relative humidity, hence longwave radiation fluxes [7–9,64].

In addition to the worldwide green-house gases effect, the local concentrations of short-lived climate forcers such as e.g. atmospheric aerosols play an important role in the fast Arctic warming [6,8]. For example, Ren et al. [8] reported that the combined total effect of sulfates and black carbon (BC) can explain approximately 20% of the Arctic warming since the early 1980s, causing a surface heating of 0.29 K. These aerosol species can act at different spatial and temporal scales by means of their direct and indirect effects [13,61], influencing the Arctic climate both as local forcers (local emissions or long-range transport from lower latitudes) and by changing poleward heat transport [7,9] through their forcing at midlatitudes. In particular BC, the main light absorbing carbon species, has been widely investigated in the last decade [81] because of its important contribution to climate change in the Arctic region [184]. For example, Sand et al. [10] found out that BC locally emitted within the Arctic has an almost five times larger surface temperature response (per unit of emitted mass) compared to emissions at mid-latitudes.

The sources of BC can be both anthropogenic (energy production, industrial activities, gas flaring, and domestic heating) and natural (forest fires, in case of the Arctic area especially those in Canada and Siberia).

As well as BC, also brown carbon (BrC; e.g. from forest fires) [18] and dust (e.g. high latitude dust) [159,185] belong to the category of Light Absorbing Aerosol (LAA).

Once suspended in the atmosphere, the LAA directly interact with the solar radiation, absorbing it and exerting a positive atmospheric forcing (direct effect). This process releases energy (heat) to the surrounding air with a specific heating rate (HR) [13,85,91–97]. The LAA

species are characterized by a significant spatial and temporal variation reflecting on their radiative effects that can be larger than those of greenhouse gases on a regional scale [186,187]. Indeed, the HR can vary greatly in function of location and local anthropogenic emission; e.g. Tripathi et al. [99] determined a BC induced HR of ~2 K/day in the urban area of Kanpur (northern India), while Ferrero et al. [188] found HR values between 0.5 and 1.5 K/day in Milan (Po Valley, Italy). Moreover, it has been found that dust aerosol can exert a positive atmospheric forcing with HR values up to ~2-3 K/day [189].

Among the LAA species, BC accounts for 70-90% of light absorption on a global scale, while the BrC contributes for the remaining 10-30% [190,191] to the total LAA absorption.

The retreat of important glaciers (i.e. Himalayan) can also be influenced by the LAA induced HR [186,192], making its estimation even more important in the Arctic, where the aforementioned AA phenomenon is present. The surface temperature response depends on the altitude at which the LAA heats the atmosphere [64,193,194] and it is known that LAA particles located near the ground (within the Arctic planetary boundary layer) cause a strong surface warming [26,193], in particular during spring and summer when solar radiation is highest. During spring the LAA (in particular BC) reaches high concentration levels due to the Arctic Haze phenomenon (transport from northern mid-latitudes). In summer, the polar dome retreats further north and transport of pollutants from lower latitudes drastically decreases, thus BC concentrations are lower in this season and local sources become more relevant: they emit BC directly within the Arctic dome, where it warms the surface due to the near surface solar heating and the greater likelihood of surface deposition [10]. Indeed, LAA can also deposit on snow and ice, affecting their surface albedo and accelerating their melting [181,195].

Moreover, the LAA can alter the atmospheric thermal structure, affecting the atmospheric stability and, consequently, the cloud vertical distribution and formation (semi-direct effect) [13,103,188].

It noteworthy that the LAA HR (once normalized for its atmospheric loading) can be larger in the Arctic with respect to other areas of the Earth because of the radiative contribution added to its absorption from highly reflective snow/ice surfaces [9], making its effect close to the surface even more important and necessary to be determined. Most of the literature findings provided exclusively modelled or experimental based radiative-transfer computed values of aerosol-induced HR in the Arctic [102,196–198]. Treffeisen et al. [196] found local solar heating rate anomalies between 0.05 and 0.3 K/day (at 2 km altitude) during an Arctic Haze event in March 2000, while Treffeisen et al. [197] calculated a daily mean HR value of 0.55 K/day at 0.5 km altitude (1.7 K/day if internal mixture, instead of external mixture of the aerosols, is considered) on 2 May 2006, due to an atypical transport of biomass burning aerosols from Eastern

Europe. An older work by Porch et al. [198] reported an increase in the mean HR of 0.01–0.06 K/day in the lowest 1–5 km of the atmosphere under cloud free, Arctic Haze conditions. These studies are thus focused on transport events, especially during spring. In a recent work Donth et al. [102] showed daily mean BC HR, for spring simulations, of maximum 0.1 K/day for the rather pristine Arctic Ocean, about an order of magnitude lower than the values at lower and tropical latitudes [99], while they found negligible HR values for the summer case. However, they focused only on the Arctic Ocean area and other Arctic sites may be characterized by higher atmospheric LAA concentrations also in summer due to local emissions.

Therefore, an experimental quantification of BC pollution (and more in general of total LAA) and associated HR together with its distribution in the Arctic area are main scientific targets to unravel the future of the Arctic from a climate change perspective [181,199]. Thus, specific studies of these phenomena are required [200].

The Svalbard Archipelago is a key area in the Arctic and it is affected by local sources such as ships and human settlements (e.g. Barentsburg, Longyearbyen, Sveagruva, Ny-Ålesund, Hornsund). Their impact needs to be investigated in terms of the BC and atmospheric heating spatial variability at a local scale [199]. Furthermore, the Arctic BC emissions are expected to rise due to new oil and gas exploration and due to enhanced marine traffic in summertime, caused by the retreat of sea ice and increasing tourist and commercial cruises [10,64,181,201,202].

Nevertheless, apart from Ny-Ålesund, BC measurements in this area are sparse and not well spatially distributed, and its radiative forcing has never been calculated in a fully experimental manner. In this chapter aims to add another contribution, focusing mainly on surface BC concentrations and their climate impact in terms of HR (only direct effect was considered here) on the Arctic Ocean around Svalbard Islands and within the anthropized fjords of Spitsbergen over two years (2018 and 2019) of summer campaigns. Considering the measuring technique applied in this study (section 2.3), the mass of LAA is hereinafter expressed in terms of equivalent Black Carbon (eBC) [84] and, according to the literature, the corresponding HR is expressed in units of K/day [98]. Moreover, eBC concentrations, radiation measurements, and the related forcing were accomplished entirely experimentally, avoiding the uncertainties and assumptions inherent in the climatic models: for instance models that quantify BC climate impacts in the Arctic region usually tend to misrepresent the real BC concentration and the amplitude of its seasonal variation [199,203]; Sobhani et al. [204] and Sharma et al. [205] proved that models can overestimate the observed eBC concentrations during summer, while other studies [8] show an opposite behavior or have conflicting results in function of the location.

In addition to eBC and its direct forcing, particle number size concentrations between different areas/case studies were investigated too, in order to better understand the role of aerosol in climate modifications in this area. Macroscopic differences in chemical composition of Total Suspended Particles (TSP) between the Artic Ocean background and two emission hotspots (Tromsø and Longyearbyen) have already been analyzed in the previous chapter. The high temporal resolution measurements considered here allowed us a much more detailed analysis in terms of spatial resolution and climate impact.

We describe the sampling campaigns and the aerosol measurements in Section 2, while the results and discussion follow in Section 3.

5.2. Specific methododology

5.2.1. AREX measurement campaigns

High temporal aerosol and radiation measurements in the Arctic region were performed on board the s/y Oceania during the AREX research campaigns, that have already been introduced in the materials and methods section. For this specific chapter, data from AREX 2018 and 2019 were considered (the same ones already addressed in the previous chapter regarding macroscopic differences in aerosol chemical composition), in particular we focused only on the Arctic, i.e the area from Tromsø onwards (Figure 54). The transects were similar in both years: they started in Tromsø (north of Norway), in the second half of June (20 and 18 June for 2018 and 2019, respectively), and then led to the Svalbard Islands, and were completed on 20th August. The ship spent most of the time in the Norwegian Sea (south of Svalbard) in the first part of the cruise, then it reached the northernmost point in the Arctic Ocean (passing the North of Svalbard). In the central part of the campaign the ship entered the main fjords of Spitsbergen and finally (in the last part) headed south, sailing further west than the outward journey.

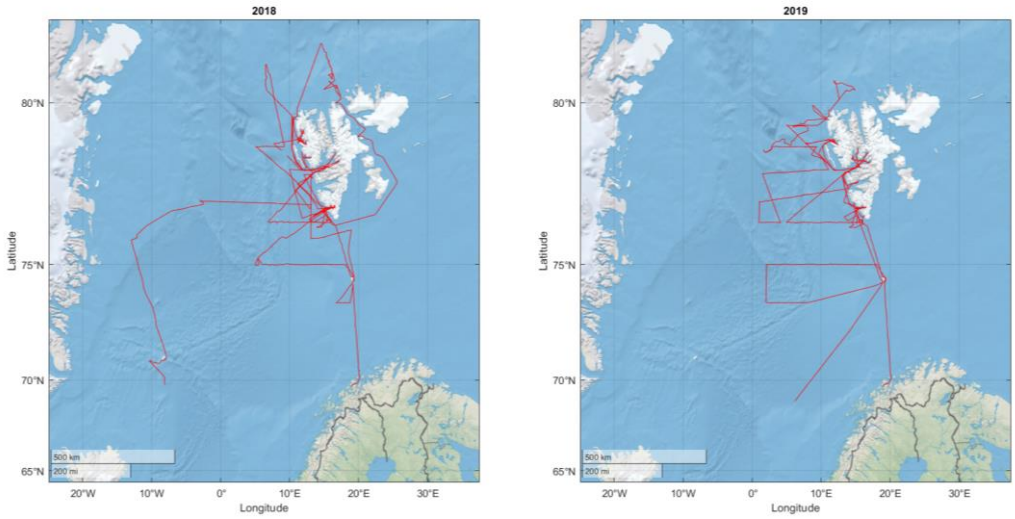

Figure 54. *Route of the s/y Oceania during the 2018 (left) and 2019 (right) AREX campaigns.*

The only difference between the two cruises was in Oceania sailing along the east coast of Spitsbergen in 2018 and going further west into the Greenland Sea, also reaching the Jan Mayen Island on the way back. These journeys enabled to assess the impact of the following anthropic settlements: Tromsø, Longyearbyen, Barentsburg, Ny-Ålesund, Hornsund, Sveagruva and Jan Mayen.

As already mentioned in section 2.1.2, instruments for solar radiation measurements were installed on the measurement platform (balcony), on the main mast (see Figure 11) of the Oceania. Moreover an Aethalometer AE33 (equipped with a dryer), to determine both the equivalent black carbon (eBC) concentrations [84] and the aerosol absorption coefficients, was installed in the tiny, sealed room (Figure 13a) to avoid any sea-spray damage. Aerosol sampling was performed through a $PM_{2.5}$ cyclone and a 2-meters sampling line above the roof of the tiny room. Both eBC and radiation time-base period was set with a 1 minute resolution.

Aethalometer and radiation instruments involved in this work are discussed in detail in chapter 2. The *C* parameter [73,74] (described in section 2.3) used by default for T60 tape (TFE-coated glass filter, Pallflex "Fiberfilm" T60A20) in the AE33 is 1.57. However, the measurements were rescaled by a constant *C* factor of 4.1, recently found in the Arctic area at the Zeppelin station (Ny Ålesund, Svalbard) [206]. As stated in the introduction and in the materials and methods chapter, we will refer to the BC concentration calculated with equation 4 as "mass-equivalent-BC" (eBC), as it depends on the whole amount of LAA in the atmosphere and because *MAC* depends on the dimension, morphology, composition and mixing of aerosol particles, as well as on the filter material, relative humidity and airflow [81–83]. eBC data (calculated with standard pressure and temperature values of the Aethalometer) were corrected using actual measured weather data of temperature, pressure and relative humidity provided by the IOPAN. Moreover, eBC data were treated with a 30 minutes moving mean, which corresponds to a maximum latitudinal spatial resolution of 9 km, considering the average speed of the ship without stopping. It was used for smoothing out the instrumental noise of the Aethalometer in the Arctic area, where the concentrations are particularly low. As was done for all the campaigns, high concentrations due to the possible interference of the vessel exhaust were eliminated by applying a vessel speed/apparent wind ($180° \pm 40°$) filter (it can occur during stops and starts and when wind is coming from the stern), before the treatment with the moving average. Figure 55 shows a day with apparent southerly wind and the effect of the wind filter on eBC concentrations. However, due to the Oceania's tendency to sail headwind and the greater height of the chimney above the sampling line, during these transects there was only a small percentage of data (less than 2%) removed from the total.

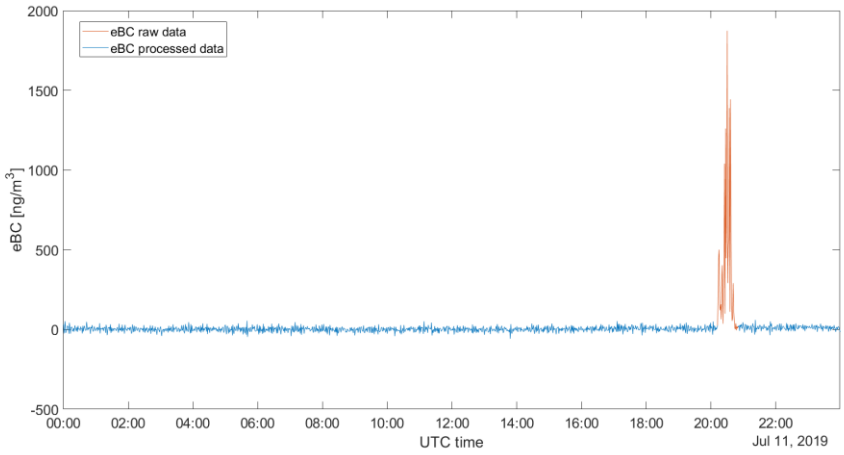

Figure 55. *eBC concentrations on 11 July; red line represents the original data, while the blue line represents eBC data after application of the wind filter.*

By means of LAA absorption coefficients and radiation measurements (both absolute, obtained with the SPN1 pyranometer, and spectral, obtained with the RoX spectroradiometer), it was possible to determine the surface atmospheric Heating Rate related to LAA, using the methodology developed by Ferrero et al. [11] and described in detail in section 2.5. One of the main novelties of this fully experimental method is that it enables to determine the HR in any sky condition and avoid the uncertainties related to input parameters of the models. The HR results obtained here although applied to the surface, can be considered representative of the mixing layer height when there are no specific gradients of LAA concentrations in the lower atmosphere [11,94,100]. HR was computed also over the broadband range of SPN1 (using the Angstrom exponent of $b_{abs(\lambda)}$), but the HR reported here is the one obtained only in the range covered by the wavelengths of the Aethalometer (370-950 nm).

In addition to LAA and radiation measurements, particle number size concentration measurements, provided by the Air-Sea Interaction Laboratory of IOPAN, were also considered in this chapter, in order to investigate more deeply the differences between areas/case studies in the Arctic.

5.2.2. CPC and LAS measurements

In order to obtain particle number concentrations, a TSI Condensation Particle Counter (CPC, Model 3771) and a laser aerosol spectrometer 3340 LAS (TSI Inc., USA) were also installed on the balcony of Oceania vessel, inside a special box to protect the instruments. The CPC measures the total aerosol concentration with a nominal minimum detectable particle size (d_{50}) of 10 nm at an aerosol flow rate of 1.0 liter per minute, over a concentration range from 0 to 10^4 particles per cubic centimeter. This device was evaluated and tested inter alia by Takegawa and Sakurai [207].

The LAS counts aerosol particles from a diameter size of 0.09 μm up to 7.5 μm in 99 channels. Thanks to the application of wide-angle optics and intracavity He-Ne laser, the LAS ensures a wider measurement range. Device was tested in aerosol measurements in many field observations [208–211]. A PM_{10} cyclone was mounted at the LAS inlet, just to prevent the entry of water.

To keep the same temporal resolution as the other real-time measurements, we set up the measurement time step at 1 minute. Finally, we applied the same vessel speed/apparent wind filter that we used to clean the eBC data from the possible influence of the ship.

5.2.3 Data analysis strategy

For the purpose of this chapter, which aims at the determination of the climatic impact (in terms of heating rate) of the anthropic settlements in the Arctic, we divided the collected real-time database into the following case studies:

1. *Arctic Background*, that represents the aerosol concentrations on the sea in pristine conditions, i.e. the concentrations found at steady state after dilution and deposition phenomena and in the absence of evident local emissions and transport phenomena.
2. *Anthropic fjords*, i.e. Spitsbergen fjords characterized by the presence of human settlements; these are Hornsund fjord (where the Polish Polar Station is located), Kongsfjorden (where Ny-Ålesund settlement is located, also including Krossfjord due to its continuity with Kongsfjorden in this analysis), Isfjorden (where Pyramiden, Barentsburg and especially Longyearbyen are located, including also the secondary fjords branching off from it) and Van Mijenfjorden (including Sveagruva).
3. Other human *hot spots* in the Arctic area, i.e. Tromsø (the main city of northern Norway) and the Jan Mayen Island, also characterized by human presence.
4. *Local Settlements Pollution Effect* (LSPE), i.e. the diffusion of the anthropogenic impact detectable in the sea area around the anthropic fjords and not within the fjords themselves (identified thanks to the proximity to the fjords and the use of back-trajectories and wind direction).
5. *Long Range Transport Events* (LRTE), characterized by aerosol concentrations, particularly BC, in the open sea clearly above the background, whose origin (Northern Europe and Russia) has been traced by air mass back-trajectories. These were computed using the on-line version of the hybrid single particle Lagrangian integrated trajectory model (HYSPLIT) developed by the National Oceanic and Atmospheric Administration Air Resource Laboratory (NOAA, http://ready.arl.noaa.gov/HYSPLIT.php). Figure 56 shows the back trajectories, obtained with

a 6-hour resolution and determined at 100 m, 500 m, and 1000 m above the sea level, for the identified Long Range Transport Events.

The analysis of the different case studies included both years (2018 and 2019). Only in the case of Jan Mayen and Van Mijenfjorden, the analysis involved just one year: 2018 for Jan Mayen and 2019 for Van Mijenfjorden due to the fact that they were reached by s/y Oceania only in these years.

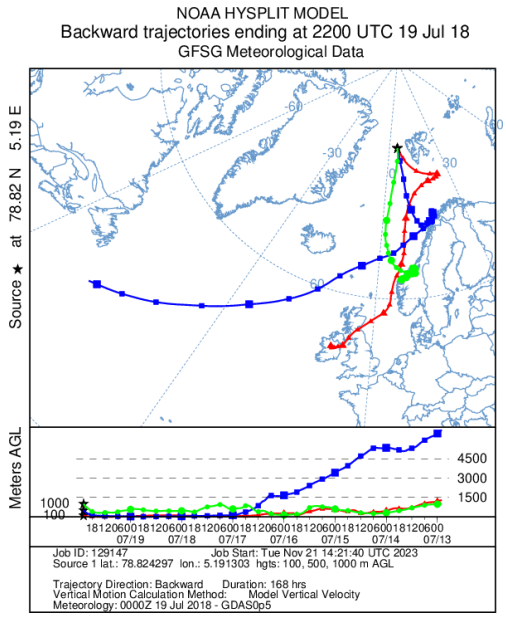

a)

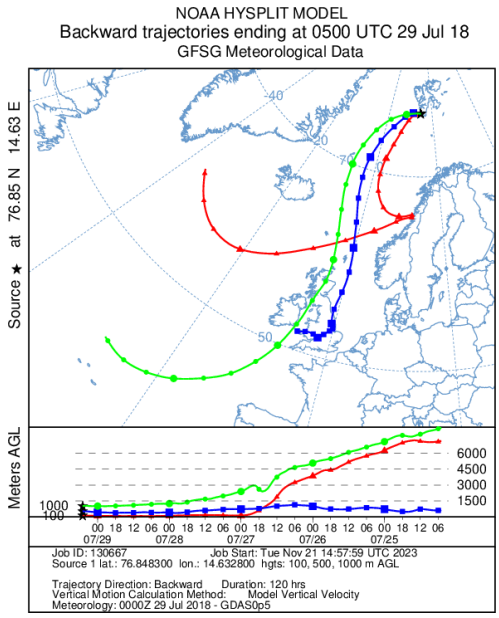

b)

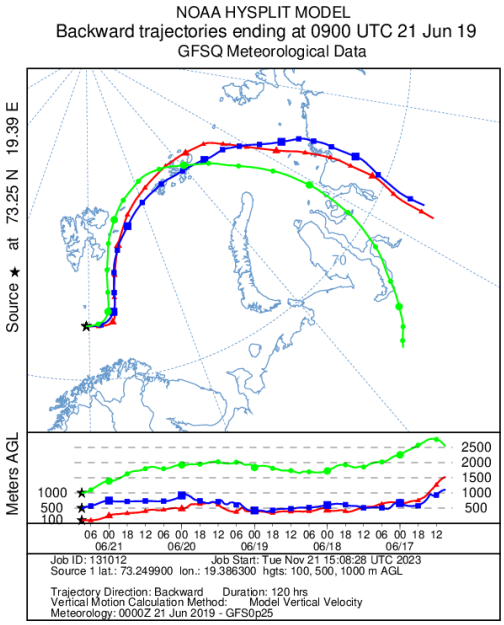

c)

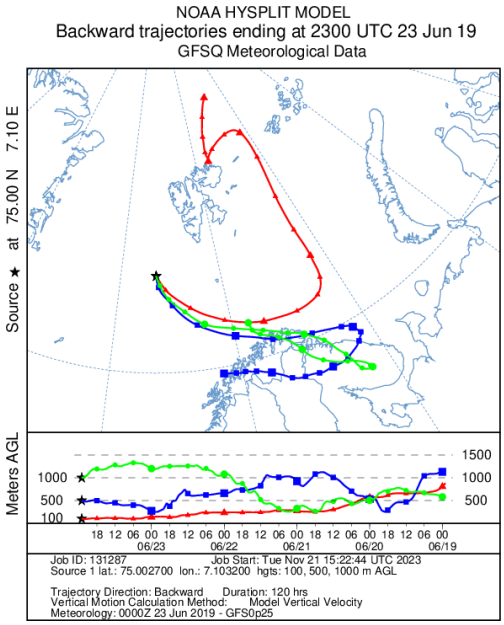

d)

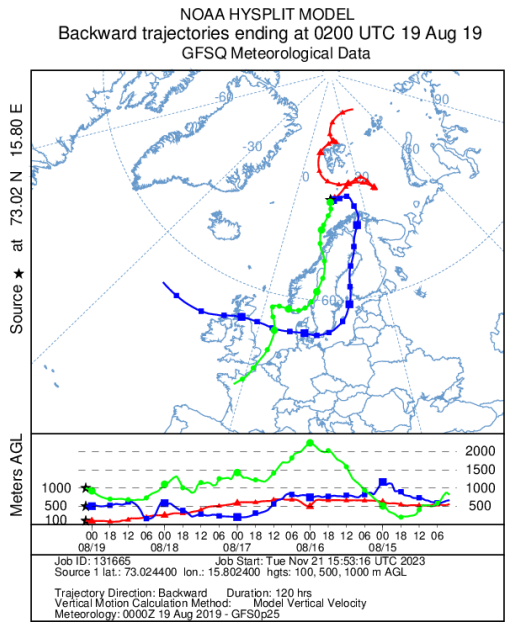

e)

Figure 56. *Seven-day* ***(a)*** *and five-day (****b-e****) air mass backtrajectories derived using HYSPLIT at 100 (red), 500 (blue) and 1000 (green) meters above ground level for the LRTEs occurred on: 19 and 20 July 2018 (****a****), 29 July 2018 (****b****), 21 June 2019 (****c****), 23 and 24 June 2019 (****d****) and 19 August 2019 (****e****).*

5.3. Results and discussion

High time resolution measurements were grouped in eBC and particle concentrations (CPC and LAS) on one hand and HR results on the other hand, and they were divided according to the areas/case-studies already presented in the methodology section: Arctic background, i.e. pristine sea conditions between 69° and 81° N; Svalbard fjords, characterized by the presence of human settlements (here called anthropic fjords); Tromsø and Jan Mayen Island, i.e. the other two arctic hotspots outside Svalbard reached by the ship; Local Settlements Pollution Effects and Long Range Transport Events. Among the anthropic fjords, Van Mijenfjorden is a special case as we will see also from the results in the next paragraphs. In fact, it is the only fjord that had been covered for half of its length, without reaching the actual settlement, Sveagruva (Figure 57). Most of the sampling time was classified as background (38.0%), while 32.2% and 4.8% of the time was spent in the anthropic fjords (14.8% Isfjorden, 8.8% Hornsund, 8.2% Ny-Ålesund and 0.4% Sveagruva) and in the other hotspots (3.4% Tromsø and 1.4% Jan Mayen), respectively. Then, 2.3% and 1.5% of the time was classified as LRTE and LSPE, respectively, while the remaining measurements (21.2%) were not used because of uncertainties in the classification or because the data were deleted due to the influence of the vessel itself. The number of real-time valid data at 1-minute time resolution for each areas/case studies is shown in Table 2. Real-time, 1-minute time resolution, valid data range from 549 in Van Mijenfjorden to 47654 for the Arctic background. The value of Van Mijenfjorden is particularly low because it is a special case

(as explained above): it is the fjord where the ship spent the least time and it has been covered only for half of its length. For all other areas/case studies, there are always more than 2000 (1-minute time resolution) valid data.

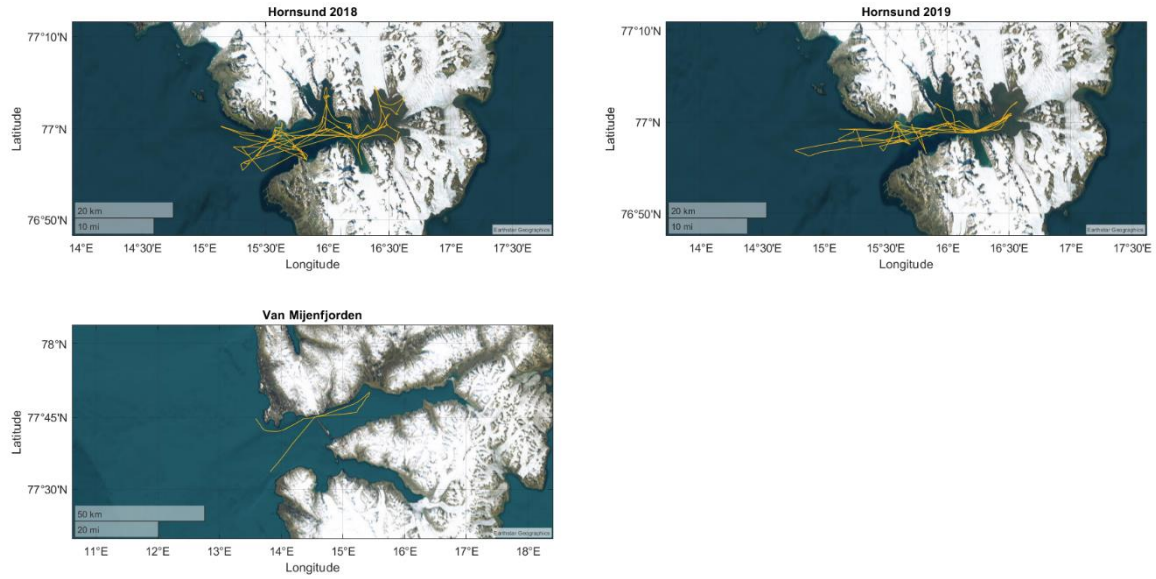

Figure 57. *Comparison between Hornsund fjord (reached by s/y Oceania in both 2018 and 2019) and Van Mijenfjorden (reached by s/y Oceania only in 2019): Hornsund, like other fjords, was covered entirely; Van Mijenfjorden, instead, is the only fjord that has been covered for half of its length, without reaching the actual settlement, Sveagruva (it is also the fjord where the ship was present for the shortest time).*

	'Back ground'	'Hornsund fjord'	'Kongs fjorden'	'Isfjorden'	'Jan Mayen'	'Van Mijen-fjorden'	'LSPE'	'LRTE'	'Tromsø'
N° of real-time valid data	*47654*	*13386*	*12291*	*23710*	*2173*	*549*	*2548*	*4020*	*6061*

Table 2. *Number of real-time valid data (see section 2.3 – 2.5) at 1-minute time resolution for each areas/case studies. Classes containing less data are: LRTE and LSPE, because they are linked to episodic phenomena; Jan Mayen and Van Mijenfjorden, because they were reached by s/y Oceania only in 2018 and 2019 respectively. The value is particularly low for Van Mijenfjorden, which is a special case (as already explained in the main text, section 3): it is the fjord where the ship spent the least time and it has been covered only for half of its length (without reaching the actual settlement, Sveagruva).*

These results allowed to explore in detail the differences already seen at the macroscopic level by means of the chemical composition between the Arctic Ocean background and the two main hotspots, i.e. Tromsø and Longyearbyen (Figure 53, section 4.2.1), in the previous chapter. Other specific areas/case studies considered here were not involved in the chemical discussion, because of the much lower temporal resolution required for filter sampling in the Arctic area. Indeed, the ship spent less time continuously in the various areas/case studies than the time

needed for sampling, except for background areas, Tromsø and Longyearbyen. As a result, there were no filters representing solely the other specific sites, without being contaminated by the background or other areas: they reflect instead mixed conditions and are the filters referred to as hybrids in the previous chapter. For this reason, the comparison between emission hotspots and ocean within the Arctic involved only the two filters of Tromsø and Longyearbyen and the filters sampled over the Arctic Ocean (that have been averaged to obtain the aerosol chemical composition of background conditions). However, already from the these analyis was clear that the aerosol chemical composition can be highly impacted by local sources, altering pristine atmospheric background conditions with anthropogenic particulate matter (particularly organic carbon from combustion and black carbon). In the next sections we will carry out a much more in-depth analysis, linking the high-temporal resolution measurements to the HR.

5.3.1. eBC and particle concentrations

As stated in the introduction section, the impact of local eBC sources in the Arctic summer is crucial: they emit BC directly within the Arctic dome, where it causes a strong surface warming [10,193]. Therefore, we present the eBC and particle concentrations on the Arctic Ocean around Svalbard Islands and within their anthropized fjords. Figure 58 shows the boxplots of eBC measurements during 2018 and 2019 AREX campaigns, divided by the areas/case-studies previously explained: the central mark indicates the median and the bottom and top edges of the box indicate the 25th and 75th percentiles, respectively; the whiskers extend to the most extreme data points not considered outliers, while the outliers are not plotted. The mean (dashed line) and the related 95% confidence interval are also represented. The numbers above the top edge of the box point out the maximum value (i.e. the maximum outlier) reached. Figure 59 shows the same boxplots, but on a logarithmic scale, including also Tromsø in the main plot (this figure is useful for comparing Tromsø with the other arctic sites, but the differences between them are flattened by the logarithmic scale).

All the measurements were carried out in summer, when on one hand eBC concentrations are lower due to reduced transport from mid-latitudes and increased wet-deposition efficiency [54,212], and on the other hand solar radiation is maximum, triggering the climatic effect of the light absorbing aerosol. Ferrero et al. [64] reported homogenous vertical profiles of eBC in summer if fresh local emissions were not present. Under these conditions (i.e. background conditions), surface concentrations can be considered representative of at least the first km of the atmosphere.

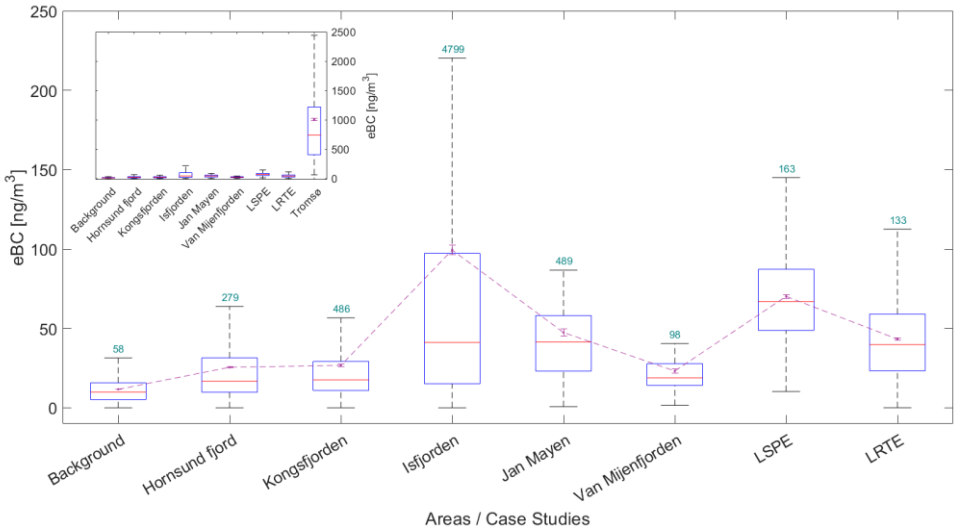

***Figure 58**. eBC boxplots for the areas/case-studies considered. The central mark indicates the median, while the bottom and top edges of the box indicate the 25th and 75th percentiles, respectively; the whiskers extend to the most extreme data points not considered outliers (outliers are not plotted). The mean (dashed line) and the related 95% confidence interval are also represented. The cyan numbers above the top edge of the box point out the maximum value (i.e. the maximum outlier) reached.*

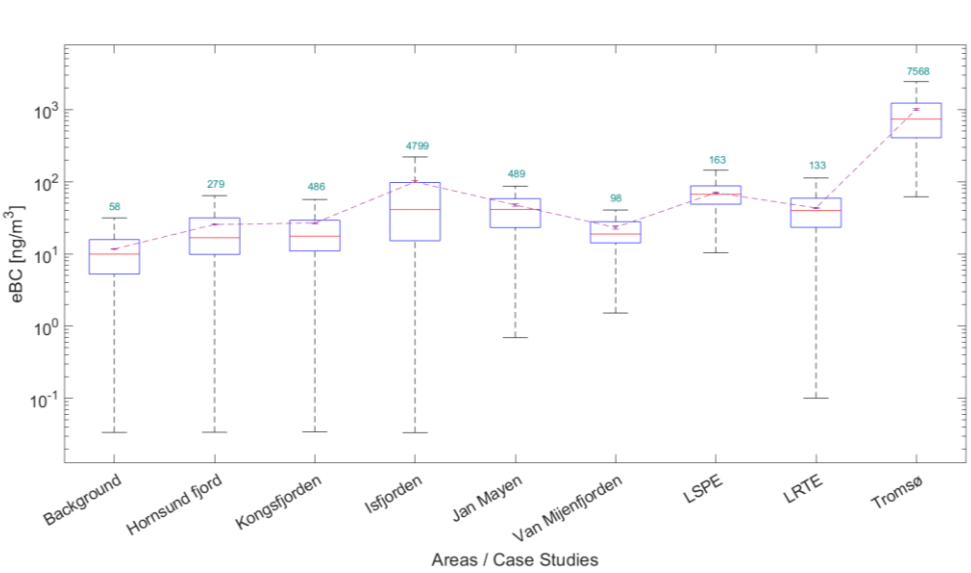

***Figure 59.** eBC boxplots for the areas/case-studies considered. The y-axis is in logarithmic scale. The central mark indicates the median, while the bottom and top edges of the box indicate the 25th and 75th percentiles, respectively; the whiskers extend to the most extreme data points not considered outliers (outliers are not plotted). The mean (dashed line) and the related 95% confidence interval are also represented. The cyan numbers above the top edge of the box point out the maximum value (i.e. the maximum outlier) reached.*

Background (BG) conditions, which correspond to pristine conditions over the sea, showed an average value of 11.7 ± 0.1 ng/m^3, similar to the median value of 9.9 ng/m^3, and a maximum value of 58.4 ng/m^3. These results agree with the summer-autumn concentrations generally <20 ng/m^3 reported by Eleftheriadis et al. [184] for the period 1998-2007 and with the EC summer concentration of 11 ng/m^3 (from 1990 to 1992) reported by Heintzenberg et

al. [213] at the Zeppelin station. They are also similar to the annual-mean surface value of observed eBC (13 ng/m^3) for the period 2009-2015, described by Matsui et al. [214]. Zeppelin station is located near Ny-Ålesund at an elevation of 464 m a.s.l. and can be considered a remote site, due to very little influence from the human settlement, and thus is compared here to background conditions. Indeed, despite measurements at the Zeppelin site being generally considered to represent free-troposphere environment, there is evidence that it is frequently representative of Boundary Layer conditions during late spring/summer [184,215]. Our BG results are similar also to summer eBC concentrations (18 ± 72 ng/m^3) recently found at the Bely Island, in western Siberia [181] (although they are characterized by a much wider confidence interval). Obviously BG concentrations were lower than all the other cases examined, also in accordance with the chemical composition of TSP (see previous results section) indicating a low presence of anthropogenic pollutants and an origin mainly linked to natural marine emissions.

eBC concentrations in Tromsø were off the charts compared to the other cases (Figure 58, inset), as expected considering its size and harbour activity, which makes it the main city of northern Norway and an important emission hotspot at the gateway to the European Arctic region. The mean eBC concentration in Tromsø was 1004.9 ± 25.1 ng/m^3 with peaks up to 7568.4 ng/m^3 measured in the harbor of the city. These results, once again, agree with the results reported in the previous section, which showed the highest relative percentages of eBC (and also NO_3^-) in Tromsø, as well as high percentages of OM and SO_4^{2-}. Jan Mayen is the other Arctic hotspot outside Svalbard reached by s/y Oceania and its mean concentration (47.4 ± 2.2 ng/m^3) was in the same order of magnitude of the other polluted cases considered in Svalbard (with maximum values very similar to those found in Ny-Ålesund).

Among the Svalbard anthropized fjords, Kongsfjorden, Hornsund fjord and Van Mijenfjorden showed analogous average concentrations: 26.7 ± 0.6 ng/m^3, 25.5 ± 0.5 ng/m^3 and 23.1 ± 1.4 ng/m^3, respectively. These 3 fjords are characterized by the presence of only one small human settlement. Mean value of Kongsfjorden included lower values measured in the deepest branches of the fjord (and also in the adjacent Krossfjord), and higher values (up to 486 ng/m^3) measured near the settlement and the harbor of Ny-Ålesund. Maximum values in Kongsfjorden agree with the mean surface value found by Ferrero et al. [64] in Ny-Ålesund for the vertical profiles affected by ship emissions (319 ± 14 ng/m^3). Our average value is similar to that reported by Gogoi et al. [216] for the summer season (19.5 ± 6.5 ng/m^3) at Gruvebadet observatory and to the average eBC observed during the period 2005-2018 (16-20 ng/m^3) [199]. Gruvebadet is located about 1 km southwest of the village of Ny-Ålesund. Its location guarantees generally low influence by local pollution sources given the prevailing southerly winds [217], but there is also evidence of frequent episodes of high absorption coefficient values, likely due

to the local emission sources constrained in the lower layers of the troposphere [199]. Hornsund fjord is characterized by the presence of the Polish Polar Station and mean and median eBC concentrations were almost identical to Kongsfjorden while maximum values were lower, probably due to a lesser naval traffic compared to Kongsfjorden. As previously mentioned, Van Mijenfjorden is a separate case, because was not entirely sailed through (unlike the other anthropized fjords) and the settlement of Sveagruva (located at the end of the fjord) was not reached. Usually, concentrations in the anthropized fjords are the result of measurements taken both in the harbor and near the human settlement of the fjord, and in remote areas of the fjord. This could be the reason why maximum values in Van Mijenfjorden were lower than in Kongsfjorden and Hornsund. Moreover, less time was spent inside it than in other fjords.

Isfjorden is characterized by the presence of Pyramiden, Barentsburg and especially Longyearbyen, the main human settlement and harbor on Svalbard. Consequently, its concentrations were particularly high for the arctic area (only lower than those measured in Tromsø): it presented the highest mean eBC value (99.4 ± 3.1 ng/m^3) among all the cases analyzed, except for Tromsø. The median value (41.2 ng/m^3) was similar to Jan Mayen and slightly lower than LSPE. The large deviation between the mean and the median highlighted the importance of freshly emitted particles. Indeed, as can be seen from Figure 7, higher mean than median values occurred for all the case studies considered, but the discrepancy between them was higher in the fjords most affected by anthropogenic activity. Maximum values reached in Isfjorden (up to about 4800 ng/m^3) were clearly the highest (excluding Tromsø), further emphasizing the presence of fresh emissions which are related to ships (intense marine traffic considered the area) and to fossil fuel combustion in Longyerabyen (mainly coal and diesel). The anthropogenic impact on Isfjorden is also confirmed by the TSP chemical composition in Longyearbyen, shown in the previous section (3.1).

The so-called Local Settlements Pollution Effect (LSPE) is the consequence of the spread of eBC outside the anthropic fjords, detectable in the surrounding sea area. Its average eBC concentration was 70.2 ± 1.1 ng/m^3, a quite high value dominated by the effect of Isfjorden. The mean was close to the median (66.9 ng/m^3) and the maximum values were lower than the anthropic fjords. This evidence means that particulate matter that had undergone local transport was detected, instead of peaks of fresh emission. This aspect is further emphasized for the Long Range Transport Events (LRTE). Moreover, in this case, mean and median values were lower (43.3 ± 0.8 ng/m^3 and 39.8 ng/m^3, respectively) than LSPE despite their emission sources being comparable to and/or greater than Longyearbyen, because these particles have been subjected to a much longer transport. The sources of LRTE were northern Europe and northwestern Russia (Figure S1-S4). eBC concentrations related to LRTE were measured over the open sea

and the average was about four times higher than the background, thus showing a non-negligible alteration of pristine conditions. It was also higher than the anthropic fjords except Isfjorden. However, probability of transport from mid-latitudes during the summer season is minimal (compared to winter when the Arctic haze phenomenon is present). Thus, we detected only few transport events.

Particle number concentration measurements were available only for the AREX 2019 campaign. Figure 8 shows the mean values and related 95% confidence intervals for the investigated case studies, with the exception of Jan Mayen (reached by s/y Oceania only in 2018) and Tromsø. Figure 60a represents the total number concentration from 10 nm (obtained from the CPC), while Figures 60b and 60c represent the number concentration of particles in the coarse (diameters larger than ~1 μm) and accumulation modes (~ 0.1 – 1 μm), respectively (obtained from the LAS channels). By subtracting the LAS from the CPC concentrations, the number concentration of particles in the Aitken regime (diameters ranging from ~10 to ~100 nm) was also determined (Fig. 60d).

The coarse fraction presented very low values, because larger particles count for little in terms of number concentration: they contributed always less than 0.15% only to the total particle number concentration. However, there are differences between LSPE or LRTE and the other cases: for background and anthropic fjords the coarse particles ranged between $0.06 \pm 0.15*10^{-2}$ and $0.1 \pm 0.24*10^{-2}$ cm^{-3}; during LSPE and LRTE, however, the values nearly tripled ($0.3 \pm 0.95*10^{-2}$ and $0.31 \pm 0.83*10^{-1}$ cm^{-3}, respectively) because of the distance from the emission sources and the processes that occurred during transport.

The total number concentration was similar for the background, Hornsund fjord and Kongsfjorden (629.86 ± 28.85, 567.51 ± 22.53 and 521.81 ± 25.44 cm^{-3}, respectively). It was about 3 times higher in Isfjorden and Van Mijenfjorden (1982.3 ± 80.52 and 1701.52 ± 37.47 cm^{-3}, respectively) due to the very high concentration of Aitken particles. In general, the summer period is dominated by fresh, small and locally formed Aitken particles [64,199,218], which in fact constituted the largest fraction of the total in all areas/cases considered (except LRTE, Table 1); however in Isfjorden and Van Mijenfjorden this contribution was even greater, both in terms of absolute and percentage values (92 and 93%, respectively). LSPE presented high total number concentration values (1080.61 ± 158.19 cm^{-3}) because of the main influence of Isfjorden, but the percentage contribution of nanoparticles (less than 100 nm, 62%) was definitely lower than Isfjorden and the other anthropic fjords, while the contribution from the accumulation mode was the highest (38%), excluding LRTE. The absolute concentration value in this dimensional range for LSPE was the greatest (410.01 ± 4.22 cm-^{3}). This can be attributed to the transport (not long-range) of particles outside the fjords towards the open sea in case of

LSPE. In background and anthropic fjord areas the emission of fresh nanoparticles or the formation of new particles through secondary processes dominated, making the Aitken particles by far the most important fraction. LRTE were different from the other cases: precisely because of long-range transport and consequent deposition phenomena, the total aerosol number concentration was the lowest (245.52 ± 4.3 cm^{-3}). Moreover, it was completely attributable to the accumulation mode (almost no nanoparticles were detected). This is in agreement also with the relatively high value of the coarse fraction, mentioned above (even if it does not contribute to the total in terms of number), and with literature data showing that Arctic haze (i.e. long-range transported particles) is dominated by accumulation mode aerosol [61].

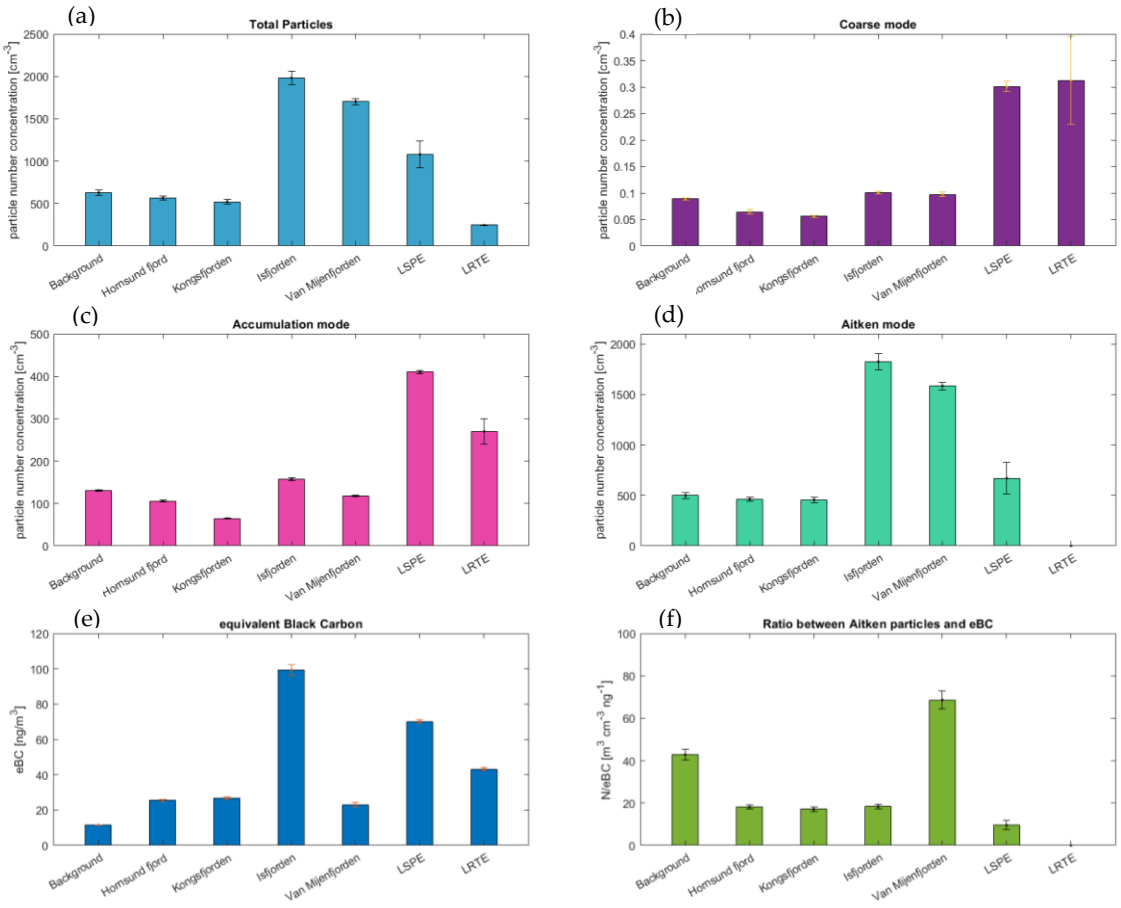

Figure 60. *Mean values and related 95% confidence intervals of particle number concentration in the different areas/case studies considered for total particles (a), coarse mode (b), accumulation mode (c) and Aitken mode (d); mean values and related 95% confidence intervals of eBC concentration (e) and N/eBC ratio (f) in the same areas/case studies.*

Particles Fraction	'Background'	'Hornsund fjord'	'Kongsfjorden'	'Isfjorden'	'Van Mijenfjorden'	'LSPE'	'LRTE'
Coarse Mode	0.01%	0.01%	0.01%	0.01%	0.01%	0.03%	0.13%
Accumulation Mode	21%	19%	12%	8%	7%	38%	100%
Aitken Mode	79%	81%	88%	92%	93%	62%	0%

Table 3. *Percentages of Coarse, Accumulation and Aitken fractions on total particles.*

In order to estimate the anthropogenic contribution (order of magnitude) to the different areas/case studies versus other origins, the method developed by Rodríguez and Cuevas [136] and based on the N_{Aitken}/eBC ratio was applied (Figure 60f). eBC is considered as a proxy of the primary aerosol in the nanoparticles range. Mean N_{Aitken}/eBC for the background was 42.82 ± 2.49. This value is comparable to that reported by Ferrero et al. [64] (54.8) at the base of summer vertical profiles influenced by surface plumes of locally formed secondary nano-particles in Ny-Ålesund, and it clearly indicates the presence of processes of secondary aerosol formation [137]. In Hornsund fjord, Kongsfjorden and Isfjorden the ratios were very similar to each other (18.09 ± 0.95, 17.1 ± 1.03 and 18.36 ± 0.99, respectively), despite the different concentrations of eBC, and significantly lower than the background, highlighting the influence of direct primary emissions (due to the anthropogenic impact) and the lower relevance of secondary formation in these areas compared to the open sea. In Van Mijenfjorden an anomalous value, higher than the background, was found. There are no obvious reasons for this behavior, however, as already mentioned, s/y Oceania sailed only half of the Van Mijenfjorden, without reaching the actual emission hotspot (Sveagruva) and measuring the related primary emissions of nanoparticles. Consequently, the relative importance of eBC compared to the total concentration of nanoparticles is lower than in other anthropic fjords.

Isfjorden and Van Mijenfjorden both showed very high values of total number aerosol concentration because they were dominated by the Aitken fraction. Nevertheless, these two elevated concentrations of nanoparticles were clearly due to different reasons, as can be seen from the N_{Aitken}/eBC ratio: in Isfjorden the Aitken mode was mainly attributable to fresh eBC emissions (lower N_{Aitken}/eBC), while in Van Mijenfjorden it was mainly attributable to secondary activity (higher N_{Aitken}/eBC). Therefore, the N_{Aitken}/eBC ratio (in addition to eBC concentrations and chemical composition) also confirmed the high anthropogenic impact in Isfjorden.

As expected, LSPE presented the lowest value (except for LRTE) of N_{Aitken}/eBC (9.55 ± 2.26) in accordance with its percentage of Aitken particles, which is the lowest. Obviously the N_{Aitken}/eBC ratio was 0 for LRTE because there were no nanoparticles (only particles in the accumulation and coarse mode).

5.3.2. Heating rate

In this section, we present the local climate impact (direct forcing in terms of atmospheric heating) of the eBC concentrations in the areas/case studies shown in the previous paragraph.

Solar radiation is necessary to trigger the climatic effect of the LAA. In the Arctic region high winter eBC concentrations cannot interact with radiation. The local LAA radiative forcing is present during spring and summer. Its effect could be stronger in spring when transport of particles from lower latitudes is still present and most of the surfaces are still covered by ice and snow [9,10]. In summer, however, radiation is higher and local emissions, which heat the lower atmospheric layer causing the maximum positive forcing [10,193], are dominant. Figure 9 shows the results of the radiation measurements, needed to compute experimentally the LAA HR. In this plot Tromsø is included in the same box with other cases. Global radiation was quite constant for all the areas/cases analysed. Indeed, excluding Tromsø and Jan Mayen, average values ranged from 117.5 ± 1.8 W/m^2 to 160.3 ± 8.8 W/m^2. The two hotspots, which are the two southernmost localities surveyed, presented the lowest average values measured along the cruises (82.7 ± 4.6 W/m^2 for Tromsø and 85.5 ± 2.5 W/m^2 for Jan Mayen).

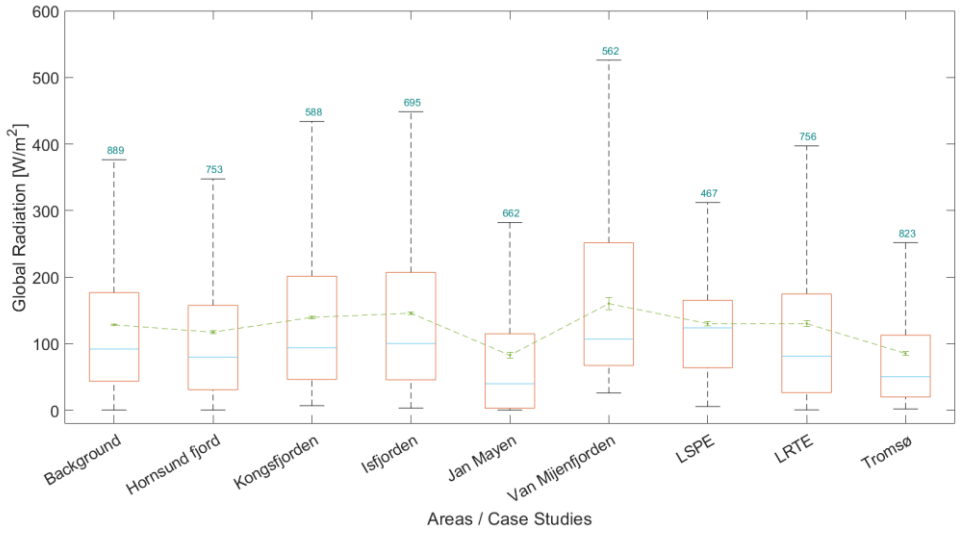

Figure 61. *Total radiation boxplots for the areas/case-studies considered. The central mark indicates the median, while the bottom and top edges of the box indicate the 25th and 75th percentiles, respectively; the whiskers extend to the most extreme data points not considered outliers (outliers are not plotted). The mean (dashed line) and the related 95% confidence interval are also represented. The cyan numbers above the top edge of the box point out the maximum value (i.e. the maximum outlier) reached.*

Thanks to the radiation (absolute values and spectral data) and absorption coefficient measurements, it was possible to determine the surface LAA HR in a completely experimental way and in any sky condition, using the method developed by Ferrero et al. [11] and described in the methodology chapter. It allowed also to avoid the errors induced by the clear-sky assumption, which can be present in some radiative-transfer calculations. The last feature is crucial in the Arctic because 87.2 ± 0.1% of the measured global radiation was on average given by the diffuse component; in fact the average cloudiness (in oktas) along the campaign was 7.4 ± 0.01. Figure 62 shows the boxplots and the average and maximum values of the computed HR (Figure 63 shows the same HR boxplots but on a logarithmic scale). Since the radiation values were quite constant, the HR variations were mainly influenced by the differences in the eBC concentrations.

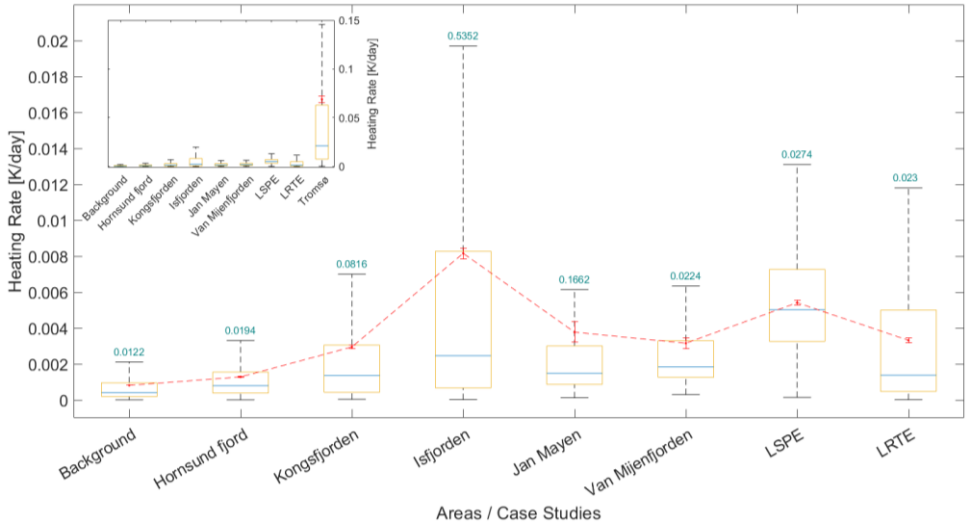

Figure 62. *HR boxplots for the areas/case-studies considered. The central mark indicates the median, while the bottom and top edges of the box indicate the 25th and 75th percentiles, respectively; the whiskers extend to the most extreme data points not considered outliers (outliers are not plotted). The mean (dashed line) and the related 95% confidence interval are also represented. The cyan numbers above the top edge of the box point out the maximum value (i.e. the maximum outlier) reached.*

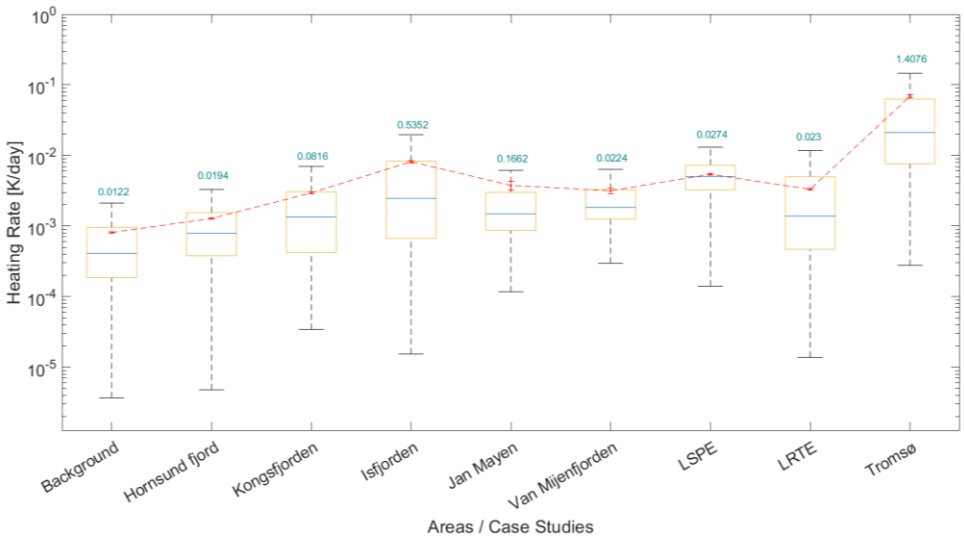

Figure 63. *HR boxplots for the areas/case-studies considered. The y-axis is in logarithmic scale. The central mark indicates the median, while the bottom and top edges of the box indicate the 25th and 75th percentiles, respectively; the whiskers extend to the most extreme data points not considered outliers (outliers are not plotted). The mean (dashed line) and the related 95% confidence interval are also represented. The cyan numbers above the top edge of the box point out the maximum value (i.e. the maximum outlier) reached.*

Also for the HR, except for LSPE, the average values were clearly greater than the median ones, in particular for Tromsø and Isfjorden where maximum values were reached. HR in Tromsø was the highest, with a mean value of $68.9*10^{-3} \pm 3.3*10^{-3}$ K/day, followed by Isfjorden, where we found the highest values for Svalbard and Arctic Ocean areas. Here the average HR was $8.2*10^{-3} \pm 0.3*10^{-3}$ K/day, while the maximum peaks reached $5.3*10^{-1}$ K/day. Although they are not high values compared to the polluted areas of the lower latitudes, the difference with respect to the pristine background of the Arctic is evident. Indeed, BG had an average HR one order of magnitude lower ($0.8*10^{-3} \pm 0.9*10^{-5}$ K/day) than Isfjorden and a maximum value of $0.1*10^{-1}$ K/day. HR in Jan Mayen remained higher than the anthropic fjords (excluding Isfjorden, in accordance with eBC concentrations), but decreased in proportion due to the lower radiation (compared to the higher latitudes). Among the anthropic fjords, the difference between the average HR in Kongsfjorden and Hornsund fjord increased ($2.9*10^{-3} \pm 10.5*10^{-5}$ K/day and $1.3*10^{-3} \pm 2.8*10^{-5}$ K/day, respectively) compared to the eBC mean concentrations, because of differences in solar radiation. Van Mijenfjorden mean HR ($3.2*10^{-3} \pm 29.5*10^{-5}$ K/day), exceeded that of Kongsfjorden and Hornsund fjord thanks to greater radiation. LSPE HR ($5.4*10^{-3} \pm 12.7*10^{-5}$ K/day) came immediately after Isfjorden because it was affected by its high eBC emissions. Also LRTE can significantly alter the BG. In fact their mean HR ($3.3*10^{-3} \pm 12.1*10^{-5}$ K/day) was higher than all the anthropic fjords except Isfjorden. LSPE and LRTE, although they had mean HR values greater than most of the anthropic fjords, were characterized by relatively low maximum values. These, indeed, were comparable to the maximum values reached in Van Mijenfjorden and Hornsund fjord and they were about 3-4 times lower than those present in Kongsfjorden. This phenomenon is attributable to the fact that LSPE and LRTE are defined by a spread or transport from source areas; therefore they don't show high peaks of eBC due to fresh emissions, but they have more homogeneous concentrations. As already mentioned Van Mijenfjorden is a separate case (a hybrid between an anthropic fjord and LSPE) because the ship did not reached the settlement of Sveagruva, avoiding possible direct and fresh eBC emissions from it. Finally, Kongsfjorden presented a maximum HR value ($0.8*10^{-1}$ K/day) much higher than Hornsund fjord ($0.2*10^{-1}$ K/day) due to the presence of Ny-Ålesund and its harbor, where ship traffic, responsible for elevated ground eBC concentrations [64], is far greater than in Hornsund, where only the Polish station is present.

Considering the maximum values (and not the averages), the HR in the hotspots or anthropic fjords of the Arctic is more similar to the HR computed at lower latitudes. For istance, maximum HR in Isfjorden (≈ 0.5 K/day), can be compared, although lower, to the highest values (2.1 and 1.8 K/day) found by Tripathi et al. [99] along vertical profiles obtained in the urban area of Kanpur (northern India). Therefore, peaks reached in the Arctic are not negligible. They are mainly due to fresh LAA emissions, which could rise in the future because of ice retreats and enhanced marine traffic. The role of local HR, induced by LAA, thus may become more important. Since experimental HR measurements (with our methodology) were carried out only in Milan, where LAA concentrations are higher than in the Arctic, it is useful to normalize the HR values to the unit mass of eBC for a comparison between Arctic and mid-latitudes. Ferrero et al. [188] used the parameter HR/eBC to report the efficiency of warming per mass concentration of eBC at different cloudiness levels (oktas) in Milan. They found a value around 0.1 K m^3 d^{-1} μg^{-1} at 7-8 oktas. We found an average cloud-cover value of 7.4 ± 0.01 oktas in the Arctic and HR/eBC values of 0.1 and 0.08 K m^3 d^{-1} μg^{-1} for maximum and average eBC concentrations respectively in Isfjorden. These numbers are very similar, highlighting the reliability of our data and their comparability with data from lower latitudes.

5.4. Conclusions

Light absorbing aerosol absorption coefficients, equivalent black carbon (eBC), radiation and particle number concentration measurements were collected during two summer Arctic campaigns (2018 and 2019), which took place in the ocean around the Svalbard Archipelago and within its anthropized fjords.

These ensemble of measurements allowed unravelling the Arctic background level (pristine conditions over the sea) with respect to the influence of local anthropized settlements in terms of aerosol concentration and direct climatic impact of light absorbing aerosol. In addition, long range transport events (from lower latitudes) and local settlements pollution effects (i.e. the spread of the anthropogenic impact in the area outside the fjords) were quantified too. All the real time measurements were carried out on the Polish research vessel s/y Oceania as a mobile Arctic platform. LAA and radiation data allowed us to asses for the first time in the Arctic the atmospheric heating rate (HR), due to the absorption of light by the atmospheric aerosol, at high temporal resolution in a completely experimental manner and in any sky condition, avoiding the inherent uncertainties in the models.

eBC and particle number concentration values confirmed the local settlement impact on the Arctic atmosphere, already highlighted at the macroscopic level by the TSP chemical com-

position (as shown in the previous chapter): eBC concentration for the Arctic Ocean background was 11.7 ± 0.1 ng/m^3, while Tromsø (the main city of northern Norway in the Arctic area with an average eBC concentration of 1004.9 ± 25.1 ng/m^3) and Longyearbyen (the main human settlement in Svalbard Islands) had the greatest impact among the anthropic settlements. All the Svalbard anthropized fjords presented roughly similar average eBC concentrations (≈ 25 ng/m^3), except Isfjorden (where Longyearbyen is located), where eBC concentrations were particularly high for the Arctic area, with an average value of 99.4 ± 3.1 ng/m^3. Moreover, the significant deviation between the mean and the median and the high maximum values (up to 4800 ng/m^3) highlighted the presence of fresh emissions which are related to ships and fossil fuel combustion. Regarding particle size, both the background and the anthropic fjords were dominated by the Aitken mode, but for different reasons: the N_{Aitken}/eBC ratio for the fjords was lower, emphasizing the importance of primary eBC emissions and, thus, of the anthropogenic impact; the mean N_{Aitken}/eBC value for the background, instead, was more than double that in the fjords and clearly indicated the presence and relevance of processes of secondary aerosol formation. Only a few Long Range Transport Events were detected (by means of back-trajectories), in accordance with the measurement season and they were dominated by the Accumulation mode, due to the processes that occur during transport, and their eBC average concentration was about four times higher than the background. Thus they show a non-negligible alteration of pristine condition, which, however, occurs only rarely in summer (when the Arctic haze is not present).

All the above data allowed the determination of climatic impact to be quantified in terms of heating rate. HR in Tromsø was the highest ($68.9*10^{-3} \pm 3.3*10^{-3}$ K/day) followed by Isfjorden, where we observed the highest values for Svalbard and the Arctic Ocean areas ($8.2*10^{-3} \pm 0.3*10^{-3}$ K/day). Although, they are not high values compared to the polluted areas of the lower latitudes, the difference with respect to the pristine background of the Arctic Ocean is evident: here the average HR is one order of magnitude lower than Isfjorden ($0.8*10^{-3} \pm 0.9*10^{-5}$ K/day). Moreover, considering the maximum values, the HR in the hotspots or anthropic fjords of the Arctic is more similar to the HR computed at lower latitudes. For istance, maximum HR in Isfjorden (≈ 0.5 K/day) can be compared to the highest values (≈2 K/day) found in the urban area of Kanpur. The parameter HR/eBC computed in Isfjorden was similar to that in Milan (the only place where the HR was determined by the same methodology) under comparable cloud cover conditions, highlighting the reliability of our data and their comparability with data from lower latitudes.

We found out that during summer there are significant differences in light absorbing aerosol concentrations and consequent direct climate impact (HR) between the different Arctic areas

considered in this study, due to the role of local sources (such as ships and human settlements on Svalbard Archipelago): they emit eBC directly within the Arctic dome, causing a strong surface warming and, thus, are necessary to explain the HR spatial variability at the local scale. Indeed, the HR peaks at the surface atmospheric layer, which are not negligible, are mainly due to fresh emissions, which could rise in the future because of ice retreats and enhanced marine traffic (tourist and commercial cruises). The role of local HR, induced by LAA, thus may become more important.

Finally, our fully experimental HR calculation methodology proved to be crucial in the Arctic area, where we found an average cloudiness of 7.4 ± 0.01 oktas. Hence, it could be useful for further studies in the Arctic and comparisons with results from models.

6. LAA induced Heating Rate between mid-latitudes and the Arctic

6.1. Introduction

Surface atmospheric warming in the Arctic is definitely faster than the globale average [6,7,219–221]. This phenomenon is known as 'Arctic Amplification' (see section 1.2) and was identified by modeling studies of Manabe and Wetherald as early as 1975 [23]. From that time, recent AA has been demonstrated both in climate models and observations [25], while paleoclimate proxy records found AA also in past climates [222,223]. The magnitude of warming in polar latitudes is more than double than the rest of the planet [27] and recent studies have pointed out that it is 3 [24] to about 4 times (in the period 1979 – 2021) [25] greater. In the 20th century, the AA started and grew since the late 1970s, following a period of about 50 years of Arctic cooling (~1930-1980) [182]. AA is not a homogeneous phenomenon, but it depends on the season and location. Indeed, Maturilli et al. [183] indicated a surface air temperature increase in Ny-Ålesund between 0.7 K per decade in summer and 3.1 K per decade in winter in the period 1993-2013. Rantanen et al. [25] found a higher temperature increase (1.25 °C per decade) in the Eurasian sector than in other parts of the Arctic Ocean (0.75 °C per decade) during the satellite period (i.e. 1979 to the present). Therefore, AA is maximum in fall/winter and near Svalbard, i.e., the survey area of this research. It is already having an influence on natural and human systems within and outside the Arctic and this impact will grow in the near future [28,219].

The causes and mechanisms beyond AA are several, act at different spatial and temporal scales, and are related to both internal feedbacks and external factors. In addition to the role of greenhouse gases (largely responsible for global warming), sea-ice related feedbacks [28] and temperature feedbacks (plank and especially lapse rate effects [221], which is correlated with the vertical structure, i.e. thermal inversion, of the Arctic troposphere [27,224]) are fundamental for AA, as discussed in the section 1.2. Lapse rate feedback can help to explain the AA seasonality, as well as sea-ice loss which determine both spatiality and seasonality. Indeed, the decrease in ice cover not only triggers an albedo reduction [225], but also an increase in sea-air exchanges (radiation fluxes [226], gas exchange and aerosol precursor emission [227]): heat uptake by the ocean in late spring and summer is enhanced by the lower presence of ice and this additional energy within the mixed layer is then released back to the atmosphere in fall and winter (as longwave radiation, latent and sensible heat) causing a surface warming [28,224]. Moreover, AA is also driven by feedbacks related to changes in water vapor content (whose increase contributes to greenhouse effect [228]), cloud cover (positive feedback associated mainly with an increase in low clouds [28]), oceanic (increased [36]) and atmospheric energy (dry static and

moisture) transport, and biosphere (e.g. increases in phytoplankton biomass [35,229], overall greening of the region [28] and remote physiological forcing [34]).

All these mechanisms are strongly interconnected and the relative contribution of each of them is still not entirely clear [182]. Models, despite significant progress, still have difficulty reproducing observations: for example, they underestimate the observed superficial warming in the Arctic [25], while simulate higher superficial warming in the tropics than observations [28]. These uncertainties can be related to the quantification of feedback strength because of their nonlinearity [27], incomplete or not entirely correct observations, internal variability, errors in model sensitivity and apportionment (between atmosphere, ocean and cryosphere) or spatial distribution (i.e. atmosphere/ocean height/depth) of the forced heating [25].

Among the previous causes, questions remain about the contribution of the poleward (PET) energy transport due to the link and competition with other phenomena (e.g. to what extent changes in atmospheric circulation are affecting temperatures in the Arctic and/or vice versa [230]), which can modify the magnitude and even the sign of the PET depending on the time [231] and location [230] considered. Most (not all) of the studies concerning the energy transport found a positive contribution to the AA [28]. PET can be divided in dry static energy (DSE) transport adnd moisture transport, whose influence on Arctic climate may diverge. Indeed, DSE transport could initially rise because of the CO_2 greater forcing at lower latitudes [28,232,233], but it decreases as the AA grows by weakening the meridional temperaure gradient [28,234]. Northward transport of moist energy, instead, increases [234,235] because of an enhanced latitudinal gradient (equator to pole) of specific humidity [37]. Moreover, the decrease of the meridional temperature gradient can also counterintuitively increase heat and moisture transport to the Pole by impacting the large-scale circulation at mid-latitudes [230,231,236–238], especially the Inter-tropical Convergence Zone (which is shifted northward [239]) and the synoptic-scale eddies [38] and planetary waves [37,39].

In general, mechanisms that preferentially heat lower latitude boost the PET [28], acting directly or indirectly (influencing feedbacks in Arctic) on the AA. Therefore, elements outside the Arctic can influence climate at higher latitudes through heating anomalies and consequent changes in PET. These include aerosols, whose role is one of the least clear aspects. Several studies focused on the aerosol contribution to the AA [7,240,241] and Schmale et al. [26] differentiated between local and remote effects. The former act within the Arctic itself and mainly concern: Arctic Haze [152], deposition and darkening of snow and ice [242,243], new particle formation [244], vertical distribution of primary and secondary aerosols [64] and aerosol-cloud interactions [219]. The local direct effect of LAA (transported or locally emitted) within the Arctic atmosphere, in particular around Svalbard, has been determined for this work

and is discussed in the previous chapter. Remote effect, intead, is related to PET and is the main topic of this chapter. It is induced by a variation in the atmospheric aerosol burden at lower latitudes that alters the energy balance from afar, which in turn influences the meridional heat transport and thus the AA [26]: additional energy (heat storage) at midlatitudes caused by relatively high LAA concentrations and/or reduced light-scattering aerosol concentrations is subjected to atmospheric transport northwards. It is therefore important to understand which of the two effects (local or remote) affects the Arctic climate the most. Total aerosol contribution to AA is due to an interplay (they may add up or hinder each other) of this two effects, but one of them is definitely greater than the other and thus prevalent in the AA?

Most of the studies related to this question are modeling ones [6–10,245] and are mainly focused on LAAs (in particular BC) and light-scattering aerosols (in particular sulfates) inside (simulating the local radiative forcing) and, especially, outside (simulating the remote effect via PET) the Arctic. Sulfates concentrations at mid-latitudes, in particular in North-America and Europe, decreased because of pollutant abatement policies, while atmospheric BC content slightly increased till 2009 [246,247]. In the following period (2009-2018), however, eBC concentrations over Central Europe also decreased. Coen et al. [248] conducted a worldwide multidecadal trend analysis of the aerosol optical properties and found that single scattering albedo (SSA) exhibited a postive trend mostly in Asia and Eastern Europe and a negative one in Western Europe and North America (i.e. the western part of the Northern Hemisphere), consistent with the mitigation policies. SSA-trends are a consequence of the scattering coefficient decreasing trends in Europe and North America (they were not statistically significant in Asia) and the absorption coefficient (related to LAA) trends (both positive and negative). Therefore, these changes in aerosol composition at lower latitudes and differences in scattering/absorption aerosol concentrations between mid-latitudes (and also tropics) and the pole affect the Arctic climate. For example, Hwang et al. [234] showed that BC in mid-latitudes and tropics is a source of heating and is thus responsible for an enhance PET at 70 °N. Moreover, Sand et al. [9] compared the BC remote influence on AA due to its forcing at mid-latitudes with the BC local forcing within the Arctic itself. Indeed, they analyze the Arctic climate response to BC perturbations in the Arctic (60–90 °N) and northern mid-latitude (28–60 °N) atmosphere and found that, despite competing phenomena occurs, the remote effect can contribute more to AA than the local effect because lead to an increased PET, causing a warming both at the surface and in the atmosphere. The simulated Arctic surface temperature response to BC was similar to an important previous work by Shindell and Faluvegi [6]. They also perturbed aerosol forcings at different latitude bands and demonstrated that remote aerosol

effect may have contributed 1.09 ± 0.81 K to the total Arctic surface warming of 1.48 ± 0.28 K.

However, there is discordance among the various modeling studies regarding the magnitude of this remote aerosol forcing and consequent temperature increase in Arctic. Navarro et al. [7] highlighted how the Arctic received 0.3 extra W m^{-2} via PET and warmed by 0.5 °C on annual average from 1980 to 2005 due to the health-connected mitigation policies. Ren at al. [8], instead, recently found an Arctic surface warming of 0.297 K (≈ 20% of the observed Arctic warming) since 1980 induced by the total effects of sulfate and BC, and as many as 0.25 K were due to changes in sulfate and BC concentrations outside the Arctic, in particular at mid-latitudes. Finally, Breider et al. [245] estimated that the aerosol emission reduction (sulfate + BC) between 1980 and 2010 is responsible for a net surface temperature increase in the Arctic of 0.27 ± 0.04 K (≈ 25%) through the PET from mid-latitudes. These discrepancies can be also due to underestimation of aerosol concentrations [8] and improperly modeled aging processes and/or boundary layer stability [9]. However, all models are in agreement on the role of aerosol remote forcing in PET over the past 20 years or so (when AA also showed a significant growth).

It is noteworthy that a contribution of the aerosol remote effect to the AA was determined only by a modeling approach and there is a lack of purely experimental measures. Some measurement campaigns were carried out (e.g. MOSAiC [86], ACLOUD/PASCAL [249], CRAICC [250] and CATCH [251]), but they were mainly focused on other research topic (without determining the LAA radiative forcing) and were bounded to the Arctic itself (without collecting data from Europe to Arctic). In order to fill this gap, we experimentally measured the LAA HR from Europe (Gdansk, 45 °N) to the Arctic Ocean (80 °N, North of Svalbard archipelago) via North Atlantic during 3 summer AREX campaigns (2018, 2019 and 2021; see section 2.1.2) on board the s/y Oceania (by IOPAN). We performed the same measurements (with the same experimental setup) also during a winter Baltic campaign at the beginning of 2022, in order to compute the LAA HR also in another seasoson. These data allowed to overreach the problem of a lack of representativeness of single monitoring stations in the Arctic with respect to the extension of the Arctic area [26,61,252], and can help to understand of how LAA influence the Arctic climate and provide experimental observations to improve the models.

Our data are mostly from the summer season and AA is stronger in fall and winter, as mentioned above. Nevertheless, summer is a key season because the warming is initiated in summer by an increase in incoming solar radiation as well as an enhanced atmospheric PET and oceanic transport. Aerosol remote forcing can therefore boost PET, which in turn contributes

to reduce sea-ice cover and trigger those feedbacks that lead to a transfer of heat from the ocean to the atmosphere and consequently to AA in fall and winter. Measurements were taken at the surface where BC has definitely a warming effect and can be considered representative of the mixing layer (which in higher summer, thus partially acquiring vertical significance as well). We have latitudinally extended the analysis by including HR data also from Milan, taken in summer of 2019 and previous years. Experimental HR measures can highlight the existence of a heat gradient between mid-latitudes and the Arctic, but from the ADRE we also computed the energy density (J/day m^3) added to the system by the LAA direct forcing along the route of the cruises (i.e. an energy gradient) and, with a few approximations, the energy (PJ/day) added within the mixing layer in 3 boxes at different latitudinal bands.

The specific methodology and reminders of some parts of the general methodology employed for this specific work are presented in section 6.2. Results and discussion follow in section 6.3.

6.2. Specific methodology

For this chapter, data from outward and return sections (Figure 64) of all three AREX summer (June – end of August) campaigns were used. In addition we performed the same measurements to infer the HR from the BALTIC winter (February) campaign (Figure 64, bottom right) too. Campaign routes (and path differences between years), accurate timelines, instruments and installation on board the s/y Oceania are explained in detail in chapter 2. Slight differences in the routes between AREX campaigns allowed us to cover a larger surface longitudinally (between 12.95 °W and 25.56 °E), enlarging the measurement area. The AREX latitudinal range was 54 – 80 °N, while it was 54 – 63 °N for the BALTIC campaign.

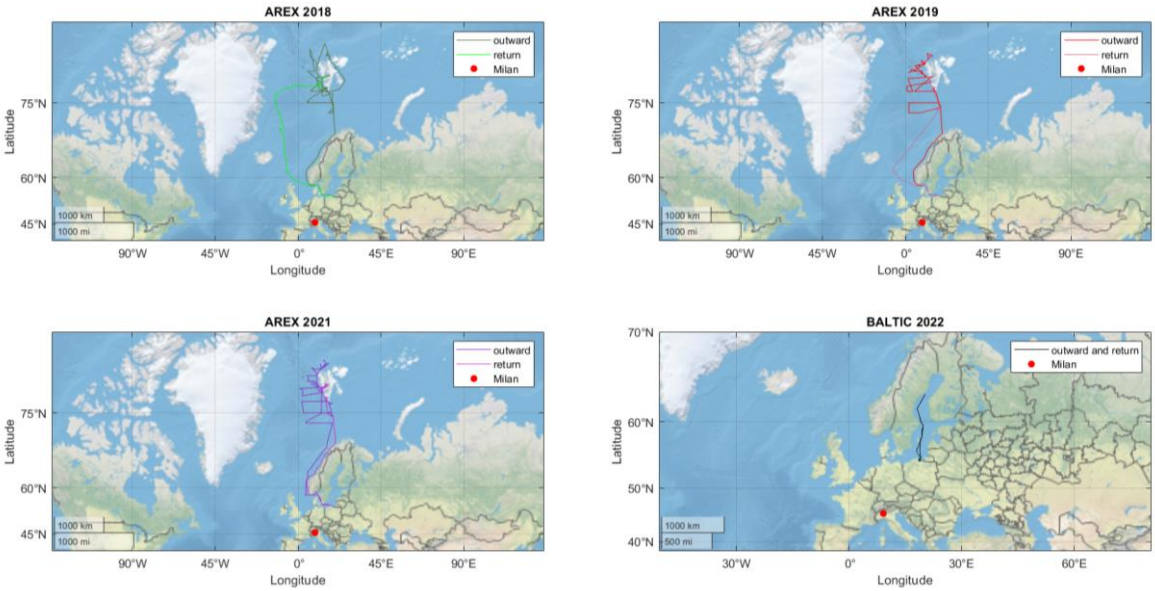

Figure 64. Outward and return routes of s/y Oceania for the AREX campaign (2018, 2019, 2021) and the BALTIC campaign (2022). Milan (red dot on the maps) is always reported too.

High temporal LAA absorption coefficients and radiation measurements allowed to compute the experimental LAA HR at 1 minute time resolution with the method described in section 2.5 [11].

The biggest difference is that in 2021, as already mentioned, only an automatic equipment was installed due to the SARS-CoV-2 pandemic. Therefore, there are no spectral radiation data from 2021. Consequently, average spectra (clear sky, cloudy and partial) from previous campaigns were used according to the type of sky on the day examined. As for the previous chapter, the same wind filter was employed to eliminate the influence of the ship's exhaust and only 2.4% of data (for all 4 campaigns) was removed due to the Oceania's tendency to sail headwind and the greater height of the chimney above the sampling line. Also in this case, LAA data were treated with a 30 minutes moving average (to smooth out the instrumental noise of the Aethalometer in the Arctic area) and were corrected using actual measured weather data (T, P and RH). Direct solar radiation values from SPN1 pyranometer were corrected to compensate the movement of the ship (using pitch, roll and yaw data). LAA concentrations reported below are those of eBC, but the HR was computed over the entire spectrum of the Aethalometer (370–950 nm, thus including all the LAA in the atmosphere).

HR data from Milan were also considered and the measurement site is shown in brief below. Moreover, also source apportionment results will be presented; thus source apportionment method is included in the next paragraphs. Finally, a new real-time methodology to infer C parameter directly from the k parameter computed by the AE33 is briefly introduced. It was used to calculate specific C parameters for each degree of latitude. HR latitudinal averages computed with a C_{fix} of 3.43 [253] were then compared with HR latitudinal averages computed with a different C for each latitude degree.

6.2.1. Milan measurement site

Aerosol and radiation measurements in Milan were performed on the rooftop (10 m above the ground level) of the U9-building (45°30'38" N, 9°12'42" E, Figure 65) of the University of Milano-Bicocca, Italy [253]. This sampling site ensures a full hemispherical sky view. In 2019 an Aethalometer AE33 was installed, while in the previous years an Aethalometer AE31 was used to infer LAA absorption coefficients. AE31 data were corrected by applying the Weingartner et al. [74,78] procedure to account for both the multiple-scattering and loading effects. Broadband (300–3000 nm) global, diffuse (obtained with the SPN1 pyranometer during the sampling campaigns) and reflected irradiance were measured using LSI Lastem radiometers (DPA154 and C201R, class 1, ISO 9060, 3% accuracy) [188]. A DPA154 global radiometer was equipped with a shadow band to infer the diffuse broadband irradiance.

Figure 65. *Roof of the U9 building at Bicocca University, Milan, where the measurement site is located*

Spectral irradiance data (obtained with the RoX system on board the Oceania) were collected using a multiplexer–radiometer–irradiometer (MRI) [90] which resolves the UV–VIS–NIR spectrum (350–1000 nm) in 3648 spectral bands (3648- element linear CCD array detector; charge-coupled device; Toshiba TCD1304AP, Japan) for both the downwelling and the upwelling radiation fluxes [188]. Up and downwelling spectra were measured simultaneously with two high-resolution HR4000 holographic grating spectrometers (Ocean Optics Inc., USA) after dark current for each measurement cycle. The instrument was equipped with a rotating shadow band to also obtain the spectra of diffuse irradiance. The reflected irradiance came from a Lambertian surface (which well represents the average spectral reflectance of Milan urban area) [11]

6.2.2. Source and species apportionment

Traditional source apportionment is based on the Aethalometer model, developed by Sandradewi et al. [68], which is founded on the following equations:

$$\frac{b_{abs}(\lambda_1)_A}{b_{abs}(\lambda_2)_A} = \left(\frac{\lambda_1}{\lambda_2}\right)^{-AAE_A} \tag{25}$$

$$\frac{b_{abs}(\lambda_1)_B}{b_{abs}(\lambda_2)_B} = \left(\frac{\lambda_1}{\lambda_2}\right)^{-AAE_B} \tag{26}$$

$$b_{abs}(\lambda_{1,2}) = b_{abs}(\lambda_{1,2})_A + b_{abs}(\lambda_{1,2})_B \tag{27}$$

A and B are two different sources, i.e. fossil fuel (FF) and biomass burning (BB). AAE_A, AAE_B, λ_1 and λ_2 are chosen in advance. For this work we used $AAE_{FF} = 1$ and $AAE_{BB} = 2$, while λ_1 and λ_2 are 470 nm and 950 nm, respectively. Then, Tian et al. [254] developed a method for the species (BC and BrC) apportionment, based on determination of $b_{abs}(\lambda)_{BC}$ considering

$b_{abs}(950)_{BrC}$=0 (i.e. no absorption by BrC at high wavelengths) and AAE_{BC} =1. Therefore, AAE_A (=AAE_{BC}) is chosen a-priori and only λ_2 (=950 nm) is used. $b_{abs}(\lambda)_{BrC}$ is inferred by subtracting the BC absorption from the total absorption and AAE_{BrC} is obtained accordingly.

Another more recent method can be employed for the source apportionment: Multi-λ fit approach reported in Bernardoni et al. [255]. In this method λ_1 and λ_2 are not chosen in advance, but all possible Aethalometer wavelengths are used by fitting $b_{abs}(\lambda)$ over the whole spectrum [253]. It is based on the following equation:

$$b_{abs}(\lambda) = A' * \lambda^{-AAE_{FF}} + B' * \lambda^{-AAE_{BB}} \quad (28)$$

where A' and B' are obtained by multi-λ fit of the input data, having already fixed AAE_{FF} and AAE_{BB} values (1 and 2, respectively).

6.2.3. C latitudinal parameter (in function of k)

Here we present a summary of the new theoretical model to infer C from the loading parameter k, recently developed by Ferrero et al. [256]. With this method we can obtain continuous values of C from the real-time k data and therefore compute dynamic C values in function of latitude. Drinovec et al. [66] defined R(ATN) as follows:

$$R(ATN)_{Drinovec} = (1 - k * ATN) \quad (29)$$

Collaud et al. [78], instead, slightly modified the equation by Weingartner et al. [74] by making R(ATN) linearly proportional to the Aethalometer ATN through the loading f parameter:

$$R(ATN) = \left(\frac{1}{f} - 1\right) * \frac{ATN}{50} + 1 \quad (30)$$

In the previous equation there is no loading (i.e. R(ATN)=1) if parameter *f* equals 1. If R(ATN)>1 (i.e. *f* >1), the loading effect is present. Therefore, for any value of $1/f$ <1 we can write:

$$\left(\frac{1}{f} - 1\right) * \frac{ATN}{50} + 1 = (f' - 1) * \frac{ATN}{50} + 1 = 1 - f'' * ATN \quad (31)$$

where *f'* =1/f is a value lower than 1; the last equivalence is obtained by posing (*f'* – 1)/50= -(1- *f*)/50=-*f''*, where *f''* is again <1. Therefore, now it is mathematically equal to the Drinovec et al. [66] definition:

$$1 - f'' * ATN = (1 - k * ATN) \quad (32)$$

f parameter is related to the aerosol single scattering albedo:

$$f = m(1 - SSA) + 1 \quad (33)$$

m is an empirical parameter defined by Weingartner et al. [74] and it is equals to 0.87 ± 0.10 and 0.85 ± 0.05 at the wavelengths of 450 and 660 nm, respectively. Moreover, Schmid et al. [257] found the following relationship between C and the single scattering albedo (SSA):

$$C = C_{ref} + \alpha \frac{SSA}{1 - SSA} \quad (34)$$

C_{ref} (i.e. the reference multiple-scattering filter parameter) depends only on the filter properties. Arnott et al. [258] defined α as the backscattered fraction of the aerosol collected on a filter tape, erroneously interpreted as absorption.

We can combine equations 31, 32 and 33 and solving in function of k:

$$k = \frac{m*(1-SSA)}{50*(m*(1-SSA)+1)} \quad (35)$$

Previous equation has some implications: if SSA=1, then k=0; if SSA<1, then k>0 leading to a R(ATN)>1. This is in keeping with the findings reported by Virkkula et al. [259]: the k values decrease by increasing the SSA. This poses the limitation to non-negative k values [256].

We can rewrite Eq. 35 in function of the SSA:

$$SSA_{AE} = \frac{m*(1-50*k)-50*k}{m*(1-50*k)} = 1 - \frac{50*k}{m*(1-50*k)} \quad (36)$$

The subscript "AE" (i.e. Aethalometer) is necessary, because SSA_{AE} is due to a complex interaction of aerosol particles and filter fiber matrix in the Aethalometer. In other words, SSA_{AE} is not the real or absolute SSA, but it is a useful parameter for linking the optical properties of the filter-particle ensemble to "k" with an empirical relationship.

Now, including also Eq. 34, we can write:

$$C_{AE} = C_{ref} + \alpha_{AE} \frac{SSA_{AE}}{(1-SSA_{AE})} = C_{ref} + \alpha_{AE} \frac{m*(1-50*k)-50*k}{50*k} \quad (37)$$

C_{ref} depends exclusively from the filter properties. The scattering fraction parameter (α), instead, is related to SSA (Eq. 34). Therefore, the C obtained from the k parameter of the AE33 (i.e. C_{AE}) is dependent from α_{AE}.

For a more detailed methodology, SSA_{AE} and C_{AE} determination, and environmetal implications of this new method we refer to Ferrero et al. [256].

Once the best combination of C_{ref} and α_{AE} values is chosen, C_{AE} can be determined from k. An important limitation is the presence of possibile negative values of k (which are sometimes seen, when aerosol with high SSA is collected). Values of k less than or equal to 0 means the absence of loading compensation. This case is found especially in remote areas (e.g. the Arctic),

where SSA is often close to 1 [160]. k_{AE} (i.e. the experimental loading value determined by the DualSpot algorithm) negative values are more frequent at longer wavelengths, because the absorption efficiency and the loading effect decrease with wavelengths. Therefore, is possible to used surrogate wavelengths shorter than 660 nm. Indeed, Ferrero et al. [256] found a good correlation between k at shorter wavelengths and k at 660 nm (R^2>0.98; they covarying with the same seasonal pattern), with the only exception of k at 370 nm. It is thus possible to use k values from 470 nm and above.

Latitude (°N)	C AREX	C BALTIC
54	2.62	2.37
55	2.46	2.39
56	2.27	2.40
57	2.22	2.46
58	2.62	2.53
59	2.43	2.53
60	2.64	2.55
61	3.49	2.56
62	2.78	2.57
63	3.45	2.57
64	3.41	
65	3.53	
66	3.72	
67	3.55	
68	3.43	
69	2.60	
70	3.79	
71	3.39	
72	3.51	
73	3.92	
74	4.21	
75	3.83	
76	3.88	
77	4.43	
78	4.42	
79	4.91	
80	5.74	

Table 4. *C values from AREX and BALTIC campaigns, computed from real-times k paramters. Data reported were obtained by averaging the C values inferred foreach latitudinal degree at shorter wavelengths*

Table 4 shows the C values we found by averaging the data obtained at shorter wavelengths with this methodology (especially in the Arctic there were several negative k values at the longer wavelengths) in function of latitude. We applied this method to both AREX and BALTIC. It is

noteworthy that the average C of the entire AREX campaign is 3.45, a value very similar to the C_{fix} (=3.43) we used to compute the absorption coefficients and the HR, instead of the default C of the AE33 (=1.57 or 1.39 in function of the filter tape). Moreover, C beyond the polar circle was 3.97, while C inferred beyond 70 °N (i.e. after Tromsø) was 4.19; these values are consistent with the C factor of 4.1 recently found in the Arctic area at the Zeppelin station (Ny Ålesund, Svalbard) [206] and used in the previous chapter to compute the HR in the Arctic region around Svalbard Islands. Finally, at 69 °N C dropped to a value very close to that found in Gdansk (54 °N), because of the presence of Tromsø, whose aerosol emissions are comparable to lower latitudes. C values for the BALTIC campaign, on the other hand, were lower than AREX (due to the different season and route, and lower latitudes) and quite similar to each other, with a slight but steady increase northward.

6.3. Results and discussion

6.3.1. LAA concentrations and HR from AREX campaigns

Figure 66 shows the latitudinal averages (at the resolution of one degree) of eBC. They include eBC values from the outward and return sections (see section 2.1.2 for a detailed analysis of the campaign routes) of all the three cruises. The relatively small values of the confidence intervals (computed at 95%) indicate the reliability of the latitudinal averages (there is enough consistency across sections and campaigns). It is clear that there was a latitudinal gradient in eBC atmospheric concentrations.

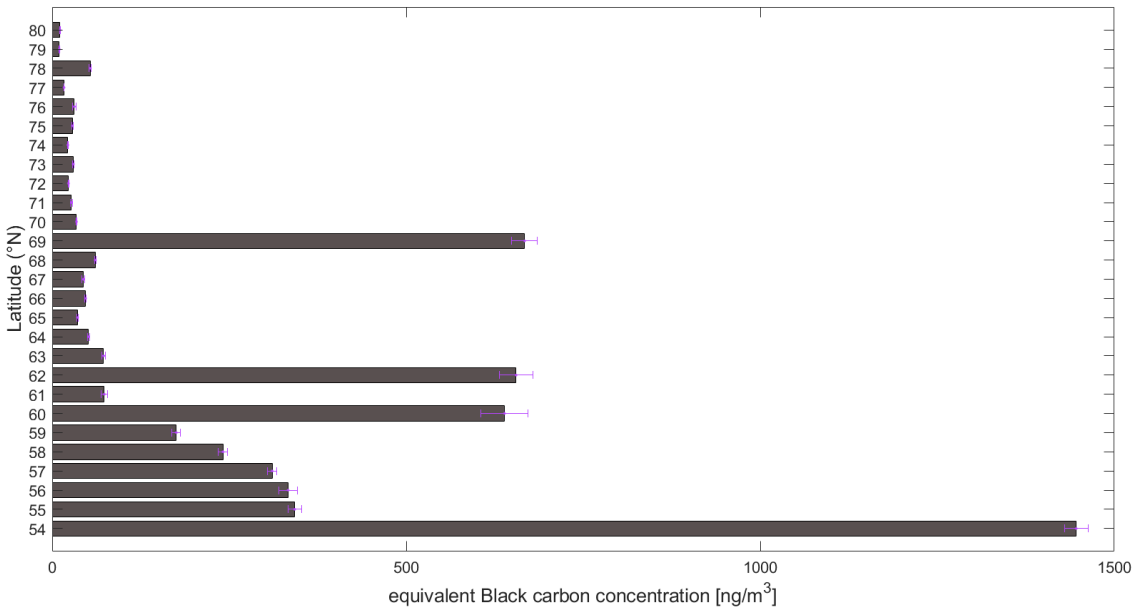

Figure 66. *eBC latitudinal averages from 54 °N to 80°N (North of Svalbard).*

The highest value (1446.2 ± 16.5 ng/m^3) was at 54°N, in the bay of Gdansk, followed by the values in the Baltic Sea and south coast of Norway areas. Here (55-58°N) average concentrations ranged from 342.5 ± 9.4 ng/m^3 (at 55°N) to 241.2 ± 6.6 ng/m^3 (at 58°N); these values are consistent with data (210 ng/m^3) reported by Sakerin et al. [260] as average of the North and Baltic Seas. eBC averages were lower (ranging from 35.8 ± 1.1 ng/m^3 to 72.6 ± 2.2 ng/m^3) in the latitudinal band of the Norwegian Sea, between 63°N and 68°N. Then, they further decreased in the stretch of sea between Northern Norway (beyond Tromsø) and Svalbard Islands (70–80°N) and the lowest values were reached at the highest latitudes (North of Svalbard): 9.9 ± 0.2 ng/m^3 and 11.0 ± 0.4 ng/m^3 at 79°N and 80°N, respectively. These latter data are perfectly in agreement with the average concentration (11.7 ± 0.1 ng/m^3) for pristine background conditions of the whole Arctic Ocean, computed in the previous chapter; they are also consistent with literature data already mentioned [181,184,213,214] and with the average BC concentration (5.96 ng/m^3) found in the central Arctic Ocean by Xing et al. [261].

The general trend of northward decline is interrupted locally, at some specific latitudes: 60°N, 62°N, 69°N and 78°N. Their particularly high BC concentrations are due to the fact that the ship stopped at the harbors of some cities and human settlements in the course of the outward and/or return section of one or more expeditions. The value at 78°N is influenced by the presence of Longyearbyen, whose specific emissions were analyzed in the previous chapter. Here the eBC average is 53.7 ± 1.3 ng/m^3. The Arctic area can be considered not beyond the polar circle (≈ 66°N), but from 70°N (i.e. beyond Tromsø), especially in our case where the Oceania often skirted Norway in the sea area below 69°N. Thus, the average for the entire Arctic area was 30.9 ± 0.6 ng/m^3. Although this value also includes some emission hotspots present in the Arctic (e.g., Longyearbyen and Jan Mayen), it is still significantly lower than values at lower latitudes, particularly those of the Baltic and North Seas. The average at 69°N, instead, included eBC concentrations of Tromsø (reached by the ship during the outward sections of 2018 and 2019), while average values at 62°N and 60°N included the emissions from Faroe Islands (Oceania stopped in Tórshavn during the return sections of 2019 and, especially, 2018) and Bergen, respectively. Bergen is the second most populated city in Norway and its harbor was reached by the ship only on the return section of AREX 2021.

Therefore, latitudinal averages are also the result of longitudinal differences: for example, sometimes, data were collected at the same latitude both from harbors/human settlements and sea areas and then averaged. In other words, latitudinal averages depend not only on the latitudes itself, but also on the longitude. The longitudinal differences between sections and years allowed to expand the measurement area (considering different sites at the same latitude) and thus have a more representative averages (because they incorporate different areas/sites and their inherent

differences within the same degree of latitude). Some of these differences can be seen from Figure 67, which shows the eBC concentrations along the routes of the three campaigns. The first panel represents AREX 2019 eBC values on a color scale between 0 and 1000 ng/m^3. Panel b shows the same campaign but on a reduced range, between 0 and 500 ng/m^3; in this way, differences over 500 ng/m^3 are flattened out, but AREX 2019 can be compared better to the other campaigns (AREX 2018 and 2021, panel c and d respectively), whose differences in eBC concentration are visible only on this scale (i.e. 0-500 ng/m^3; differences are flattened almost entirely on the scale 0-1000 ng/m^3).

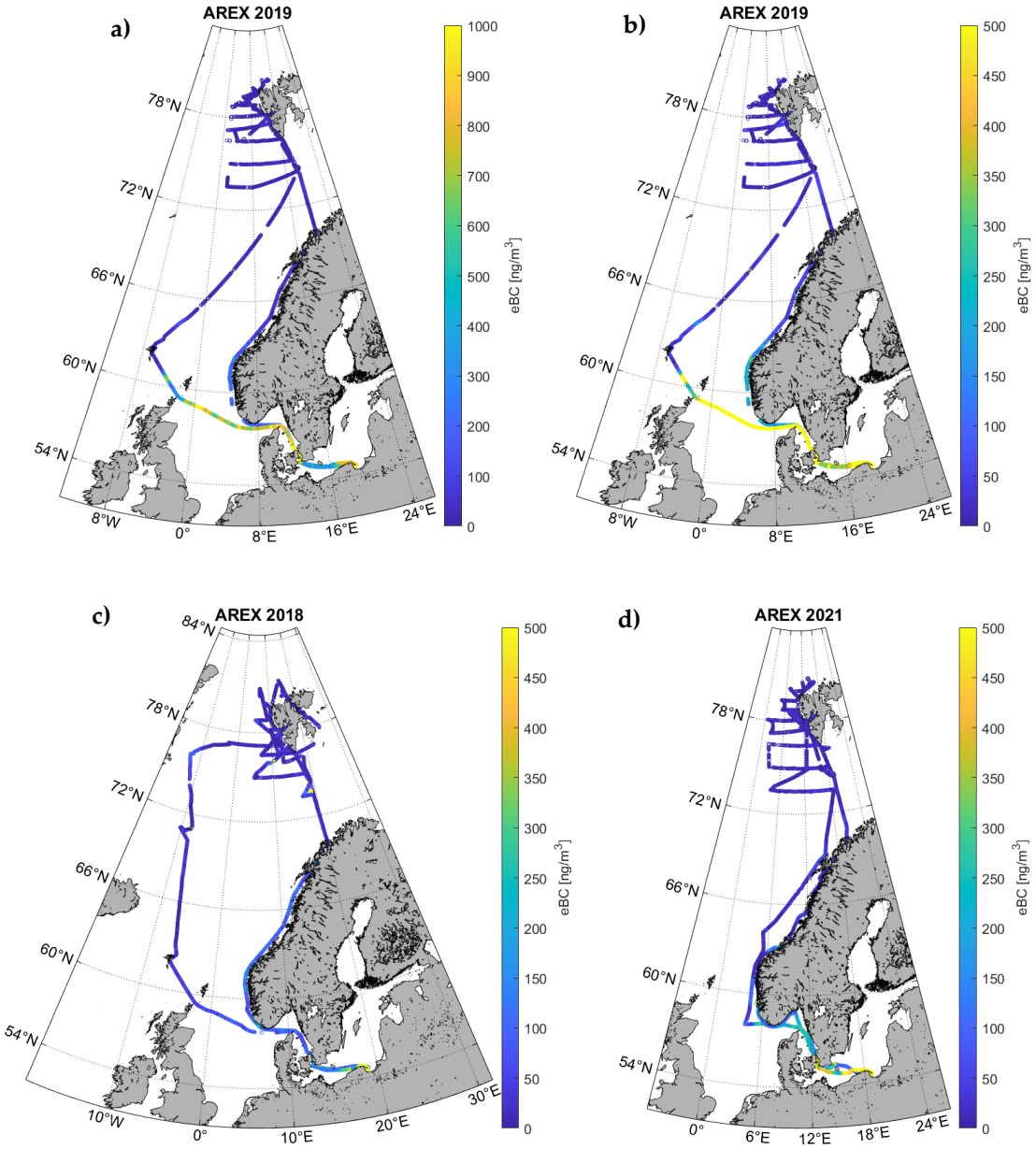

Figure 67. *eBC concentrations along the routes of the ship in 2019 (a, b), 2018 (c) and 2021 (d). Panel a shows eBC concentrations between 0 and 100 ng/m^3, while other panels show eBC concentrations from 0 to 500 ng/m^3*

These maps not allow to see the high concentrations in the hotspots (because of the low spatial resolution), but it emerges that eBC values in the Baltic area were higher in 2019 and 2021 than 2018, and that the stretch of sea between northern Great-Britain and northern Denmark showed higher concentrations during the 2019 return than during 2018. Lower concentrations in Gdansk were always found in June than in late August and early September. However, despite some inter-annual differences and some higher averages due to the presence of emission hotspots, the latitudinal trend is clear, with a sharp decline in eBC toward the pole.

Figure 68 represents the latitudinal averages of global solar radiation from all AREX campaigns, which ranged from 72.7 ± 2.7 W/m^2 (at 72°N) to 375.3 ± 9.4 W/m^2 (at 56°N). Average values of the entire campaign were similar for the three years (143.6 ± 1.0 W/m^2, 173.4 ± 1.2 W/m^2 and 153.6 ± 1.1 for AREX 2018, 2019 and 2021, respectively) and, despite higher maximum values during the outward sections (in keeping with the period of the year), there was no significant variation between outward section averages and return sections averages. Therefore, the discrepancy between different years and different sections was small. Instead, there was a latitudinal gradient of solar radiation, which decreased northwards.

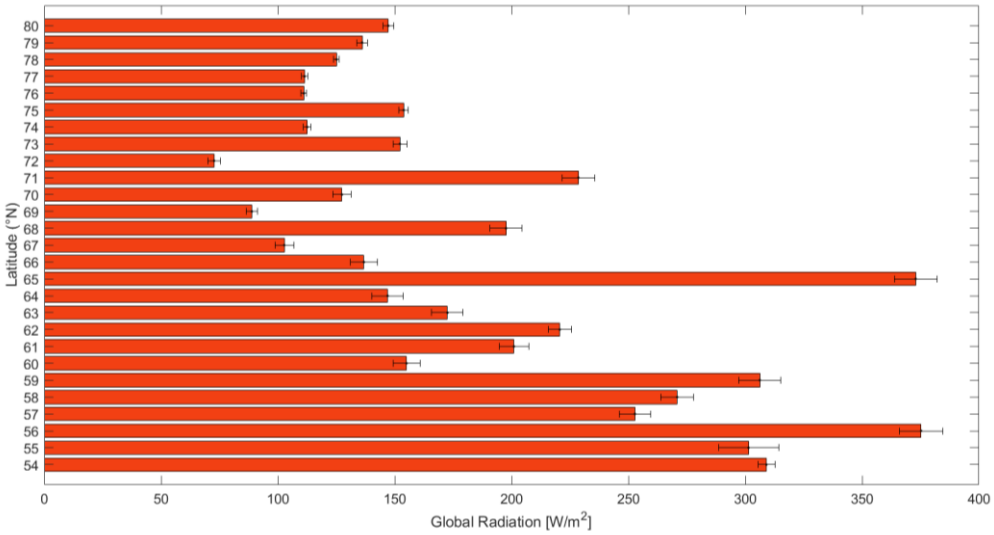

Figure 68. *Latitudinal averages of global radiation from 54 °N to 80°N (North of Svalbard).*

At the same time, the percentage of diffuse radiation increased polewards (blue bars in Figure 69). The contribution of diffuse component to the global radiation rose from 56.3 ± 0.66 % to 75.7 ± 0.61 % beyond 70°N. Thus, the role of diffuse radiation in the LAA HR in the Arctic region is prevalent and the completely experimental HR computation method we employed allowed to consider any sky condition (avoiding the errors induced by the clear-sky assumption, which can be present in some radiative-transfer calculations) and split the HR in function of the radiation components (Figure 70).

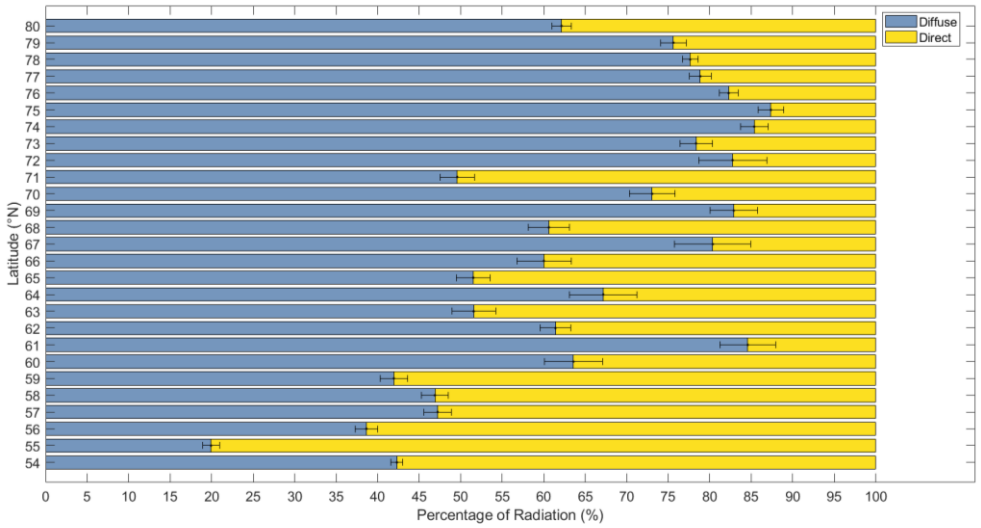

Figure 69. *Percentages of direct and diffuse component of global radiation as a function of latitude.*

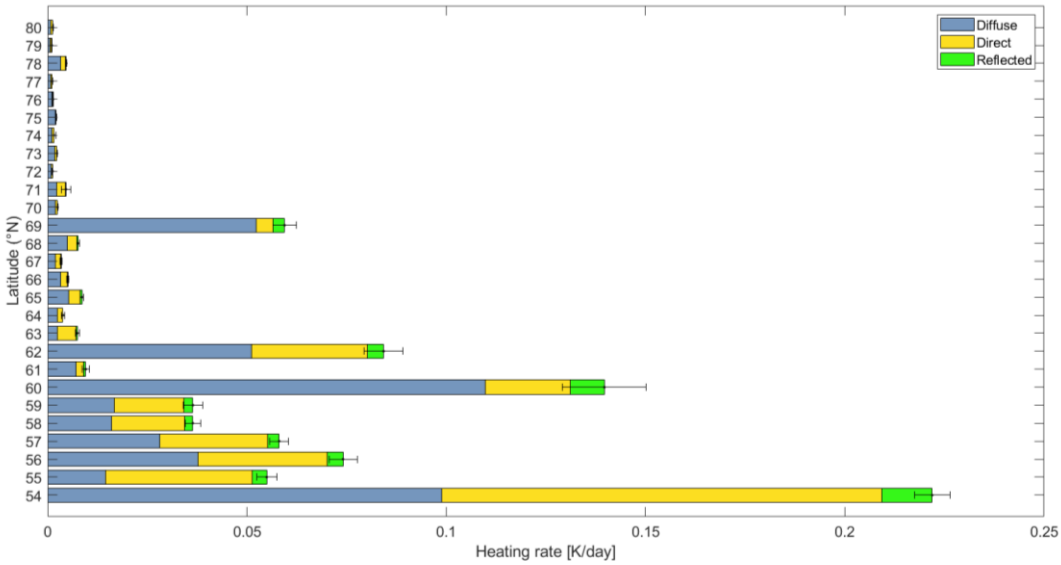

Figure 70. *Latitudinal averages of HR from 54 °N to 80°N (North of Svalbard). Total HR is the sum of direct, diffuse and reflected components.*

The clear latitudinal HR decrease northwards is a consequence of both the global radiation decrease and the sharp decline in LAA concentrations: the influence of LAA was prevalent, but the radiation values were responsible for some adjustments in the trend of HR compared with that of eBC. Indeed, for example, eBC concentrations at 69°N were slightly higher than concentrations at 62°N, which in turn were higher than those at 60°N. This trend was inverted in the HR averages due to radiation, with higher HR at 60°N (0.140 ± 0.010 K/day) and lower HR at 69°N (0.059 ± 0.003 K/day). Except for these two values, influenced by the presence of Bergen and Tromsø respectively, and the value at 62°N (0.084 ± 0.005 K/day) where Faroe Islands are located, the drop of HR between Gdansk and the Arctic (considered here from 70°N) was progressive. Average HR at 54°N was 0.222 ± 0.013 K/day (the highest value of the

entire campaign), while between 55°N and 59°N (i.e. Baltic Sea and south of Norway) the HR ranged between 0.036 ± 0.002 K/day and 0.074 ± 0.004 K/day. In the Norwegian Sea (between 60°N and 69°N, excluding the three hotspots) ranged between 0.009 ± 0.001 K/day (at 61°N) and 0.003 ± $2*10^{-4}$ K/day. Excluding Longyearbyen, HR in the Arctic ranged between $1.0*10^{-3}$ ± $3.4*10^{-5}$ K/day and $4.6*10^{-3}$ ± $1.2*10^{-3}$ K/day (at 71°N). However, all averages after the maximum value were less than $2.5*10^{-3}$ K/day. The minimum value was reached at 79°N (North of Svalbard), while at the northernmost point (80°N) the average HR was $1.3*10^{-3}$ ± $1.1*10^{-4}$ K/day. Therefore, there is a difference of 2 order of magnitude between 54°N and the Arctic. Also considering the value at 78°N ($4.7*10^{-3}$ ± $1.3*10^{-4}$ K/day), where Longyearbyen is located, which was the highest latitudinal average measured in the Arctic (we have also seen in the previous chapter that it is the main emission hotspots at those latitudes), the HR difference remains remarkable.

As expected from previous considerations on solar radiation, the contribution of direct radiation to total HR decreased toward the north, as well as the role of the reflected radiation. The diffuse component, instead, became even more relevant for total HR poleward.

In order to expand the analysis to lower latitudes, we can consider the HR calculated with the same methodology in Milan, one of the most polluted cities in Europe (located in the Po Valley). The average HR of the whole summer (from early June to early September) of 2019 was 0.49 ± 0.02 K/day (about twice the HR value at 54°N). It was achieved using an AE33 and a C value of 3.43 (as for AREX data). Moreover, Ferrero et al. [11] computed the surface HR in Milan in 2015 and found an average summer HR of 1.04 ± 0.01 K/day. However, they used an AE31 with the C value (2.14) found by Weingartner et al. [74]. Since the AREX HR (as well as in Milan in summer 2019) was computed by rescaling the results (obtained with the AE33 default C value [66]) with the C (=3.43) found by Ferrero et al. [253], then this HR value must also be rescaled with the C found with the same method for the AE31 (i.e. 4.44; see Table 1 in Ferrero et al. [253]). In this way we get the correct HR value for summer 2015, i.e. 0.50 ± 0.05 K/day, which is very similar to that of 2019. Therefore, including polluted areas in Europe, it seems that the difference in HR between the mid-latitudes and the Pole may be even greater. Looking at the HR values between Gdansk and North of Svalbard, values only in the Arctic (reported in the previous chapter) and values computed in different years in Milan, we can affirm that the LAA direct forcing is significantly greater at lower latitudes and thus can create an atmospheric heat storage at mid-latitudes.

Moreover, if we use the dynamic C values (reported in Table 4) to rescale the HR latitudinal averages (instead of C_{fix}=3.43), the difference between lower and higher latitudes is further emphasized, as can be seen in Figure 71. Indeed, C parameter tends to increase northward (due to

the aerosol properties) and consequently the HR decreased. All the averages in the Baltic and South of Norway area increased, while all the averages after Tromsø decreased with the only exception of the value at 71°N. All the values at the latitudes where human settlements are present (including Tromsø) rose, except Longyearbyen, i.e. the settlement in the middle of the Arctic, which dropped to $3.6*10^{-3} \pm 1.0*10^{-4}$ K/day. Lowest values remained at 79°N and 80°N, but decreased further to $7.3*10^{-4} \pm 2.4*10^{-5}$ K/day and $7.8*10^{-4} \pm 6.8*10^{-5}$ K/day, respectively. The average at 54 °N, instead, increased to 0.290 ± 0.016 K/day and the Baltic averages ranged between 0.048 ± 0.002 K/day and 0.112 ± 0.005 K/day with the new C values.

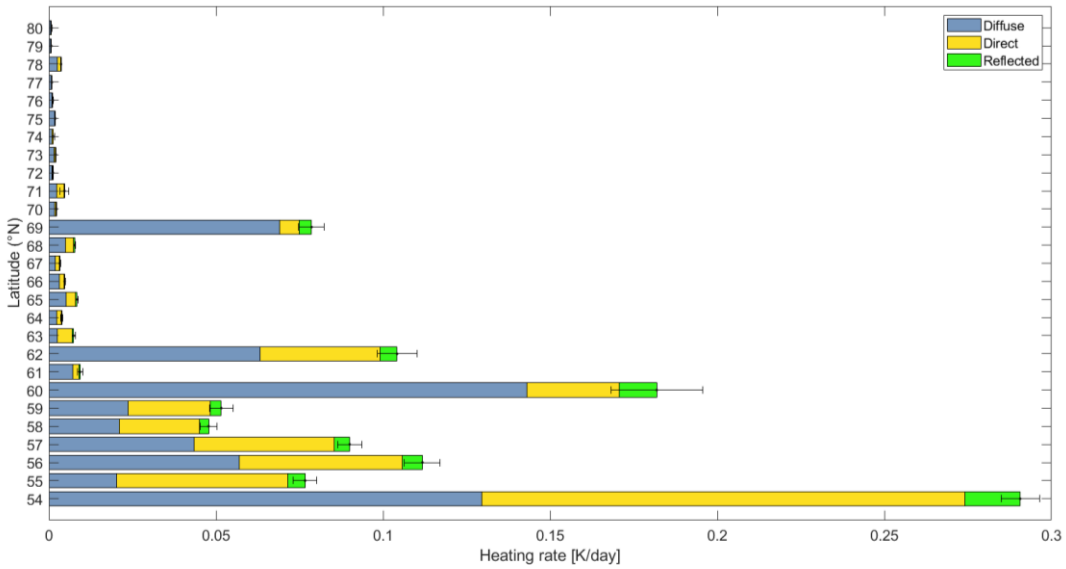

Figure 71. *Latitudinal averages of HR from 54 °N to 80°N (North of Svalbard). Total HR is the sum of direct, diffuse and reflected components. Latitudinal averages were rescaled with different C according to latitude*

Finally, the HR source and species apportionment were performed with the methods expained in section 6.2.2 (Multi-λ fit for sources and Tian method for species).

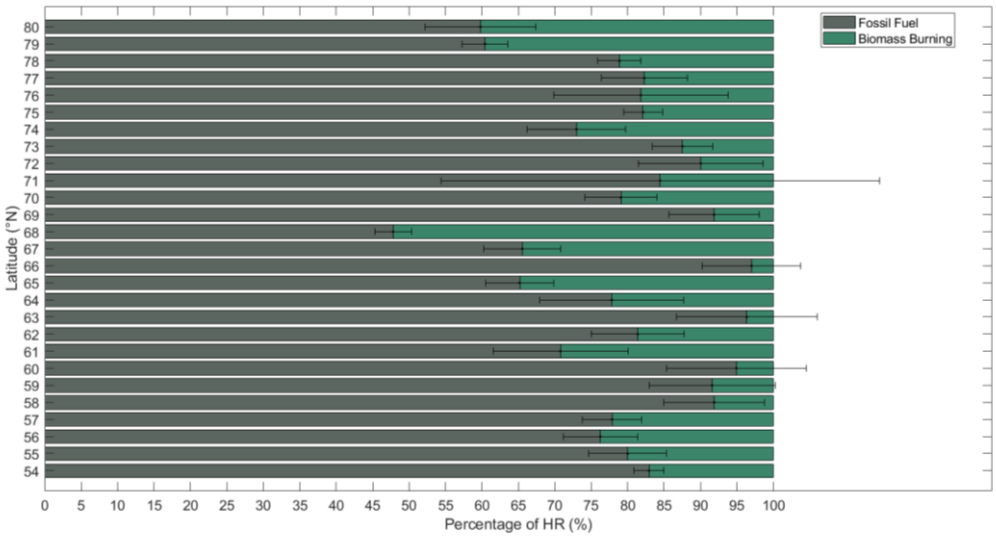

Figure 72. *Percentages of FF and BB on total HR as a function of latitude (source apportionment).*

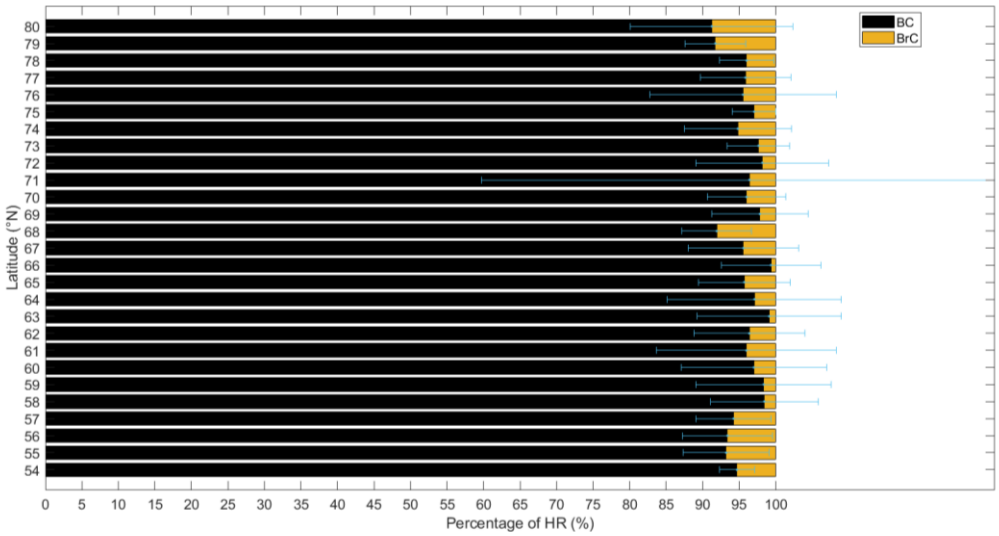

Figure 73. *Percentages of BC and BrC on total HR as a function of latitude (species apportionment).*

From Figure 72 and 73 is evident how there is no clear latitudinal trend in BB and BrC percentages. Except for 68°N, lowest FF contributions to the HR on average were at 79°N and 80°N (60.4 ± 3.2 % and 59.8 ± 7.6 %). There was a slight increase in the BB contribution in the Arctic (from 19.4 ± 1.7 % to 21.9 ± 3.3 % beyond 70°N), but it was highly variable from one latitude to another (there was no consistent behavior) and it was not statistically significant. In any case, the contribution of FF was dominant, with percentages well above 50% at every latitude degree except 68°N. The same behavior (even more marked) was found for BrC contribution to the HR, with dominant percentages of BC always above 90% and lowest BC percentage values (91.7 ± 4.1 % and 91.2 ±11.1 %) at 79°N and 80°N. The average BrC percentage below 70°N was 3.9 ± 2.0 %, while it was 4.5 ± 3.9 % in the Arctic.

6.3.2. Energy gradient between mid-latitudes and the Arctic

In addition to HR, the energy added to system by the LAA direct forcing can also be calculated from the ADRE (data reported here were computed using the C_{fix} of 3.43). So we can verify the existence of an atmospheric energy gradient between lower latitudes and the Arctic induced exclusively by the LAA. To compute the density of energy (J/m^3), the ADRE was multiplied by the seconds of irradiation in a day. In this regard we can use $J/m^3\ day^{-1}$ as the unit of measurement. Results are shown in Figure 74.

The difference between Northern Europe (Baltic and Norwegian sea area) and the Arctic region is evident (as expected from the HR latitudinal averages): the highest value was at 54°N (189.8 $J/m^3\ day^{-1}$); the values ranged between 33.6 $J/m^3\ day^{-1}$ and 65.3 $J/m^3\ day^{-1}$ in the 55-59°N latitudinal band, while ranged between 4.2 $J/m^3\ day^{-1}$ and 9.6 $J/m^3\ day^{-1}$ in the 63-68°N latitudinal band (Norwegian Sea area); in the Arctic (after 70°N) the energy density ranged from 1.3

J/m^3 day^{-1} (at 79°N) to 5.9 J/m^3 day^{-1} (at 78°N, where Longyearbyen is located), while the value at 80°N was 1.6 J/m^3 day^{-1}. Except 78°N and 71°N, all the Arctic values were below 3.2 J/m^3 day^{-1}. Also in this case we can use the average summer ADRE (relative to 2015) reported in Ferrero et al. [11] and the average ADRE computed in summer 2019 in Milan to compare the atmospheric energy density induced by LAA in a polluted site in Europe with results from other latitudes. ADRE from summer of 2019 was 6.43 ± 0.21 mW/m^3, while ADRE from summer of 2015 (rescaled for a C_{fix} of 4.44 [253]) was 6.71 ± 0.04 mW/m^3. By averaging the two (6.57 ± 0.11 mW/m^3) and multiplying by the irradiation time, we get 366.2 J/m^3 day^{-1} of energy.

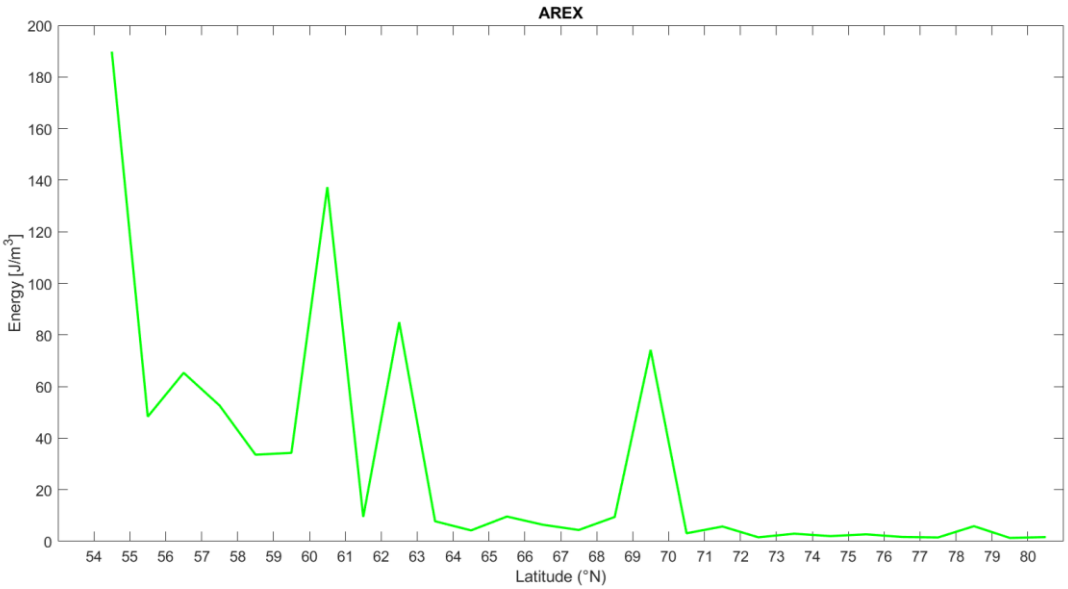

Figure 74. *Energy density gradient between 54°N and 80°N, induced by the LAA direct forcing. The results refers to the energy added (per cubic meter) in a single summer day.*

Again, there are two order of magnitude of difference between the mid-latitudes (Milan and Gdansk) and the Arctic (even considering the highest latitudinal averages). Thus, there is experimental evidence of a clear energy gradient between Europe and the Arctic, induced by the absorption of solar radiation by LAAs. As a result, the LAA species seem to influence the Arctic climate (i.e. AA) more through their remote forcing, rather than through the local forcing within the Arctic itself: they add much more energy in the atmosphere at lower latitudes, increasing the PET.

The prominent role of remote aerosol effects in the AA may decrease in the future due to emission reduction at lower latitudes and increased human activities in the Arctic as the climate warms.

We have already discussed the fact that ADRE and HR measurements can be considered representative of the mixing layer. Therefore, we also expand our considerations along the vertical direction to the height of the mixing layer (PBL). We used the reanalysis data from ERA5

to know the PBL height along the route of the ship (during the three campaigns). Then, we predefined 3 boxes, representative of the following areas (Figure 75): Baltic and Southern Norway/Northern Great Britain box; Norwegian Sea box; Arctic box. The first one is encompassed between 54°N and 60°N and between the minimum and maximum longitudes (18.96°W and 4.96°E) reached during the campaigns in that latitude range. The second one is encompassed between 61°N and 71.5°N and between the minimum and maximum longitudes (20.35°W and 10.36°E) within that latitudinal range. The last one is between 71.5°N and 81°N (the maximum latitude reached during the cruises) and between the minimum and maximum longitudes (25.57°W and 12.95°E) within that latitudinal range.

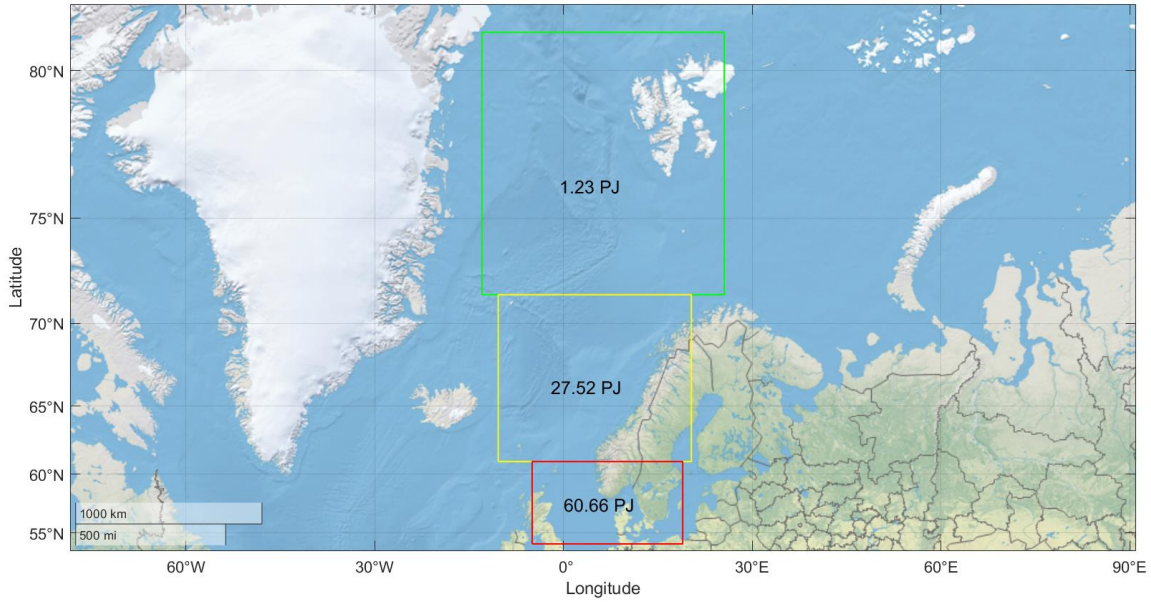

***Figure 75**. Energy added by LAA direct forcing within the mixing layer in the three areas marked on the map. The results refers to the energy added in a single summer day (June 21).*

The average ADRE (over the three years) of each box was multiplied by the average PBL and the surface of each box. The results were then multiplied by the average irradiation time in those specific areas on June 21, thus obtaining the PJ/day of energy added in summer by the LAA direct forcing in those areas within the PBL: 60.66 PJ/day in the first box, 27.52 PJ/day in the second one and 1.23 PJ/day in the Arctic box. Once again the difference between Northern Europe and Arctic is evident, highlighting the presence of a strong energy gradient and consequent PET.

Our HR and energy results relates to summer season, when AA is lower. However, as mentioned in the introduction and pointed out by Navarro er al. [7], summer is a key season during which additional heating can trigger the mechanisms that then lead to AA in the fall and winter. In summer arctic BC concentrations are lower (because of the lack of arctic haze) and, despite the presence of solar radiation, their local direct effect is not high; on the other hand (as

we have experimentally verified), their remarkable remote effect induces an energy gradient, which can lead to northward transport and surplus heat in the Arctic, which in turn contributes to ice melt and subsequent feedbacks responsible for AA. In winter short-wave radiation is minimal and thus the higher BC concentrations cannot act as direct forcer (their local direct effect is not present). However, they can have indirect effects, influencing the low-clouds formation, which in winter retain long-wave radiation emitted from the surface contributing to an increase in surface atmospheric temperature (their net effect in this season is positive because there is no short-wave radiation to reflect). Moreover, the lack of solar radiation and local HR means that there can still be a relevant latitudinal energy gradient (induced by LAA at lower latitudes), despite the higher LAA concentrations in Arctic. In order to start to verify the presence of an energy gradient even in winter and compare it to the summer gradient, in the next section we analyze the results from the winter campaign in the Baltic.

6.3.3. Winter HR and energy gradient

The BALTIC 2022 cruise departed from Gdansk and reached the northern Baltic Sea along a latitudinal vertical transect from 54°N to about 63.5°N (Figure 64), crossing some rather polluted areas (such as the gulf of Gdansk and the island of Gotland) and areas with little pollution (such as the northernmost points of the Gulf of Bothnia reached by the ship).

Figure 76 shows the latitudinal averages of: eBC concentrations, global solar radiation, percentages of diffuse radiation on the total, LAA HR (divided in direct, diffuse and reflected components). eBC concentrations at 54°N were 1497.8 ± 33.4 ng/m^3, a value very similar to the average AREX concentration. So there seems to be no significant variation between summer and winter in the bay of Gdansk. Then, there was a progressive decrease from 55°N (988.4 ± 62.6 ng/m^3) to 57°N (414.8 ± 10.1 ng/m^3, near Gotland Island) but concentrations remained significantly higher than the summer averages in the same latitudinal range, due to the different season and sector of the Baltic Sea. Beyond 57°N there was a considerable drop in the eBC values, with a negative trend from 58°N (132.6 ± 7.6 ng/m^3) to 63°N (18.4 ± 0.3 ng/m^3). The minimum value was 16.1 ± 0.6 ng/m^3 at 62°N. Average concentrations between 59°N and 61°N (75.1 ± 1.3 ng/m^3 – 37.5 ± 1.3 ng/m^3) were comparable with those found during summer in the Norwegian Sea (63°N – 68°N), while eBC averages at 62°N and 63°N in the Baltic were quite low and similar to that found at higher latitudes (after Tromsø) in AREX cruises. Therefore, there was a larger eBC drop in a shorter (latitudinal) transect than AREX, with higher concentrations at lower latitudes and lower concentrations from 58°N.

Global solar radiation trend was quite constant with a slight increase northward, while the percentage of diffuse component decreased at the higher latitudes (62°N and 63°N), an opposite

behavior to summer AREX data. Except for 60°N, incoming solar radiation ranged from 64.0 ± 4.3 W/m^2 to 146.1 ± 4.4 W/m^2. These values were lower than AREX, in keeping with the different season. We measured slightly higher data further north, but of course the radiation would have dropped close to 0 if we were above the polar circle. As evident from Figure 76, radiation data were missing at 55°N and 61°N. The reason is that in some sections the ship sailed quite fast (also because of stormy weather), influencing the availability of radiation data. Indeed, in this season and at those latitudes sunlight is present for only a few hours a day. Thus, the Oceania, proceeding quickly and without stopping, traveled some stretches in the hours of darkness. Bad weather, along with the presence of ice, is also the reason why we did not go beyond 63°N, without reaching the polar circle.

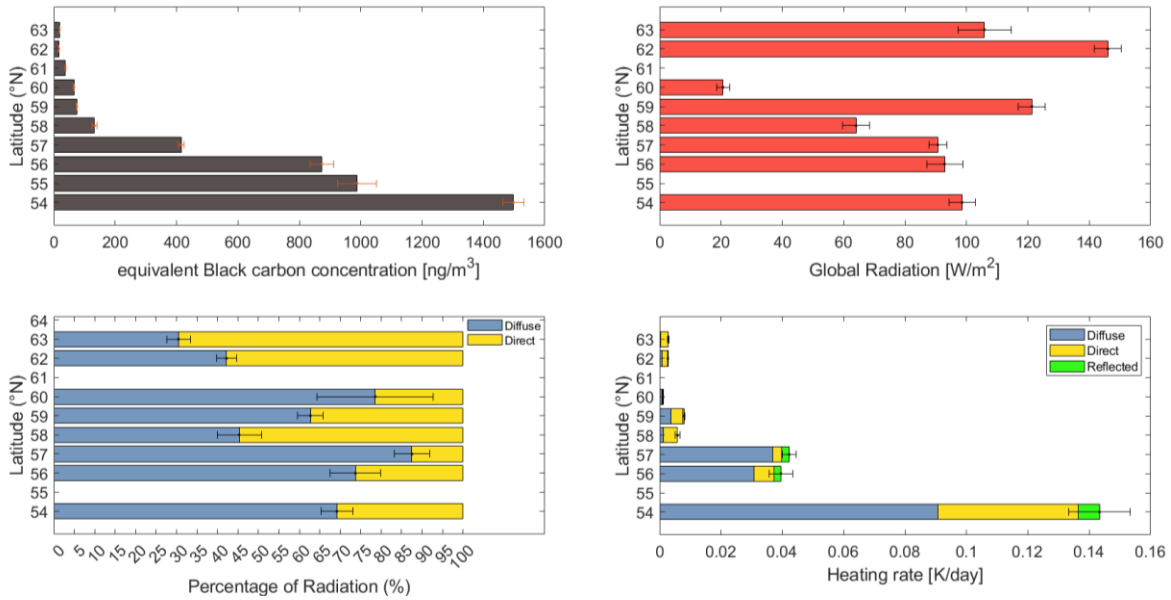

Figure 76. *Latitudinal averages of eBC, global radiation, percentages of diffuse/direct radiation and HR (divided in direct, diffuse and reflected components) during the BALTIC campaign.*

From LAA absorption coefficients and radiation measures we computed the HR. The HR trend generally followed that of eBC latitudinal averages, with the highest values at 54°N (0.14 ± 0.01 K/day), followed by the values at 56°N and 57°N. Then there was a sharp decrease from 58°N and the HR was 0.003 ± 3*10^{-4} K/day at 63°N, i.e. the highest latitude reached. As visible from the average HR at 54°N (where AREX and winter eBC averages were very similar, but HR was higher in summer), HR values were lower at the same eBC concentration due to the lower solar radiation.

The HR source apportionment (Figure 77) showed an opposite trend to AREX: during summer campaigns the BB percentages, albeit slightly, increased northward; in this campaign, instead, the BB contribution to the total HR decreased with latitude and especially it was signif-

icantly greater at lower latitudes, with BB percentages over 60% at 56°N and 57°N. This difference could be attributable to increased burning of biomass for heating, because of the winter season.

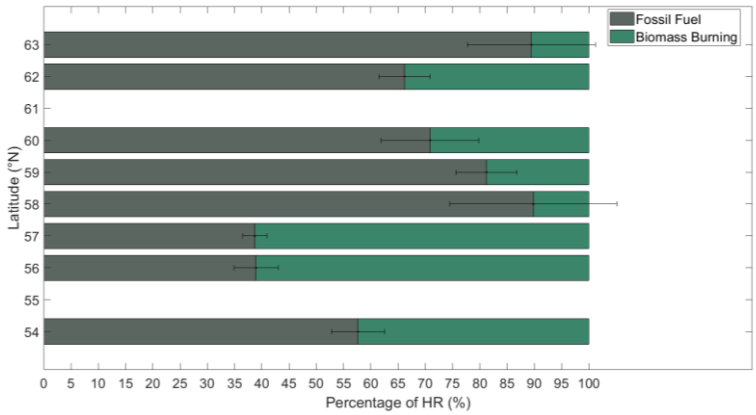

Figure 77. *Percentages of FF and BB on total HR as a function of latitude (source apportionment).*

Also in this case, the HR values were rescaled using different C in function of latitude (Table 4) instead of C_{fix} (3.43) and results are shown in Figure 78. However, all new C values were below 3.43 (they ranged from 2.37 to 2.57) and all the latitudinal HR averages increased. Moreover, C increased a little northward. Therefore, the increase in proportion has been about constant at all latitudes. In other words, using dynamic C, the HR increased at all latitudes and the difference (HR gradient) between lower and higher latitudes increased very little.

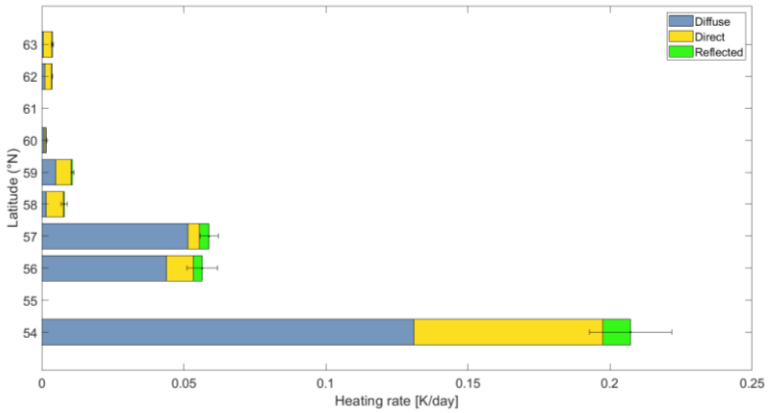

Figure 78. *Latitudinal averages of HR from 54°N to 63°N (BALTIC campaign). Total HR is the sum of direct, diffuse and reflected components. Latitudinal averages were rescaled with different C according to latitude*

Obviously the absence of radiation at some latitudes (due to the causes mentioned above) affected the calculation of HR, which was not present at those specific locations. Looking at the data in more detail with higher spatial resolution, we found the latitudinal ranges where there was no sensible correlation between ADRE (and HR) and eBC concentrations, because of the unreliable radiation values: from 55°N to 56.5°N, from 58°N to 58.5°N and from 60.5°N to

62°N. Therefore, we decided to average the ADRE and HR values in 4 macroregions, containing diurnal data and representative of some specific areas: Bay of Gdansk (54°N – 55°N), Gotland (56.5°N – 58°N), Åland Sea (58.5°N – 60.5°N) and Gulf of Bothnia (62°N – 63.5°N). Figure 79 shows the HR averages (computed with C_{fix} = 3.43, the same of AREX) for these areas (red boxes on the Baltic map) on the right, while the AREX HR averages in the same latitudinal bands are shown on the left for comparison. AREX HR averaged data are only from the AREX outward sections, because the outward transects were closer to the Baltic longitudinally than the return transects (as visible from the map on the bottom left of Figure 79). HR averages are indicated on the maps. In the first range, HR values were similar (slightly higher those of AREX, despite lower LAA concentrations). Also in the second one were similar, but slightly higher in Gotland area (higher LAA concentrations were still balanced by the lower winter radiation). From the third latitudinal band the HR averages began to differ and be lower in the Baltic. This was not only due to the smaller radiation, but mainly due to the rapid decrease in LAA concentrations. Indeed, the difference between AREX and BALTIC was maximum in the northernmost latitudinal range, because LAA concentrations fell faster moving northward in the BALTIC than in AREX. The average HR in the Gulf of Bothnia was 0.003 ± $1*10^{-4}$ K/day, about an order of magnitude lower than the HR found at the same latitudes during AREX. Moreover, this value is comparable to those found in the Arctic in summer. Although we have not measured it, the HR after the polar circle is 0 in winter by definition due to the absence of solar radiation.

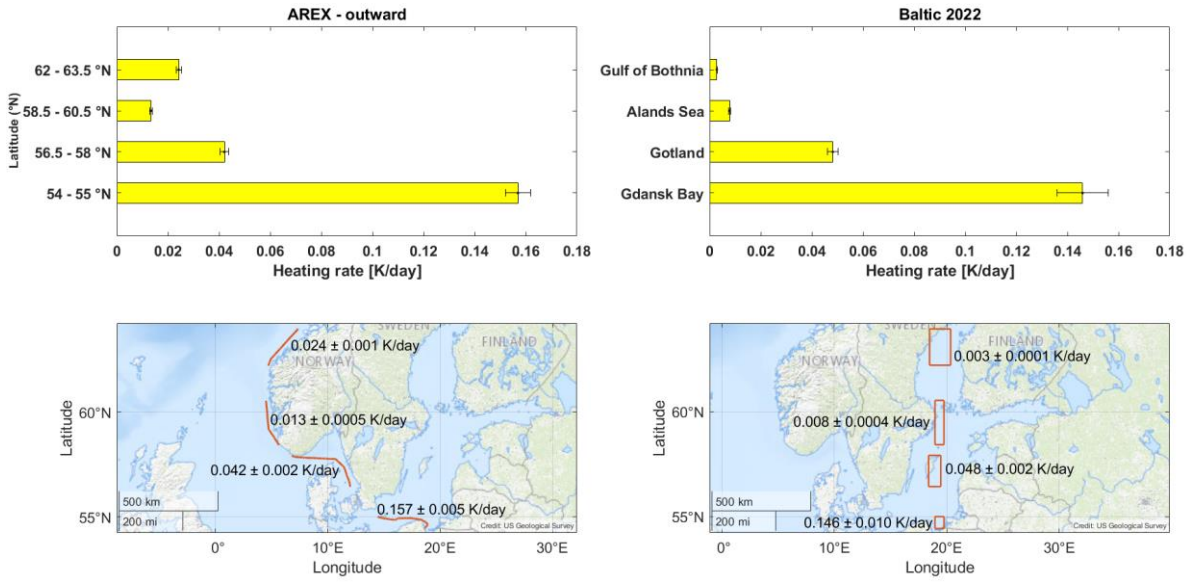

Figure 79. *Averages of HR in the same four latitudinal bands for AREX outward (left) and BALTIC (right) campaigns.*

Therefore, it seems that, at least along the Baltic, there is a winter HR gradient between Gdansk and the Arctic, which develops over a shorter latitudinal distance. Clearly this is a limited area (covering a narrow longitudinal distance and confined to the Baltic Sea) and a single campaign, which lasted much less than an AREX campaign. However, this first results, combined with the rather high LAA HR values measured in winter at the tropics, suggest us the possible presence of a HR gradient between lower latitudes and the Arctic even in winter, given also the absence of short-wave radiation in the Pole. This aspect should be better investigated in the future, notwithstanding the greater difficulty in carrying out winter campaigns.

Finally, from the ADRE we calculated the energy density for this campaign as well. The computation was done only for the 4 areas mentioned earlier, using the seconds of sunlight present on the days we crossed those latitudinal bands. The energy gradient and related values are shown in Figure 80. The value in the Botnia Gulf is very low, as much as those found in the Arctic at higher latitudes in summer. Therefore, also in winter an energy gradient induced by the direct effect of LAA was present: again there was a significant difference between 54°N (where we found the maximum value) and 63°N. However, the winter value in Gdansk was about half of the summer value. Therefore, despite the higher LAA winter concentrations (and only if mid-latitudes are considered, not the tropics) the PET induced by LAA seems greater in summer. Indeed, currently, the presence of light in the Arctic (in summer) seems to have little influence, as the HR is low anyway (because of low LAA concentrations). Conversely, the solar radiation has an important role in increasing HR at mid-latitudes in summer and is thus responsible for a greater gradient than in winter.

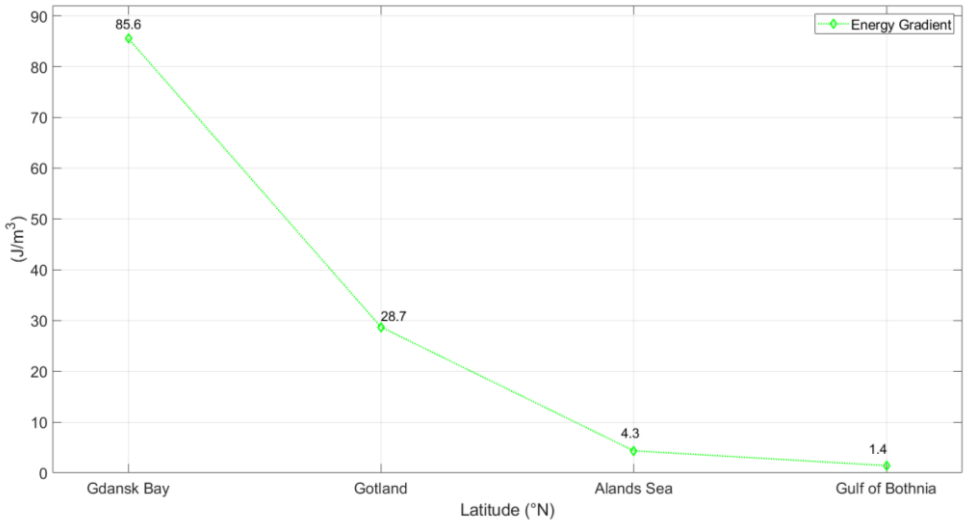

Figure 80. *Energy density gradient between 54°N and 63°N, induced by the LAA direct forcing. The results refers to the energy added (per cubic meter) in a February (winter) typical day.*

6.4. Conclusions

LAA concentrations and absorption coefficients, as well as solar radiation were measured between mid-latitudes and North of Svalbard for three years, in the summer of 2018, 2019 and 2021 on board the s/y Oceania. The same measurements were performed also during a winter campaign (2022), which took place in the Baltic between Gdansk and the Gulf of Botnia.

These data allowed to compute the LAA ADRE and HR at high time and spatial resolution, investigating the latitudinal differences in an entirely experimental way for the first time. From the ADRE the energy gradient (J/m^3) between Northern Europe and the Arctic and the joule of extra energy added within the PBL in three different areas by the LAA direct forcing were also determined. Indeed, the main goal was to verify the existence of an increased energy gradient and consequent PET due to the LAA remote effect and compare it with LAA local effect in the Arctic.

There are several causes and feedbacks beyond the AA, which are strongly interconnected, and the contribution of each of them is still not entirely clear. PET is one of the mechanisms that can influence the Arctic surface atmospheric temperature. While the moisture transport northward is generally considered positive, major uncertainties concern the contribution of dry static energy transport. It is enhanced or reduced by feedbacks which alter the meridional gradient of atmospheric heating: they can preferentially heat the Arctic (negative effect on PET) or they can preferentially heat lower latitudes (positive effect on PET) [28]. Some aerosols directly affect the energy budget by reflecting or absorbing solar radiation. Since the intensity of this effect depends on their concentration, which is not homogeneous over the earth, they may cool or warm the atmosphere differently at different latitudes, influencing the PET. This is the reason why we aimed to measure the LAA HR along south-north transects.

Role of aerosols in this mechanism is one of the less clear aspects. Most of the studies are modeling and found that aerosol remote effect contributed more to AA (via PET) than the local effect, due to sulfates reductions (in recent decades) and eBC forcing at lower latitudes. However, there is discordance among the various modeling studies regarding the magnitude of this remote aerosol forcing and consequent temperature increase in Arctic and there is a lack of purely experimental measures. Our results want to begin to fill this gap.

In summer we found a clear latitudinal negative trend in eBC atmospheric concentrations, which were higher at Gdansk and in the Baltic Sea and Southern Norway areas (from 1446.2 ± 16.5 ng/m^3 at 54°N to 241.2 ± 6.6 ng/m^3 at 58°N) and then gradually decreased to the Arctic, where they were very low (11.0 ± 0.4 ng/m^3 at 80°N). This trend was interrupted only at some specific latitudes, where the ship stopped at the harbors of some human settlements (e.g. Tromsø and Longyearbyen). Global solar radiation diminished northward, while the percentage

of diffuse component increased, highlighting the role of diffuse radiation in the Arctic and the importance of HR determination in any sky condition (as we have accomplished through experimental measurements). Latitudinal trend of LAA HR followed the behavior of eBC and radiation: diffuse radiation contribution to total HR was the highest and became more relevant in the Arctic; despite local interruptions, there was a sharp decline in northward HR. The difference between Gdansk (0.222 ± 0.013 K/day) and the Arctic and between the Baltic area (from 0.036 ± 0.002 K/day to 0.074 ± 0.004 K/day) and the Arctic was two and one order of magnitude, respectively. Indeed, HR at 80°N was $1.3*10^{-3} \pm 1.1*10^{-4}$ K/day and also considering HR at 78°N ($4.7*10^{-3} \pm 1.3*10^{-4}$ K/day), where Longyearbyen is located, the gap remained remarkable. When we included also Milan (summer HR ≈ 0.5 K/day) in the analysis, i.e. a polluted city in central-south Europe, this trend became more pronounced. The same thing happened using different C values in function of latitude, instead of a C_{fix} (0.290 ± 0.016 K/day at 54 °N and $7.8*10^{-4} \pm 6.8*10^{-5}$ K/day at (80°N).

As a result, the density of energy added to the system from mid-latitudes to North of Svalbard was always less moving northward (from 366.2 J/m^3 day^{-1} in Milan and 189.8 J/m^3 day^{-1} at 54°N to 1.6 J/m^3 day^{-1} at 80°N), demonstrating the presence of a great surface energy gradient, induced by LAA remote effect, which can increase the PET. Therefore, the greatest influence of LAA on AA appears to be due to remote forcing and not lo local forcing. These results were expanded vertically within the mixing layer, considering 3 areas: one that encompasses parts of the Baltic, Southern Norway and Northern Great Britain; another one in the Norwegian Sea and the last one in the Arctic. The energy added on a single summer day by LAA forcing in these 3 boxes were 60.66 PJ/day, 27.52 PJ/day and 1.23 PJ/day, respectively.

Winter data from the BALTIC campaign suggested the presence of an HR and energy gradient also in winter, at least in the Baltic sector. Indeed, HR in 4 key areas (Bay of Gdansk, Gotland, Åland Sea and Bothnia Gulf) showed a negative northward trend. Despite higher eBC concentrations than in winter, HR at lower latitudes was similar to summer due to the lower radiation. However, already at 63°N HR ($0.003 \pm 1*10^{-4}$ K/day) was similar to summer Arctic values because of the rapid decline of LAA concentrations, while obviously it tends to 0 beyond the polar circle due to the polar night. Therefore, there was a winter HR gradient in a shorter latitudinal distance. However, the shorter irradiation time is responsible for a reduced energy gradient when ADRE at lower latitudes is converted to energy (at equal HR) in winter. Indeed, although the value is almost 0 in the Arctic, energy density at 54°N (85.6 J/m^3 day^{-1}) was about half that in summer.

Winter results come so far from only one short campaign, limited to the Baltic. The first comparison with summer data, however, suggests that an energy gradient induced by LAA between mid-latitudes and the Arctic exists also in winter, but is lower than in summer, when a greater PET may thus be present. Despite AA is larger in fall and winter, an increased summer PET can play a key role in AA, because the extra heat contributes to an enhanced melting of sea ice, triggering those feedbacks that then lead to AA in the following seasons.

Other summer and, especially, winter campaigns should be conducted in the future over a wider area to better understand the seasonality of the energy gradient. A future use of more accurate C parameter as a function of latitude and study region will help determine the HR gradient more accurately. Moreover, the study area can be expanded to continental Europe with a hybrid approach, using also eBC reanalysis data. Our entirely experimental data may ultimately be useful for comparison with results from models and to improve the models themselves.

Local feedbacks, such the feedbacks related to sea-ice, are partly determined by PET changes [28] (e.g. changes in aerosol direct forcing), but they in turn affect PET. In other words, as AA proceeds, the general atmospheric transport of dry energy northward will be inhibited in the future. Moreover, whether summer LAA emissions in the Arctic will increase, the local LAA direct forcing (HR) will also rise. This phenomenon, along with a reduction in emissions at mid-latitudes, will decrease the energy gradient and transport northward. Therefore, the current relative weight of aerosol local and remote effects may change: the prominent role of remote effects in the Arctic climate may decrease, while that of local effects may increase in the future. The interplay between local and remote forcing can change over time, as well as the intensity of the AA itself and it is thus important to better understand and continue to monitor these phenomena.

7. Future perspectives

In this last short chapter, we discuss the future prospects of this research. As already mentioned, further campaigns in the Arctic should be carried out to continue to collect data, even in the winter season, expanding the measurement area. However, some initial steps have already been implemented, which can be included in the next upcoming studies. First of all, a drone equipped with miniaturized instrumentation for LAA HR determination was developed. It will allow the HR measurement to be extended along the vertical direction beyond the mixing layer. HR measures have also been conducted in the past few months at the Jungfraujoch station, in the free troposphere. Finally, aerosol and radiation measurements were performed last year also in the Antarctic and this data will allow the first experimental study of LAA HR in this region and a comparison with the Arctic.

7.1. Drone for HR measurements

In the last two years we equipped and integrated a drone with a set of miniaturized instruments for aerosol and radiation measurements, in order determine the LAA HR also along the vertical direction (3D measurements) with the same fully experimental methodology [11] used in this wotk. Indeed, this method can be applied to any atmospheric layer if the absorption due to reflected radiation from the underlying layers is also considered.

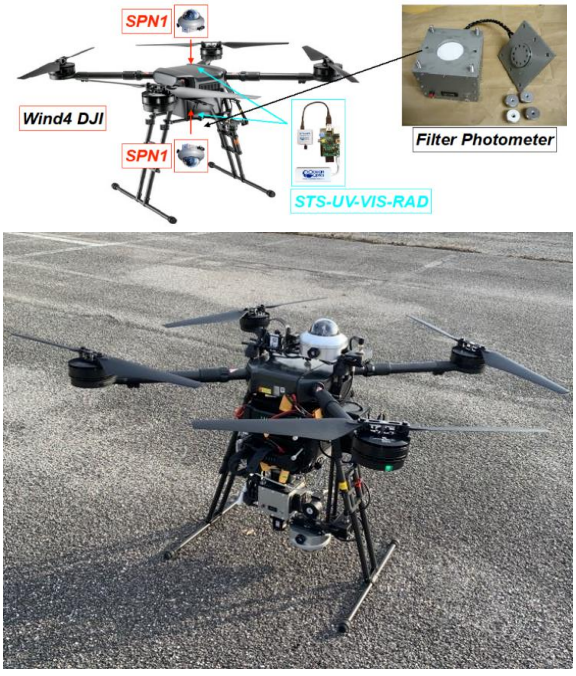

Figure 81. *UAV model DJI WIND4, equipped with miniaturized instruments for the HR determination*

The modified drone is an aircraft UAV model DJI WIND4 (Figure 81) and it was equipped with:

- one Partector 2 (by Naneos, Switzerland) for nanoparticle concentration;

- one filter absorption photometer model FAP-3 (by HAZE Instruments, Ljubljana, Slovenia) for eBC atmospheric concentrations and absorption coefficients (Figure 82a-b); it works at 3 wavelengths (467, 529, 653 nm) and it can sample on 8 different spots (Figure 82c) of the filter (47 mm filter, Azumi 371M), while other 2 spots are used as blanks;
- two (up and down) broadband pyranometers (SPN1, DELTA-T) for absolute values of global, diffuse and drect (by subtraction) radiation (Figure 82d);
- two micro-spectroradiometers (Ocean Optics, SVS-VIS-RAD, up and down) with their respective shadowbands for spectral measurements of global, diffuse and reflected radiation (Figure 82e);
- one meteorological sensor (DELTA-T) for atmospheric temperature, pressure and relative humidity;
- one Camera Zenmuse X3 for high resolution RGB images and surface digital model (Figure 82f).

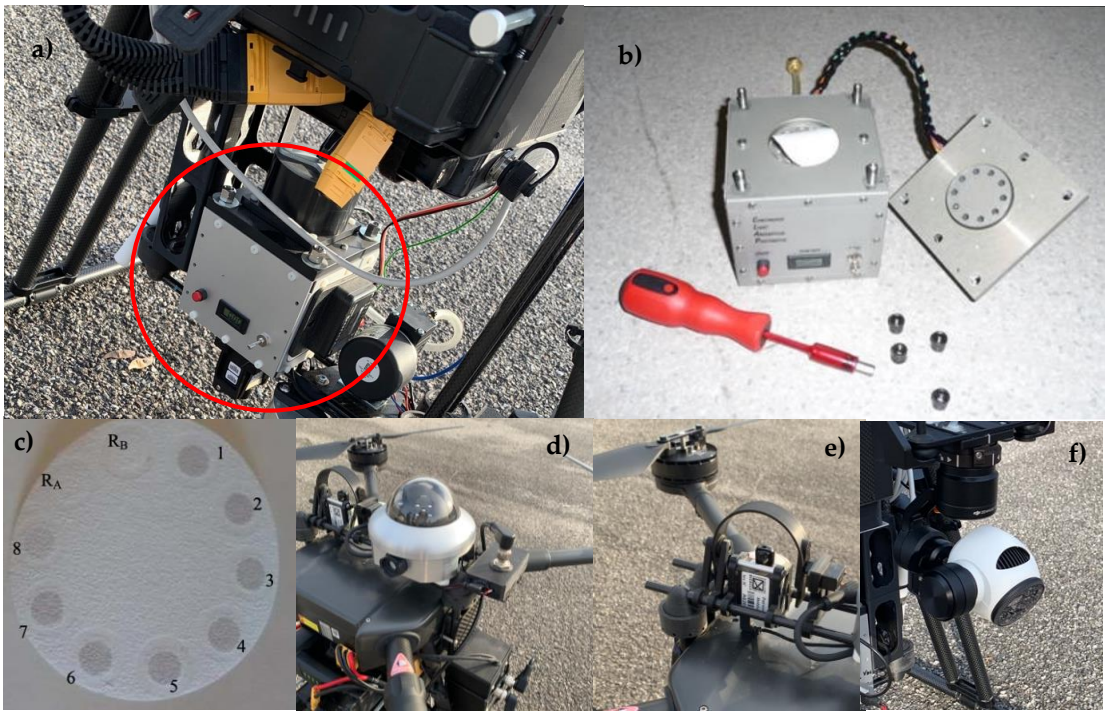

Figure 82. *Some intruments on board the UAV: FAP (**a**-**c**), SPN1 pyranometer (**d**), spectroradiometer (**e**), camera (**f**).*

First test flights and measurements were performed last winter and spring in the Po Valley, near Milan. The experimental set-up has been fine-tuned and a measurements campaign in the Po Valley will be carried out in the coming months. Figure 83 shows one vertical profile of LAA HR (ascending and descending) determined during one of those measurements days, specifically on February 3, 2023 at 3:16 p.m. (UTC). Discussion of the results obtained from the first flights

is beyond the scope of this work, but the idea (inherent to this research) is to make LAA and HR vertical profiles also onboard research ships during future midlatitudes – Arctic campaings, in order to explore the latitudinal HR and energy gradient also at higher altitudes (always in a fully experimental way).

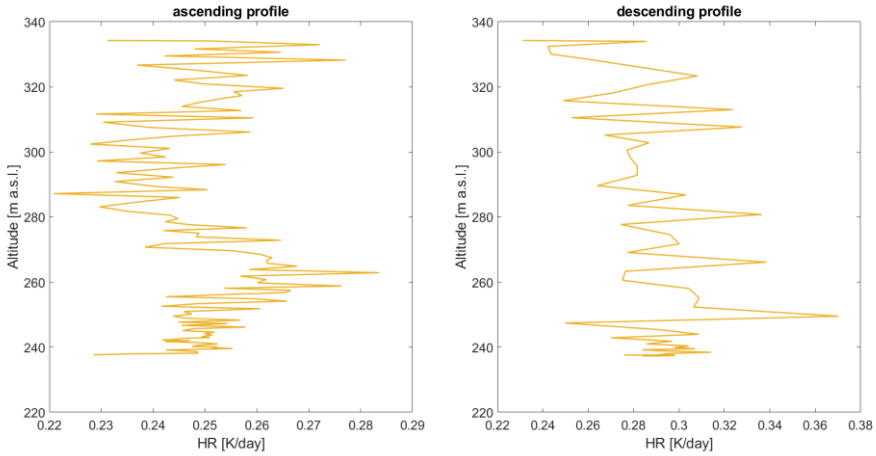

Figure 83. *HR vertical profiles (ascending on left and descending on right side) measured with the UAV on February 3*

7.2. HR measurements at the Jungfraujoch

A measurement campaign has been ongoing for the past 9 months and is drawing to a close at this time. It took place at the Jungfraujoch facility (JFJ), a high altitude research station located at 3600 m in the Swiss Alps (Figure 84a).

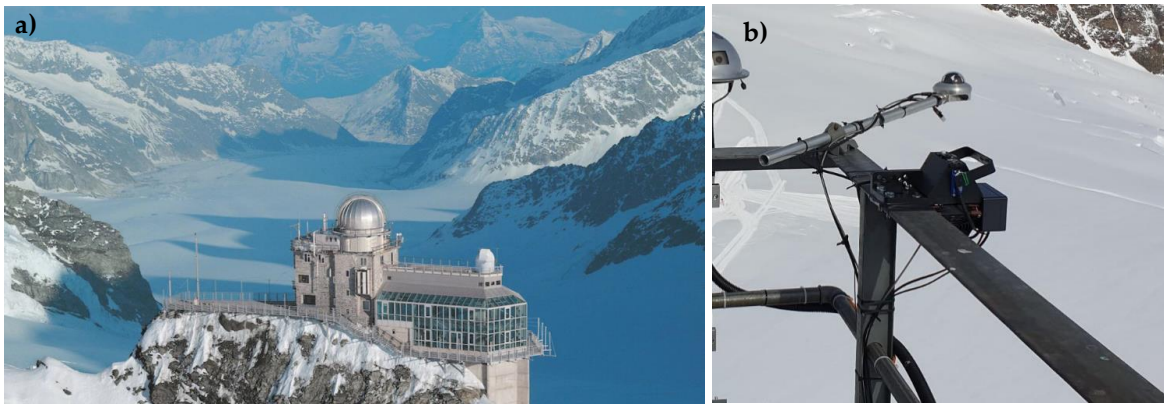

Figure 84. *JFJ research station (**a**); radiometers installed at the JFJ (**b**): SPN1 and RoX system*

We are exploiting the instrumentation for aerosol measurements already present at the JFJ, thanks to the ATMO-ACCESS project. We also added our instrumentation for solar radiation measurements, i.e. a pyranometer SPN1 and a RoX spectroradiometer (Figure 85b). Therefore, we will be able to determine LAA HR in the alpine free-troposphere and compare measurements at high altitude remote sites with high latitude remote sites. We will try also to improve the determination of the HR due to dust component, since dust events and dust optical properties are detected at the JFJ research station. An improvement in dust HR apportionment will

allow us to apply this method to EUREC^{4}A data as well, because in the tropical North Atlantic dust has an important role in light absorption and thus in the energy budget at the surface and in the energy gradient between tropics and higher latitudes.

In Figure 85a,b, the first very preliminary results of eBC concentrations and LAA HR from May 1 to June 30 are shown. The average HR in that period was 0.035 ± 4*10^{-4} K/day. This value is not particularly low: it is about an order of magnitude less than that found in Gdansk and Milan, but is comparable to values found in Southern Norway and is an order of magnitude higher than the values found in the Arctic. It will be interesting to understand whether the rather high values (given the measurement site) of BC and HR were due to combustion products or dust transport

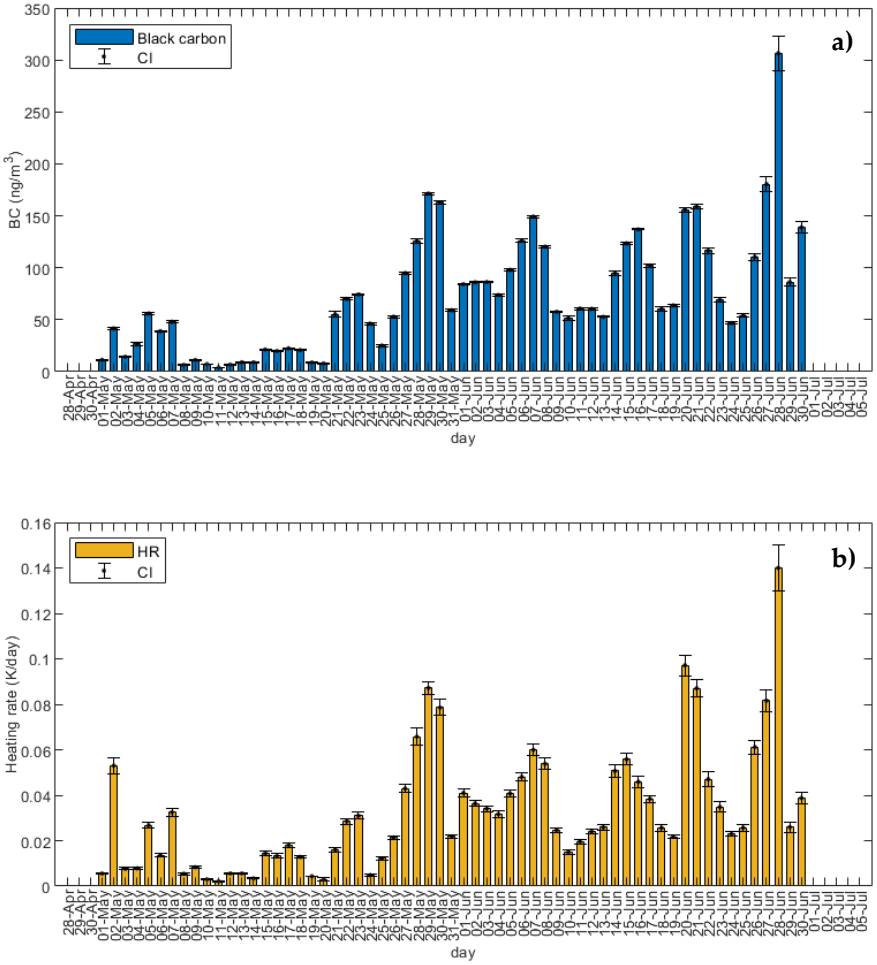

Figure 85. *eBC (**a**) and (**HR**) daily averages at the JFJ from April 28 to June 5*

7.3. Antarctic campaign

Last winter, the same experimental setup used for the HR computation in previous campaigns was installed also on board of the R/V Laura Bassi, during the 38° Antarctic Italian Campaign (PNRA). Our measurements are in the framework of the CAIAC (oCean Atmosphere Interactions in the Antarctic regions and Convergence latitude) project, which aims to

investigate the aerosol forcing and its role in Climate Change in order to provide first results of georeferenced climatic direct effect of different aerosol sources and types in all sky conditions along the Ross Sea region and during the transept between New Zealand and the Antarctic Coast. Figure 86 shows the route of the ship (from New Zealand to Antartic and return), while Figure 87 shows the first preliminary results of eBC concentrations. Determination of the HR will allow to obtain the first experimental data of this parameter in the Antarctic region and a comparison with the Arctic. Currently, there is evidence that the magnitude of polar amplification is different in the two hemispheres [28] and it is stronger in the Arctic [27]. Indeed, a more negative cloud albedo feedback, a less positive lapse rate feedback and a strong ocean heat uptake in the Souther Ocean contribute to limiting warming relative to the Arctic [27]; however polar amplification is still present because of weak Planck response and positive surface albedo feedback. Our measurements may help to better understand the role of aerosols in the Antarctic climate and compare polar amplification between Arctic and Antarctic.

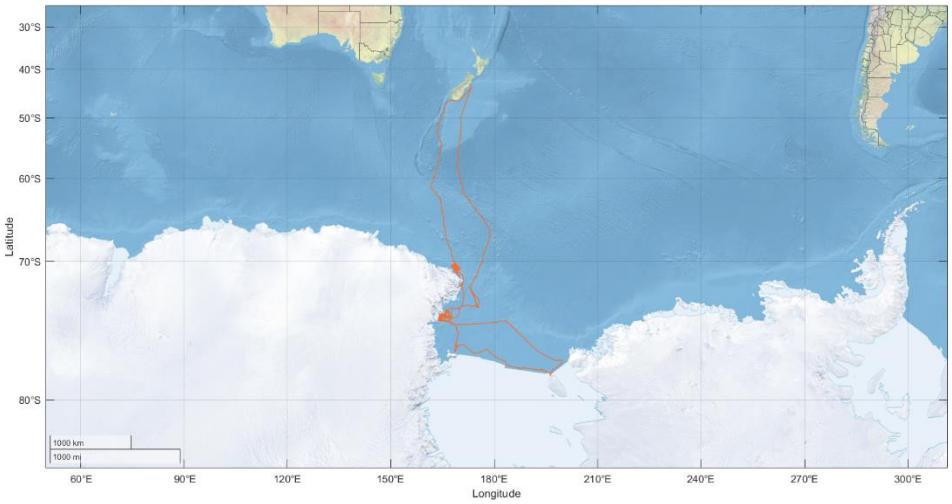

***Figure 86**. Ship's route during the Antarctic campaign (from New Zealand to Ross Sea and come back)*

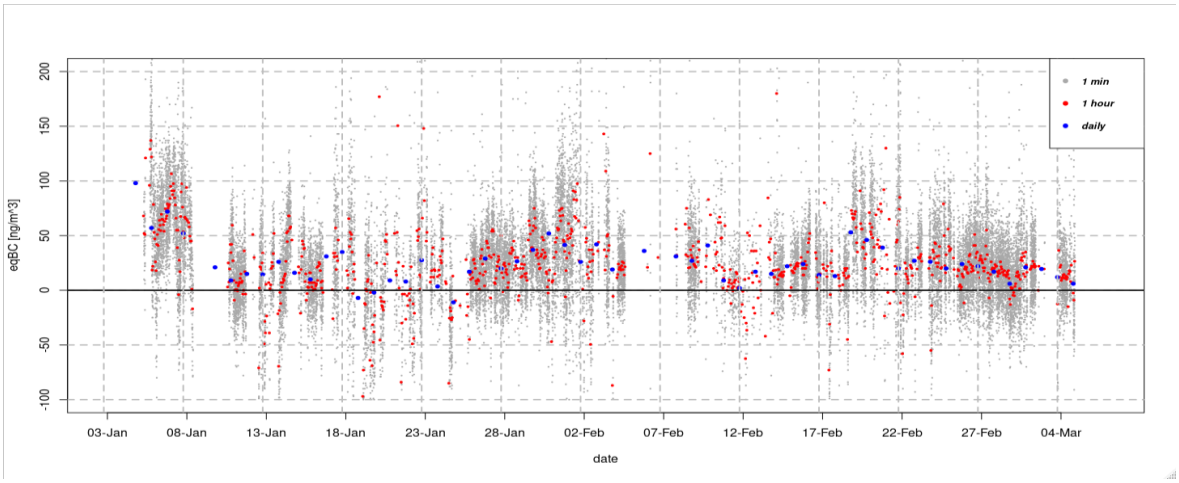

***Figure 87**. eBC concentrations time series: 1 minute (grey), 1 hour (red) and daily (blue) data.*

8. Conclusions

Climate change is a global phenomenon, but in the Arctic region the surface temperature increase is much faster, up to 3 – 4 times [24,25], as pointed out by recent studies. This phenomenon is known as 'Arctic Amplification' and has significant consequences for the ecosystems [7]. It is induced by certain characteristics peculiar to this area (such as the presence of sea-ice) that trigger positive feedbacks, thus amplifying the warming. AA is maximum in fall and winter, but summer is a key season when mechanisms are initiated that then lead to AA in the following months. Moreover, it is not homogeneous, but it is higher in the European sector of the Arctic, near Svalbard. The causes beyond AA are strongly interconnected and the relative contribution of each of them is still not entirely clear. In addition to internal feedbacks (e.g. surface albedo feedback, temperature feedbacks and changes in water vapor atmospheric content and cloud cover), also external factors, such as the poleward energy transport, play an important role in AA.

The PET is driven by the ocean and atmosphere. Several mechanisms affect the atmospheric PET (e.g. changes in the atmospheric large-scale circulation and the latitudinal gradient of heat and specific humidity), but in general mechanisms that preferentially heat higher latitudes inhibit the PET, while mechanisms that preferentially heat lower latitudes boost it [28]. The latter include aerosol forcings, whose role in the AA is one of the least clear aspects and it is due to an interplay of local effects and remote effects. The current remote and local contributions of aerosols to Arctic climate change are not well constrained [26].

In particular, the light absorbing aerosols interact directly with solar radiation, exerting a positive forcing. Local direct forcing of LAA (i.e. within the Arctic atmosphere) in summer (when sunlight is present) contributes to surface warming, but meanwhile reduces the meridian temperature gradient and thus the PET (aerosols can locally influence the Arctic climate also indirectly by acting as CCN and affecting the cloud formation, distribution and properties; however in this research we consider only the effects of the LAA direct forcing). Remote LAA direct forcing, instead, heats the atmosphere at lower latitudes, increasing the PET. In other words, atmospheric LAA concentrations at lower latitudes can cause an energy (heat) surplus that is then transported northward. Therefore, the main question is: total LAA contribution to AA is due to an interplay (they may add up or hinder each other) of local and remote effects, but one of them is definitely greater than the other and thus prevalent in the AA? This topic is particularly relevant in in our day and age, which are characterized by major changes in the Arctic region due to human impact.

Most of the studies which have tried to answer to this question are modelling ones [6–10,245]. Several of them focused on both LAA (as we did) and scattering aerosols. They are in

agreement on the main role of aerosol remote forcing (via PET), despite competing phenomena occurs. For example Ren at al. [8] recently found an Arctic surface warming of 0.297 K (≈ 20% of the observed Arctic warming) since 1980 induced by the total effects of sulfate and BC, and as many as 0.25 K were due to changes in sulfate and BC concentrations outside the Arctic, in particular at mid-latitudes. However, there is discordance among the various modeling studies (induced by underestimation of aerosol concentrations [8] and improperly modeled aging processes and/or boundary layer stability [9]) regarding the magnitude of this remote aerosol forcing and consequent temperature increase in Arctic. Moreover, there is a lack of purely experimental measures, concerning the LAA direct foring from lower latitudes to the Arctic.

For these reasons, we took part in 5 measurements campaigns on board research vessels: three of them (AREX) took place in summer between Gdansk and North of Svalbard; one in the Baltic Sea (from Gdansk to 63.5 °N) in winter; one in the tropical North Atlantic in winter. These expeditions made it possible to collect TSP on filters (so as to determine its chemical composition) and measure solar radiation (and its components), LAA concentrations and absorption coefficients in these areas. From this data we computed (for the first time) the LAA direct forcing in terms of heating rate, using a completely experimental method [11].

By means of the aerosol chemistry, we found the first macroscopic differences: the anthropic impact decreased progressively northward and away from human settlements, while the natural components increased. In addition to clear latitudinal dissimilarities, there were also some differences within the Arctic itself. The lowest anthropogenic influence was found in east and north of Svalbard, which represented the most pristine sites among the different Arctic Ocean areas. Moreover, Tromsø and Longyearbyen proved to be two important emission hotspots in the region. In particular Longyearbyen is located rather far north (78°N) and thus can have a non-negligible impact on the rather pristine Arctic atmosphere, especially in summer when the long-range transport is strongly inhibited.

These differences within the Arctic have been confirmed by high-resolution measurements. We outlined the Arctic background level, particularly in terms of LAA concentrations and consequent HR, compared to the anthropized fjords and hotspots in the region. eBC concentration for the Arctic Ocean background (sea area around Svalbard) was 11.7 ± 0.1 ng/m^3. Higher eBC average concentration (99.4 ± 3.1 ng/m^3) in Svalbard fjords was found in Isfjorden (where Longyearbyen is located). Moreover, the background was dominated by secondary aerosol in the Aitken mode (in keeping with the summer period), while nanoparticles in the fjords (above all Isfjorden) were highly influenced by primary aerosol linked to combustion (i.e. eBC). Local sources are thus necessary to explain the aerosol spatial variability at the local scale. Only a few

Long Range Transport Events were detected, consistently with the season. As a result, we determined a very low LAA HR for the Arctic Ocean ($8.2*10^{-3} \pm 0.3*10^{-3}$ K/day) and an HR one order of magnitude higher ($0.8*10^{-3} \pm 0.9*10^{-5}$ K/day) in Isfjorden. This last value is lower compared to HR at mid-latitudes; however, maximum HR in Isfjorden (≈ 0.5 K/day) was decidedly higher. This indicates that summer LAA direct forcing could reach significant values due to local emissions in a warmer future, characterized by more human activities in the Arctic. By the way, local sources emit eBC directly within the Arctic dome, causing a strong surface warming, especially since the Arctic sensitivity to BC locally emitted is considerably higher than to BC emitted at lower latitudes [10].

However, in the present day, we found a clear latitudinal negative trend in eBC atmospheric concentrations: latitudinal averages were sharply higher at Gdansk and in the Baltic Sea and Southern Norway areas (from 1446.2 ± 16.5 ng/m^3 at 54°N to 241.2 ± 6.6 ng/m^3 at 58°N); then they gradually decreased to the Arctic, where they were very low (11.0 ± 0.4 ng/m^3 at 80°N). This trend was interrupted only at some specific latitudes, where the ship stopped at the harbors of some human settlements (e.g. Tromsø and Longyearbyen, as seen also from local emission analysis). Also the global solar radiation diminished northward. it is noteworthy that the percentage of diffuse radiation increased northward. This result, along with the high average cloudiness we found in the Arctic area (7.4 ± 0.01 oktas), highlights the role of diffuse radiation at high latitudes and thus the importance of our fully experimental method, which allow the HR determination in any sky condition. Latitudinal trend of LAA HR followed the behavior of eBC and radiation, with a sharp decline poleward (except the local interruptions). The difference between the Baltic area and the Arctic was one order of magnitude, while it was by two orders of magnitude between Gdansk (0.222 ± 0.013 K/day) and the Arctic ($1.3*10^{-3} \pm 1.1*10^{-4}$ K/day at 80°N). Considering also Milan (HR ≈ 0.5 K/day), the difference increases. We mentioned that Isfjorden is the main hotspot in the Arctic, but also comparing to the HR at 78°N ($4.7*10^{-3} \pm 1.3*10^{-4}$ K/day), where Longyearbyen is located, the gap remained remarkable. Our results have also highlighted the importance of using C values scaled in function of the area in future research. Indeed, using different latitudinal C values, the difference between mid-latitudes and higher latitudes has risen. These measurements allowed us to determine the latitudinal surface energy gradient in terms of J/m^3 added in a summer day. Again there were 2 order of magnitude of difference between Europe and North of Svalbard (366.2 J/m^3 day^{-1} in Milan, 189.8 J/m^3 day^{-1} at 54°N and 1.6 J/m^3 day^{-1} at 80°N). If we consider the PBL (and not only the surface) and 3 areas at different latitudes (Baltic and Southern Norway, Norwegian Sea and Arctic), the energy added on a single summer day by LAA forcing was 60.66 PJ/day, 27.52 PJ/day and 1.23 PJ/day, respectively. Therefore, the great latitudinal energy difference, induced by LAA direct

forcing, can increase the PET and contribute to AA. This emphasizes the importance of remote aerosol effect over the local one.

The BALTIC campaign allowed to collect data also in the winter season and make the first comparisons between different seasons in an area comparable, at least in part, to that of the summer campaigns. We found the presence of an HR and energy gradient also in winter, at least in the Baltic sector, in a shorter latitudinal distance. Indeed, HR at 63 °N ($0.003 \pm 1*10^{-4}$ K/day) was similar to summer Arctic values because of the rapid decline of LAA concentrations, while obviously it tends to 0 beyond the polar circle due to the polar night. However, the winter energy gradient is smaller than in summer (85.6 J/m^3 day^{-1} at 54°N) due to the shorter irradiation time at lower latitudes. Therefore, PET due to LAA seems to be greater in summer. As mentioned above, despite AA is larger in fall and winter, an increased summer PET can play a key role in AA, because the extra heat contributes to an enhanced melting of sea ice, triggering those feedbacks that then lead to AA in the following seasons.

Winter data from the tropical area of the Northern Hemisphere were also collected during the EUREC^{4}A campaign. Average HR was $0.175 \pm 3*10^{-3}$ K/day and it is 2 order of magnitude higher than HR over the Arctic Ocean we found in summer. This highlights the importance that the tropical North Atlantic Ocean could have in the PET in winter, when HR at midlatitudes is lower and in the Arctic is 0. Therefore, this aspect will be deepened in future. The high EUREC^{4}A HR value was mainly due to two transport events of mixtures of BB and dust particles. Indeed, winter aerosol transport from West Africa is frequent in that area (at lower latitudes and altitudes than in summer), altering background conditions. Aerosol chemical composition for background conditions was not free of anthropogenic influences, but during the two transport events eBC concentrations increased significantly, reaching values comparable to those in mid-latitudes (965.18 ± 5.43 ng/m^3 and 770.21 ± 11.17 ng/m^3). As a result, the HR was $0.047 \pm 2*10^{-3}$ K/day, $0.279 \pm 5*10^{-3}$ K/day and $0.186 \pm 6*10^{-3}$ K/day for background, first and second transport events, respectively. Differently from mid-latitudes (where LAA from combustion prevails), mineral dust plays a key role here. A future goal is therefore to improve the apportionment of HR, so as to investigate the role of dust separately and compare it to other species and sources. Moreover, hygroscopic data measured will be useful for studying the activation of particles as CCN and thus the link between aerosol and clouds. These will be important because clouds also influence the energy balance and the climate.

In general, our data data allowed to overreach the problem of a lack of representativeness of single monitoring stations in remote areas, in particular in the Arctic, with respect to their extension. They can help to better understand how the LAA influence the Arctic climate and

provide experimental observations to improve the models (as well as being able to be compared with the model outputs).

As the AA proceeds, the poleward transport of dry energy will be inhibited. Moreover, whether summer LAA emissions in the Arctic will increase, the local LAA direct forcing (HR) will also rise. This phenomenon, along with a reduction in emissions at mid-latitudes, will further decrease the PET. Thus, the current relative importance (i.e. the interplay) between aerosol local and remote effects may change. Therefore, is essential to continue to monitor these phenomena.

In the future there is a need to collect new data, especially in winter (over a wider area), because they currently are limited to one short campaign in the Baltic and one in the Tropics. Moreover, the study area can be expanded to continental Europe with a hybrid approach, using also eBC reanalysis data. Some novelties are already being implemented. We will extend HR measurements above the PBL by means of a UAV system. We are also measuring the HR in the free troposphere at the Jungfraujoch station. Finally, we took part in an Antarctic campaign to better understand the role of aerosols also in the Antarctic climate. Indeed, albeit lower, polar amplification is present also in some parts of the Antarctica.

.

.

.

References

1. Intergovernmental Panel on Climate Change *Climate Change 2021 – The Physical Science Basis*; 2023; ISBN 9781009157896.
2. Fu, B.; Gasser, T.; Li, B.; Tao, S.; Ciais, P.; Piao, S.; Balkanski, Y.; Li, W.; Yin, T.; Han, L.; et al. Short-Lived Climate Forcers Have Long-Term Climate Impacts via the Carbon--Climate Feedback. *Nat. Clim. Chang.* **2020**, *10*, 851–855.
3. Szopa, S.; Naik, V.; Adhikary, B.; Artaxo, P.; Berntsen, T.; Collins, W.; Fuzzi, S.; Gallardo, L.; Kiendler-Scharr, A.; Klimont, Z.; et al. Short-Lived Climate Forcers. In Proceedings of the AGU Fall Meeting Abstracts; 2021; Vol. 2021, pp. U13B--06.
4. Haines, A.; Amann, M.; Borgford-Parnell, N.; Leonard, S.; Kuylenstierna, J.; Shindell, D. Short-Lived Climate Pollutant Mitigation and the Sustainable Development Goals. *Nat. Clim. Chang.* **2017**, *7*, 863–869.
5. Lohmann, U.; Feichter, J. Global Indirect Aerosol Effects: A Review. *Atmos. Chem. Phys.* **2005**, *5*, 715–737, doi:10.5194/acp-5-715-2005.
6. Shindell, D.; Faluvegi, G. Climate Response to Regional Radiative Forcing during the Twentieth Century. *Nat. Geosci.* **2009**, *2*, 294–300, doi:10.1038/ngeo473.
7. Navarro, J.C.A.; Varma, V.; Riipinen, I.; Seland; Kirkevåg, A.; Struthers, H.; Iversen, T.; Hansson, H.C.; Ekman, A.M.L. Amplification of Arctic Warming by Past Air Pollution Reductions in Europe. *Nat. Geosci.* **2016**, *9*, 277–281, doi:10.1038/ngeo2673.
8. Ren, L.; Yang, Y.; Wang, H.; Zhang, R.; Wang, P.; Liao, H. Source Attribution of Arctic Black Carbon and Sulfate Aerosols and Associated Arctic Surface Warming during 1980-2018. *Atmos. Chem. Phys.* **2020**, *20*, 9067–9085, doi:10.5194/acp-20-9067-2020.
9. Sand, M.; Berntsen, T.K.; Kay, J.E.; Lamarque, J.F.; Seland; Kirkeväg, A. The Arctic Response to Remote and Local Forcing of Black Carbon. *Atmos. Chem. Phys.* **2013**, *13*, 211–224, doi:10.5194/acp-13-211-2013.
10. Sand, M.; Berntsen, T.K.; Seland, Ø.; Kristjánsson, J.E. Arctic Surface Temperature Change to Emissions of Black Carbon within Arctic or Midlatitudes. *J. Geophys. Res. Atmos.* **2013**, *118*, 7788–7798, doi:10.1002/jgrd.50613.
11. Ferrero, L. Heating Rate of Light Absorbing Aerosols : Time-Resolved Measurements ,

the Role of Clouds , and Source Identification. *Environ. Sci. Technol.* **2018**, doi:10.1021/acs.est.7b04320.

12. Moosmüller, H.; Chakrabarty, R.K.; Arnott, W.P. Aerosol Light Absorption and Its Measurement: A Review. *J. Quant. Spectrosc. Radiat. Transf.* **2009**, *110*, 844–878.
13. Bond, T.C.; Doherty, S.J.; Fahey, D.W.; Forster, P.M.; Berntsen, T.; Deangelo, B.J.; Flanner, M.G.; Ghan, S.; Kärcher, B.; Koch, D.; et al. Bounding the Role of Black Carbon in the Climate System : A Scienti Fi c Assessment. **2013**, *118*, 5380–5552, doi:10.1002/jgrd.50171.
14. Contini, D.; Vecchi, R.; Viana, M. Carbonaceous Aerosols in the Atmosphere. *Atmosphere (Basel).* **2018**, *9*, 1–8, doi:10.3390/atmos9050181.
15. Heidenreich, R.D.; Hess, W.M.; Ban, L.L. A Test Object and Criteria for High Resolution Electron Microscopy. *J. Appl. Crystallogr.* **1968**, *1*, 1–19.
16. Kondo, Y.; Oshima, N.; Kajino, M.; Mikami, R.; Moteki, N.; Takegawa, N.; Verma, R.L.; Kajii, Y.; Kato, S.; Takami, A. Emissions of Black Carbon in East Asia Estimated from Observations at a Remote Site in the East China Sea. *J. Geophys. Res. Atmos.* **2011**, *116*.
17. EPA, M. Report to Congress on Black Carbon. *Dep. Inter. Relat. Agencies, Ed.* **2012**.
18. Laskin, A.; Laskin, J.; Nizkorodov, S.A. Chemistry of Atmospheric Brown Carbon. *Chem. Rev.* **2015**, *115*, 4335–4382, doi:10.1021/cr5006167.
19. Gliß, J.; Mortier, A.; Schulz, M.; Andrews, E.; Balkanski, Y.; Bauer, S.E.; Benedictow, A.M.K.; Bian, H.; Checa-Garcia, R.; Chin, M.; et al. AeroCom Phase III Multi-Model Evaluation of the Aerosol Life Cycle and Optical Properties Using Ground- and Space-Based Remote Sensing as Well as Surface in Situ Observations. *Atmos. Chem. Phys.* **2021**, *21*, 87–128, doi:10.5194/acp-21-87-2021.
20. Wang, R.; Balkanski, Y.; Boucher, O.; Ciais, P.; Schuster, G.L.; Chevallier, F.; Samset, B.H.; Liu, J.; Piao, S.; Valari, M.; et al. Estimation of Global Black Carbon Direct Radiative Forcing and Its Uncertainty Constrained by Observations. *J. Geophys. Res. Atmos.* **2016**, *121*, 5948–5971.
21. Kelesidis, G.A.; Neubauer, D.; Fan, L.; Lohmann, U.; Pratsinis, S.E. Enhanced Light Absorption and Radiative Forcing by Black Carbon Agglomerates. **2022**,

doi:10.1021/acs.est.2c00428.

22. Sand, M.; Samset, B.H.; Myhre, G.; Gliß, J.; Bauer, S.E.; Bian, H.; Chin, M. Aerosol Absorption in Global Models from AeroCom Phase III. **2021**, 15929–15947.
23. Manabe, S.; Wetherald, R.T. The Effects of Doubling the CO 2 Concentration on the Climate of a General Circulation Model. *J. Atmos. Sci.* **1975**, *32*, 3–15.
24. AMAP, 2021. Arctic Climate Change Update 2021: Key Trends and Impacts 2021, 16 pp.
25. Rantanen, M.; Karpechko, A.Y.; Lipponen, A.; Nordling, K.; Hyvärinen, O.; Ruosteenoja, K.; Vihma, T.; Laaksonen, A. The Arctic Has Warmed Nearly Four Times Faster than the Globe since 1979. *Commun. Earth Environ.* **2022**, *3*, 1–10, doi:10.1038/s43247-022-00498-3.
26. Schmale, J.; Zieger, P.; Ekman, A.M.L. Aerosols in Current and Future Arctic Climate. *Nat. Clim. Chang.* **2021**, *11*, 95–105, doi:10.1038/s41558-020-00969-5.
27. Goosse, H.; Kay, J.E.; Armour, K.C.; Bodas-Salcedo, A.; Chepfer, H.; Docquier, D.; Jonko, A.; Kushner, P.J.; Lecomte, O.; Massonnet, F.; et al. Quantifying Climate Feedbacks in Polar Regions. *Nat. Commun.* **2018**, *9*, doi:10.1038/s41467-018-04173-0.
28. Previdi, M.; Smith, K.L.; Polvani, L.M. Arctic Amplification of Climate Change: A Review of Underlying Mechanisms. *Environ. Res. Lett.* **2021**, *16*, doi:10.1088/1748-9326/ac1c29.
29. Henry, M.; Merlis, T.M. The Role of the Nonlinearity of the Stefan--Boltzmann Law on the Structure of Radiatively Forced Temperature Change. *J. Clim.* **2019**, *32*, 335–348.
30. Carton, J.A.; Ding, Y.; Arrigo, K.R. The Seasonal Cycle of the Arctic Ocean under Climate Change. *Geophys. Res. Lett.* **2015**, *42*, 7681–7686, doi:10.1002/2015GL064514.
31. Boeke, R.C.; Taylor, P.C.; Sejas, S.A. On the Nature of the Arctic's Positive Lapse-Rate Feedback. *Geophys. Res. Lett.* **2021**, *48*, 1–11, doi:10.1029/2020GL091109.
32. Philipp, D.; Stengel, M.; Ahrens, B. Analyzing the Arctic Feedback Mechanism between Sea Ice and Low-Level Clouds Using 34 Years of Satellite Observations. *J. Clim.* **2020**, *33*, 7479–7501.
33. Edwards, T.L.; Fettweis, X.; Gagliardini, O.; Gillet-Chaulet, F.; Goelzer, H.; Gregory,

J.M.; Hoffman, M.; Huybrechts, P.; Payne, A.J.; Perego, M.; et al. Probabilistic Parameterisation of the Surface Mass Balance--Elevation Feedback in Regional Climate Model Simulations of the Greenland Ice Sheet. *Cryosph.* **2014**, *8*, 181–194.

34. Park, S.W.; Kim, J.S.; Kug, J.S. The Intensification of Arctic Warming as a Result of CO2 Physiological Forcing. *Nat. Commun.* **2020**, *11*, 1–7, doi:10.1038/s41467-020-15924-3.
35. Park, J.Y.; Kug, J.S.; Bader, J.; Rolph, R.; Kwon, M. Amplified Arctic Warming by Phytoplankton under Greenhouse Warming. *Proc. Natl. Acad. Sci. U. S. A.* **2015**, *112*, 5921–5926, doi:10.1073/pnas.1416884112.
36. Beer, E.; Eisenman, I.; Wagner, T.J.W. Polar Amplification Due to Enhanced Heat Flux Across the Halocline. *Geophys. Res. Lett.* **2020**, *47*, 1–10, doi:10.1029/2019GL086706.
37. Graversen, R.G.; Burtu, M. Arctic Amplification Enhanced by Latent Energy Transport of Atmospheric Planetary Waves. *Q. J. R. Meteorol. Soc.* **2016**, *142*, 2046–2054.
38. Fajber, R.; Kushner, P.J.; Laliberté, F. Influence of Midlatitude Surface Thermal Anomalies on the Polar Midtroposphere in an Idealized Moist Model. *J. Atmos. Sci.* **2018**, *75*, 1089–1104.
39. Baggett, C.; Lee, S.; Feldstein, S. An Investigation of the Presence of Atmospheric Rivers over the North Pacific during Planetary-Scale Wave Life Cycles and Their Role in Arctic Warming. *J. Atmos. Sci.* **2016**, *73*, 4329–4347.
40. Ye, K.; Jung, T. How Strong Is Influence of the Tropics and Midlatitudes on the Arctic Atmospheric Circulation and Climate Change? *Geophys. Res. Lett.* **2019**, *46*, 4942–4952.
41. Hall, R.J.; Hanna, E.; Chen, L. Winter Arctic Amplification at the Synoptic Timescale, 1979--2018, Its Regional Variation and Response to Tropical and Extratropical Variability. *Clim. Dyn.* **2021**, *56*, 457–473.
42. Clarke, A.D.; Noone, K.J. Soot in the Arctic Snowpack: A Cause for Perturbations in Radiative Transfer. *Atmos. Environ.* **2007**, *41*, 64–72.
43. Holland, M.M.; Bailey, D.A.; Briegleb, B.P.; Light, B.; Hunke, E. Improved Sea Ice Shortwave Radiation Physics in CCSM4: The Impact of Melt Ponds and Aerosols on Arctic Sea Ice. *J. Clim.* **2012**, *25*, 1413–1430.
44. Mauritsen, T.; Sedlar, J.; Tjernström, M.; Leck, C.; Martin, M.; Shupe, M.; Sjogren, S.;

Sierau, B.; Persson, P.O.G.; Brooks, I.M.; et al. An Arctic CCN-Limited Cloud-Aerosol Regime. *Atmos. Chem. Phys.* **2011**, *11*, 165–173, doi:10.5194/acp-11-165-2011.

45. Abbatt, J.P.D.; Leaitch, W.R.; Aliabadi, A.A.; Bertram, A.K.; Blanchet, J.; Boivin-rioux, A.; Bozem, H.; Burkart, J.; Chang, R.Y.W.; Charette, J.; et al. Overview Paper : New Insights into Aerosol and Climate in the Arctic. **2019**, 1–34.

46. McCarty, J.L.; Smith, T.E.L.; Turetsky, M.R. Arctic Fires Re-Emerging. *Nat. Geosci.* **2020**, *13*, 658–660.

47. Willis, M.D.; Burkart, J.; Thomas, J.L.; Köllner, F.; Schneider, J.; Bozem, H.; Hoor, P.M.; Aliabadi, A.A.; Schulz, H.; Herber, A.B.; et al. Growth of Nucleation Mode Particles in the Summertime Arctic:\hack{\newline} a Case Study. *Atmos. Chem. Phys.* **2016**, *16*, 7663–7679, doi:10.5194/acp-16-7663-2016.

48. Willis, M.D.; Köllner, F.; Burkart, J.; Bozem, H.; Thomas, J.L.; Schneider, J.; Aliabadi, A.A.; Hoor, P.M.; Schulz, H.; Herber, A.B.; et al. Evidence for Marine Biogenic Influence on Summertime Arctic Aerosol. *Geophys. Res. Lett.* **2017**, *44*, 6460–6470.

49. Croft, B.; Martin, R. V; Leaitch, W.R.; Burkart, J.; Chang, R.Y.-W.; Collins, D.B.; Hayes, P.L.; Hodshire, A.L.; Huang, L.; Kodros, J.K.; et al. Arctic Marine Secondary Organic Aerosol Contributes Significantly to Summertime Particle Size Distributions in the Canadian Arctic Archipelago. *Atmos. Chem. Phys.* **2019**, *19*, 2787–2812, doi:10.5194/acp-19-2787-2019.

50. Ardyna, M.; Babin, M.; Gosselin, M.; Devred, E.; Rainville, L.; Tremblay, J.-É. Recent Arctic Ocean Sea Ice Loss Triggers Novel Fall Phytoplankton Blooms. *Geophys. Res. Lett.* **2014**, *41*, 6207–6212.

51. Bring, A.; Shiklomanov, A.; Lammers, R.B. Pan-Arctic River Discharge: Prioritizing Monitoring of Future Climate Change Hot Spots. *Earth's Futur.* **2017**, *5*, 72–92.

52. Baccarini, A.; Karlsson, L.; Dommen, J.; Duplessis, P.; Vüllers, J.; Brooks, I.M.; Saiz-Lopez, A.; Salter, M.; Tjernström, M.; Baltensperger, U.; et al. Frequent New Particle Formation over the High Arctic Pack Ice by Enhanced Iodine Emissions. *Nat. Commun.* **2020**, *11*, 1–11, doi:10.1038/s41467-020-18551-0.

53. Law, K.S.; Stohl, A. Arctic Air Pollution: Origins and Impacts. *Science (80-.).* **2007**, *315*,

1537–1540.

54. Shen, Z.; Ming, Y.; Horowitz, L.W.; Ramaswamy, V.; Lin, M. On the Seasonality of Arctic Black Carbon. *J. Clim.* **2017**, *30*, 4429–4441, doi:10.1175/JCLI-D-16-0580.1.

55. Ström, J.; Umegård, J.; Tørseth, K.; Tunved, P.; Hansson, H.-C.; Holmén, K.; Wismann, V.; Herber, A.; König-Langlo, G. One Year of Particle Size Distribution and Aerosol Chemical Composition Measurements at the Zeppelin Station, Svalbard, March 2000--March 2001. *Phys. Chem. Earth, Parts A/B/C* **2003**, *28*, 1181–1190.

56. Thomas, M.A.; Devasthale, A.; Tjernström, M.; Ekman, A.M.L. The Relation Between Aerosol Vertical Distribution and Temperature Inversions in the Arctic in Winter and Spring. *Geophys. Res. Lett.* **2019**, *46*, 2836–2845, doi:10.1029/2018GL081624.

57. Stevens, B.; Bony, S.; Farrell, D.; Ament, F.; Blyth, A.; Fairall, C.; Karstensen, J.; Quinn, P.K.; Speich, S.; Acquistapace, C.; et al. EUREC^4A. *Earth Syst. Sci. Data* **2021**, *13*, 4067–4119, doi:10.5194/essd-13-4067-2021.

58. Fierz, M.; Houle, C.; Steigmeier, P.; Burtscher, H. Design, Calibration, and Field Performance of a Miniature Diffusion Size Classifier. *Aerosol Sci. Technol.* **2011**, *45*, 1–10, doi:10.1080/02786826.2010.516283.

59. Perrone, M.G.; Gualtieri, M.; Ferrero, L.; Porto, C. Lo; Udisti, R.; Bolzacchini, E.; Camatini, M. Seasonal Variations in Chemical Composition and in Vitro Biological Effects of Fine PM from Milan. *Chemosphere* **2010**, *78*, 1368–1377, doi:10.1016/j.chemosphere.2009.12.071.

60. Owoade, O.K.; Olise, F.S.; Obioh, I.B.; Olaniyi, H.B.; Bolzacchini, E.; Ferrero, L.; Perrone, G. PM10 Sampler Deposited Air Particulates: Ascertaining Uniformity of Sample on Filter through Rotated Exposure to Radiation. *Nucl. Instruments Methods Phys. Res. Sect. A Accel. Spectrometers, Detect. Assoc. Equip.* **2006**, *564*, 315–318, doi:https://doi.org/10.1016/j.nima.2006.03.037.

61. Ferrero, L.; Sangiorgi, G.; Perrone, M.G.; Rizzi, C.; Cataldi, M.; Markuszewski, P.; Pakszys, P.; Makuch, P.; Petelski, T.; Becagli, S.; et al. Chemical Composition of Aerosol over the Arctic Ocean from Summer Arctic Expedition (AREX) 2011-2012 Cruises: Ions, Amines, Elemental Carbon, Organic Matter, Polycyclic Aromatic Hydrocarbons, n-

Alkanes, Metals, and Rare Earth Elements. *Atmosphere (Basel).* **2019**, *10*, 2011–2012, doi:10.3390/atmos10020054.

62. Ferrero, L.; D'Angelo, L.; Rovelli, G.; Sangiorgi, G.; Perrone, M.G.; Moscatelli, M.; Casati, M.; Rozzoni, V.; Bolzacchini, E. Determination of Aerosol Deliquescence and Crystallization Relative Humidity for Energy Saving in Free-Cooled Data Centers. *Int. J. Environ. Sci. Technol.* **2015**, *12*, 2777–2790, doi:10.1007/s13762-014-0680-2.

63. Rigler, M.; Drinovec, L.; Lavrič, G.; Vlachou, A.; Prévôt, A.S.H.; Jaffrezo, J.L.; Stavroulas, I.; Sciare, J.; Burger, J.; Kranjc, I.; et al. The New Instrument Using a TC--BC (Total Carbon--Black Carbon) Method for the Online Measurement of Carbonaceous Aerosols. *Atmos. Meas. Tech.* **2020**, *13*, 4333–4351, doi:10.5194/amt-13-4333-2020.

64. Ferrero, L.; Cappelletti, D.; Busetto, M.; Mazzola, M.; Lupi, A.; Lanconelli, C.; Becagli, S.; Traversi, R.; Caiazzo, L.; Giardi, F.; et al. Vertical Profiles of Aerosol and Black Carbon in the Arctic: A Seasonal Phenomenology along 2 Years (2011-2012) of Field Campaigns. *Atmos. Chem. Phys.* **2016**, *16*, 12601–12629, doi:10.5194/acp-16-12601-2016.

65. Turpin, B.J.; Lim, H.J. Species Contributions to Pm2.5 Mass Concentrations: Revisiting Common Assumptions for Estimating Organic Mass. *Aerosol Sci. Technol.* **2001**, *35*, 602–610, doi:10.1080/02786820119445.

66. Drinovec, L.; Močnik, G.; Zotter, P.; Prévôt, A.S.H.; Ruckstuhl, C.; Coz, E.; Rupakheti, M.; Sciare, J.; Müller, T.; Wiedensohler, A.; et al. The "Dual-Spot" Aethalometer: An Improved Measurement of Aerosol Black Carbon with Real-Time Loading Compensation. *Atmos. Meas. Tech.* **2015**, *8*, 1965–1979, doi:10.5194/amt-8-1965-2015.

67. Drinovec, L.; Gregoric, A.; Zotter, P.; Wolf, R.; Anne Bruns, E.; Bruns, E.A.; Prevot, A.S.H.; Favez, O.; Sciare, J.; Arnold, I.J.; et al. The Filter-Loading Effect by Ambient Aerosols in Filter Absorption Photometers Depends on the Coating of the Sampled Particles. *Atmos. Meas. Tech.* **2017**, *10*, 1043–1059, doi:10.5194/amt-10-1043-2017.

68. Sandradewi, J.; Prévôt, A.S.H.; Weingartner, E.; Schmidhauser, R.; Gysel, M.; Baltensperger, U. A Study of Wood Burning and Traffic Aerosols in an Alpine Valley Using a Multi-Wavelength Aethalometer. *Atmos. Environ.* **2008**, *42*, 101–112, doi:10.1016/j.atmosenv.2007.09.034.

69. Hansen, A.D.A. *The Aethalometer*; Magee Scientific: Berkeley, California, USA, 2005;

70. Watson, J.G.; Chow, J.C. Comparison and Evaluation of in Situ and Filter Carbon Measurements at the Fresno Supersite. *J. Geophys. Res. Atmos.* **2002**, *107*, doi:10.1029/2001JD000573.

71. Snyder, D.C.; Schauer, J.J. An Inter-Comparison of Two Black Carbon Aerosol Instruments and a Semi-Continuous Elemental Carbon Instrument in the Urban Environment. *Aerosol Sci. Technol.* **2007**, *41*, 463–474, doi:10.1080/02786820701222819.

72. Liu, X.; Zheng, M.; Liu, Y.; Jin, Y.; Liu, J.; Zhang, B.; Yang, X.; Wu, Y.; Zhang, T.; Xiang, Y.; et al. Intercomparison of Equivalent Black Carbon (EBC) and Elemental Carbon (EC) Concentrations with Three-Year Continuous Measurement in Beijing, China. *Environ. Res.* **2022**, *209*, 112791, doi:10.1016/j.envres.2022.112791.

73. Ballach, J.; Hitzenberger, R.; Schultz, E.; Jaeschke, W. Development of an Improved Optical Transmission Technique for Black Carbon (BC) Analysis. *Atmos. Environ.* **2001**, *35*, 2089–2100, doi:https://doi.org/10.1016/S1352-2310(00)00499-4.

74. Weingartner, E.; Saatho, H.; Schnaiter, M.; Streit, N. Absorption of Light by Soot Particles : Determination of the Absorption Coefficient by Means of Aethalometers. **2003**, *34*, 1445–1463, doi:10.1016/S0021-8502(03)00359-8.

75. Liousse, C.; Cachier, H.; Jennings, S.G. Optical and Thermal Measurements of Black Carbon Aerosol Content in Different Environments: Variation of the Specific Attenuation Cross-Section, Sigma ($σ$). *Atmos. Environ. Part A. Gen. Top.* **1993**, *27*, 1203–1211.

76. Lack, D.A.; Moosmüller, H.; McMeeking, G.R.; Chakrabarty, R.K.; Baumgardner, D. Characterizing Elemental, Equivalent Black, and Refractory Black Carbon Aerosol Particles: A Review of Techniques, Their Limitations and Uncertainties. *Anal. Bioanal. Chem.* **2014**, *406*, 99–122, doi:10.1007/s00216-013-7402-3.

77. Gundel, L.A.; Dod, R.L.; Rosen, H.; Novakov, T. The Relationship between Optical Attenuation and Black Carbon Concentration for Ambient and Source Particles. *Sci. Total Environ.* **1984**, *36*, 197–202, doi:https://doi.org/10.1016/0048-9697(84)90266-3.

78. Collaud Coen, M.; Weingartner, E.; Apituley, A.; Ceburnis, D.; Fierz-Schmidhauser, R.;

Flentje, H.; Henzing, J.S.; Jennings, S.G.; Moerman, M.; Petzold, A.; et al. Minimizing Light Absorption Measurement Artifacts of the Aethalometer: Evaluation of Five Correction Algorithms. *Atmos. Meas. Tech.* **2010**, *3*, 457–474, doi:10.5194/amt-3-457-2010.

79. Virkkula, A.; Mäkelä, T.; Hillamo, R.; Yli-Tuomi, T.; Hirsikko, A.; Hämeri, K.; Koponen, I.K. A Simple Procedure for Correcting Loading Effects of Aethalometer Data. *J. Air Waste Manag. Assoc.* **2007**, *57*, 1214–1222, doi:10.3155/1047-3289.57.10.1214.
80. Bond, T.C.; Anderson, T.L.; Campbell, D. Calibration and Intercomparison of Filter-Based Measurements of Visible Light Absorption by Aerosols. *Aerosol Sci. \& Technol.* **1999**, *30*, 582–600.
81. Stone, R.S.; Sharma, S.; Herber, A.; Eleftheriadis, K.; Nelson, D.W. A Characterization of Arctic Aerosols on the Basis of Aerosol Optical Depth and Black Carbon Measurements. *Elementa* **2014**, *2*, 1–22, doi:10.12952/journal.elementa.000027.
82. Sharma, S.; Lavoué, D.; Cachier, H.; Barrie, L.A.; Gong, S.L. Long-term Trends of the Black Carbon Concentrations in the Canadian Arctic. *J. Geophys. Res. Atmos.* **2004**, *109*.
83. Bond, T.C.; Bergstrom, R.W. Light Absorption by Carbonaceous Particles: An Investigative Review. *Aerosol Sci. Technol.* **2006**, *40*, 27–67.
84. Petzold, A.; Ogren, J.A.; Fiebig, M.; Laj, P.; Li, S.-M.; Baltensperger, U.; Holzer-Popp, T.; Kinne, S.; Pappalardo, G.; Sugimoto, N.; et al. Recommendations for Reporting "Black Carbon" Measurements. *Atmos. Chem. Phys.* **2013**, *13*, 8365–8379, doi:10.5194/acp-13-8365-2013.
85. Andreae, M.O.; Gelencsér, A. Black Carbon or Brown Carbon? The Nature of Light-Absorbing Carbonaceous Aerosols. *Atmos. Chem. Phys.* **2006**, *6*, 3131–3148, doi:10.5194/acp-6-3131-2006.
86. Frickenhaus, S.; Ransby, D.; Shupe, M.; Jaiser, R.; Nicolaus, M. Data from the MOSAiC Arctic Ocean Drift Experiment. *Sci. Data* **2022**, *9*, 9–11, doi:10.1038/s41597-022-01678-8.
87. Long, C.N.; Bucholtz, A.; Jonsson, H.; Schmid, B.; Vogelmann, A.; Wood, J. A Method of Correcting for Tilt from Horizontal in Downwelling Shortwave Irradiance

Measurements on Moving Platforms. *Open Atmos. Sci. J.* **2010**, *4*, 78–87, doi:10.2174/1874282301004010078.

88. Wood, J.; Smyth, T.J.; Estellés, V. Autonomous Marine Hyperspectral Radiometers for Determining Solar Irradiances and Aerosol Optical Properties. *Atmos. Meas. Tech.* **2017**, 1723–1737, doi:10.5194/amt-10-1723-2017.

89. Badosa, J.; Wood, J.; Blanc, P.; Long, C.N.; Vuilleumier, L.; Demengel, D.; Haeffelin, M. Solar Irradiances Measured Using SPN1 Radiometers: Uncertainties and Clues for Development. *Atmos. Meas. Tech.* **2014**, *7*, 4267–4283, doi:10.5194/amt-7-4267-2014.

90. Cogliati, S.; Rossini, M.; Julitta, T.; Meroni, M.; Schickling, A.; Burkart, A.; Pinto, F.; Rascher, U.; Colombo, R. Continuous and Long-Term Measurements of Reflectance and Sun-Induced Chlorophyll Fluorescence by Using Novel Automated Field Spectroscopy Systems. *Remote Sens. Environ.* **2015**, *164*, 270–281, doi:https://doi.org/10.1016/j.rse.2015.03.027.

91. Andreae, M.O.; Ramanathan, V. Climate's Dark Forcings. *Science (80-.).* **2013**, *340*, 280–281, doi:10.1126/science.1235731.

92. Ramanathan, V.; Ramana, M. V; Roberts, G.; Kim, D.; Corrigan, C.; Chung, C.; Winker, D. Warming Trends in Asia Amplified by Brown Cloud Solar Absorption. *Nature* **2007**, *448*, 575–578, doi:10.1038/nature06019.

93. Mallet, M.; Tulet, P.; Serça, D.; Solmon, F.; Dubovik, O.; Pelon, J.; Pont, V.; Thouron, O. Impact of Dust Aerosols on the Radiative Budget, Surface Heat Fluxes, Heating Rate Profiles and Convective Activity over West Africa during March 2006. *Atmos. Chem. Phys.* **2009**, *9*, 7143–7160, doi:10.5194/acp-9-7143-2009.

94. Ferrero, L.; Castelli, M.; Ferrini, B.S.; Moscatelli, M.; Perrone, M.G.; Sangiorgi, G.; Angelo, L.D.; Rovelli, G. Impact of Black Carbon Aerosol over Italian Basin Valleys : High-Resolution Measurements along Vertical Profiles , Radiative Forcing and Heating Rate. **2014**, 9641–9664, doi:10.5194/acp-14-9641-2014.

95. Chakrabarty, R.K.; Garro, M.A.; Wilcox, E.M.; Moosmller, H. Strong Radiative Heating Due to Wintertime Black Carbon Aerosols in the Brahmaputra River Valley. *Geophys. Res. Lett.* **2012**, *39*, 1–5, doi:10.1029/2012GL051148.

96. Kedia, S.; Ramachandran, S.; Kumar, A.; Sarin, M.M. Spatiotemporal Gradients in Aerosol Radiative Forcing and Heating Rate over Bay of Bengal and Arabian Sea Derived on the Basis of Optical, Physical, and Chemical Properties. *J. Geophys. Res. Atmos.* **2010**, *115*, 1–17, doi:10.1029/2009JD013136.

97. Liou, K.N. *An Introduction to Atmospheric Radiation*; 2nd ed.; Academic Press: San Diego, CA, 2007;

98. Lu, Q.; Liu, C.; Zhao, D.; Zeng, C.; Li, J.; Lu, C.; Wang, J.; Zhu, B. Atmospheric Heating Rate Due to Black Carbon Aerosols: Uncertainties and Impact Factors. *Atmos. Res.* **2020**, *240*, doi:10.1016/j.atmosres.2020.104891.

99. Tripathi, S.N.; Srivastava, A.K.; Dey, S.; Satheesh, S.K.; Krishnamoorthy, K. The Vertical Profile of Atmospheric Heating Rate of Black Carbon Aerosols at Kanpur in Northern India. **2007**, *41*, 6909–6915, doi:10.1016/j.atmosenv.2007.06.032.

100. Ferrero, L.; Mocnik, G.; Ferrini, B.S.; Perrone, M.G.; Sangiorgi, G.; Bolzacchini, E. Science of the Total Environment Vertical pro Fi Les of Aerosol Absorption Coef Fi Cient from Micro-Aethalometer Data and Mie Calculation over Milan. *Sci. Total Environ.* **2011**, *409*, 2824–2837, doi:10.1016/j.scitotenv.2011.04.022.

101. Srivastava, A.K.; Ram, K.; Pant, P.; Hegde, P.; Joshi, H. Black Carbon Aerosols over Manora Peak in the Indian Himalayan Foothills: Implications for Climate Forcing. *Environ. Res. Lett.* **2012**, *7*, doi:10.1088/1748-9326/7/1/014002.

102. Donth, T.; Jakel, E.; Ehrlich, A.; Heinold, B.; Schacht, J.; Herber, A.; Zanatta, M.; Wendisch, M. Combining Atmospheric and Snow Radiative Transfer Models to Assess the Solar Radiative Effects of Black Carbon in the Arctic. *Atmos. Chem. Phys.* **2020**, *20*, 8139–8156, doi:10.5194/acp-20-8139-2020.

103. Koch, D.; Genio, A.D. Del And Physics Black Carbon Semi-Direct Effects on Cloud Cover : Review and Synthesis. **2010**, 7685–7696, doi:10.5194/acp-10-7685-2010.

104. Stjern, C.W.; Lund, M.T.; Samset, B.H.; Myhre, G.; Forster, P.M.; Andrews, T.; Boucher, O.; Faluvegi, G.; Fläschner, D.; Iversen, T.; et al. Arctic Amplification Response to Individual Climate Drivers. *J. Geophys. Res. Atmos.* **2019**, *124*, 6698–6717, doi:10.1029/2018JD029726.

105. Nordmann, S.; Cheng, Y.F.; Carmichael, G.R.; Yu, M.; van der Gon, H.A.C.; Zhang, Q.; Saide, P.E.; Pöschl, U.; Su, H.; Birmili, W.; et al. Atmospheric Black Carbon and Warming Effects Influenced by the Source and Absorption Enhancement in Central Europe. *Atmos. Chem. Phys.* **2014**, *14*, 12683–12699, doi:10.5194/acp-14-12683-2014.

106. Heald, C.L.; Ridley, D.A.; Kroll, J.H.; Barrett, S.R.H.; Cady-Pereira, K.E.; Alvarado, M.J.; Holmes, C.D. Contrasting the Direct Radiative Effect and Direct Radiative Forcing of Aerosols. *Atmos. Chem. Phys.* **2014**, *14*, 5513–5527.

107. Das, S.K.; Jayaraman, A. Role of Black Carbon in Aerosol Properties and Radiative Forcing over Western India during Premonsoon Period. *Atmos. Res.* **2011**, *102*, 320–334.

108. Drummond, A.J. Comments on "Sky Radiation Measurements and Corrections." *J. Appl. Meteorol.* **1964**, *3*, 810−811.

109. Bony, S.; Stevens, B.; Ament, F.; Bigorre, S.; Chazette, P.; Crewell, S.; Delanoë, J.; Emanuel, K.; Farrell, D.; Flamant, C.; et al. EUREC 4 A: A Field Campaign to Elucidate the Couplings between Clouds, Convection and Circulation. *Surv. Geophys.* **2017**, *38*, 1529–1568.

110. Chazette, P.; Baron, A.; Flamant, C. Mesoscale Spatio-Temporal Variability of Airborne Lidar-Derived Aerosol Properties in the Barbados Region during EUREC4A. *Atmos. Chem. Phys.* **2022**, *22*, 1271–1292, doi:10.5194/acp-22-1271-2022.

111. Cooper, W.A.; Lasher-Trapp, S.G.; Blyth, A.M. The Influence of Entrainment and Mixing on the Initial Formation of Rain in a Warm Cumulus Cloud. *J. Atmos. Sci.* **2013**, *70*, 1727–1743.

112. Li, X.-Y.; Brandenburg, A.; Svensson, G.; Haugen, N.E.L.; Mehlig, B.; Rogachevskii, I. Effect of Turbulence on Collisional Growth of Cloud Droplets. *J. Atmos. Sci.* **2018**, *75*, 3469–3487.

113. Pöhlker, M.L.; Ditas, F.; Saturno, J.; Klimach, T.; de Angelis, I.; Araùjo, A.C.; Brito, J.; Carbone, S.; Cheng, Y.; Chi, X.; et al. Long-Term Observations of Cloud Condensation Nuclei over the Amazon Rain Forest--Part 2: Variability and Characteristics of Biomass Burning, Long-Range Transport, and Pristine Rain Forest Aerosols. *Atmos. Chem. Phys.* **2018**, *18*, 10289–10331.

114. Wyszogrodzki, A.A.; Grabowski, W.W.; Wang, L.-P.; Ayala, O. Turbulent Collision-Coalescence in Maritime Shallow Convection. *Atmos. Chem. Phys.* **2013**, *13*, 8471–8487.

115. Farmer, D.K.; Cappa, C.D.; Kreidenweis, S.M. Atmospheric Processes and Their Controlling Influence on Cloud Condensation Nuclei Activity. *Chem. Rev.* **2015**, *115*, 4199–4217.

116. Chazette, P.; Totems, J.; Baron, A.; Flamant, C.; Bony, S. Trade-Wind Clouds and Aerosols Characterized by Airborne Horizontal Lidar Measurements during the EUREC4A Field Campaign. *Earth Syst. Sci. Data* **2020**, *12*, 2919–2936, doi:10.5194/essd-12-2919-2020.

117. Cakmur, R. V; Miller, R.L.; Perlwitz, J.; Geogdzhayev, I. V; Ginoux, P.; Koch, D.; Kohfeld, K.E.; Tegen, I.; Zender, C.S. Constraining the Magnitude of the Global Dust Cycle by Minimizing the Difference between a Model and Observations. *J. Geophys. Res. Atmos.* **2006**, *111*.

118. Prenni, A.J.; Petters, M.D.; Kreidenweis, S.M.; Heald, C.L.; Martin, S.T.; Artaxo, P.; Garland, R.M.; Wollny, A.G.; Pöschl, U. Relative Roles of Biogenic Emissions and Saharan Dust as Ice Nuclei in the Amazon Basin. *Nat. Geosci.* **2009**, *2*, 402–405.

119. Gutleben, M.; Groß, S.; Heske, C.; Wirth, M. Wintertime Saharan Dust Transport towards the Caribbean: An Airborne Lidar Case Study during EUREC4A. *Atmos. Chem. Phys.* **2022**, *22*, 7319–7330, doi:10.5194/acp-22-7319-2022.

120. Haarig, M.; Ansmann, A.; Althausen, D.; Klepel, A.; Groß, S.; Freudenthaler, V.; Toledano, C.; Mamouri, R.-E.; Farrell, D.A.; Prescod, D.A.; et al. Triple-Wavelength Depolarization-Ratio Profiling of Saharan Dust over Barbados during SALTRACE in 2013 and 2014. *Atmos. Chem. Phys.* **2017**, *17*, 10767–10794, doi:10.5194/acp-17-10767-2017.

121. Trapp, J.M.; Millero, F.J.; Prospero, J.M. Temporal Variability of the Elemental Composition of African Dust Measured in Trade Wind Aerosols at Barbados and Miami. *Mar. Chem.* **2010**, *120*, 71–82, doi:https://doi.org/10.1016/j.marchem.2008.10.004.

122. Prospero, J.M. Atmospheric Dust Studies on Barbados. *Bull. Am. Meteorol. Soc.* **1968**, *49*, 645–652.

123. Tsamalis, C.; Chédin, A.; Pelon, J.; Capelle, V. The Seasonal Vertical Distribution of the Saharan Air Layer and Its Modulation by the Wind. *Atmos. Chem. Phys.* **2013**, *13*, 11235–11257, doi:10.5194/acp-13-11235-2013.

124. Ben-Ami, Y.; Koren, I.; Altaratz, O. Patterns of North African Dust Transport over the Atlantic: Winter vs. Summer, Based on CALIPSO First Year Data. *Atmos. Chem. Phys.* **2009**, *9*, 7867–7875, doi:10.5194/acp-9-7867-2009.

125. van der Does, M.; Korte, L.F.; Munday, C.I.; Brummer, G.-J.A.; Stuut, J.-B.W. Particle Size Traces Modern Saharan Dust Transport and Deposition across the Equatorial North Atlantic. *Atmos. Chem. Phys.* **2016**, *16*, 13697–13710, doi:10.5194/acp-16-13697-2016.

126. Prospero, J.M.; Carlson, T.N. Vertical and Areal Distribution of Saharan Dust over the Western Equatorial North Atlantic Ocean. *J. Geophys. Res.* **1972**, *77*, 5255–5265.

127. Messager, C.; Parker, D.J.; Reitebuch, O.; Agusti-Panareda, A.; Taylor, C.M.; Cuesta, J. Structure and Dynamics of the Saharan Atmospheric Boundary Layer during the West African Monsoon Onset: Observations and Analyses from the Research Flights of 14 and 17 July 2006. *Q. J. R. Meteorol. Soc.* **2010**, *136*, 107–124.

128. Groß, S.; Tesche, M.; Freudenthaler, V.; Toledano, C.; Wiegner, M.; Ansmann, A.; Althausen, D.; Seefeldner, M. Characterization of Saharan Dust, Marine Aerosols and Mixtures of Biomass-Burning Aerosols and Dust by Means of Multi-Wavelength Depolarization and Raman Lidar Measurements during SAMUM 2. *Tellus, Ser. B Chem. Phys. Meteorol.* **2011**, *63*, 706–724, doi:10.1111/j.1600-0889.2011.00556.x.

129. Haarig, M.; Walser, A.; Ansmann, A.; Dollner, M.; Althausen, D.; Sauer, D.; Farrell, D.; Weinzierl, B. Profiles of Cloud Condensation Nuclei, Dust Mass Concentration, and Ice-Nucleating-Particle-Relevant Aerosol Properties in the Saharan Air Layer over Barbados from Polarization Lidar and Airborne in Situ Measurements. *Atmos. Chem. Phys.* **2019**, *19*, 13773–13788, doi:10.5194/acp-19-13773-2019.

130. Bègue, N.; Tulet, P.; Pelon, J.; Aouizerats, B.; Berger, A.; Schwarzenboeck, A. Aerosol Processing and CCN Formation of an Intense Saharan Dust Plume during the EUCAARI 2008 Campaign. *Atmos. Chem. Phys.* **2015**, *15*, 3497–3516, doi:10.5194/acp-15-3497-2015.

131. Boose, Y.; Sierau, B.; Garc\'\ia, M.I.; Rodr\'\iguez, S.; Alastuey, A.; Linke, C.; Schnaiter, M.; Kupiszewski, P.; Kanji, Z.A.; Lohmann, U. Ice Nucleating Particles in the Saharan Air Layer. *Atmos. Chem. Phys.* **2016**, *16*, 9067–9087, doi:10.5194/acp-16-9067-2016.

132. Seinfeld, J.H.; Pandis, S.N. *Atmospheric Chemistry and Physics: From Air Pollution to Climate Change*; John Wiley \& Sons, 2016;

133. Ferrero, L.; Riccio, A.; Ferrini, B.S.; D'Angelo, L.; Rovelli, G.; Casati, M.; Angelini, F.; Barnaba, F.; Gobbi, G.P.; Cataldi, M.; et al. Satellite AOD Conversion into Ground PM10, PM2.5 and PM1 over the Po Valley (Milan, Italy) Exploiting Information on Aerosol Vertical Profiles, Chemistry, Hygroscopicity and Meteorology. *Atmos. Pollut. Res.* **2019**, *10*, 1895–1912, doi:https://doi.org/10.1016/j.apr.2019.08.003.

134. D'Angelo, L.; Rovelli, G.; Casati, M.; Sangiorgi, G.; Perrone, M.G.; Bolzacchini, E.; Ferrero, L. Seasonal Behavior of PM2. 5 Deliquescence, Crystallization, and Hygroscopic Growth in the Po Valley (Milan): Implications for Remote Sensing Applications. *Atmos. Res.* **2016**, *176*, 87–95.

135. Yu, H.; Chin, M.; Yuan, T.; Bian, H.; Remer, L.A.; Prospero, J.M.; Omar, A.; Winker, D.; Yang, Y.; Zhang, Y.; et al. The Fertilizing Role of African Dust in the Amazon Rainforest: A First Multiyear Assessment Based on Data from Cloud-Aerosol Lidar and Infrared Pathfinder Satellite Observations. *Geophys. Res. Lett.* **2015**, *42*, 1984–1991.

136. Rodríguez, S.; Cuevas, E. The Contributions of "Minimum Primary Emissions" and "New Particle Formation Enhancements" to the Particle Number Concentration in Urban Air. *J. Aerosol Sci.* **2007**, *38*, 1207–1219, doi:https://doi.org/10.1016/j.jaerosci.2007.09.001.

137. Dall'Osto, M.; Querol, X.; Alastuey, A.; O'Dowd, C.; Harrison, R.M.; Wenger, J.; Gómez-Moreno, F.J. On the Spatial Distribution and Evolution of Ultrafine Particles in Barcelona. *Atmos. Chem. Phys.* **2013**, *13*, 741–759, doi:10.5194/acp-13-741-2013.

138. Reche, C.; Querol, X.; Alastuey, A.; Viana, M.; Pey, J.; Moreno, T.; Rodr\'\iguez, S.; González, Y.; Fernández-Camacho, R.; la Rosa, J.; et al. New Considerations for PM, Black Carbon and Particle Number Concentration for Air Quality Monitoring across Different European Cities. *Atmos. Chem. Phys.* **2011**, *11*, 6207–6227.

139. Bates, T.S.; Quinn, P.K.; Coffman, D.J.; Johnson, J.E.; Miller, T.L.; Covert, D.S.; Wiedensohler, A.; Leinert, S.; Nowak, A.; Neusüss, C. Regional Physical and Chemical Properties of the Marine Boundary Layer Aerosol across the Atlantic during Aerosols99: An Overview. *J. Geophys. Res. Atmos.* **2001**, *106*, 20767–20782.

140. MIHALOPOULOS, N.; STEPHANOU, E.; KANAKIDOU, M.; PILITSIDIS, S.; BOUSQUET, P. Tropospheric Aerosol Ionic Composition in the Eastern Mediterranean Region. *Tellus B* **1997**, *49*, 314–326, doi:https://doi.org/10.1034/j.1600-0889.49.issue3.7.x.

141. Xu, G.; Gao, Y.; Lin, Q.; Li, W.; Chen, L. Characteristics of Water-Soluble Inorganic and Organic Ions in Aerosols over the Southern Ocean and Coastal East Antarctica during Austral Summer. *J. Geophys. Res. Atmos.* **2013**, *118*, 13,303-13,318, doi:10.1002/2013JD019496.

142. Legrand, M.; Ducroz, F.; Wagenbach, D.; Mulvaney, R.; Hall, J. Ammonium in Coastal Antarctic Aerosol and Snow: Role of Polar Ocean and Penguin Emissions. *J. Geophys. Res. Atmos.* **1998**, *103*, 11043–11056.

143. Blackall, T.D.; Wilson, L.J.; Theobald, M.R.; Milford, C.; Nemitz, E.; Bull, J.; Bacon, P.J.; Hamer, K.C.; Wanless, S.; Sutton, M.A. Ammonia Emissions from Seabird Colonies. *Geophys. Res. Lett.* **2007**, *34*.

144. Riddick, S.N.; Dragosits, U.; Blackall, T.D.; Daunt, F.; Wanless, S.; Sutton, M.A. The Global Distribution of Ammonia Emissions from Seabird Colonies. *Atmos. Environ.* **2012**, *55*, 319–327.

145. Flamant, C.; Pelon, J.; Chazette, P.; Trouillet, V.; Quinn, P.K.; Frouin, R.; Bruneau, D.; François Leon, J.; Bates, T.S.; Johnson, J.; et al. Airborne Lidar Measurements of Aerosol Spatial Distribution and Optical Properties over the Atlantic Ocean during a European Pollution Outbreak of ACE-2. *Tellus B* **2000**, *52*, 662–677.

146. Martin, S.T. Phase Transitions of Aqueous Atmospheric Particles. *Chem. Rev.* **2000**, *100*, 3403–3454.

147. Wexler, A.S.; Clegg, S.L. Atmospheric Aerosol Models for Systems Including the Ions H+, NH4+, Na+, SO42-, NO3-, Cl-, Br-, and H2O. *J. Geophys. Res. Atmos.* **2002**, *107*,

ACH--14.

148. Petters, M.D.; Kreidenweis, S.M. A Single Parameter Representation of Hygroscopic Growth and Cloud Condensation Nucleus Activity. *Atmos. Chem. Phys.* **2007**, *13*, 1081–1091, doi:10.5194/acp-13-1081-2013.

149. Tesche, M.; Gross, S.; Ansmann, A.; Mueller, D.; Althausen, D.; Freudenthaler, V.; Esselborn, M. Profiling of Saharan Dust and Biomass-Burning Smoke with Multiwavelength Polarization Raman Lidar at Cape Verde. *Tellus B* **2011**, *63*, 649–676.

150. Tesche, M.; Ansmann, A.; Müller, D.; Althausen, D.; Engelmann, R.; Freudenthaler, V.; Groß, S. Vertically Resolved Separation of Dust and Smoke over Cape Verde Using Multiwavelength Raman and Polarization Lidars during Saharan Mineral Dust Experiment 2008. *J. Geophys. Res. Atmos.* **2009**, *114*.

151. Becagli, S.; Caiazzo, L.; Di Iorio, T.; di Sarra, A.; Meloni, D.; Muscari, G.; Pace, G.; Severi, M.; Traversi, R. New Insights on Metals in the Arctic Aerosol in a Climate Changing World. *Sci. Total Environ.* **2020**, *741*, 140511, doi:10.1016/j.scitotenv.2020.140511.

152. Law, K.S.; Stohl, A. Arctic Air Pollution: Origins and Impacts. *Science (80-.).* **2007**, *315*, 1537–1540, doi:10.1126/science.1137695.

153. Chow, J.C.; Wang, X.; Sumlin, B.J.; Gronstal, S.B.; Chen, L.A.; Trimble, D.L.; Kohl, S.D.; Mayorga, S.R.; Riggio, G.; Hurbain, P.R.; et al. Optical Calibration and Equivalence of a Multiwavelength Thermal / Optical Carbon Analyzer. **2015**, 1145–1159, doi:10.4209/aaqr.2015.02.0106.

154. Cavalli, F.; Viana, M.; Yttri, K.E.; Genberg, J.; Putaud, J.-P. Toward a Standardised Thermal-Optical Protocol for Measuring Atmospheric Organic and Elemental Carbon: The EUSAAR Protocol. *Atmos. Meas. Tech.* **2010**, *3*, 79–89, doi:10.5194/amt-3-79-2010.

155. Ivančič, M.; Gregorič, A.; Lavrič, G.; Alföldy, B.; Ježek, I.; Hasheminassab, S.; Pakbin, P.; Ahangar, F.; Sowlat, M.; Boddeker, S.; et al. Two-Year-Long High-Time-Resolution Apportionment of Primary and Secondary Carbonaceous Aerosols in the Los Angeles Basin Using an Advanced Total Carbon–Black Carbon (TC-BC(λ)) Method. *Sci. Total Environ.* **2022**, *848*, doi:10.1016/j.scitotenv.2022.157606.

156. Savadkoohi, M.; Pandolfi, M.; Favez, O.; Putaud, J.P.; Eleftheriadis, K.; Fiebig, M.;

Hopke, P.K.; Laj, P.; Wiedensohler, A.; Alados-Arboledas, L.; et al. Recommendations for Reporting Equivalent Black Carbon (EBC) Mass Concentrations Based on Long-Term Pan-European in-Situ Observations. *Environ. Int.* **2024**, *185*, doi:10.1016/j.envint.2024.108553.

157. Ballabio, D. A MATLAB Toolbox for Principal Component Analysis and Unsupervised Exploration of Data Structure. *Chemom. Intell. Lab. Syst.* **2015**, *149*, 1–9, doi:10.1016/j.chemolab.2015.10.003.

158. Pilson, M.E.Q. *An Introduction to the Chemistry of the Sea*; 2nd ed.; Cambridge university press: Cambridge, UK, 2012; ISBN 1139619209.

159. Moroni, B.; Arnalds, O.; Dagsson-Waldhauserová, P.; Crocchianti, S.; Vivani, R.; Cappelletti, D. Mineralogical and Chemical Records of Icelandic Dust Sources upon Ny-Ålesund (Svalbard Islands). *Front. Earth Sci.* **2018**, *6*, 1–13, doi:10.3389/feart.2018.00187.

160. Moroni, B.; Becagli, S.; Bolzacchini, E.; Busetto, M.; Cappelletti, D.; Crocchianti, S.; Ferrero, L.; Frosini, D.; Lanconelli, C.; Lupi, A.; et al. Vertical Profiles and Chemical Properties of Aerosol Particles upon Ny-Ålesund (Svalbard Islands). *Adv. Meteorol.* **2015**, *2015*, doi:10.1155/2015/292081.

161. Massling, A.; Nielsen, I.E.; Kristensen, D.; Christensen, J.H.; Sorensen, L.L.; Jensen, B.; Nguyen, Q.T.; Nøjgaard, J.K.; Glasius, M.; Skov, H. Atmospheric Black Carbon and Sulfate Concentrations in Northeast Greenland. *Atmos. Chem. Phys.* **2015**, *15*, 9681–9692, doi:10.5194/acp-15-9681-2015.

162. Amore, A.; Giardi, F.; Becagli, S.; Caiazzo, L.; Mazzola, M.; Severi, M.; Traversi, R. Source Apportionment of Sulphate in the High Arctic by a 10 Yr-Long Record from Gruvebadet Observatory (Ny-Ålesund, Svalbard Islands). *Atmos. Environ.* **2022**, *270*, 118890, doi:10.1016/j.atmosenv.2021.118890.

163. Moffett, C.E.; Barrett, T.E.; Liu, J.; Gunsch, M.J.; Upchurch, L.M.; Quinn, P.K.; Pratt, K.A.; Sheesley, R.J. Long-Term Trends for Marine Sulfur Aerosol in the Alaskan Arctic and Relationships With Temperature. *J. Geophys. Res. Atmos.* **2020**, *125*, 1–19, doi:10.1029/2020JD033225.

164. Udisti, R.; Bazzano, A.; Becagli, S.; Bolzacchini, E.; Caiazzo, L.; Cappelletti, D.; Ferrero,

L.; Frosini, D.; Giardi, F.; Grotti, M.; et al. Sulfate Source Apportionment in the Ny-Ålesund (Svalbard Islands) Arctic Aerosol. *Rend. Lincei* **2016**, *27*, 85–94, doi:10.1007/s12210-016-0517-7.

165. "Vestreng, V.; "Kallenborn, R.; "Oekstad, E. *Norwegian Arctic Climate. Climate Influencing Emissions, Scenarios and Mitigation Options at Svalbard*; Olso, Norway, 2010;

166. Weinbruch, S.; Drotikova, T.; Kallenborn, R. *Particulate and Gaseous Emissions of Power Generation at Svalbard (AtmoPart)*; 2015;

167. Ringkjøb, H.K.; Haugan, P.M.; Nybø, A. Transitioning Remote Arctic Settlements to Renewable Energy Systems – A Modelling Study of Longyearbyen, Svalbard. *Appl. Energy* **2020**, *258*, 114079, doi:10.1016/j.apenergy.2019.114079.

168. Conca, E.; Abollino, O.; Giacomino, A.; Buoso, S.; Traversi, R.; Becagli, S.; Grotti, M.; Malandrino, M. Source Identification and Temporal Evolution of Trace Elements in PM10 Collected near to Ny-Ålesund (Norwegian Arctic). *Atmos. Environ.* **2019**, *203*, 153–165, doi:https://doi.org/10.1016/j.atmosenv.2019.02.001.

169. Giardi, F.; Traversi, R.; Becagli, S.; Severi, M.; Caiazzo, L.; Ancillotti, C.; Udisti, R. Determination of Rare Earth Elements in Multi-Year High-Resolution Arctic Aerosol Record by Double Focusing Inductively Coupled Plasma Mass Spectrometry with Desolvation Nebulizer Inlet System. *Sci. Total Environ.* **2018**, *613–614*, 1284–1294, doi:https://doi.org/10.1016/j.scitotenv.2017.09.247.

170. Paatero, J.; Vaattovaara, P.; Vestenius, M.; Meinander, O.; Makkonen, U.; Kivi, R.; Hyvärinen, A.; Asmi, E.; Tjernström, M.; Leck, C. Finnish Contribution to the Arctic Summer Cloud Ocean Study (ASCOS) Expedition, Arctic Ocean 2008. *Geophysica* **2009**, *45*, 119–146.

171. Maenhaut, W.; Ducastel, G.; Leck, C.; Nilsson, E.D.; Heintzenberg, J. Multi-Elemental Composition and Sources of the High Arctic Atmospheric Aerosol during Summer and Autumn. *Tellus B* **1996**, *48*, 300–321.

172. Shevchenko, V.; Lisitzin, A.; Vinogradova, A.; Stein, R. Heavy Metals in Aerosols over the Seas of the Russian Arctic. *Sci. Total Environ.* **2003**, *306*, 11–25.

173. Heidam, N.Z.; Christensen, J.; Wåhlin, P.; Skov, H. Arctic Atmospheric Contaminants

in NE Greenland: Levels, Variations, Origins, Transport, Transformations and Trends 1990--2001. *Sci. Total Environ.* **2004**, *331*, 5–28.

174. Kyllönen, K.; Vestenius, M.; Anttila, P.; Makkonen, U.; Aurela, M.; Wängberg, I.; Nerentorp Mastromonaco, M.; Hakola, H. Trends and Source Apportionment of Atmospheric Heavy Metals at a Subarctic Site during 1996–2018. *Atmos. Environ.* **2020**, *236*, doi:10.1016/j.atmosenv.2020.117644.

175. Nguyen, Q.T.; Skov, H.; Sørensen, L.L.; Jensen, B.J.; Grube, A.G.; Massling, A.; Glasius, M.; Nøjgaard, J.K. Source Apportionment of Particles at Station Nord, North East Greenland during 2008-2010 Using COPREM and PMF Analysis. *Atmos. Chem. Phys.* **2013**, *13*, 35–49, doi:10.5194/acp-13-35-2013.

176. Gautier, D.L.; Bird, K.J.; Charpentier, R.R.; Grantz, A.; Houseknecht, D.W.; Klett, T.R.; Moore, T.E.; Pitman, J.K.; Schenk, C.J.; Schuenemeyer, J.H.; et al. Assessment of Undiscovered Oil and Gas in the Arctic. *Science (80-.).* **2009**, *324*, 1175–1179.

177. Ødemark, K.; Dalsøren, S.B.; Samset, B.H.; Berntsen, T.K.; Fuglestvedt, J.S.; Myhre, G. Short-Lived Climate Forcers from Current Shipping and Petroleum Activities in the Arctic. *Atmos. Chem. Phys.* **2012**, *12*, 1979–1993.

178. Sander, R.; Bottenheim, J. A Compilation of Tropospheric Measurements of Gas-Phase and Aerosol Chemistry in Polar Regions. *Earth Syst. Sci. Data* **2012**, *4*, 215–282, doi:10.5194/essd-4-215-2012.

179. Wang, D.; Wilhelmy, S.A.S. Vanadium Speciation and Cycling in Coastal Waters. *Mar. Chem.* **2009**, *117*, 52–58.

180. Li, C.; Cornett, J. Increased Zinc Concentrations in the Canadian Arctic Air. *Atmos. Pollut. Res.* **2011**, *2*, 45–48.

181. Popovicheva, O.B.; Evangeliou, N.; Kobelev, V.O.; Chichaeva, M.A.; Eleftheriadis, K.; Gregorič, A.; Kasimov, N.S. Siberian Arctic Black Carbon: Gas Flaring and Wildfire Impact. *Atmos. Chem. Phys.* **2022**, *22*, 5983–6000, doi:10.5194/acp-22-5983-2022.

182. England, M.R.; Eisenman, I.; Lutsko, N.J.; Wagner, T.J.W. The Recent Emergence of Arctic Amplification. *Geophys. Res. Lett.* **2021**, *48*, 1–10, doi:10.1029/2021GL094086.

183. Maturilli, M.; Herber, A.; König-langlo, G. Surface Radiation Climatology for Ny-

Ålesund , Svalbard (78 . 9 ° N), Basic Observations for Trend Detection Corresponding Author : Short- and Longwave Radiation Are Operated since August 1992 in the Frame of the Baseline since August 1993 . The Long-Te. *Theor Appl Clim.* **2015**, *120*, 331–339, doi:10.1594/PANGAEA.150000.

184. Eleftheriadis, K.; Vratolis, S.; Nyeki, S. Aerosol Black Carbon in the European Arctic: Measurements at Zeppelin Station, Ny-Ålesund, Svalbard from 1998-2007. *Geophys. Res. Lett.* **2009**, *36*, 1–5, doi:10.1029/2008GL035741.

185. Groot Zwaaftink, C.D.; Arnalds, Ó.; Dagsson-Waldhauserova, P.; Eckhardt, S.; Prospero, J.M.; Stohl, A. Temporal and Spatial Variability of Icelandic Dust Emissions and Atmospheric Transport. *Atmos. Chem. Phys.* **2017**, *17*, 10865–10878, doi:10.5194/acp-17-10865-2017.

186. Ramanathan, V.; Feng, Y. Air Pollution , Greenhouse Gases and Climate Change : Global and Regional Perspectives. *Atmos. Environ.* **2009**, *43*, 37–50, doi:10.1016/j.atmosenv.2008.09.063.

187. Ramana, M. V; Ramanathan, V.; Kim, D.; Roberts, G.C.; Corrigan, C.E. Albedo , Atmospheric Solar Absorption and Heating Rate Measurements with Stacked UAVs. **2007**, *1931*, 1913–1931, doi:10.1002/qj.

188. Ferrero, L.; Gregoriˇ, A.; Moˇ, G.; Liberto, L. Di; Gobbi, G.P.; Losi, N.; Bolzacchini, E. The Impact of Cloudiness and Cloud Type on the Atmospheric Heating Rate of Black and Brown Carbon in the Po Valley. **2021**, 4869–4897.

189. WON, J.-G.; YOON, S.-C.; KIM, S.-W.; JEFFERSON, A.; DUTTON, E.G.; HOLBEN, B.N. Estimation of Direct Radiative Forcing of Asian Dust Aerosols with Sun/Sky Radiometer and Lidar Measurements at Gosan, Korea. *気象集誌. 第2輯* **2004**, *82*, 115–130, doi:10.2151/jmsj.82.115.

190. Chung, C.E.; Ramanathan, V.; Decremer, D. Observationally Constrained Estimates of Carbonaceous Aerosol Radiative Forcing. *Proc. Natl. Acad. Sci.* **2012**, *109*, 11624–11629, doi:10.1073/pnas.1203707109.

191. Shamjad, P.M.; Tripathi, S.N.; Pathak, R.; Hallquist, M.; Arola, A.; Bergin, M.H. Contribution of Brown Carbon to Direct Radiative Forcing over the Indo-Gangetic Plain.

Environ. Sci. Technol. **2015**, *49*, 10474–10481, doi:10.1021/acs.est.5b03368.

192. Lau, W.K.M.; Kim, M.-K.; Kim, K.-M.; Lee, W.-S. Enhanced Surface Warming and Accelerated Snow Melt in the Himalayas and Tibetan Plateau Induced by Absorbing Aerosols. *Environ. Res. Lett.* **2010**, *5*, 25204, doi:10.1088/1748-9326/5/2/025204.

193. Flanner, M.G. Arctic Climate Sensitivity to Local Black Carbon. *J. Geophys. Res. Atmos.* **2013**, *118*, 1840–1851, doi:10.1002/jgrd.50176.

194. Levy, H.; Schwarzkopf, M.D.; Horowitz, L.; Ramaswamy, V.; Findell, K.L. Strong Sensitivity of Late 21st Century Climate to Projected Changes in Short-Lived Air Pollutants. *J. Geophys. Res. Atmos.* **2008**, *113*, 1–13, doi:10.1029/2007JD009176.

195. Quinn, P.K.; Bates, T.S.; Baum, E.; Doubleday, N.; Fiore, A.M.; Flanner, M.; Fridlind, A.; Garrett, T.J.; Koch, D.; Menon, S.; et al. Short-Lived Pollutants in the Arctic: Their Climate Impact and Possible Mitigation Strategies. *Atmos. Chem. Phys.* **2008**, *8*, 1723–1735, doi:10.5194/acp-8-1723-2008.

196. Treffeisen, R.; Rinke, A.; Fortmann, M.; Dethloff, K.; Herber, A.; Yamanouchi, T. A Case Study of the Radiative Effects of Arctic Aerosols in March 2000. *Atmos. Environ.* **2005**, *39*, 899–911, doi:10.1016/j.atmosenv.2004.09.066.

197. Treffeisen, R.; Tunved, P.; Ström, J.; Herber, A.; Bareiss, J.; Heibig, A.; Stone, R.S.; Hoyningen-Huene, W.; Krejci, R.; Stohl, A.; et al. Arctic Smoke - Aerosol Characteristics during a Record Smoke Event in the European Arctic and Its Radiative Impact. *Atmos. Chem. Phys.* **2007**, *7*, 3035–3053, doi:10.5194/acp-7-3035-2007.

198. Porch, W.M.; MacCracken, M.C. Parametric Study of the Effects of Arctic Soot on Solar Radiation. *Atmos. Environ.* **1982**, *16*, 1365–1371, doi:10.1016/0004-6981(82)90057-9.

199. Gilardoni, S.; Lupi, A.; Mazzola, M.; Cappelletti, D.M.; Moroni, B.; Ferrero, L.; Markuszewski, P.; Rozwadowska, A.; Krejci, R.; Zieger, P.; et al. *Atmospheric Black Carbon in Svalbard (ABC Svalbard)*; 2020;

200. Zbizika, R.; Pakszys, P.; Zielinski, T. Deep Neural Networks for Aerosol Optical Depth Retrieval. *Atmosphere (Basel).* **2022**, *13*, doi:10.3390/atmos13010101.

201. Eckhardt, S.; Hermansen, O.; Grythe, H.; Fiebig, M.; Stebel, K.; Cassiani, M.; Baecklund, A.; Stohl, A. The Influence of Cruise Ship Emissions on Air Pollution in Svalbard

– a Harbinger of a More Polluted Arctic? *Atmos. Chem. Phys.* **2013**, *13*, 8401–8409, doi:10.5194/acp-13-8401-2013.

202. Aliabadi, A.A.; Staebler, R.M.; Sharma, S. Air Quality Monitoring in Communities of the Canadian Arctic during the High Shipping Season with a Focus on Local and Marine Pollution. *Atmos. Chem. Phys.* **2015**, *15*, 2651–2673, doi:10.5194/acp-15-2651-2015.

203. Winiger, P.; Andersson, A.; Eckhardt, S.; Stohl, A.; Semiletov, I.P.; Dudarev, O. V; Charkin, A.; Shakhova, N.; Klimont, Z.; Heyes, C.; et al. Siberian Arctic Black Carbon Sources Constrained by Model and Observation. *Proc. Natl. Acad. Sci.* **2017**, *114*, E1054–E1061, doi:10.1073/pnas.1613401114.

204. Sobhani, N.; Kulkarni, S.; Carmichael, G.R. Source Sector and Region Contributions to Black Carbon and PM2.5 in the Arctic. *Atmos. Chem. Phys.* **2018**, *18*, 18123–18148, doi:10.5194/acp-18-18123-2018.

205. Sharma, S.; Ishizawa, M.; Chan, D.; Lavoué, D.; Andrews, E.; Eleftheriadis, K.; Maksyutov, S. 16-Year Simulation of Arctic Black Carbon: Transport, Source Contribution, and Sensitivity Analysis on Deposition. *J. Geophys. Res. Atmos.* **2013**, *118*, 943–964, doi:10.1029/2012JD017774.

206. Kalogridis, A-C.; Fiebig, M.; Močnik, G.; Muller, T.; Krejci, R.; Vratolis, S.; Gini, M.; Wiedensholer, A.; Eleftheriadis, K. Aethalometer Multiple Scattering Correction for Measuring Aerosol Absorption in the Arctic. In Proceedings of the European Aerosol Conference 2020; Aachen, Germany, 2020; p. 341.

207. Takegawa, N.; Sakurai, H. Laboratory Evaluation of a TSI Condensation Particle Counter (Model 3771) under Airborne Measurement Conditions. *Aerosol Sci. Technol.* **2011**, *45*, 272–283, doi:10.1080/02786826.2010.532839.

208. Dart, A.; Thornburg, J. Collection Efficiencies of Bioaerosol Impingers for Virus-Containing Aerosols. *Atmos. Environ.* **2008**, *42*, 828–832, doi:https://doi.org/10.1016/j.atmosenv.2007.11.003.

209. Hofmann, W.; Winkler-Heil, R.; McAughey, J. Regional Lung Deposition of Aged and Diluted Sidestream Tobacco Smoke. *J. Phys. Conf. Ser.* **2009**, *151*, doi:10.1088/1742-6596/151/1/012020.

210. Markuszewski, P.; Rozwadowska, A.; Cisek, M.; Makuch, P.; Petelski, T. Aerosol Physical Properties in Spitsbergen's Fjords: Hornsund and Kongsfjorden during AREX Campaigns in 2014 and 2015. *Oceanologia* **2017**, *59*, 460–472, doi:10.1016/j.oceano.2017.03.012.

211. Ferrero, L.; Scibetta, L.; Markuszewski, P.; Mazurkiewicz, M.; Drozdowska, V.; Makuch, P.; Jutrzenka-Trzebiatowska, P.; Zaleska-Medynska, A.; Andò, S.; Saliu, F.; et al. Airborne and Marine Microplastics from an Oceanographic Survey at the Baltic Sea: An Emerging Role of Air-Sea Interaction? *Sci. Total Environ.* **2022**, *824*, 153709, doi:https://doi.org/10.1016/j.scitotenv.2022.153709.

212. Liu, J.; Fan, S.; Horowitz, L.W.; Levy, H. Evaluation of Factors Controlling Long-Range Transport of Black Carbon to the Arctic. *J. Geophys. Res. Atmos.* **2011**, *116*, doi:10.1029/2010JD015145.

213. Heintzenberg, J.; Leck, C. Seasonal Variation of the Atmospheric Aerosol near the Top of the Marine Boundary Layer over Spitsbergen Related to the Arctic Sulphur Cycle. *Tellus B Chem. Phys. Meteorol.* **1994**, *46*, 52–67.

214. Matsui, H.; Liu, M. Importance of Supersaturation in Arctic Black Carbon Simulations. *J. Clim.* **2021**, *34*, 7843–7856, doi:10.1175/JCLI-D-20-0994.1.

215. Beine, H.J.; Argentini, S.; Maurizi, A.; Mastrantonio, G.; Viola, A. The Local Wind Field at Ny-Å Lesund and the Zeppelin Mountain at Svalbard. *Meteorol. Atmos. Phys.* **2001**, *78*, 107–113.

216. Gogoi, M.M.; Babu, S.S.; Moorthy, K.K.; Thakur, R.C.; Chaubey, J.P.; Nair, V.S. Aerosol Black Carbon over Svalbard Regions of Arctic. *Polar Sci.* **2016**, *10*, 60–70, doi:10.1016/j.polar.2015.11.001.

217. Rinaldi, M.; Hiranuma, N.; Santachiara, G.; Mazzola, M.; Mansour, K.; Paglione, M.; Rodriguez, C.A.; Traversi, R.; Becagli, S.; Cappelletti, D. Ice-Nucleating Particle Concentration Measurements from Ny-Ålesund during the Arctic Spring–Summer in 2018. *Atmos. Chem. Phys.* **2021**, *21*, 14725–14748.

218. Tunved, P.; Ström, J.; Krejci, R. Arctic Aerosol Life Cycle: Linking Aerosol Size Distributions Observed between 2000 and 2010 with Air Mass Transport and

Precipitation at Zeppelin Station, Ny-Ålesund, Svalbard. *Atmos. Chem. Phys.* **2013**, *13*, 3643–3660, doi:10.5194/acp-13-3643-2013.

219. Serreze, M.C.; Barry, R.G. Processes and Impacts of Arctic Amplification: A Research Synthesis. *Glob. Planet. Change* **2011**, *77*, 85–96, doi:10.1016/j.gloplacha.2011.03.004.

220. Holland, M.M.; Bitz, C.M. Polar Amplification of Climate Change in Coupled Models. *Clim. Dyn.* **2003**, *21*, 221–232, doi:10.1007/s00382-003-0332-6.

221. Pithan, F.; Mauritsen, T. Arctic Amplification Dominated by Temperature Feedbacks in Contemporary Climate Models. *Nat. Geosci.* **2014**, *7*, 181–184, doi:10.1038/ngeo2071.

222. Park, H.S.; Kim, S.J.; Stewart, A.L.; Son, S.W.; Seo, K.H. Mid-Holocene Northern Hemisphere Warming Driven by Arctic Amplification. *Sci. Adv.* **2019**, *5*, doi:10.1126/sciadv.aax8203.

223. Miller, G.H.; Alley, R.B.; Brigham-Grette, J.; Fitzpatrick, J.J.; Polyak, L.; Serreze, M.C.; White, J.W.C. Arctic Amplification: Can the Past Constrain the Future? *Quat. Sci. Rev.* **2010**, *29*, 1779–1790, doi:https://doi.org/10.1016/j.quascirev.2010.02.008.

224. Chung, E.S.; Ha, K.J.; Timmermann, A.; Stuecker, M.F.; Bodai, T.; Lee, S.K. Cold-Season Arctic Amplification Driven by Arctic Ocean-Mediated Seasonal Energy Transfer. *Earth's Futur.* **2021**, *9*, 1–17, doi:10.1029/2020EF001898.

225. Thackeray, C.W.; Hall, A. An Emergent Constraint on Future Arctic Sea-Ice Albedo Feedback. *Nat. Clim. Chang.* **2019**, *9*, 972–978, doi:10.1038/s41558-019-0619-1.

226. Dai, A.; Luo, D.; Song, M.; Liu, J. Arctic Amplification Is Caused by Sea-Ice Loss under Increasing CO 2. *Nat. Commun.* **2019**, *10*, 1–13, doi:10.1038/s41467-018-07954-9.

227. Dallósto, M.; Beddows, D.C.S.; Tunved, P.; Krejci, R.; Ström, J.; Hansson, H.C.; Yoon, Y.J.; Park, K.T.; Becagli, S.; Udisti, R.; et al. Arctic Sea Ice Melt Leads to Atmospheric New Particle Formation. *Sci. Rep.* **2017**, *7*, 1–10, doi:10.1038/s41598-017-03328-1.

228. Cao, Y.; Liang, S.; Chen, X.; He, T.; Wang, D.; Cheng, X. Enhanced Wintertime Greenhouse Effect Reinforcing Arctic Amplification and Initial Sea-Ice Melting. *Sci. Rep.* **2017**, *7*, 8462.

229. Pabi, S.; van Dijken, G.L.; Arrigo, K.R. Primary Production in the Arctic Ocean, 1998--2006. *J. Geophys. Res. Ocean.* **2008**, *113*.

230. Mewes, D.; Jacobi, C. Heat Transport Pathways into the Arctic and Their Connections to Surface Air Temperatures. *Atmos. Chem. Phys.* **2019**, *19*, 3927–3937, doi:10.5194/acp-19-3927-2019.

231. Graversen, R.G. Do Changes in the Midlatitude Circulation Have Any Impact on the Arctic Surface Air Temperature Trend? *J. Clim.* **2006**, *19*, 5422–5438, doi:10.1175/JCLI3906.1.

232. Roe, G.H.; Feldl, N.; Armour, K.C.; Hwang, Y.-T.; Frierson, D.M.W. The Remote Impacts of Climate Feedbacks on Regional Climate Predictability. *Nat. Geosci.* **2015**, *8*, 135–139.

233. Feldl, N.; Bordoni, S.; Merlis, T.M. Coupled High-Latitude Climate Feedbacks and Their Impact on Atmospheric Heat Transport. *J. Clim.* **2017**, *30*, 189–201.

234. Hwang, Y.-T.; Frierson, D.M.W.; Kay, J.E. Coupling between Arctic Feedbacks and Changes in Poleward Energy Transport. *Geophys. Res. Lett.* **2011**, *38*.

235. Graversen, R.G.; Langen, P.L. On the Role of the Atmospheric Energy Transport in 2$\times$ CO 2--Induced Polar Amplification in CESM1. *J. Clim.* **2019**, *32*, 3941–3956.

236. Cohen, J.; Screen, J.A.; Furtado, J.C.; Barlow, M.; Whittleston, D.; Coumou, D.; Francis, J.; Dethloff, K.; Entekhabi, D.; Overland, J.; et al. Recent Arctic Amplification and Extreme Mid-Latitude Weather. *Nat. Geosci.* 2014, *7*.

237. Francis, J.A.; Vavrus, S.J.; Cohen, J. Amplified Arctic Warming and Mid-Latitude Weather: New Perspectives on Emerging Connections. *Wiley Interdiscip. Rev. Clim. Chang.* **2017**, *8*, e474.

238. Zhang, P.; Chen, G.; Ting, M.; Ruby Leung, L.; Guan, B.; Li, L. More Frequent Atmospheric Rivers Slow the Seasonal Recovery of Arctic Sea Ice. *Nat. Clim. Chang.* **2023**, *13*, 266–273, doi:10.1038/s41558-023-01599-3.

239. Yim, B.Y.; Yeh, S.-W.; Kug, J.-S. Inter-Model Diversity of Arctic Amplification Caused by Global Warming and Its Relationship with the Inter-Tropical Convergence Zone in CMIP5 Climate Models. *Clim. Dyn.* **2017**, *48*, 3799–3811.

240. Deser, C.; Phillips, A.S.; Simpson, I.R.; Rosenbloom, N.; Coleman, D.; Lehner, F.; Pendergrass, A.G.; DiNezio, P.; Stevenson, S. Isolating the Evolving Contributions of

Anthropogenic Aerosols and Greenhouse Gases: A New CESM1 Large Ensemble Community Resource. *J. Clim.* **2020**, *33*, 7835–7858.

241. Mueller, B.L.; Gillett, N.P.; Monahan, A.H.; Zwiers, F.W. Attribution of Arctic Sea Ice Decline from 1953 to 2012 to Influences from Natural, Greenhouse Gas, and Anthropogenic Aerosol Forcing. *J. Clim.* **2018**, *31*, 7771–7787.

242. Groot Zwaaftink, C.D.; Grythe, H.; Skov, H.; Stohl, A. Substantial Contribution of Northern High-Latitude Sources to Mineral Dust in the Arctic. *J. Geophys. Res.* **2016**, *121*, 13,678-13,697, doi:10.1002/2016JD025482.

243. Dou, T.F.; Xiao, C. De An Overview of Black Carbon Deposition and Its Radiative Forcing over the Arctic. *Adv. Clim. Chang. Res.* **2016**, *7*, 115–122, doi:10.1016/j.accre.2016.10.003.

244. Beck, L.J.; Sarnela, N.; Junninen, H.; Hoppe, C.J.M.; Garmash, O.; Bianchi, F.; Riva, M.; Rose, C.; Peräkylä, O.; Wimmer, D.; et al. Differing Mechanisms of New Particle Formation at Two Arctic Sites. *Geophys. Res. Lett.* **2021**, *48*, 1–11, doi:10.1029/2020GL091334.

245. Breider, T.J.; Mickley, L.J.; Jacob, D.J.; Ge, C.; Wang, J.; Sulprizio, M.P.; Croft, B.; Ridley, D.A.; McConnell, J.R.; Sharma, S.; et al. Multidecadal Trends in Aerosol Radiative Forcing over the Arctic: Contribution of Changes in Anthropogenic Aerosol to Arctic Warming since 1980. *J. Geophys. Res.* **2017**, *122*, 3573–3594, doi:10.1002/2016JD025321.

246. Vestreng, V.; Myhre, G.; Fagerli, H.; Reis, S.; Tarrasón, L. Twenty-Five Years of Continuous Sulphur Dioxide Emission Reduction in Europe. *Atmos. Chem. Phys.* **2007**, *7*, 3663–3681, doi:10.5194/acp-7-3663-2007.

247. Wang, R.; Tao, S.; Shen, H.; Huang, Y.; Chen, H.; Balkanski, Y.; Boucher, O.; Ciais, P.; Shen, G.; Li, W.; et al. Trend in Global Black Carbon Emissions from 1960 to 2007. *Environ. Sci. Technol.* **2014**, *48*, 6780–6787, doi:10.1021/es5021422.

248. Collaud Coen, M.; Andrews, E.; Lastuey, A.; Petkov Arsov, T.; Backman, J.; Brem, B.T.; Bukowiecki, N.; Couret, C.; Eleftheriadis, K.; Flentje, H.; et al. Multidecadal Trend Analysis of in Situ Aerosol Radiative Properties around the World. *Atmos. Chem. Phys.* **2020**, *20*, 8867–8908, doi:10.5194/acp-20-8867-2020.

249. Wendisch, M.; Macke, A.; Ehrlich, A.; Lüpkes, C.; Mech, M.; Chechin, D.; Dethloff, K.; Velasco, C.B.; Bozem, H.; Brückner, M.; et al. The Arctic Cloud Puzzle: Using ACLOUD/PASCAL Multiplatform Observations to Unravel the Role of Clouds and Aerosol Particles in Arctic Amplification. *Bull. Am. Meteorol. Soc.* **2019**, *100*, 841–871.

250. Boy, M.; Thomson, E.S.; Acosta Navarro, J.-C.; Arnalds, O.; Batchvarova, E.; Bäck, J.; Berninger, F.; Bilde, M.; Brasseur, Z.; Dagsson-Waldhauserova, P.; et al. Interactions between the Atmosphere, Cryosphere, and Ecosystems at Northern High Latitudes. *Atmos. Chem. Phys.* **2019**, *19*, 2015–2061.

251. Thomas, J.L.; Stutz, J.; Frey, M.M.; Bartels-Rausch, T.; Altieri, K.; Baladima, F.; Browse, J.; Dall'Osto, M.; Marelle, L.; Mouginot, J.; et al. Fostering Multidisciplinary Research on Interactions between Chemistry, Biology, and Physics within the Coupled Cryosphere-Atmosphere System. *Elem Sci Anth* **2019**, *7*, 58.

252. Losi, N.; Markuszewski, P.; Rigler, M.; Gregorič, A.; Močnik, G.; Drozdowska, V.; Makuch, P.; Zielinski, T.; Pakszys, P.; Kitowska, M.; et al. Anthropic Settlements' Impact on the Light-Absorbing Aerosol Concentrations and Heating Rate in the Arctic. *Atmosphere (Basel).* **2023**, *14*, 1768.

253. Ferrero, L.; Bernardoni, V.; Santagostini, L.; Cogliati, S.; Soldan, F.; Valentini, S.; Massabò, D.; Mo, G. Science of the Total Environment Consistent Determination of the Heating Rate of Light-Absorbing Aerosol Using Wavelength- and Time-Dependent Aethalometer Multiple-Scattering Correction. **2021**, *791*, doi:10.1016/j.scitotenv.2021.148277.

254. Tian, P.; Liu, D.; Zhao, D.; Yu, C.; Liu, Q.; Huang, M.; Deng, Z.; Ran, L.; Wu, Y.; Ding, S.; et al. In Situ Vertical Characteristics of Optical Properties and Heating Rates of Aerosol over Beijing. *Atmos. Chem. Phys.* **2020**, *20*, 2603–2622, doi:10.5194/acp-20-2603-2020.

255. Bernardoni, V.; Ferrero, L.; Bolzacchini, E.; Corina Forello, A.; Gregorič, A.; Massabò, D.; Mocnik, G.; Prati, P.; Rigler, M.; Santagostini, L.; et al. Determination of Aethalometer Multiple-Scattering Enhancement Parameters and Impact on Source Apportionment during the Winter 2017/18 EMEP/ACTRIS/COLOSSAL Campaign in

Milan. *Atmos. Meas. Tech.* **2021**, *14*, 2919–2940, doi:10.5194/amt-14-2919-2021.

256. Luca, F.; Losi, N.; Rigler, M.; Gregorič, A.; Colombi, C.; D'Angelo, L.; Cuccia, E.; others Determining the Aethalometer Multiple Scattering Enhancement Factor C from the Filter Loading Parameter. *Sci. Total Environ.* **2024**, *in press*.

257. Schmid, O.; Artaxo, P.; Arnott, W.P.; Chand, D.; Gatti, L. V; Frank, G.P.; Hoffer, A.; Schnaiter, M. And Physics Spectral Light Absorption by Ambient Aerosols Influenced by Biomass Burning in the Amazon Basin . I : Comparison and Field Calibration of Absorption Measurement Techniques. **2006**, 3443–3462.

258. Arnott, W.P.; Hamasha, K.; Moosmüller, H.; Sheridan, P.J.; Ogren, J.A. Towards Aerosol Light-Absorption Measurements with a 7-Wavelength Aethalometer: Evaluation with a Photoacoustic Instrument and 3-Wavelength Nephelometer. *Aerosol Sci. Technol.* **2005**, *39*, 17–29.

259. Virkkula, A.; Chi, X.; Ding, A.; Shen, Y.; Nie, W.; Qi, X.; Zheng, L.; Huang, X.; Xie, Y.; Wang, J.; et al. On the Interpretation of the Loading Correction of the Aethalometer. *Atmos. Meas. Tech.* **2015**, *8*, 4415–4427, doi:10.5194/amt-8-4415-2015.

260. Sakerin, S.M.; Kabanov, D.M.; Kopeikin, V.M.; Kruglinsky, I.A.; Novigatsky, A.N.; Pol'kin, V. V.; Shevchenko, V.P.; Turchinovich, Y.S. Spatial Distribution of Black Carbon Concentrations in the Atmosphere of the North Atlantic and the European Sector of the Arctic Ocean. *Atmosphere (Basel).* **2021**, *12*, doi:10.3390/atmos12080949.

261. Xing, J.; Bian, L.; Hu, Q.; Yu, J.; Sun, C.; Xie, Z. Atmospheric Black Carbon along a Cruise Path through the Arctic Ocean during the Fifth Chinese Arctic Research Expedition. *Atmosphere (Basel).* **2014**, *5*, 292–306, doi:10.3390/atmos5020292.